Freie Universität Berlin

Temporal Variations of Crustal Properties in Northern Chile Analyzed with Receiver Functions and Passive Image Interferometry

Dissertation

eingereicht von

Tom Richter

im
Fachbereich Geowissenschaften
der Freien Universität Berlin
2014

Tag der Abgabe: 13.01.2014
Tag der Disputation: 28.02.2014

1. Gutachter: Prof. Dr. Rainer Kind
2. Gutachter: Prof. Dr. Serge A. Shapiro

Abstract

This thesis analyzes temporal variations of crustal properties in northern Chile. The seismic broadband stations of the Integrated Plate Boundary Observatory Chile which started operating in 2006 deliver the data for this work. In the neighborhood of the seismic stations a M_W 7.7 earthquake occurred near Tocopilla on 14 November 2007 at 52 km depth. Velocity changes following large earthquakes have been observed by different authors in ambient noise data. There are indications that also receiver functions could be used for that purpose. Though the origin of crustal velocity changes is still debated, they certainly provide insights into physical processes in the Earth's crust.

In this work I employ two complementary methods to study the velocity variations. In the first part of the work, the feasibility to use receiver functions for monitoring purposes in northern Chile is investigated and an appropriate method is developed. The receiver function technique could permit to locate possible velocity variations in depth. To avoid varying travel paths of different events the arrival of converted phases is compared for events located in a small source region. Although temporal variations are found in this study, the conclusion on a spatially persistent velocity change is not possible because statistical variations are still too high.

In the second part of the thesis the temporal variability of Green's functions constructed from the cross- and auto-correlation of ambient noise is studied with the help of a technique called passive image interferometry. Daily cross-correlation and autocorrelation functions are calculated over a period of 5 years for low (under 0.5 Hz) and high (above 1 Hz) frequencies. Earthquake and temperature related velocity changes in the correlation functions are observed only for high frequencies. The necessary stacking over 10 days hides potential velocity changes on a shorter time scale for low frequencies. Short-term velocity drops recovering after several days to weeks are observed for the Tocopilla earthquake at most stations. At the two stations PB05 and PATCX a velocity decrease is observed, which recovers over the course of around two years. While station PB05 is located in the rupture area of the Tocopilla earthquake this is not the case for station PATCX. Station PATCX is situated in an area with particular geological conditions and presents superior sensitivity to ground acceleration and periodic surface induced changes. Due to this high sensitivity a velocity response of several regional earthquakes at PATCX is observed. It can be shown that a linear relationship between the amplitude

of velocity drops and peak ground acceleration exists for data from a single station. This relationship does not hold true when comparing different stations due to the different sensitivities of the station environments. Besides, periodic annual velocity changes measured at PATCX are presented. By analyzing data at a temporal resolution below one day it is possible to identify velocity changes with a period of 24 hours. The results indicate an atmospheric origin of the velocity changes that can be confirmed with a model based on thermally induced stress. This comprehensive model explains the frequency and lag time dependence of the temperature-related seismic velocity changes involving the distribution of temperature fluctuations, the relationship between temperature, stress and velocity change plus autocorrelation sensitivity kernels.

Zusammenfassung

Diese Dissertation analysiert zeitliche Variationen der Krusteneigenschaften im Norden Chiles. Die seismischen Breitbandstationen des „Integrated Plate Boundary Observatory Chile“, das 2006 gestartet wurde, liefern die Daten für diese Arbeit. In der Nähe von Tocopilla in 52 km Tiefe wurde am 14. November 2007 ein M_W 7,7 starkes Erdbeben registriert. Geschwindigkeitsveränderungen nach großen Erdbeben konnten von verschiedenen Autoren mit Hilfe von Techniken, die das seismische Rauschen benutzen, nachgewiesen werden. Es gibt auch Hinweise darauf, dass Receiver-Funktionen für diesen Zweck verwendet werden könnten. Der Ursprung der krustalen Geschwindigkeitsänderungen wird noch diskutiert, sicher ist jedoch, dass sie wertvolle Einblicke in die physikalischen Prozesse der Erdkruste liefern.

In dieser Arbeit verwende ich zwei komplementäre Methoden, um Geschwindigkeitsvariationen zu studieren. Im ersten Teil der Arbeit wird untersucht, ob es möglich ist mit Hilfe von Receiver-Funktionen im Norden Chiles zeitliche Veränderungen der Geschwindigkeit nachzuweisen. Die Receiver-Funktionen-Technik könnte es erlauben, mögliche Geschwindigkeitsschwankungen in der tieferen Kruste zu beobachten. Um schwankende Laufwege und Ankunftszeiten der konvertierten Phasen von verschiedenen Erdbeben zu vermeiden, wird nur die Variation der Ankunftsverzögerung für Erdbeben aus einer kleinen Quellregion verglichen. Obwohl zeitliche Variationen in dieser Studie beobachtet werden, kann der Schluss auf eine räumlich ausgedehnte Geschwindigkeitsänderung aufgrund von immer noch zu hohen statistischen Variationen nicht erfolgen.

Im zweiten Teil der Arbeit wird die zeitliche Variabilität Greenscher Funktionen, die durch Kreuz- und Autokorrelation des seismischen Rauschens konstruiert werden, mit Hilfe einer Streckungs- und Stauchungstechnik (Passive Image Interferometry) untersucht. Aus den Daten eines Tages konstruierte Kreuzkorrelations- und Autokorrelationsfunktionen werden über einen Zeitraum von 5 Jahren für niedrige (unter 0,5 Hz) beziehungsweise hohe (über 1 Hz) Frequenzen berechnet. Von Erdbeben und Temperaturschwankungen induzierte Geschwindigkeitsänderungen in den Korrelationsfunktionen werden für hohe Frequenzen beobachtet. Die für niedrige Frequenzen notwendige Stapelung über 10 Tage verdeckt potenzielle Geschwindigkeitsänderungen, die auf einer kürzeren Zeitskala erfolgen. Kurzzeitige Geschwindigkeitsabfälle, welche sich nach mehreren Tagen bis Wochen wieder regenerieren, werden für das Tocopilla-Erdbeben bei den meisten Stationen beobachtet. An den zwei Stationen PB05 und PATCX wird ein länger andauernder Geschwindigkeitsrückgang beobachtet, so dass erst im Laufe von etwa zwei Jahren das Geschwindigkeitsniveau vor dem Erdbeben erreicht wird. Während die Station PB05

über der Bruchfläche des Tocopilla-Erdbebens liegt, trifft dies auf die Station PATCX nicht zu. PATCX liegt in einem Gebiet mit besonderen geologischen Bedingungen und hat eine höhere Sensitivität gegenüber Bodenbeschleunigungen und periodisch induzierten oberflächennahen Veränderungen. Aufgrund dieser hohen Empfindlichkeit ist eine vorübergehende Geschwindigkeitsreduktion bei mehreren regionalen Erdbeben an der Station PATCX beobachtbar. Es kann gezeigt werden, dass eine lineare Beziehung zwischen der Amplitude der Geschwindigkeitsreduktion und der Spitzenbodenbeschleunigung für Daten einer Station vorhanden ist. Diese Beziehung gilt nicht beim Vergleich verschiedener Stationen aufgrund der unterschiedlichen Empfindlichkeit der Stationsumgebungen. Außerdem werden periodisch auftretende, jährliche Geschwindigkeitsänderungen an der Station PATCX gemessen. Durch die Analyse der Daten mit einer zeitlichen Auflösung von unter einem Tag können auch Geschwindigkeitsänderungen mit einer Periodizität von 24 Stunden nachgewiesen werden. Die Ergebnisse implizieren einen atmosphärischen Ursprung der Geschwindigkeitsänderungen, der mit einem Modell, das thermisch induzierte Spannungen beschreibt, bestätigt werden kann. Dieses Modell erklärt die Abhängigkeit der temperaturbedingten seismischen Geschwindigkeitsänderungen von der Frequenz und vom ausgewerteten Zeitfenster der benutzten Daten und umfasst die Verteilung der Temperaturschwankungen, die Beziehung zwischen Temperatur-, Spannungs- und Geschwindigkeitsvariationen sowie räumliche Kernel für die Empfindlichkeit der Autokorrelationsfunktionen.

Contents

1. Introduction

Geophysical research is not only concerned with the study of Earth's structure and its atmosphere but also involves understanding the physical processes inside and outside the Earth. Plate tectonics for example is a concept involving a system of processes inside the Earth's crust and mantle, and is therefore a subject of scientific interest. Tectonic plates move and bend at their boundaries according to the elastic rebound theory culminating in the release of stored energy by earthquakes. Monitoring physical parameters is a substantial contribution to understand these and other geophysical processes.

Continuous observation of geophysical parameters of the atmosphere and the surface of the Earth often is technically feasible. The monitoring of physical parameters of the Earth's subsurface and interior is more challenging. Seismology is able to monitor seismic P- and S-wave velocities by repeated experiments with identical source and receiver locations. Monitoring experiments using explosive sources (e.g. *McEvilly and Johnson*, 1974; *Li et al.*, 1998, 2003, 2006; *Nishimura et al.*, 2000; *Niu et al.*, 2008) have been employed since almost 40 years. Among the disadvantages of explosive sources are their relatively high costs and the low temporal resolution dependent on the repetition intervals of the shots. Air gun shots or artificial vibrators are cheaper sources that can be used with a shorter repeat time and therefore have a better temporal resolution on one hand, but are less powerful and cover only a small area on the other hand (e.g. *Reasenberg and Aki*, 1974; *Ando et al.*, 1980; *Yukutake et al.*, 1988; *Ikuta et al.*, 2002; *Wegler et al.*, 2006).

Poupinet et al. (1984) discovered temporal variations using the coda of earthquake doublets with identical source parameters which consist of multiple scattered waves. If the medium is subject to a homogeneous velocity variation the time shifts are proportional to the lapse time. Therefore time shifts in the late coda can be better observed than time shifts of unscattered P- and S-waves. *Snieder et al.* (2002) and *Snieder* (2006) termed this technique *coda wave interferometry* and embedded it into a theoretical framework. Monitoring with the help of earthquakes embracing coda wave interferometry have been conducted by different authors (e.g. *Poupinet et al.*, 1984; *Ratdomopurbo and Poupinet*, 1995; *Peng and Ben-Zion*, 2006).

Lately new techniques evolved using ambient seismic noise. The Green's function between two receivers can be constructed by a cross-correlation of ambient noise data. The Green's function can be described as the response of the medium to a peak-like point source at one receiver (called virtual source) as seen by the other receiver. This concept was developed first in acoustics (*Weaver and Lobkis*, 2001, 2002; *Lobkis and Weaver*, 2001), and was introduced to seismology by *Shapiro and Campillo* (2004). The *Green's function retrieval* opens the field to a range of new applications when it is combined with other seismological methods like surface wave tomography (*Shapiro et al.*, 2005) or the mentioned coda wave interferometry. Especially, the permanent availability of ambient noise qualifies it for the use in monitoring applications. The usage of ambient noise eliminates the necessity of repeating sources, like earthquake multiplets or repeatable active sources.

Passive image interferometry introduced by *Sens-Schönfelder and Wegler* (2006) combines noise-based Green's functions with coda wave interferometry. Green's functions can be calculated for different time periods and a stretching technique is used to estimate relative velocity variations. Although an isotropic noise field is needed for the retrieval of a Green's function, this is not the case for monitoring applications. Here, the temporal stability of the cross-correlation functions (respective designated noise sources) is a sufficient requirement for the successful application of passive image interferometry.

On the one hand, precision better than 0.1 % can be achieved with passive image interferometry. On the other hand, velocity variations can not be located easily. Furthermore, passive imaging is most sensitive only to near-surface velocity fluctuations depending on the frequency range used. For analyzing velocity variations in the deeper crust I want to use additionally a monitoring technique based on receiver functions. This is motivated by a study of *Audet* (2010) who detected a drop in the level of power spectral densities of receiver functions due to the 2003 M6.5 San Simeon earthquake. Receiver functions adversely have a lower precision depending on the variation of hypocenter locations of the different teleseismic earthquakes used. The advantage is that receiver functions are not only sensitive to the upper crust, but also to the deeper crust and upper mantle.

Different authors have observed seismic velocity changes due to different causative processes. *Sens-Schönfelder and Wegler* (2006) detected seasonal velocity changes caused by changes in fluid saturation of the medium due to precipitation and ground water level changes. Seasonal velocity changes were also detected by *Meier et al.* (2010), *Hobiger et al.* (2012) and other authors. *Reasenberg and Aki* (1974) and *Yukutake et al.* (1988) observed changes in the seismic velocity due to tidal straining and atmospheric pressure changes. Coseismic velocity drops were detected for different events, e.g. the

2004 M_W 6.6 Mid-Niigata earthquake (*Wegler and Sens-Schönfelder*, 2007; *Wegler et al.*, 2009), the 2008 M_W 7.9 Wenchuan earthquake (*Chen et al.*, 2010; *Froment et al.*, 2013), the 2008 M_W 6.9 Iwate-Miyagi Nairiku earthquake (*Hobiger et al.*, 2012) and the 2011 M_W 9.0 Tohoku earthquake (*Takagi and Okada*, 2012; *Sawazaki and Snieder*, 2013). In most cases the velocity recovers in the course of several years after the earthquake. *Rivet et al.* (2011) related the velocity change due to a M 7.5 slow slip event in Mexico not emitting any seismic waves to the strain rate. *Maeda et al.* (2010) speculated about a fluid induced origin of velocity decreases correlating with earthquake swarms in a geothermal environment. The physical meaning of seismic velocity reductions due to crustal earthquakes is still under debate. *Rubinstein and Beroza* (2004) and *Sens-Schönfelder and Wegler* (2011) propose the following mechanisms: A static deeply penetrating stress change due to the event causes a closure and opening of cracks and therefore changes the seismic velocity. However, stress changes and velocity changes should be observed with both positive and negative polarity. Another model assumes physical damage of the fault zone resulting in lower velocities. A different proposed mechanism assumes damage caused by strong ground motion in the shallow subsurface. Models involving pore pressure variations due to changes of the amount of water in the pores can be used to describe velocity variations corresponding to ground water level change.

In this thesis I use the receiver function method and passive image interferometry to monitor seismic velocities in the subsurface in northern Chile. The region between Mejillones in the south and Arica in the north last ruptured completely in 1877. The region is therefore considered to be a seismic gap, because the continuing subduction of the Nazca plate is building up stress in locked areas of the subduction surface which will probably be released in a future major earthquake. The *Integrated Plate boundary Observatory in northern Chile* (IPOC), a multi-parameter network with around 20 seismic stations, has been designed to observe physical processes before, during and after the expected major event. The data of the IPOC seismic stations are used to analyze the variation of seismic velocities of the north Chilean subsurface caused by the M_W 7.7 Tocopilla earthquake (14 November 2007) and other effects.

This thesis starts with a description of the tectonic and geological setting in northern Chile (chapter 2) and continues with the presentation of the IPOC seismic network (chapter 3). Chapter 4 deals with the receiver function monitoring technique and its results. Passive image interferometry and its applications are presented in chapter 5. After introducing the method in sections 5.1 and 5.2, low-frequency cross-correlations are analyzed for temporal changes of the seismic velocity in section 5.3. Section 5.4 describes

the observations of the high-frequency autocorrelations that include the co-seismic variations of all IPOC stations and the periodic variations at station PATCX. A model that explains the periodic changes as caused by thermal stresses in the subsurface is introduced and its predictions are compared with the observations (section 5.5). Finally, conclusions are drawn in chapter 6.

2. Tectonic and geological setting in northern Chile

The Andean Cordillera forms a more than 8000 km long continuous mountain chain along the western margin of the South American continent with elevations up to 7000 m above sea level. The orogeny of the Andes is a result of Pacific seafloor subducting under the South American plate causing a compression and uplift of the continental crust. Volcanism is spread over four separate regions – the Northern, Central (CVZ), Southern and Austral Volcanic Zones. A schematic map of the South American and Pacific plates with the main geological features is displayed in figure 2.1.

The central sector of the Central Andes between the latitudes 14°S and 27°S is characterized by classical Andean type subduction of the 50 to 60 Ma old (*Norabuena et al.*, 1998; *Angermann et al.*, 1999) Nazca plate. The dip angle of subducted Nazca plate is around 25° up to a depth of 90 to 100 km (*Stern*, 2004). However one distinct feature is the dip angle varying in strike direction at greater depth from flat-slab segments to normal subduction (*Engdahl et al.*, 1995, 1998). The flat-slab segments are located between the volcanic zones and lack recent volcanic activity. The transition between flat and normal subduction can be gradual or associated with sharp bends in the subducting plate (*Stern*, 2004). Sharp bends occur in the area of the Nazca and Juan Fernández ridges. The present-day convergence rate between the Pacific Nazca and South American plate is around 6.5 cm per year (*Angermann et al.*, 1999).

Apart from the Peru-Chile trench with the deepest point at around 8000 m below sea level the along-strike topography in northern Chile is characterized by two parallel chains of mountains separated by a central valley (figure 2.2). These main geological provinces are from west to east the Coastal Cordillera with elevations between 1000 and 2000 m consisting predominantly of Late Paleozoic and Mesozoic volcanic rocks, the Central Depression filled by Mesozoic to Quaternary sediments and the Andes with elevations from 4000 m up to 7000 m whose primary uplift dates back to a Miocene event (*Pankhurst and Hervé*, 2007). The elevation of the Andes is accompanied by significant crustal shortening and eastward thrusting.

As *Allmendinger et al.* (1997) pointed out the Andean mountain range in northern

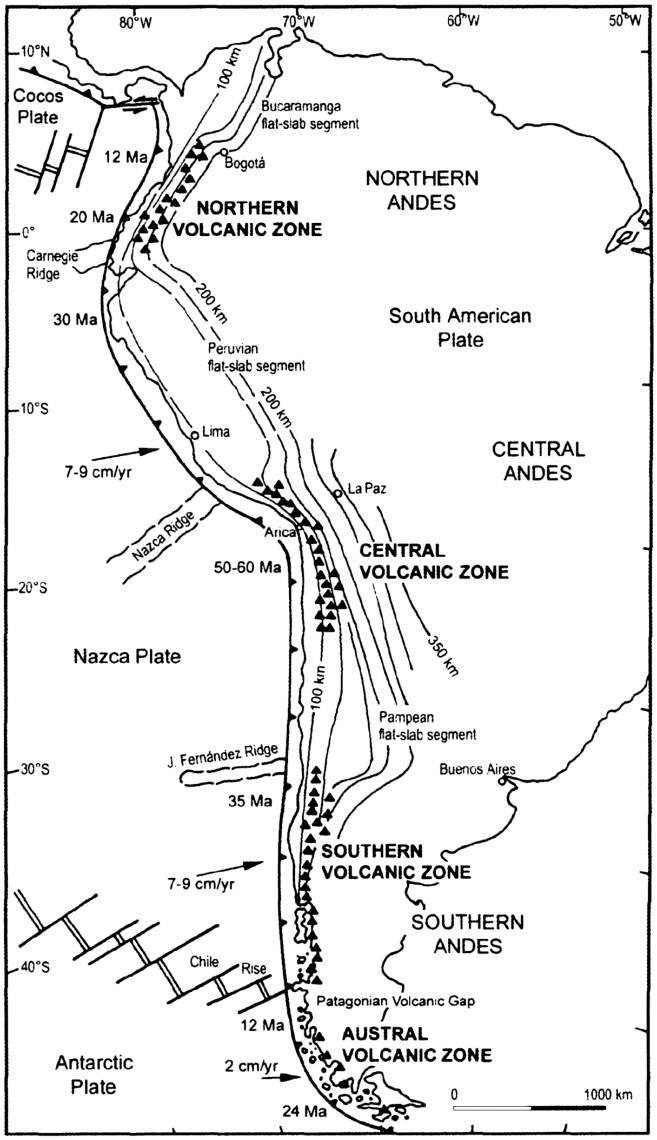

Figure 2.1.: Schematic map of South America and the Pacific oceanic plates modified by *Stern* (2004) from *Ramos and Alemán* (2000). Displayed are the four volcanic zones in the Andes, subduction geometry indicated by depth to the Wadati–Benioff zone (*Engdahl et al.*, 1995, 1998), oceanic ridges (*Gutscher*, 2002), ages of oceanic plates close to the Peru-Chile trench, and convergence rates and directions at the plate boundaries to the South American plate (*Norabuena et al.*, 1998; *Angermann et al.*, 1999).

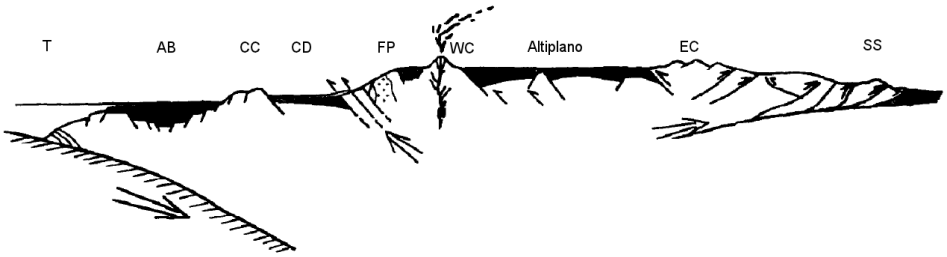

Figure 2.2.: Schematic west-to-east section across the subduction segment in northern Chile modified after *Muñoz and Charrier* (1996). Abbreviations: T Trench, AB Arica Basin, CC Coastal Cordillera, CD Central Depression, FP Forearc Precordillera, WC Western Cordillera, EC Eastern Cordillera, SS Subandean Sierras

Chile is composed of the Forearc Precordillera, the Western Cordillera, the Altiplano and Puna plateaus, the Eastern Cordillera and Subandean Ranges. In the Chilean Precordillera, a belt of intense Incaic (38 Ma) shortening involves rocks of the early Tertiary and Mesozoic magmatic arc as well as pre-Andean igneous and basement rocks (e.g. *Scheuber et al.*, 1994). The Western Cordillera, the modern magmatic front, is marked by a line of stratovolcanoes overlying older ignimbrite sheets. The uplift of the Altiplano and Puna plateaus is considered to be the result of a combination of crustal shortening and thickening, and lithospheric thinning (e.g. *Isacks*, 1988). Broad band analysis indicate that the crust is around 70 km thick under the western edge of the Altiplano (*Beck et al.*, 1996) and around 50 km under the Puna plateau (*Yuan et al.*, 2000). The Altiplano surface is covered by several large salars with Quaternary fill, and locally Late Oligocene to Recent volcanic rocks, including immense Late Miocene to Pliocene ignimbrite deposits at the southern end of the plateau. The eastern limit of the plateau is marked by the Eastern Cordillera province. The Subandean belt is a classic thin-skinned fold and thrust belt (*Roeder and Chamberlain*, 1995; *Sheffels*, 1990).

The convergence of the oceanic Nazca plate is building up stress that is released in ruptures of large segments of the interface of the two plates. Along the Chilean and southern Peruvian margin, all segments have ruptured at least once in the past 150 years. After the Maule earthquake near Concepción in February 2010, the segment along the northern Chilean coast between 23°S and 18°S is considered to be the most likely segment to re-rupture (*Kelleher*, 1972; *Comte and Pardo*, 1991). The entire segment last ruptured in 1877 in a M 8.8 earthquake. The segment to the north ruptured last in 1868 and to a large part in 2001. The segment to the south ruptured in the M 8.1 1995 Antofagasta earthquake. Figure 2.3 compiled by *Béjar-Pizarro et al.* (2010) shows a map of significant ruptures in northern Chile and southern Peru.

In November 2007 the M 7.7 Tocopilla earthquake ruptured a small part of the seismic gap left behind by the 1877 earthquake. The hypocenter was located at 22.30°S, 69.89°W at a depth of 37 km according to GEOFON (`http://geofon.gfz-potsdam.de/`). *Schurr et al.* (2012) pointed out that the moment tensor double couple of the main shock shows a pure thrust mechanism on a weakly dipping plane with the slip vector parallel to the plate convergence. The source rupture propagated with about 2.8 km/s and lasted for about 40 s based on kinematic inversions of seismic data (*Delouis et al.*, 2009; *Peyrat et al.*, 2010). It ruptured the deeper part of the subduction interface over a length of 150 km. The Mejillones peninsula acted as a propagation barrier like in the 1995 Antofagasta earthquake. The modeled slip distribution shown in figure 2.4 consists of two patches, one with the maximum amplitude near the epicenter and one at a latitude

of 23.0°S. In the southern part of the rupture aftershocks and postseismic slip propagate up to a depth of 10 km and do not correlate with the slip of the main event. In contrast there is good correlation of aftershock distribution and seismic slip without postseismic slip in the northern part, where the main seismogenic zone extends just to a depth of 35 km (see figure 2.4). This is probably because of the total locking of the upper segment of the subduction interface (*Schurr et al.*, 2012).

The Tocopilla earthquake released about 2.5 % of the total moment deficit accumulated in the northern Chile seismic gap (*Béjar-Pizarro et al.*, 2010). It can be noticed that the 2007 Tocopilla earthquake is similar to the M 7.5 earthquake that broke in 1987 the deeper region of the seismogenic interface, immediately downdip of the centroid of the 1995 M 8.1 Antofagasta earthquake (*Béjar-Pizarro et al.*, 2010).

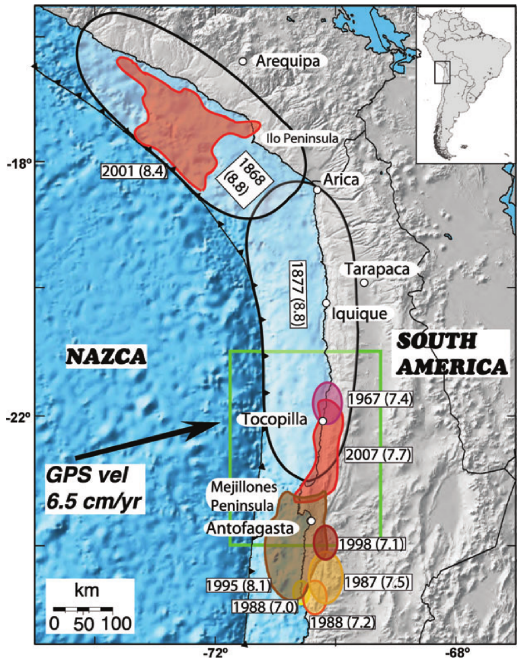

Figure 2.3.: Map of rupture areas with date and magnitude of historical and recent earthquakes in northern Chile compiled by *Béjar-Pizarro et al.* (2010). Estimates of the rupture areas of the two large historical earthquakes in South Peru and Iquique are shown in transparent gray ellipses. Color filled areas represent rupture areas of large shallow interplate thrust earthquakes. The convergence rate and direction of Nazca plate are shown by the black arrow (*Angermann et al.*, 1999) and the trench is shown by the black barbed line.

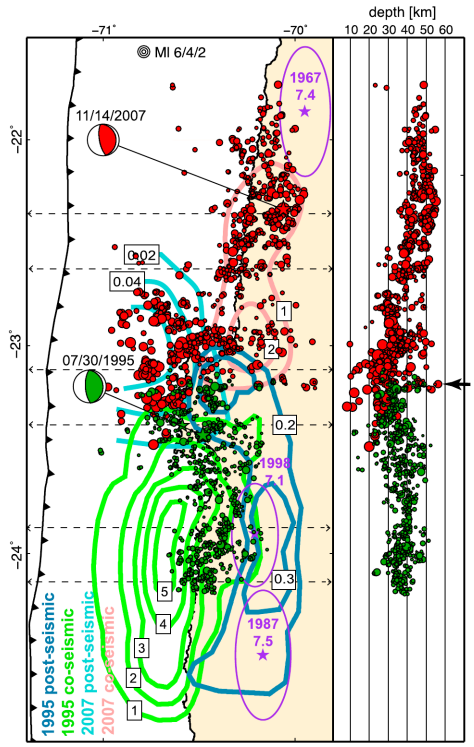

Figure 2.4.: Slip and aftershocks of the M 8.1 1995 Antofagasta and M 7.7 2007 Tocopilla earthquakes compiled by *Schurr et al.* (2012). Green circles are relocated aftershocks of the Antofagasta event (*Nippress and Rietbrock*, 2007). Red circles indicate aftershocks of the Tocopilla event. Slip and net aseismic afterslip of the Antofagasta event are from *Chlieh et al.* (2004), afterslip for the Tocopilla event from *Béjar-Pizarro et al.* (2010). The values in the boxes are slip in meters. Displayed parameters of the main shocks are epicenter (stars) and moment tensor (beachballs). Three events with a magnitude bigger than 7 are additionally indicated (*Malgrange and Madariaga*, 1983; *Pritchard et al.*, 2006).

3. Seismological part of the Integrated Plate boundary Observatory Chile

The Integrated Plate boundary Observatory Chile (IPOC, *Schurr et al.*, 2009) is a multi-parameter observatory operated by a collaboration of European and South-American scientists. One important part of IPOC is its seismograph network. It consists of 20 broadband stations equipped with STS-2/N seismometers with 100 Hz acquisition rate. Installation sites were chosen carefully and at most sites a cavern was blasted into bedrock to ensure stable conditions for the high resolution and dynamic sensors. 16 of the stations (PB01 to PB17) are operated by the *Deutsches Geoforschungszentrum GFZ* and 4 stations (HMBCX, MNMCX, PSGCX, PATCX) by the *Institut de Physique du Globe Paris* (IPGP). The first station PB01 was installed in February 2006 followed by the installations of PB02 to PB05 in May 2006. In 2007 the French stations started operating along with PB06 to PB08. In the course of the years stations PB09 to PB17 got deployed. PB13 was closed in October 2011 and was replaced by station PB16 at a close-by location. Additionally I use data of the nearby GEOFON station LVC. Because the 100 Hz channel of station LVC is not working properly, the 20 Hz data channel will be used. Figure 3.1 shows a map of the study region with topographic information, station locations, epicenter, moment tensor and rupture slip distribution of the Tocopilla earthquake and the Peru-Chile Trench. A table with station coordinates is given in the appendix A.1. The data availability is very good and plotted in figure 3.2. 12 stations were operating when the Tocopilla earthquake occurred on 14 November 2007.

The IPOC stations are equipped with STS-2/N sensors from the manufacturer Streckeisen. A Guralp CMG-3T sensor is installed at station LVC. The frequency response of both broadband sensors is displayed in figure 3.3. Up to 2 Hz the frequency response of gain and phase are identical for both instruments. Above 2 Hz the phase response is slightly different and the gain of the Guralp instrument drops away at higher frequencies. The lower corner frequency is 0.008 Hz for both instruments. The upper corner frequency is 43 Hz for he Guralp sensor and 84 Hz for the STS-2 sensor. Because of the very flat gain frequency response, instrument correction will be neglected for most parts of this work. Probability density functions of power spectral densities are calculated with the

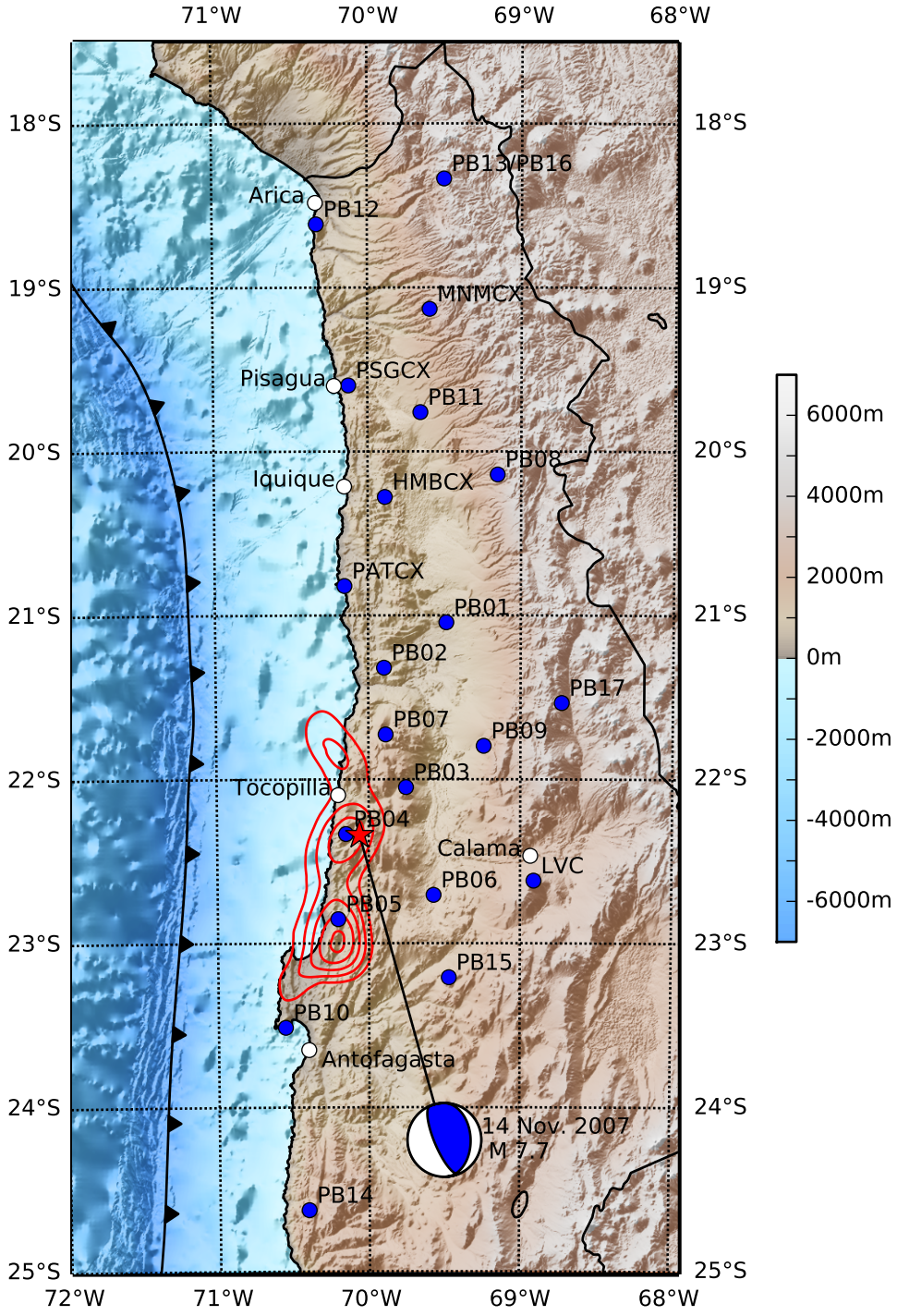

Figure 3.1.: Shaded relief map with IPOC stations, the Tocopilla earthquake, elevation, bathymetry and trench. Epicenter and moment tensor of the Tocopilla earthquake are displayed together with the rupture slip distribution from *Schurr et al.* (2012) showing isolines between 0.5 m and 3.0 m.

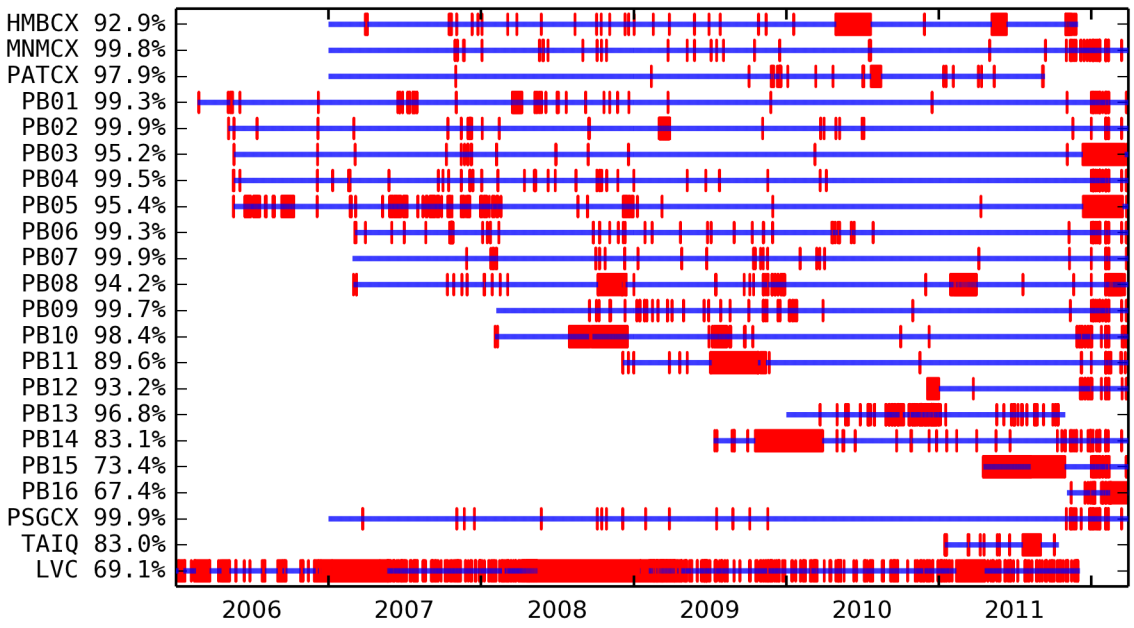

Figure 3.2.: Data availability of IPOC stations and GEOFON LVC station (blue: continuous data, blue and red: data containing gaps, just red: no data available)

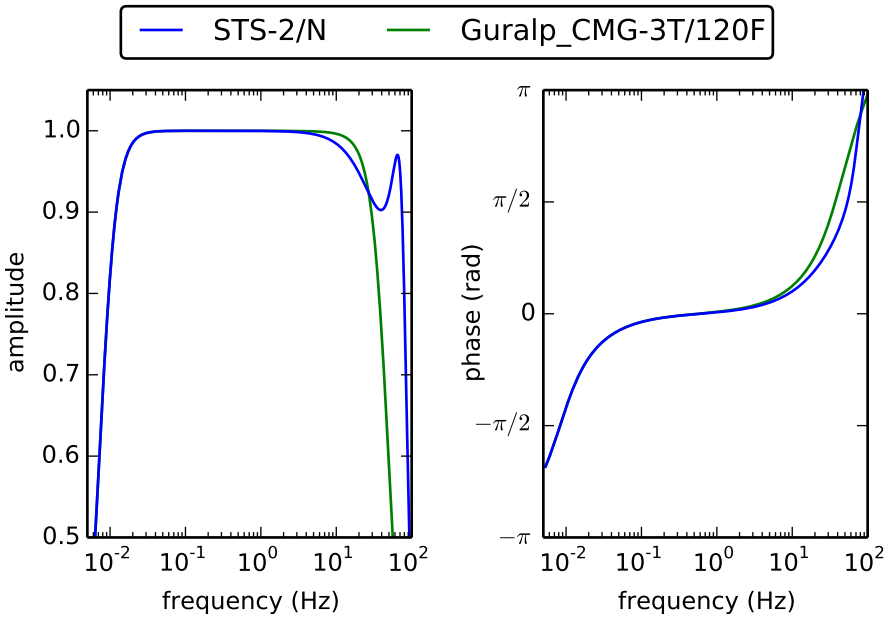

Figure 3.3.: Frequency response of seismometers. STS-2 instruments are used for all IPOC stations. The GEOFON station LVC is equipped with the Guralp sensor.

method described by *McNamara and Buland* (2004). These probabilistic power spectral densities can be used to characterize station sites and are displayed in appendix A.2. All stations show stable conditions with minor transients for long periods probably caused by problems with the mass centering. Only station PB14, which was not installed inside a cavern, shows partially high power levels for periods above 20 s. This fact confirms the high quality of the data for all other stations.

4. Receiver function study

4.1. Method and work flow

The P receiver function method is a popular technique to investigate crustal and upper mantle velocity discontinuities. Basic concept of the method is that a small part of incident P-waves from a teleseismic event gets converted to S-waves at significant discontinuities under the receiver (see figure 4.1). These converted Ps phases arrive at the station after the main P phase. The response function of the receiver side (receiver function) is constructed by removing the source and deep mantle propagation effects. Firstly the S-wave field is separated from the P-wave field by a rotation from the station coordinate system (ZNE - vertical, north, east) to the wave coordinate system (LQT – P-wave polarization, approx. SV-wave polarization, SH-wave polarization). The waveform on the L component is deconvolved from the other components, which removes source side and propagation effects. The resulting functions are the Q and T component of the P receiver function. Multiple reflected waves are also visible in the receiver function. A synthetically calculated receiver function with Ps phase and multiples is displayed in figure 4.2. The conversion points of the rays are called piercing points (figure 4.1).

Data preparation

The work flow is shown in figure 4.3. Data are analyzed with the the help of the Python package ObsPy (*Beyreuther et al.*, 2010). In a first step adequate teleseismic earthquakes with a magnitude bigger than 5.5 are selected. The epicentral distance of the used events is chosen between 27° and 93° from the coordinates of station PB01 in the center of the IPOC array. It must not be too small (waves do not travel deep enough) nor too big (conversion is not efficient because of the steep incidence angle). The data are cut around the arrival time of the P-waves (P-onset), demeaned and detrended. A band-pass filter between 0.5 s and 30 s is applied to suppress signals in the uninteresting frequency bands. Finally data are resampled to 20 Hz.

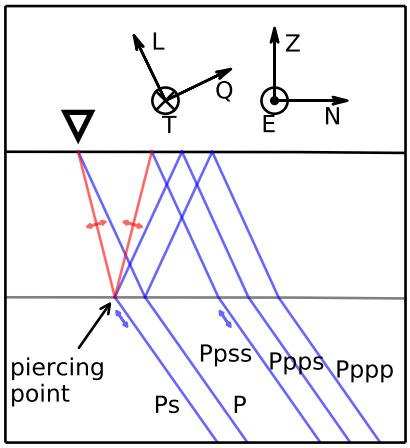

Figure 4.1.: In a two-layer-model part of the incoming P-wave is converted to a S-wave at the layer boundary. Major multiples are Pppp, Ppps and Ppss. The piercing point of the Ps phase is indicated.

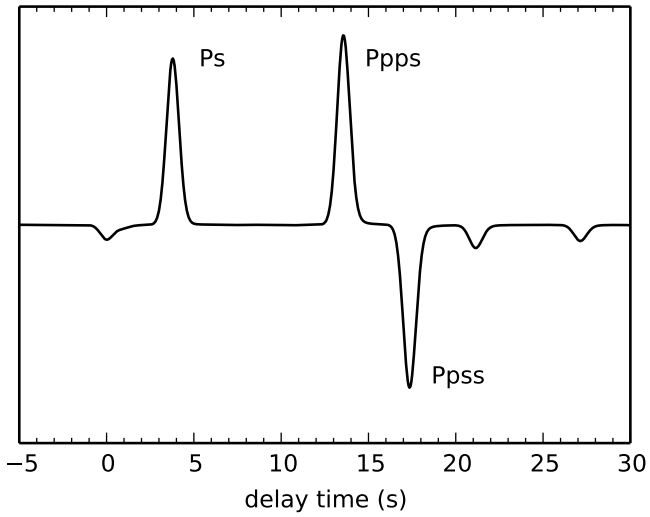

Figure 4.2.: Synthetic receiver function of Q component in a two-layer-model with a discontinuity at 30 km depth. Major phases are labeled. Synthetic receiver functions are calculated with the method described in *Ammon et al.* (1990).

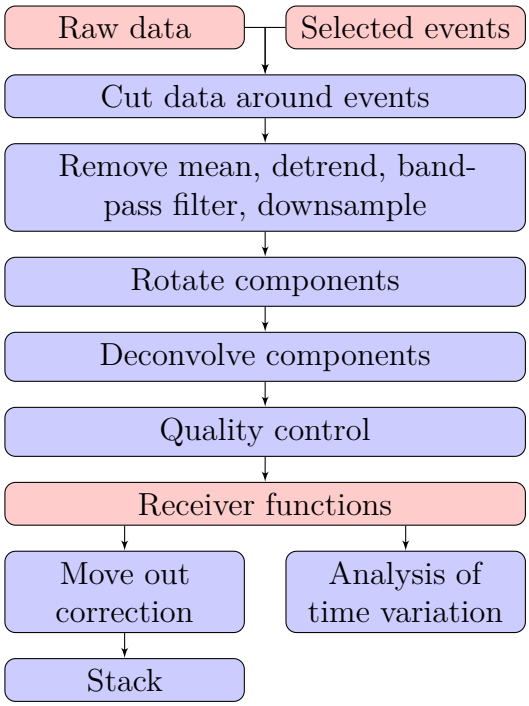

Figure 4.3.: Flow chart of the data processing for receiver function calculations.

Rotation

The separation of the S- and P-wave field is done by rotation. There are two main possibilities to calculate the rotation angles. The first possibility is to use the theoretical back azimuth ϕ between station and event and the incidence angle of the P-wave $\theta = \arcsin(pv_\mathrm{p}/r_\mathrm{e})$ calculated with the help of Snell's law with the ray parameter or angular slowness p, Earth's radius $r_\mathrm{e} = 6371\,\mathrm{km}$ and the P-wave velocity at the surface v_p. The ray parameter p depends on epicentral distance and depth of the event and is computed for the standard *iasp91* Earth model by *Kennett and Engdahl* (1991). The incidence angle is calculated with the P-wave velocity 5.8 km/s of the topmost layer of the *iasp91* model. An error of 10 % in the assumed surface velocity results in an acceptable maximal error of 3° in the incidence angle.

The second possibility is to derive the incidence angle and back azimuth directly from the data e.g. by calculating the eigenvalues of the polarization matrix in a time window around the P-onset. Thus the procedure maximizes the energy on the L component and minimizes the energy on the Q and T component around P-onset. For simplicity the first method is used in this study. The conversion from the left-handed ZNE coordinate system to the right-handed LQT coordinate system can be expressed by the equations

$$\begin{pmatrix} \mathrm{L} \\ \mathrm{Q} \\ \mathrm{T} \end{pmatrix} = \begin{pmatrix} \cos(\theta) & -\sin(\theta)\cos(\phi) & -\sin(\theta)\sin(\phi) \\ \sin(\theta) & \cos(\theta)\cos(\phi) & \cos(\theta)\sin(\phi) \\ 0 & \sin(\phi) & -\cos(\phi) \end{pmatrix} \begin{pmatrix} \mathrm{Z} \\ \mathrm{N} \\ \mathrm{E} \end{pmatrix}. \tag{4.1}$$

Deconvolution

After the rotation there is approximately the P waveform on the L component, the SV waveform on the Q component and the SH waveform on the T component. This is not necessarily valid in the case of anisotropy or lateral heterogeneity beneath the station. The Q component can be considered as the S-response of the medium near the receiver to the incident P-wave. Furthermore the P signal before entering the receiver region is assumed to be similar to the observed P waveform on the L component. This assumption does not hold exactly, because the P response of the medium is recorded on the L component, too. This does not matter, since the P response has got a minor amplitude compared to the direct P-wave. By deconvolving the L component (source) from the Q or T component (response) the response of the medium can be calculated near the receiver to a peak-like source (receiver function). After the deconvolution the traces are aligned so that the P-onset is at 0 s. The time of the Q or T-component receiver

function indicates the delay time between the primary P-wave and converted phases. One disadvantage of this method is that information on the L component e.g. the Ppp multiple is considered part of the source and is therefore not available for analysis. Some authors try to avoid this disadvantage by not performing the deconvolution. Instead they use a plain summation after move out correction (*Kumar et al.*, 2010). Source-side effects cancel when summing over many traces from different source regions.

Different deconvolution techniques are presented by *Ligorría and Ammon* (1999) and references therein. Here, I want to focus on two regularly applied methods. The first method – water-level deconvolution – takes advantage of the fact, that deconvolution in frequency domain is just a division $S_\mathrm{p}/S_\mathrm{s} = S_\mathrm{p}S_\mathrm{s}^*/S_\mathrm{s}S_\mathrm{s}^*$ of source spectrum S_s and response spectrum S_p. S_s^* is the complex conjugate of the source spectrum S_s. To prevent noise in the source spectrum being amplified in frequency bands with a low signal the divisor is replaced by the water-level w if the divisor is smaller than w. Finally a Gauss filter G is applied. The spectrum of the receiver function is calculated with the formula

$$S_\mathrm{rf} = G\frac{S_\mathrm{p}S_\mathrm{s}^*}{\max\left(w, S_\mathrm{s}S_\mathrm{s}^*\right)} \tag{4.2}$$

and is back-transformed to time-domain.

The other deconvolution method works directly in the time domain. The convolution of receiver function and source function can be expressed with matrices:

$$\boldsymbol{p} = \boldsymbol{S}\,\boldsymbol{r} \text{ with } \boldsymbol{S} = \begin{pmatrix} s_0 & s_{N-1} & s_{N-2} & \dots & s_1 \\ s_1 & s_0 & s_{N-1} & \dots & s_2 \\ \dots & & & & \\ s_{N-1} & s_{N-2} & \dots & & s_0 \end{pmatrix} \text{ and } \begin{array}{l} s_\mathrm{i} \text{ ... data points of the} \\ \quad \text{source waveform} \\ N \text{ ... number of data points} \end{array} \tag{4.3}$$

$\boldsymbol{S}$ is the circulant source matrix for circular convolution. $\boldsymbol{p}$ and $\boldsymbol{r}$ are the data vectors of the response and the receiver function, respectively. Equation 4.3 can be solved for $\boldsymbol{r}$ and expanded. Thus the deconvolution of source from response is:

$$\boldsymbol{r} = \boldsymbol{S}^{-1}\boldsymbol{p} = \left(\boldsymbol{S}^\mathsf{T}\boldsymbol{S}\right)^{-1}\boldsymbol{S}^\mathsf{T}\boldsymbol{p}\,. \tag{4.4}$$

$\boldsymbol{S}^\mathsf{T}\boldsymbol{p}$ is the cross-correlation vector between $\boldsymbol{S}$ and $\boldsymbol{p}$. $\boldsymbol{S}^\mathsf{T}\boldsymbol{S}$ is the autocorrelation matrix with entries $\left(\boldsymbol{S}^\mathsf{T}\boldsymbol{S}\right)_{i,j} = \sum_{k=0}^{N-1} s_k s_l$ with $l =$ mod $(k+i-j, N)$ and i, j in the range $0...N-1$. To embrace the existence of noise in the data a spiking factor $w\boldsymbol{I}$ with the identity matrix $\boldsymbol{I}$ is added to the autocorrelation matrix. The inversion of the symmetric Toeplitz matrix is done with the help of the TOEPLITZ package (*Arushanian et al.*,

1983). The final equation for calculating the deconvolution in time-domain is

$$\boldsymbol{r} = \left(\boldsymbol{S}^{\mathsf{T}}\boldsymbol{S} + w\boldsymbol{I}\right)^{-1} \boldsymbol{S}^{\mathsf{T}}\boldsymbol{p}\,. \tag{4.5}$$

Technically both methods are the same, but the solution of the noise problem is implemented differently. For this study the second deconvolution method is used. The autocorrelation matrix $\left(\boldsymbol{S}^{\mathsf{T}}\boldsymbol{S} + w\boldsymbol{I}\right)^{-1}$ and the cross-correlation vector $\boldsymbol{S}^{\mathsf{T}}\boldsymbol{p}$ are both calculated from the L and Q (resp. T) component in a time window $[-20\,\mathrm{s}, 80\,\mathrm{s}]$ around P-onset. The source waveform is cosine tapered at the edges by a length of 5 s beforehand. After several tests the spiking factor is fixed at the typically used value of $w = 1$ to obtain a compromise between noise in the receiver functions (small w) and insufficient compensation for the source time function (large w). Finally L and T components are multiplied by -1, so that a positive phase is seen for a positive velocity contrast as the Moho.

Quality control

Receiver functions of bad quality have to be rejected. In a first step the signal-to-noise ratio of the data before deconvolution is calculated. The signal-to-noise ratio is defined here as the quotient of the maxima of the envelope of the L component of the waveform (before deconvolution) in the time windows $[-5\,\mathrm{s}, 25\,\mathrm{s}]$ and $[-50\,\mathrm{s}, -20\,\mathrm{s}]$ around P-onset. If the signal-to-noise ratio is smaller than 2 the traces are discarded automatically. In a second step traces will be removed after manual inspection if one of the following criteria applies to the data before deconvolution:

- high long-period noise,
- very small signal from the teleseismic earthquake or
- disturbance by local, high-frequency earthquakes.

Move out correction

Converted phases of the same layer in the receiver function are not aligned at the same delay time for different events. This is because waves of different events have different travel paths and the delay time of P- and S-wave depend on the ray parameter of the wave, which itself depends on the epicentral distance and depth of an event. To make receiver functions of different events comparable and stackable a move out correction

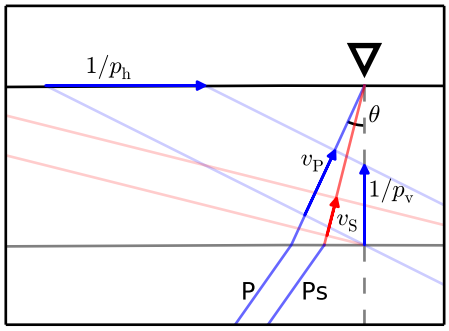

Figure 4.4.: Wave fronts of P- and converted S-wave in a two-layer-model. Marked are the velocities of the P- and S-wave, apparent horizontal and vertical velocities of the P-wave front as an expression for the horizontal and vertical slownesses, and the incidence angle.

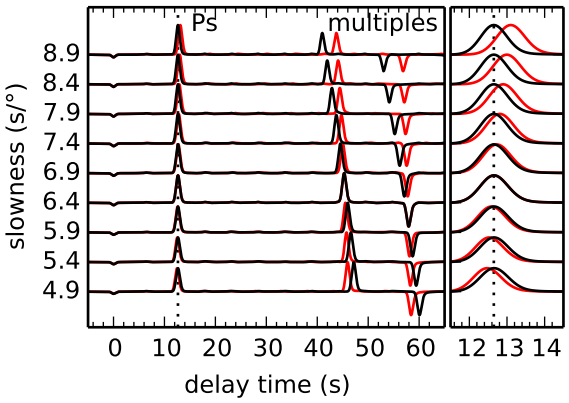

Figure 4.5.: Move out correction for the Ps phase applied to synthetic receiver functions of different slowness in a two-layer model. The Ps phase is aligned by the move out correction (right panel). A different move out correction has to be applied for different phases. Consequently multiples are misaligned in this figure. Red: before, black: after move out correction.

is applied. For this the horizontal and vertical slowness p_h and p_v are introduced. Horizontal slowness p_h and vertical slowness p_v are the decomposition of the inverse of the velocity v^{-1} to a horizontal and a vertical component and represent the inverse of the apparent velocity of the wave front on a horizontal layer or a vertical plain, respectively. Velocity v, p_h, p_v and the incidence angle θ are connected with each other by the equations

$$v^{-2} = p_v^2 + p_h^2\,, \qquad p_h = \frac{\sin\theta}{v}\,, \text{ and} \qquad p_v = \frac{\cos\theta}{v}\,. \tag{4.6}$$

Figure 4.4 displays the geometrical relations between the different slownesses leading to the above equations. Furthermore the horizontal slowness is constant for one ray and its converted waves due to Snell's law. The horizontal slowness is connected to the ray parameter p of a spherical earth (also called slowness) by $p = p_h r_{earth}$. The infinitesimal apparent travel time of P- and S-waves dt_P and dt_S on a vertical surface in a horizontal layer of thickness dz can be expressed with the vertical slowness and therefore is:

$$dt_P = p_{v,P}\,dz = \sqrt{v_P^{-2}(z) - p_h^2}\,dz\,, \qquad dt_S = \sqrt{v_S^{-2}(z) - p_h^2}\,dz\,. \tag{4.7}$$

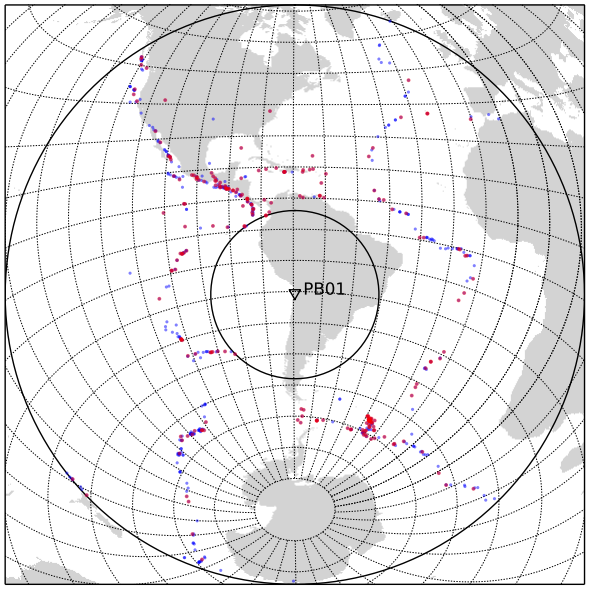

Figure 4.6.: All eligible (blue) and all used (red) events for station PB01. The circles mark epicentral distances of 27° and 93°.

The delay time of a Ps wave which was converted at depth z is given by

$$t_{\mathrm{Ps}}(z,p) = \int_0^z \mathrm{d}t_{\mathrm{S}} - \mathrm{d}t_{\mathrm{P}} = \int_0^z \sqrt{v_{\mathrm{S}}^{-2}(z') - p_{\mathrm{h}}^2} - \sqrt{v_{\mathrm{P}}^{-2}(z') - p_{\mathrm{h}}^2}\,\mathrm{d}z' \,. \tag{4.8}$$

For a data sample of the delay time t_{Ps} the conversion depth z can be calculated for known velocity depth profiles $v_{\mathrm{P}}(z')$, $v_{\mathrm{S}}(z')$ and known ray parameter p. Finally samples at a delay time of t_{Ps} are shifted to the delay time $t_{\mathrm{Ps}}(z, p_{\mathrm{ref}})$ resulting in a receiver function with ray parameter p_{ref}. The common reference slowness of $p_{\mathrm{ref}} = 6.4\,\mathrm{s}/^\circ$ is chosen. With this technique receiver functions of smaller slowness than p_{ref} are stretched and receiver functions of bigger slowness are compressed. For calculating the integrals in equation (4.8) a velocity model is needed. Here the *IASP91* model by *Kennett and Engdahl* (1991) is used. A move out correction on synthetic receiver functions is displayed in figure 4.5. Note that multiple phases are misaligned by a Ps move out correction. Multiple phases can be aligned by a different move out correction with an adapted formula (4.8). Ppss move out correction is e.g. performed with $t_{\mathrm{Ppss}} = \int_0^z (\mathrm{d}t_{\mathrm{P}} + 2\mathrm{d}t_{\mathrm{S}}) - \mathrm{d}t_{\mathrm{P}} = 2\int_0^z \left(v_{\mathrm{S}}^{-2} - p_{\mathrm{h}}^2\right)^{1/2} \mathrm{d}z$.

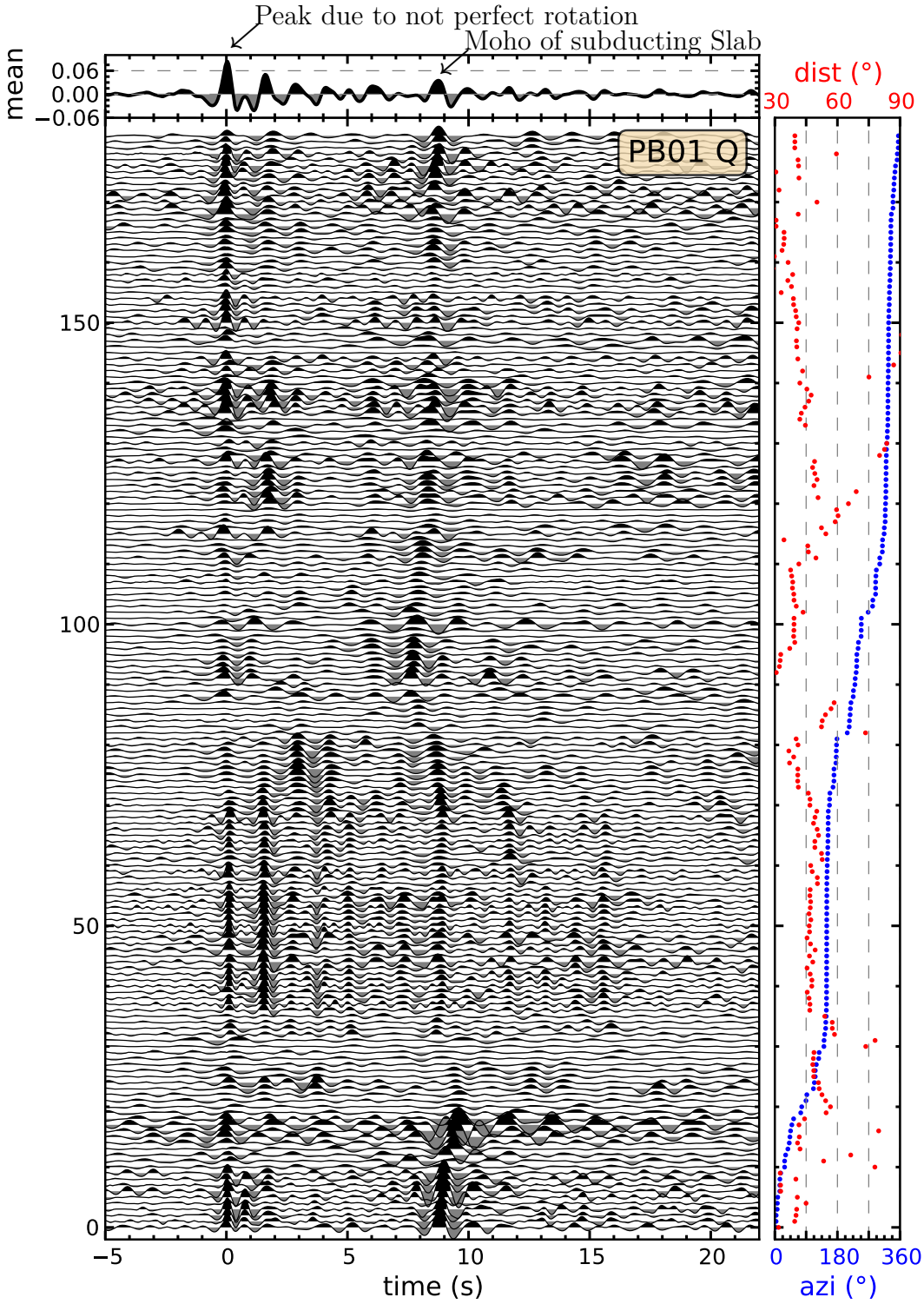

Figure 4.7.: Q components of the P-receiver functions for station PB01. The mean over all traces is displayed in the top panel. Azimuth and epicentral distance of the events in relation to the station location are displayed in the right panel.

4.2. Imaging the subducting plate

To test the receiver function method before using it for monitoring I want to try to reproduce some first-order observations. Therefore receiver functions are calculated in the time period from March 2006 to February 2012. The considered teleseismic events with an epicentral distance between 27° and 93° are reproduced in a table in appendix B.1. As an example figure 4.6 shows the epicenters of events used at station PB01. The calculated receiver functions sorted according to back azimuth of the events are displayed in figure 4.7 for station PB01. The interested reader is referred to appendix B.2 for plots of the calculated receiver functions for all other stations.

Several arriving phases can be seen in figure 4.7. There is one strong phase at 0 s which occurs because the P- and S-wave field are not separated cleanly with the rotation by theoretical incidence angle. Another strong phase can be seen at an arrival time of 9 s caused by a conversion interface at around 80 km depth. This is supposed to be the Mohorovičić discontinuity (Moho) of the subducting Nazca plate (*Sodoudi et al.*, 2011). Other phases before 9 s are caused by inhomogeneities inside the continental crust. Because none of these phases is outstanding it cannot be deduced if one is originating from the continental Moho. The phase at 6 s would be the most prominent candidate.

Another observation is that the shape of the receiver functions highly depends on the event's back azimuth and epicentral distance. The major reason is that events from different source regions map different locations under the receiver. For example the exact appearance of the phase that is located at 9 s in the stack varies from 7.5 s for events from the west to 9.2 s for events from the east. Assuming the standard *IASP91* 1D Earth velocity model this delay between the main P arrival and the converted Ps phase originates from inhomogeneities in depths of around 65 km and 81 km, respectively. With a horizontal distance of 35 km between the piercing points it can be concluded that the layer is inclined with an angle of around 24° giving another evidence that this phase represents the Moho of the subducting plate.

To see a clear variation with longitude i.e. in dip direction piercing points at 80 km depth are calculated to stack receiver functions of all stations according to their piercing point longitude. The results are displayed in figures 4.8 and 4.9. The most prominent phase is again the conversion from the Moho of the subducting Nazca plate. A subduction angle of around 16° can be observed. In the eastern most part around 69°W longitude the stack does not lead to a clear phase. The reason for this observation is that the plate dipping angle changes with latitude. If receiver functions are stacked in two different profiles north and south of 21°S latitude, it can be recognized that the plate is dipping

Table 4.1.: Regions with relatively dense earthquake distribution

identifier	latitude, longitude of center	radius	Flinn-Engdahl region of center
R1	58.3°S, 22.0°W	800 km	South Sandwich Islands Region
R2	14.1°N, 91.2°W	600 km	Guatemala
R3	13.5°N, 92.1°W	1400 km	Off Coast of Chiapas, Mexico

with a different angle of 16° in the south and around 23° in the north. *Sodoudi et al.* (2011) determined a dipping angle between 19° in the south and 23° in the north with the same methodology. The presented results show that the receiver function method is working very well. In the following I want to use the method for monitoring purposes.

4.3. Time variance due to the Tocopilla earthquake

To use the receiver function method for monitoring velocity changes in the crust the variability of the positions of the converted phases due to other reasons than velocity changes has to be minimized. As demonstrated in the previous section the position of the converted phases depend on the ray path under the receiver which depends itself on the epicentral distance, depth and back azimuth of the analyzed event. For monitoring purposes it is therefore important to select only events of a small region with similar ray paths. Here three relatively active circular regions are chosen. The first region is at the South Sandwich Islands and the center of the other two regions is located in Mexico and Guatemala (table 4.1, figure 4.10). Figure 4.11 shows the selected receiver functions from region R1 sorted according to origin time for station PB01. The time of the Tocopilla earthquake is marked with a horizontal red line. Receiver functions are displayed for a phase delay between −5 and 22 s. After 22 s no clear phases are visible in the receiver functions except for the conversions from deeper discontinuities (410 km, 660 km) which are not interesting in the context of this study.

The intention is to find out if there is a significant time shift in the receiver functions which can be correlated to changes in the Earth's crust caused by the Tocopilla earthquake. Therefore each individual receiver function is compared with the mean of all receiver functions in selected 1 s time windows in a first step. Three different methods are used:

Maximum: The time difference of the maximum (respective minimum for negative phases) between the individual receiver function and the mean in a specified time window is determined.

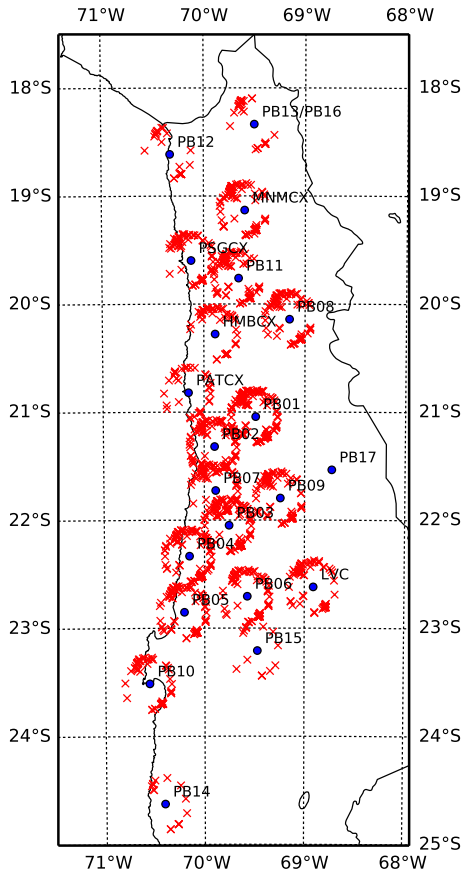

Figure 4.8.: Map of piercing points at 80 km depth

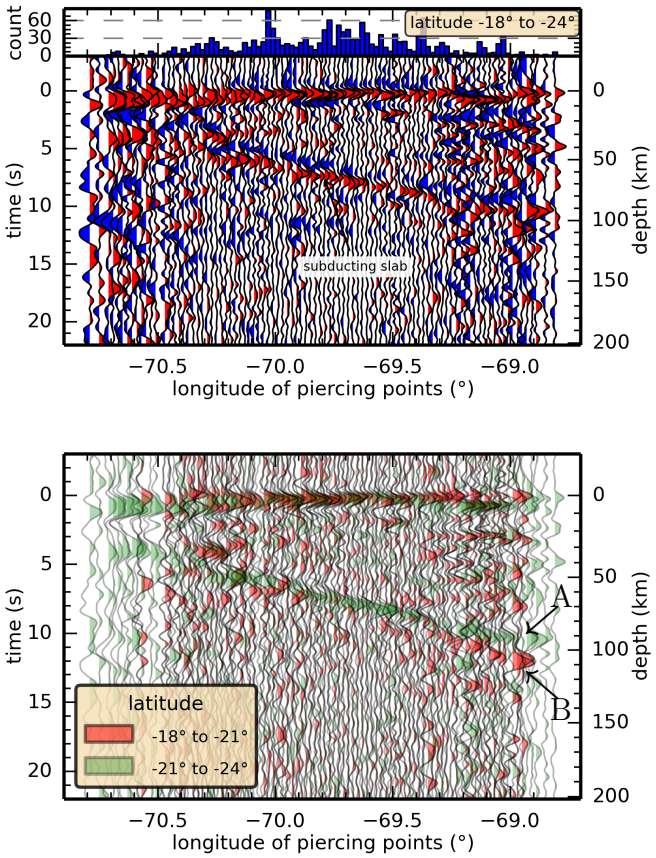

Figure 4.9.: Receiver functions stacked by piercing point longitude. *Top:* All receiver functions with the top panel showing the number of events stacked in one bin. The Moho of the subducting Nazca plate (slab) is clearly visible. *Bottom:* Comparison of receiver functions with piercing points south and north of latitude 21°S. The dipping angle is observed at around 16° (A) and 23° (B), respectively.

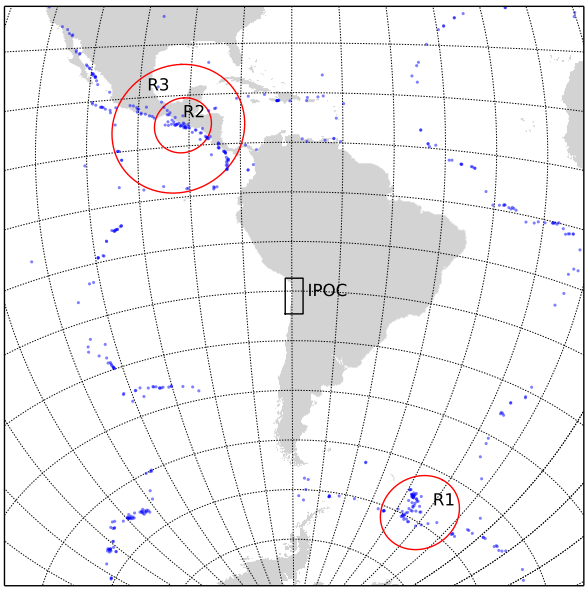

Figure 4.10.: Map of regions (table 4.1) used for the selection of events to reduce the impact of the different ray paths on the variance of the receiver functions.

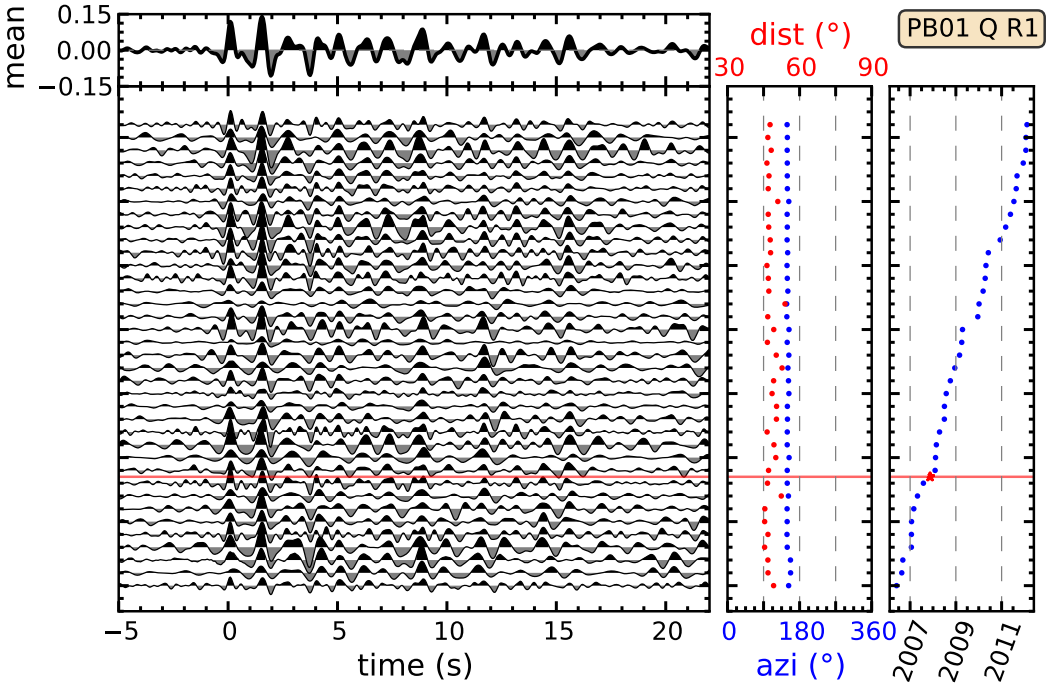

Figure 4.11.: Receiver functions from events of region R1 for station PB01 sorted according to event occurrence time. Top panel: mean of all traces. Right panels: distance and back azimuth of event, time of event. Time of Tocopilla event marked as red line and star.

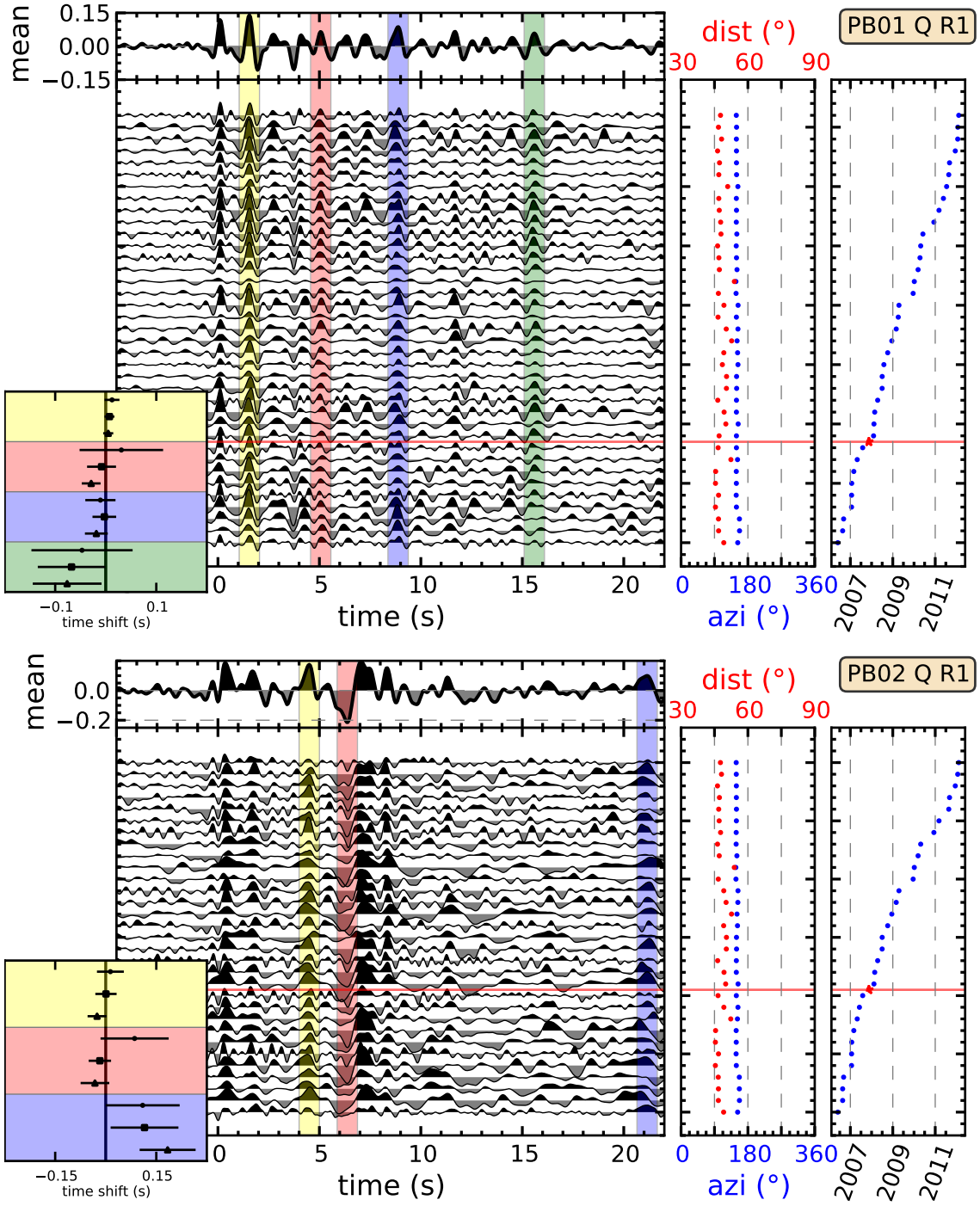

Figure 4.12.: Selected receiver functions from events of region R1 for stations PB01 and PB02 with measured time shifts. Top and right panels: same as in figure 4.11. The time of Tocopilla event is marked as red line and star. The analyzed phases are highlighted. In the lower left the time shifts of the analyzed phases in the course of the Tocopilla earthquake are plotted. The time shift is calculated as the difference of the mean phase position of receiver functions after the event and before the event. The phase position of an individual receiver function is determined by three different methods represented by a different marker type (dot: maximum, square: correlation, triangle: correlation above score). The error bars represent the sum of the two standard deviations of the mean of the two populations of receiver functions after and before the event, respectively.

Table 4.2.: Time shifts for stations PB01, PB02 and PB03 and region R1 calculated with different methods (see main text). Number of used receiver functions in brackets.

station region	phase	method	time shift (s) and number of traces (in brackets) before Tocopilla event	after Tocopilla event	difference	rel. diff. (%)
PB01 R1	1.55 s (+)	maxima	-0.009 ± 0.009 (9)	0.004 ± 0.006 (28)	0.012 ± 0.015	0.80 ± 0.95
		correlation	-0.006 ± 0.006 (9)	0.001 ± 0.003 (28)	0.007 ± 0.010	0.47 ± 0.63
		cor. above 0.95	-0.006 ± 0.006 (9)	-0.001 ± 0.003 (24)	0.005 ± 0.010	0.32 ± 0.64
	5.07 s (+)	maxima	-0.027 ± 0.061 (9)	0.004 ± 0.022 (28)	0.031 ± 0.083	0.61 ± 1.63
		correlation	-0.020 ± 0.016 (9)	-0.028 ± 0.012 (28)	-0.008 ± 0.029	-0.16 ± 0.57
		cor. above 0.80	-0.012 ± 0.013 (6)	-0.041 ± 0.006 (20)	-0.029 ± 0.019	-0.57 ± 0.37
	8.88 s (+)	maxima	-0.033 ± 0.015 (9)	-0.044 ± 0.015 (28)	-0.011 ± 0.030	-0.12 ± 0.34
		correlation	0.002 ± 0.013 (9)	-0.001 ± 0.010 (28)	-0.003 ± 0.023	-0.03 ± 0.26
		cor. above 0.85	0.017 ± 0.010 (7)	-0.001 ± 0.013 (22)	-0.019 ± 0.023	-0.21 ± 0.25
	15.59 s (+)	maxima	0.058 ± 0.080 (9)	0.011 ± 0.020 (28)	-0.047 ± 0.100	-0.30 ± 0.64
		correlation	0.078 ± 0.054 (9)	0.011 ± 0.013 (28)	-0.068 ± 0.067	-0.43 ± 0.43
		cor. above 0.90	0.093 ± 0.055 (5)	0.017 ± 0.013 (22)	-0.076 ± 0.068	-0.49 ± 0.44
PB02 R1	4.50 s (+)	maxima	-0.021 ± 0.021 (11)	-0.008 ± 0.018 (20)	0.014 ± 0.040	0.31 ± 0.89
		correlation	0.007 ± 0.015 (11)	0.008 ± 0.017 (20)	0.001 ± 0.032	0.02 ± 0.70
		cor. above 0.90	0.018 ± 0.018 (8)	-0.008 ± 0.011 (12)	-0.026 ± 0.028	-0.57 ± 0.63
	6.38 s (−)	maxima	-0.193 ± 0.064 (11)	-0.107 ± 0.037 (20)	0.086 ± 0.101	1.34 ± 1.59
		correlation	-0.013 ± 0.015 (11)	-0.031 ± 0.018 (20)	-0.017 ± 0.033	-0.27 ± 0.52
		cor. above 0.85	-0.011 ± 0.016 (10)	-0.043 ± 0.026 (13)	-0.032 ± 0.043	-0.50 ± 0.67
	21.15 s (+)	maxima	-0.163 ± 0.073 (11)	-0.053 ± 0.037 (20)	0.110 ± 0.110	0.52 ± 0.52
		correlation	-0.087 ± 0.063 (11)	0.028 ± 0.037 (20)	0.115 ± 0.101	0.54 ± 0.48
		cor. above 0.90	-0.152 ± 0.047 (6)	0.032 ± 0.036 (14)	0.184 ± 0.083	0.87 ± 0.39
PB03 R1	7.86 s (+)	maxima	0.036 ± 0.026 (9)	-0.007 ± 0.018 (19)	-0.043 ± 0.044	-0.55 ± 0.56
		correlation	0.021 ± 0.015 (9)	-0.018 ± 0.011 (19)	-0.039 ± 0.026	-0.50 ± 0.33
		cor. above 0.95	0.021 ± 0.015 (9)	-0.021 ± 0.012 (17)	-0.043 ± 0.026	-0.55 ± 0.34
	19.16 s (+)	maxima	0.014 ± 0.080 (9)	0.091 ± 0.065 (19)	0.076 ± 0.145	0.40 ± 0.76
		correlation	-0.045 ± 0.087 (9)	0.026 ± 0.059 (19)	0.070 ± 0.147	0.37 ± 0.76
		cor. above 0.90	0.098 ± 0.049 (4)	-0.086 ± 0.066 (10)	-0.184 ± 0.116	-0.96 ± 0.60

Correlation: The correlation function of the specified time window of the individual receiver function with the mean receiver function is calculated. The time shift for the best correlation is selected.

Correlation above score: Same as in the second method but only receiver functions with a best correlation over a specified score – but at least half of all eligible receiver functions – are used.

The application of this method results in a series of time shift values for each method and phase for each station-region pair. The series are divided into two populations with values of receiver functions before the Tocopilla event and values of receiver functions after the Tocopilla event. For each population the mean t_{mean} is calculated. The standard deviation of the mean

$$s_{\text{mean}} = \sqrt{\frac{\sum_i (t_i - t_{\text{mean}})^2}{N(N-1)}} \quad (t_i ...\text{samples},\ N ...\text{number of samples}) \tag{4.9}$$

is used as error approximation. With t_{before} being the mean time shift of a phase t_{mean} of the population of receiver functions before the Tocopilla and t_{after} being the mean time shift after the Tocopilla earthquake I can calculate the time shift of the phase in

receiver functions after the event compared to receiver functions before the event by $t_{\mathrm{dif}} = t_{\mathrm{after}} - t_{\mathrm{before}}$. For example for station PB01, region R1 and the phase at 15.6 s two populations of 9 and 28 samples can be analyzed with the first method (maximum). The mean and standard deviation of the mean of these two populations is

$$t_{\mathrm{before}} = (0.058 \pm 0.080)\,\mathrm{s} \quad \text{and} \quad t_{\mathrm{after}} = (0.011 \pm 0.020)\,\mathrm{s}$$

yielding a difference and apparent relative velocity change $\epsilon_{\mathrm{dif}} = -t_{\mathrm{dif}}/t$ of

$$t_{\mathrm{dif}} = (-0.047 \pm 0.100)\,\mathrm{s} \quad \text{and} \quad \epsilon_{\mathrm{dif}} = (0.30 \pm 0.64)\,\%\,.$$

This procedure is applied to stations PB01 to PB05 for all three source regions and two to four distinct phases. Stations PB06, PB07 and PB08 are analyzed, too, but they do only have sparse data before the Tocopilla earthquake. Some results are displayed in table 4.2 and together with the receiver functions in figure 4.12. The table with calculated time shifts and figures for all analyzed stations can be found in appendix B.3. Additionally the results of the analysis are presented in a compact way in figure 4.13. The broken line represents expected time shifts for an assumed homogeneous velocity decrease of 0.5 % due to the Tocopilla event. Evidences for a significant velocity change in the crust would be time shift values with the same trend – i.e. sign – for different properties. These properties are: event region, station, selected phase and method. In other words if the trend of the values is the same for one station and different methods, phases and regions, it can be concluded that there is an observable change in the crust near this station. At least values for different methods and the same phase, station and region should be similar. In the analysis it should furthermore be considered that the regions R2 and R3 are not independent, because R2 is fully enclosed by R3. For example at station PB01 and region R1 three relative stable phases with small errors and one phase at 15.6 s with a negative time shift are observed. For the other two regions and station PB01 just one phase is useful for the analysis; this phase does not show a clear trend. The other analyzed stations show similar behavior, some phases show a clear shift in one direction with a small error approximation, but then the other phases of the same receiver function show a shift in the opposite direction or receiver functions of another region show different results. Sometimes even the different methods give different results.

Generally it can be observed that a lot of stations show an apparent velocity change due to the Tocopilla earthquake. Though, it has to be mentioned that the statistical

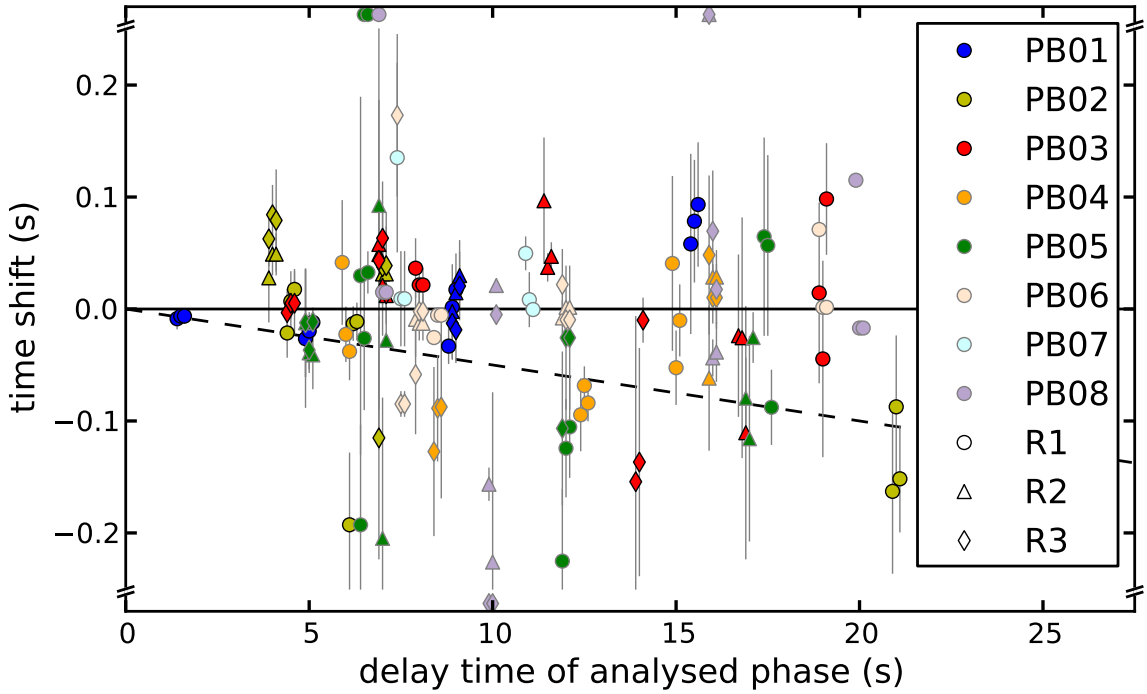

Figure 4.13.: Time shifts with error bars over delay time of analyzed phase. Stations are color-coded, event regions are represented by the marker type. The different methods are displayed with a horizontal offset of 0.1 s. The y-axis is broken at −0.25 s and 0.25 s. Data points with an absolute value larger than 0.25 s are displayed at a constant value at the top or the bottom without error bars. The dotted line represents expected time shifts if the medium would be subject to a homogeneous velocity decrease of 0.5 %. Phases and receiver functions corresponding to the displayed data points can be found in appendix B.3.

error is high – in the order of the mean time shift value itself. Furthermore the values scatter considerably and therefore a trend as exemplarily indicated by the broken line in figure 4.13 can not be discovered. Taking into account all analyzed time shifts it has to be noticed that there is no evidence for any change in the Earth's crust in the data using this method.

5. Monitoring with passive image interferometry

5.1. Method

Ambient noise refers to seismic signals which are recorded in the absence of earthquakes or other identifiable seismic sources. Figure 5.1 displays the probability density function (PDF) of power spectral densities (PSDs) at station PB01 calculated with the method by *McNamara and Buland* (2004, appendix A.2). This probabilistic power spectral densities can be used to characterize station sites including properties of the noise field, because the recordings of seismic stations consist mainly of noise. Teleseismic and local earthquakes occur only in a temporally small part of the data volume and contribute to less probable (pink-colored) areas at high levels in figure 5.1. Clearly visible are the first and secondary microseism peaks at around 15 s and 4 s−6 s. The first microseism peak originates from the transfer of energy from water gravity waves to the ocean bottom near coasts. The larger secondary microseism peak is caused by the interference of oceanic gravity waves with different propagation directions and similar frequencies and their transmittance to the ocean bottom. The natural oscillation of the Earth (Earth hum, at around 100 s) excited by ocean waves is only visible in some of the plots in appendix A.2. Noise at high frequencies often originates from wind, human activities, rivers and other local sources. Noise at lower frequencies is most likely caused by atmospheric pressure changes, Earth tides or thermally induced strain tilts.

Cross-correlations of diffuse waves recorded at two stations can be used to construct the Green's function between the stations if the waves propagate on average isotropically near the receivers (*Snieder*, 2004). The Green's function is the seismic response at a station (virtual receiver) to a peak-like source at another station (virtual source). The technique is referred to as *Green's function retrieval* or *seismic interferometry* and can be applied to the late coda of earthquake records in which on average isotropic illumination by multiple scattered waves is guarantied (*Campillo and Paul*, 2003). In the case of the retrieval of the Green's function with from ambient noise the technique is called *passive imaging* and was successfully applied to extract surface waves (*Shapiro and Campillo*,

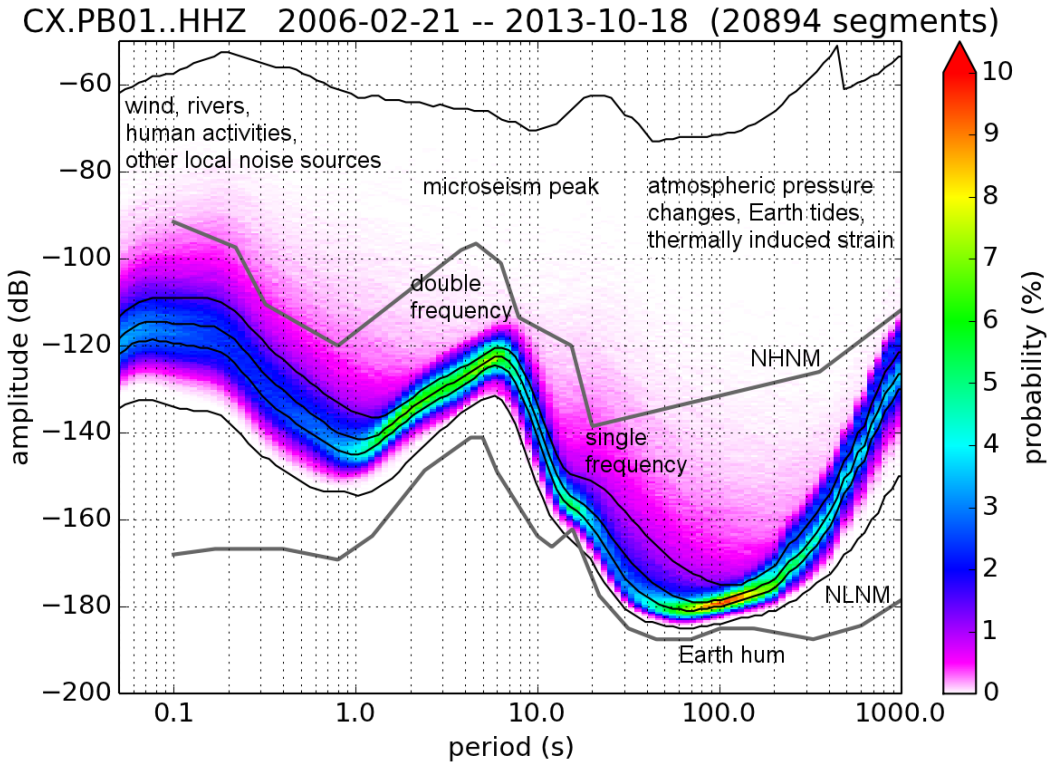

Figure 5.1.: Probability density function of power spectral densities for the channel HHZ of station PB01 calculated with the method of *McNamara and Buland* (2004). Black lines represent the 0, 25, 50, 75 and 100 percentiles. The new low and new high noise models (NLNM and NHNM, *Peterson*, 1993) are plotted with gray lines. Main contributions to the noise spectrum at different frequency bands are indicated.

2004; *Shapiro et al.*, 2005), body waves (e.g. *Roux et al.*, 2005) and scattered coda waves.

A numerical example from *Wapenaar et al.* (2010) demonstrates the retrieval of the Green's function in a two-dimensional case: Consider randomly located sources as in figure 5.2a each releasing a transient signal at $t = 0\,\mathrm{s}$ in a homogeneous lossless medium. The cross-correlation of the signals at the receivers $\boldsymbol{x_A}$ and $\boldsymbol{x_B}$ can be seen in figure 5.2d in dependence of the polar source coordinate Φ_S. The sum of the cross-correlations lead to the emergence of the Green's function between $\boldsymbol{x_A}$ and $\boldsymbol{x_B}$ at positive lag times and the Green's function between $\boldsymbol{x_B}$ and $\boldsymbol{x_A}$ at negative lag-times (figure 5.2e). If the considered sources emit uncorrelated noise signals, the Green's function can be constructed directly by the cross-correlation of the signals at $\boldsymbol{x_A}$ and $\boldsymbol{x_B}$ (figure 5.2f). This is because the cross-terms of signals from different sources vanish in the cross-correlation for *uncorrelated* sources. In contrary, the transient signals used to construct the cross-correlation function in figure 5.2e are identical and thus not uncorrelated. Cross-terms therefore have to be avoided by summing over the individual cross-correlations of signals from each source.

The sources are not necessarily primary sources as in the above example but can also be secondary sources like scatterers. Single scattered waves are not independent, but multiple scattered waves of direct arrivals or originating from noise sources are reasonable uncorrelated for Green's function retrieval. In the case of Green's function retrieval with data from ambient noise, the noise distribution has to be isotropic on average. A large discrepancy from isotropy lead to unphysical arrivals and signals partly overlapping the Green's function. Small variations in the isotropy lead to acceptable noise in the retrieved Green's function. Important is that sources or scatterers in the Fresnel zones (zones behind the receivers near the line connecting the receivers) contribute adequately to the noise wave field, because the waves originating from these sources interfere constructively. An indication for an on average isotropic noise wave field is the symmetry of the cross-correlation function for positive lag times and negative lag times. Depending on the azimuthal distribution of the noise field the direct wave of the positive or negative part is emphasized more. For example considering the cross-correlation between the stations PB02 and LVC, the direct wave of the positive side dominates, because sources in the Fresnel zone behind PB02 dominate over sources behind LVC (figure 5.3).

In the course of this study it will become obvious that the noise field in the data analyzed here is far from being isotropic. Anyway, the calculated cross-correlations can be regarded as an approximation for the Green's function. Furthermore correlation functions can be calculated for different time periods e.g. for each day combining the advantage of

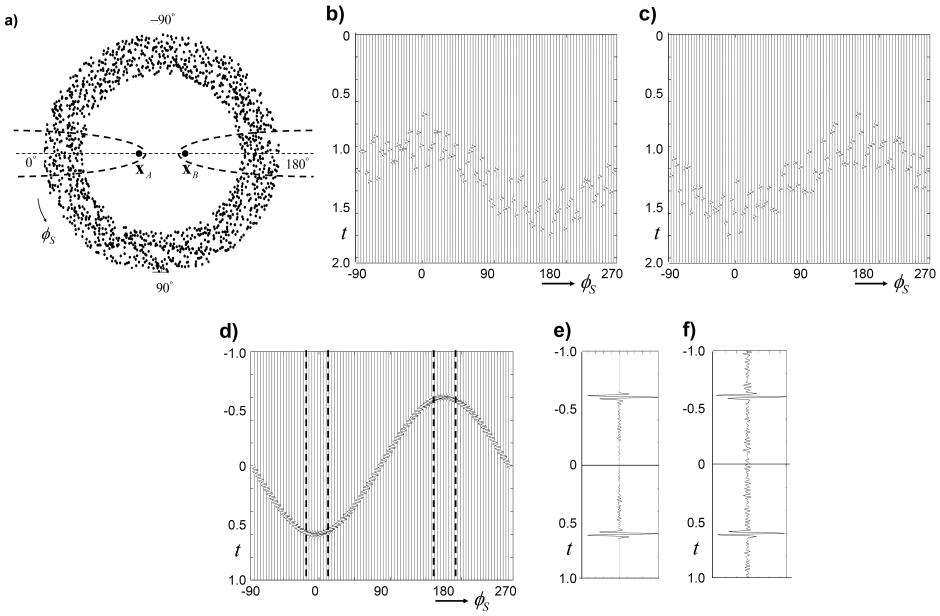

Figure 5.2.: Illustration of Green's function retrieval from *Wapenaar et al.* (2010). *(a)* Distribution of point sources isotropically illuminating the receivers at $\boldsymbol{x_A}$ and $\boldsymbol{x_B}$. The dashed lines indicate the Fresnel zones. *(b+c)* Responses at $\boldsymbol{x_A}$ and $\boldsymbol{x_B}$ as a function of the polar source coordinate Φ_S to a transient signal at time $t = 0\,\mathrm{s}$. *(d)* Cross-correlation of the responses at $\boldsymbol{x_A}$ and $\boldsymbol{x_B}$ separately for each source as a function of Φ_S. The dashed lines indicate the Fresnel zones. *(e)* The sum of the correlations in (d). This can be interpreted as Green's function emerging from constructively interfering signals of sources inside the Fresnel zones. *(f)* Single cross-correlation of the responses at $\boldsymbol{x_A}$ and $\boldsymbol{x_B}$ of simultaneously acting uncorrelated noise sources lead to a similar cross-correlation function. The duration of the noise signal is 9600 s

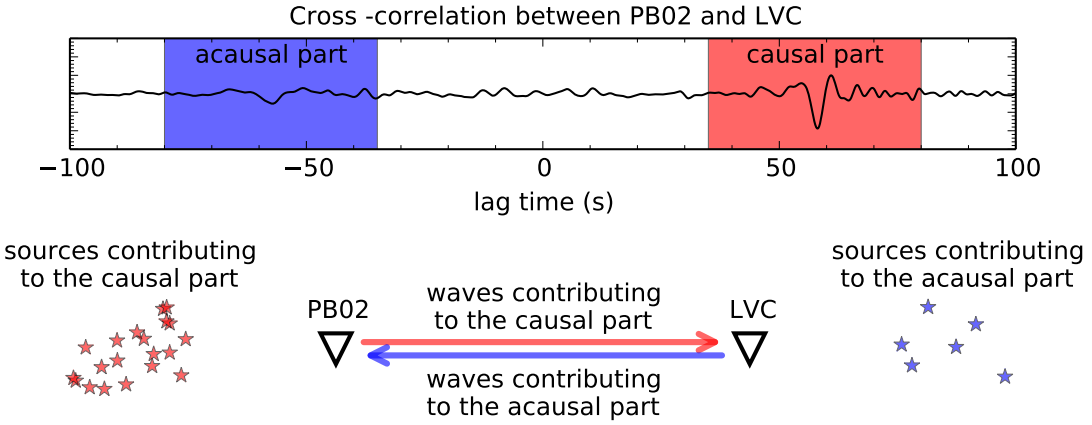

Figure 5.3.: Positive and negative part of the cross-correlation-function (CCF). *Top:* CCF between the Z components of stations PB02 and LVC consisting of a positive (causal) and negative (acausal) side. *Bottom:* Sketch of noise sources and wave paths contributing to the positive and negative side of the CCF. The direct waves leading to the positive side of the CCF are dominating over the ones leading to the negative side because more noise sources are situated at the side of PB02 on a line connecting the two stations. This is because station PB02 is located at the Coastal Cordillera relatively near to the ocean (with dominant noise sources) and station LVC further away from the coast in the Andes.

the knowledge of the virtual source location as in controlled-source experiments with the long-term availability of ambient noise. The comparison of the phases of the wave coda in the correlation functions is used for continuous monitoring of the subsurface between the stations. Possible reasons for phase shifts in the correlation function are clock errors in stations, changes in the noise distribution and changes in the seismic velocity of the medium. The technique is capable of identifying velocity changes down to 1‰. It is called *passive image interferometry* because it makes use of coda wave interferometry techniques (*Snieder et al.*, 2002; *Snieder*, 2006) on correlation functions obtained by passive imaging (*Sens-Schönfelder and Wegler*, 2006). Possible applications range from volcano monitoring (*Duputel et al.*, 2009) or clock correction (*Sens-Schönfelder*, 2008) to monitoring of fault systems (*Wegler and Sens-Schönfelder*, 2007); the technique has even been used with data from the moon (*Sens-Schönfelder and Larose*, 2008).

5.2. Work flow

I use both low frequency (0.01 Hz−0.5 Hz) cross- and high frequency (above 1 Hz) autocorrelation functions as input for the passive image interferometry. Waves of low

frequency penetrate deeper into the subsurface and therefore sample it up to a larger depth than high-frequency waves. The spatial resolution of low-frequency waves is inferior compared to higher frequencies. Still, low-frequency waves can be used to detect spatially extensive velocity changes. A hypothetical velocity change effect introduced by the Tocopilla earthquake and observed by the analysis of low-frequency data can lead to interesting insights into earthquake related changes in the Earth's crust. Contrary high-frequency waves sample the subsurface closer to the surface and more local because of higher scattering and the shorter wavelength. Above 1 Hz waves are subject to strong attenuation and the coherence between cross-correlations of station pairs is often lost depending on the interstation distance suggesting the use of autocorrelation functions for high frequency data. In this work only the vertical component of the data is used. In another study I confirmed that the usage of cross-correlations of the other 8 component combinations (respective other 5 independent component combinations for autocorrelations) leads to similar results as presented in the following sections for a subset of the used stations. Although the analysis of other component combinations for all stations would provide more confinement on the error estimates, analysis is restricted solely to the Z component for the sake of simplicity. The Z component is chosen over the horizontal components as it depicts the largest signal from direct surface waves in the cross-correlation functions.

Before calculating the correlations the data have to be prepared. For each day data are detrended, filtered and downsampled to 10 Hz (for cross-correlations) and 50 Hz (for autocorrelations), respectively. Then the data have to be normalized to reduce the effects of earthquakes in the correlations. An overview of normalization methods is presented by *Bensen et al.* (2007). The high amount of local seismicity in northern Chile leads to corrupt noise correlations for some days even when normalization is applied. This is, because earthquakes do not only have a higher amplitude than noise which is successfully dealt with by the normalization but also occur during a significant time span. Therefore, a part of the earthquakes is suppressed completely with an automated method. Samples with an envelope larger than 10 times the root mean square of the envelope in quiet periods are set to zero. The 1-bit normalization is then applied additionally. All samples are set to $+1$ if they are positive and -1 if they are negative. Gaps and data suppressed in the first step stay at zero. This combined normalization approach enhances the noise correlation of days with a high amount of local events. The quality of noise correlations of interesting days immediately after moderate earthquakes is improved in spite of a potentially large amount of aftershocks. Data intended for cross-correlation are spectrally whitened before the final 1-bit normalization to broaden the spectrum. For that purpose

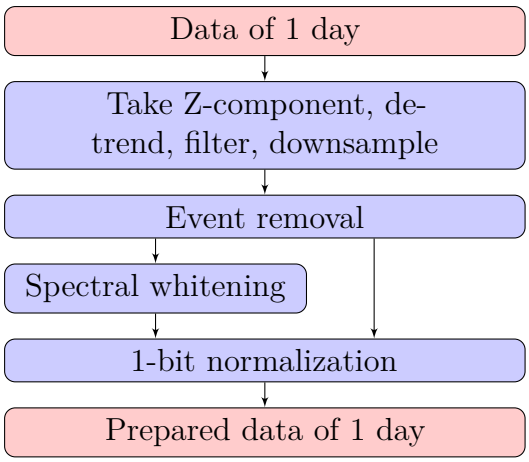

Figure 5.4.: Flow chart of the data preparation. Spectral whitening is not performed when preparing data for autocorrelations.

the absolute values are set to the same level in the Fourier domain. Data has to be filtered again before going back to the time domain for the 1-bit normalization. Data prepared for autocorrelation cannot be spectrally whitened because the lag of phase information would lead to a peak-like deformation of the autocorrelation in the time domain.

Daily correlation functions are computed in the frequency domain by calculating the product of the Fourier spectrum of one station and the conjugate complex Fourier spectrum of the other station. When calculating autocorrelations this equals the square of the absolute value of the Fourier spectrum. The correlation functions are normalized after back-transformation to the time domain, so that the value of 1 represents a perfect correlation. This means, autocorrelation functions at 0 s lag time equal 1. The cross- and autocorrelations, which represent the response of the station environment to a peak-like source at the other station or the station itself, respectively, are used as input for passive image interferometry.

Relative travel time variations can be determined for different lag time windows in the correlation functions (CFs) that start at t_1 and end at t_2. First a reference correlation function ϕ_{ref} is computed as the mean over all available daily CFs for this station. Then the daily CF ϕ_{d} is stretched and compressed on the time axis with respect to zero lag time. For determining travel time fluctuations the similarity between the unstretched reference and the stretched daily CF in the chosen time window is determined for each

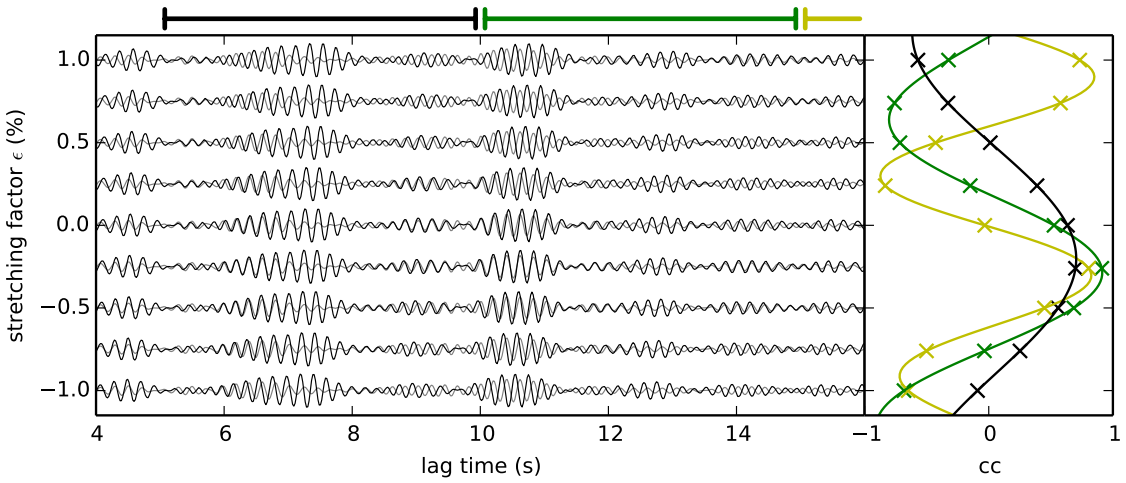

Figure 5.5.: Illustration of the stretching method. A daily correlation function (CF, black) is stretched and compressed relative to 0 s according to the stretching factor ϵ. The correlation coefficient of the stretched CF and an unstretched reference CF (gray) for different time windows (indicated at top) is displayed in the right panel. Here the autocorrelation function of station PATCX in the frequency band 4 Hz−6 Hz is analyzed in the time windows 5 s−10 s, 10 s−15 s and 15 s−20 s. The stretching factor resulting in the highest correlation coefficient is around −0.25 % for all three time windows, indicating a homogeneous velocity decrease of 0.25 %.

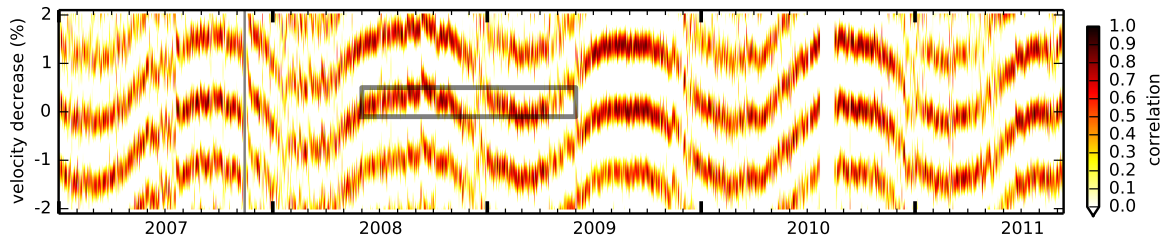

Figure 5.6.: Similarity matrix of the autocorrelation function at PATCX for the frequency band 9 Hz to 11 Hz and lag time window 7 s to 9 s as produced by equation (5.1) for different days. The vertical bar marks the time of the Tocopilla earthquake. The relative velocity changes cause neighboring phases to occur at the same lag time for different times in the year (see box). This corresponds to a phase shift of 2π between the respective noise correlation functions. The interferometry method is adapted to deal with this – firstly by the iterative reference calculation described in section 5.2, secondly by the alternative fitting procedure for long-term changes in section 5.4.2.

stretching factor ϵ by the correlation coefficient

$$\mathrm{cc}(\epsilon) = \frac{\int_{t_1}^{t_2} \phi_\mathrm{d}(t\,(1+\epsilon))\,\phi_\mathrm{ref}(t)\,\mathrm{d}t}{\left(\int_{t_1}^{t_2} \phi_\mathrm{d}^2(t\,(1+\epsilon))\,\mathrm{d}t \int_{t_1}^{t_2} \phi_\mathrm{ref}^2(t)\,\mathrm{d}t\right)^{1/2}} \tag{5.1}$$

adopting values between $+1$ and -1. The stretching factor with the highest similarity can be directly translated into relative travel time variation $-\Delta t/t$, which corresponds to the relative velocity change $\Delta v/v$ if this change is homogeneous:

$$\epsilon = -\frac{\Delta t}{t} = \frac{\Delta v}{v}\,. \tag{5.2}$$

Figure 5.5 illustrates this method. This procedure can be repeated for every available daily autocorrelation to construct a similarity matrix in which each column represents the correlation coefficients $\mathrm{cc}(\epsilon)$ for a single day. The maxima of the similarity matrix for each column (day) can be used to trace the relative velocity change over time. Both, observed velocity changes and stretching factors, will be termed ϵ in the following. If the velocity change is not homogeneous in space the obtained apparent relative velocity is also termed ϵ. A non-constant noise field can also lead to an apparent velocity change.

Because a relatively high frequency range is used for the analysis of the autocorrelation functions, velocity variations can cause phase shifts at late lag times that are significant compared to the dominant period. A reference correlation function ϕ_ref calculated by simple stacking of all daily autocorrelation functions will possibly be deteriorated, because correlation functions from different periods interfere destructively for high

frequencies (figure 5.6). Therefore a new scheme is introduced to calculate the reference autocorrelation in an iterative manner. A preliminary estimate ϵ_{prel} of the relative velocity variations is obtained by using a stack of the correlation functions as preliminary reference. The final reference function is not calculated as the mean of daily autocorrelations over all N days t_i, as before, but as the mean of all autocorrelations corrected for the preliminary estimate of the velocity change ϵ_{prel}:

$$\phi_{\mathrm{ref}}(t') = \frac{1}{N}\sum_{i=1}^{N}\phi_{\mathrm{d}}(t'\,(1-\epsilon_{\mathrm{prel}}(t_i)))\ . \tag{5.3}$$

5.3. Observations from low-frequency cross-correlations

Daily cross-correlations of the Z component of 208 station pairs are computed in the frequency band from 0.01 Hz to 0.5 Hz as described in the previous section. Figure 5.7 shows the stack over all calculated cross-correlation functions for all station pairs sorted according to interstation distance. These functions are used as a reference for the stretching procedure. Clearly visible is the direct surface wave traveling at a speed of around 3.0 km/s. Some examples of calculated daily cross-correlation functions are reproduced in figure 5.8 and in appendix C.1. Daily cross-correlation functions are sorted from early times (bottom) to later times (top). The top panel shows the stack over all daily cross-correlations. The color scale has its maximum at the respective maxima of the stacked cross-correlation multiplied by 1.5 and rounded to the first significant digit. Therefore the color scale is different for each plot. The x-scale (lag time) is also different to account for different interstation distances.

Because scattered waves are less dependent on the variability of noise sources, time windows are analyzed following the direct surface wave. To get a reasonable signal in the late coda, firstly, a long time window is chosen for the stretching procedure and secondly, the correlation functions are stacked over several days. The analyzed time window has a length of 80 s and starts 30 s behind the direct surface wave. The stack is calculated over 10 days with an overlap of 8 days. Thus, a signal used as input into the stretching procedure is obtained for every second day. The resulting similarity matrices of the daily cross-correlation functions from figure 5.8 and appendix C.1 are plotted in figure 5.9 and appendix C.2 for the years 2007 and 2008, respectively. The concentration on the years 2007 and 2008 is motivated by the goal to analyze variations of the seismic velocity caused by the Tocopilla earthquake. The similarity matrices show the correlation coefficients for the different stretching factors for every second day. The course of the

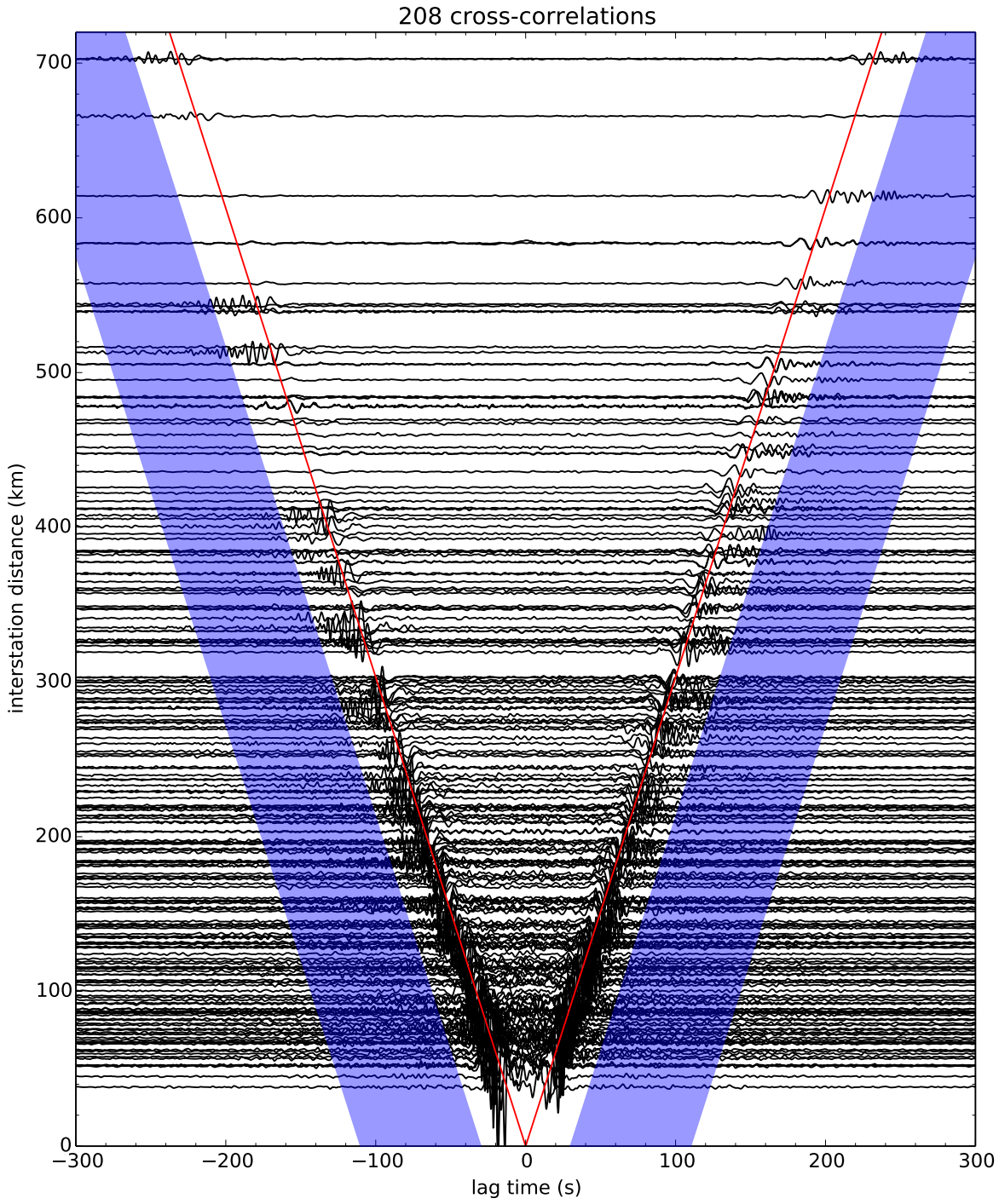

Figure 5.7.: Cross-correlations of the Z component of different station pairs sorted according to interstation distance. Each trace represents the stack over all available daily cross-correlation functions for this station pair. The maxima of the envelope of the waveforms are fitted by the red lines. The lines represent the arrival of the direct surface wave traveling at a speed of around 3.0 km/s. The time window chosen as input for the stretching method extends from 30 s to 110 s behind the maximum and is marked by the blue area.

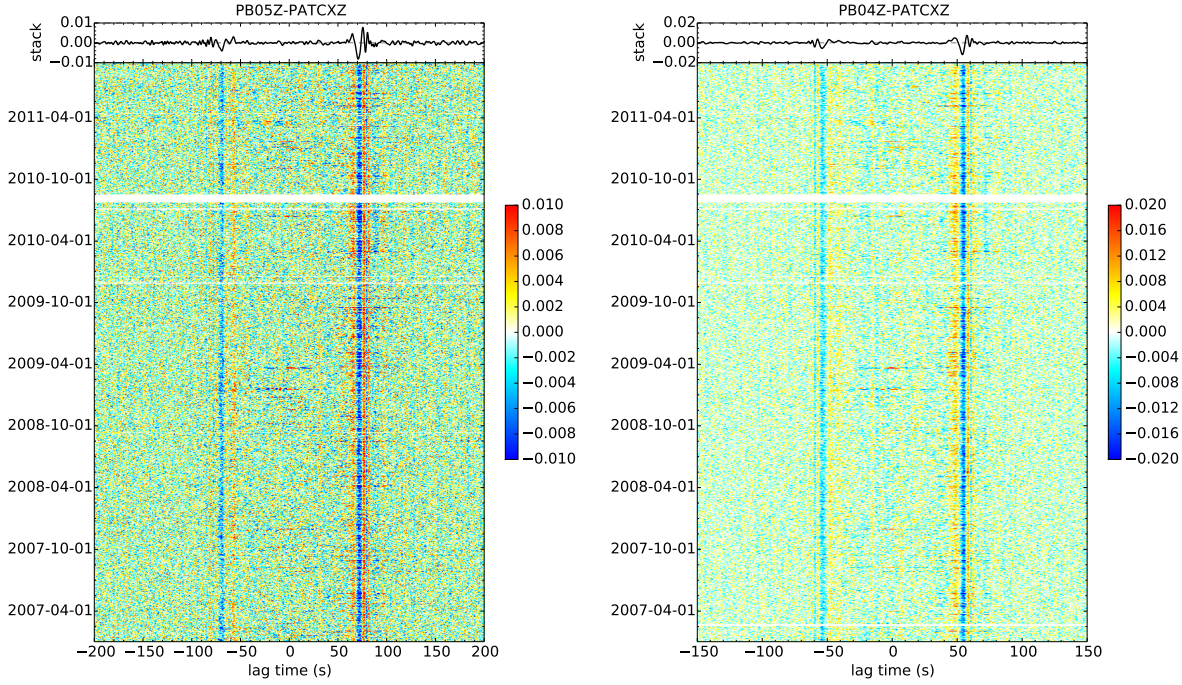

Figure 5.8.: Daily cross-correlation functions of station pairs PB04-PB05 and PB05-PATCX in the frequency band 0.01 Hz−0.5 Hz. Daily cross-correlation functions are sorted from early times (bottom) to later times (top). The top panel shows the stack over all daily cross-correlations. More examples of daily cross-correlation functions are reproduced in appendix C.1.

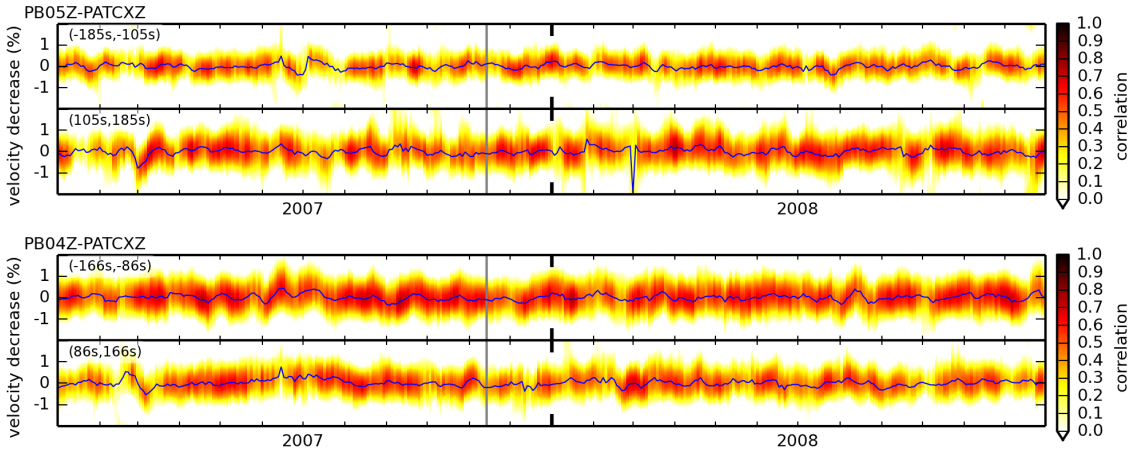

Figure 5.9.: Similarity matrices for cross-correlation functions of station pairs PB05-PATCX and PB04-PATCX for the time window from 30 s to 110 s behind the direct surface wave for the years 2007 and 2008. The similarity matrix shows the correlation coefficients for the different stretching factors for every second day. Each column represents a stack over 10 subsequent days. The maxima over time allow to determine the observed apparent velocity change (blue line). Each plot consists of a top panel for the time window of the acausal part of the correlation function and a bottom panel for the causal part. The gray vertical line is drawn at the occurrence time of the Tocopilla earthquake. Plots show velocity decrease $-\epsilon$.

maxima over time allows to determine the observed apparent velocity change (blue line). The gray vertical line is drawn at the occurrence time of the Tocopilla earthquake. A good criterion for a velocity change is an apparent velocity change both for the time window on the causal and acausal side of the cross-correlation function. Therefore each plot consists of a top panel for the time window of the acausal part and a bottom panel for the causal part.

None of the station pairs show a distinct velocity change associated with the Tocopilla earthquake in the analyzed frequency band. This is surprising at first sight, because long-term changes of the velocity have been observed by many authors for earthquakes of similar strength (e.g. *Brenguier et al.* (2008); *Hobiger et al.* (2012)). It is suspected that the deeper hypocenter of the Tocopilla earthquake (around 37 km, compared to the more shallow earthquakes with observed long-term changes) is the main reason for the absence of any coseismic velocity change. Furthermore, the similarity matrices show fluctuations with periods of weeks to one month, presumably caused by the variability of the ambient noise generation conditions in this frequency band (moving storms over Pacific ocean, etc.). The fluctuations effectively limit the resolution to values around 0.1 %. Besides, it is not possible to observe a possible short-term velocity change because

of the necessary stacking of the daily cross-correlation functions.

5.4. Observations from high-frequency autocorrelations

To analyze the shallow subsurface at the different stations for velocity changes higher frequencies are used. Waves constructed by cross-correlations are then subject to higher scattering and therefore I want to limit this analysis to autocorrelations. It will become apparent that autocorrelations in the analyzed frequency bands for some stations do not suffer from the same variability as the cross-correlations. Obviously the ambient noise is not as variable as in the low-frequency band or the higher scattering provides a randomization that leads to a more constant noise field with time.

Autocorrelations of 12 IPOC stations installed at the time of the Tocopilla earthquake (PB01-PB08, HMBCX, MNMCX, PATCX and PSGCX) are calculated with the method described in section 5.2. The data are filtered in the two frequency bands 1 Hz−3 Hz and 4 Hz−6 Hz before the application of the normalization. Spectral whitening is not applied for the autocorrelations, because it would lead to a single peaked, totally useless correlation function. Appendix C.3 shows the calculated daily autocorrelation functions sorted from early times (bottom) to later times (top). The top panel shows the stack over all daily autocorrelations. The color scale has its maximum at a value of 0.1 to embrace the signal at later lag times. Additionally the daily autocorrelation functions of station PATCX in the 4 Hz−6 Hz frequency band are shown in figure 5.10 with a maximum value for the color scale of 0.02. The autocorrelations of some stations (e.g. for 1 Hz−3 Hz: PB02, PB04, PB05, PB07, MNMCX, PATCX, PSGCX) are relatively stable with time and therefore well suited for the analysis with passive image interferometry. Other stations show an unstable daily autocorrelation (e.g. PB01, PB08). The instability and variation of the high frequency noise sources (e.g. human activities: mining street building) is the most probable reason for fluctuating autocorrelations. But also other reasons are plausible in some case. For example stations PB07 and PB08 show a significant different autocorrelation at the time between April and October 2007. This is because the mass-centering was not working properly at this period distorting the response spectrum of the seismometer and distorting the daily autocorrelation functions even at high frequencies. All stations except PATCX, HMBCX, PSGCX and PB04 after 2008 show an autocorrelation signal with low attenuation in the 4 Hz−6 Hz frequency band. A combination of different environmental scattering and noise field properties for these stations is probably the reason for the low attenuation.

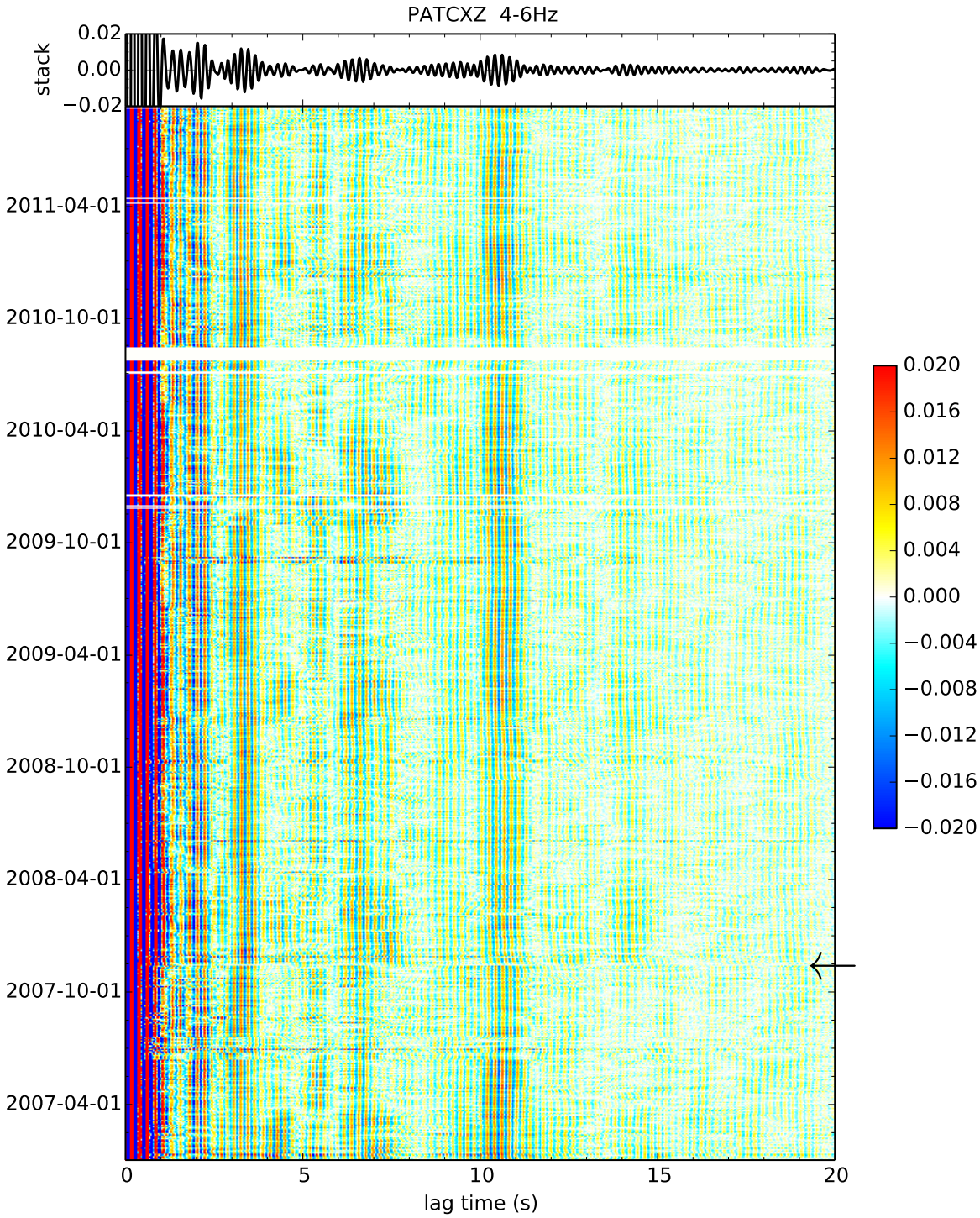

Figure 5.10.: Daily autocorrelations of station PATCX in the frequency band 4 Hz−6 Hz. Daily autocorrelation functions are sorted from early times (bottom) to later times (top). The top panel shows the stack over all daily autocorrelations. The color scale has its maximum at a value of 0.02. The black arrow indicates the occurrence time of the Tocopilla earthquake.

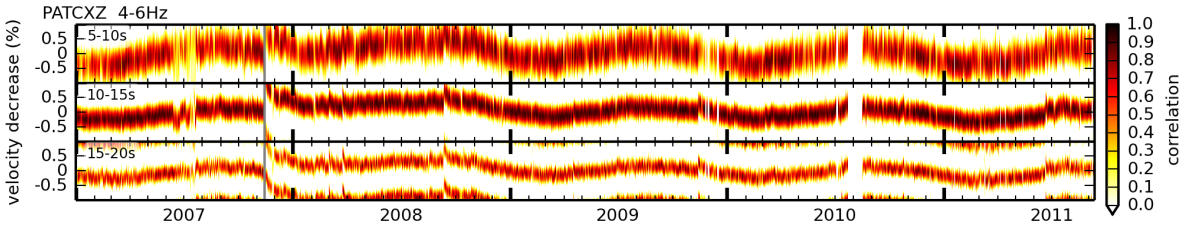

Figure 5.11.: Similarity matrices for the autocorrelation of station PATCX in the frequency band 4 Hz−6 Hz in the three time windows 5 s−10 s, 10 s−15 s and 15 s−20 s.

Similarity matrices are calculated for the daily autocorrelation functions with the stretching method described in section 5.2. Contrary to the analysis of cross-correlation functions stacking is not needed here. As input into the stretching method I choose the three time windows 5 s−10 s, 10 s−15 s and 15 s−20 s, so that three independent values of the apparent velocity change can be estimated for each day. Figure 5.11 shows the similarity matrices for station PATCX and the frequency band 4 Hz−6 Hz. Illustrations for all stations and the two frequency bands are provided in appendix C.4. The similarity matrix consists of the correlation coefficients cc for the different stretching factors for each day. The maxima over time represent the observed apparent velocity change. The gray vertical line is drawn at the time of the Tocopilla earthquake. Notice that the plots show velocity *decrease* $-\epsilon$. To answer the question if the apparent velocity changes represent the real velocity changes of the subsurface or a variability of the noise sources the following indicators are used.

1. In the case of a homogeneous velocity decrease all three values for the different time window should lead to a similar velocity change, at least they should show the same trend.

2. A high maxima of the similarity matrix for each day (above 0.9) is an indication for a relatively stable waveform of the autocorrelation with time. Station PB01 for the frequencies 1 Hz−3 Hz is an example for an unstable waveform and low correlation values.

3. A highly fluctuating or with high frequency abruptly changing apparent velocity change without any reason is an indicator of abrupt significant variations in the noise field.

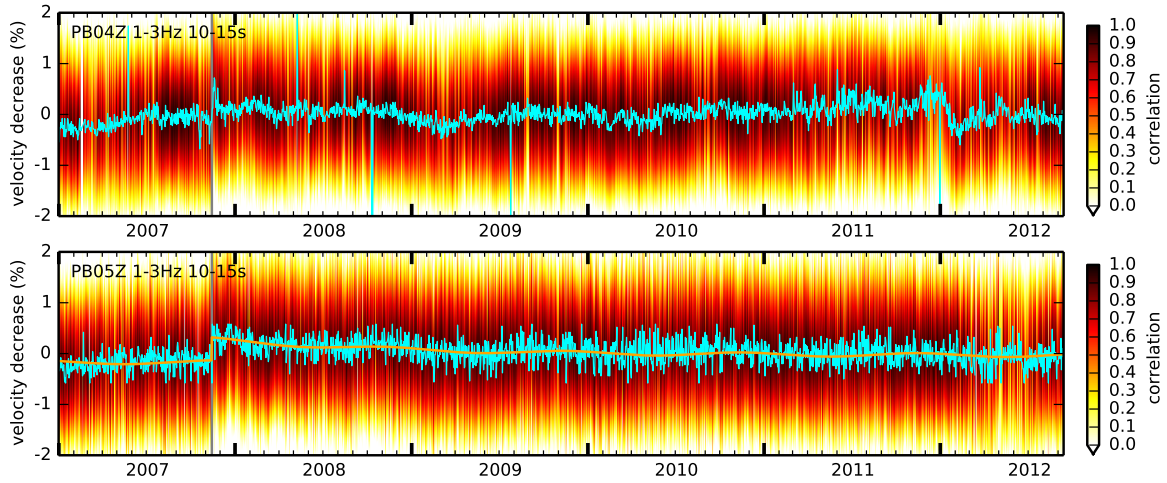

Figure 5.12.: Similarity matrices of the autocorrelation function of stations PB04 and PB05 (frequency band 1 Hz−3 Hz, time window 10 s−15 s). The vertical bar marks the time of the Tocopilla earthquake. Maxima of the similarity matrices for each day are connected by a cyan line. While station PB04 shows only a short-term velocity decrease because of the Tocopilla earthquake, the velocity decrease of station PB05 does not recover until around 2 years after the event. The orange line is a fit of a model for the long-time changes to the similarity matrix. The long-time changes are described by the empirical model of equation (5.4) plus a constant velocity decrease caused by the Tocopilla earth.

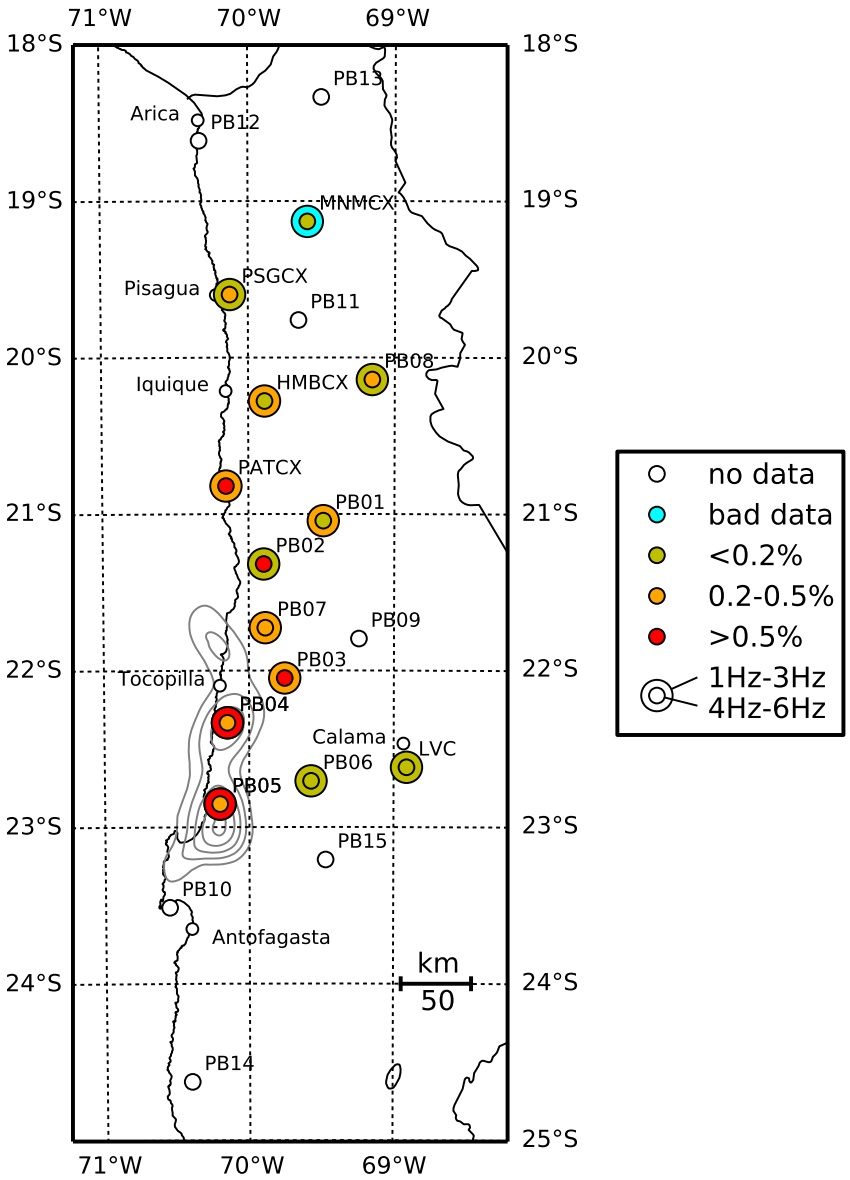

Figure 5.13.: Map of the IPOC network indicating velocity decrease at the time of the Tocopilla earthquake at different stations in two different frequency bands. The rupture slip distribution from *Schurr et al.* (2012) is displayed in gray isolines (0.5 m to 3 m). Stations with no data had not yet been installed at the time of the Tocopilla event.

5.4.1. Velocity changes associated with Tocopilla event

Instantaneous velocity changes caused by seismic events can be distinguished from possible noise source variations by their step-like shape. This is valid because stacking was not performed and therefore possible short-term velocity changes can be observed, too. Indeed, a coseismic velocity decrease is observed at different stations. Figure 5.12 for example displays the similarity matrices for stations PB04 and PB05, which are situated in the rupture area of the Tocopilla earthquake, in the frequency band 1 Hz−3 Hz. A velocity decrease at the time of the Tocopilla earthquake is clearly distinguishable from effects presumably caused by the variation of the noise field (e.g. the apparent velocity increase for PB04 at 01/2012). Figure 5.13 shows the velocity drops at the time of the Tocopilla earthquake at the 13 running stations in the two analyzed frequency bands. 10 of the 13 stations experience a velocity drop higher than 0.2 %. Stations PB04 and PB05 located near the maxima of the slip distribution as calculated by *Schurr et al.* (2012) show the highest velocity drop in the 1 Hz−3 Hz frequency band. Station PATCX more than 100 km north of the epicenter and outside the rupture area shows the highest velocity drop in the 4 Hz−6 Hz frequency band. At all stations except for stations PB05 (1 Hz−3 Hz) and PATCX (4 Hz−6 Hz) the velocities return to the level before the earthquake in several days to weeks. In the case of stations PB05 and PATCX this recovery takes about 2 years (figure 5.14a, figure 5.12). Different local noise properties for both stations are probably the reason, why a velocity drop is observed at different frequency bands. Because long-term velocity variations cannot be observed at lower frequencies, it can be concluded that the velocity drops caused by the Tocopilla earthquake occur in relatively shallow material.

5.4.2. Long-term velocity changes at station PATCX

Station PATCX shows contrary to the other IPOC stations additionally velocity drops at smaller earthquakes and periodic annual velocity changes. Figure 5.14a presents the results of the stretching procedure for station PATCX in the 4 to 6 Hz frequency band for lag times from 10 to 15 s together with daily mean temperatures at Iquique airport. First order observations are the annual velocity change which correlates to temperature and a velocity drop at the time of the Tocopilla earthquake recovering in the course of

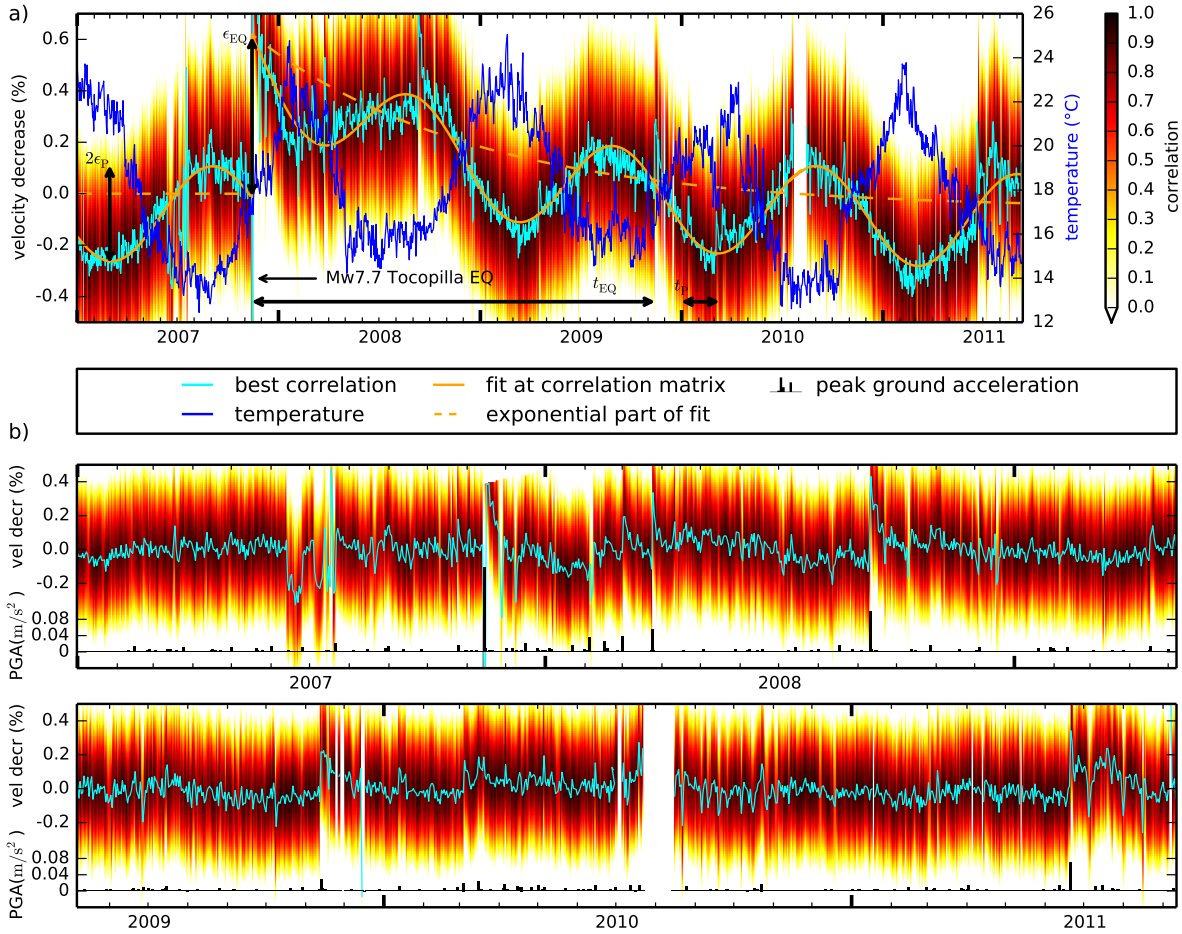

Figure 5.14.: a) Similarity matrix of station PATCX for the time window of 10 s to 15 s of the autocorrelation function in the frequency band 4 Hz−6 Hz. The stretching factors resulting in the best correlation to the reference trace for each day are connected by a cyan line and represent the observed velocity variations. Note that the y-axis displays velocity *decrease* ($-\epsilon$). There is a clear correlation between temperature variations (blue line, daily mean temperature at Iquique airport) and the periodic component of the velocity changes. Additionally there is a sudden drop of seismic velocity at the time of the Tocopilla earthquake. Seismic velocity is recovering to the level before the Tocopilla event in the course of around 2 years. These two effects are fitted to the similarity matrix with an exponentially decaying offset (broken orange line) added to a sinusoidal function (orange line). The fitting parameters amplitude of periodic relative velocity change ϵ_P, amplitude of coseismic relative velocity drop ϵ_{EQ}, phase of periodic velocity change t_P and recovery time of coseismic velocity drop t_{EQ} are marked by thick, black arrows.
b) Same similarity matrix as described in a) with long-term effects subtracted. Therefore the orange line in a) was used. Additionally the peak ground acceleration for each day is plotted at the bottom. A clear correlation between peak ground acceleration and short-term velocity drops can be observed. Most of the high values of PGA originate from local earthquakes within 200 km with a magnitude above 5.5.

around 2 years. These observations are fitted with the function

$$\begin{aligned}\epsilon_{\mathrm{mod}}(t) = \epsilon_0 &+ \epsilon_{\mathrm{P}} \cos\left[\frac{2\pi}{1\,\mathrm{a}}\,(t - t_{\mathrm{P0}} - t_{\mathrm{P}})\right] \\ &- \epsilon_{\mathrm{EQ}} \exp\left(-\ln 10\,\frac{t - t_{\mathrm{EQ0}}}{t_{\mathrm{EQ}}}\right) H(t - t_{\mathrm{EQ0}})\end{aligned} \tag{5.4}$$

with t_{P0} marking the day 1 Jan 2010 and t_{EQ0} marking 14 Nov 2007, the day of the Tocopilla earthquake. H is the Heaviside function yielding 0 for negative arguments and 1 otherwise. The fitting parameters are associated with different causative processes. ϵ_{P} is the amplitude of the relative velocity change with annual period. t_{P} is the phase of the maximum velocity of this periodic change relative to 1 Jan 2010. ϵ_{EQ} is the amplitude of the velocity drop at 14 Nov 2007 and t_{EQ} the recovery time to 10 % of this earthquake related change. The meaning of these 4 parameters is indicated with thick, black arrows in figure 5.14a. ϵ_0 is a constant offset and of no further importance.

For calculating the 5 optimal fitting parameters the most obvious solution would be to minimize the sum of the quadratic difference between ϵ_{mod} and the stretching factor with the best similarity over all N days t_i: $\sum_{i=1}^{N} \left(\epsilon_{\mathrm{mod}}(t_i) - \epsilon_{\mathrm{max}}(t_i)\right)^2$. This strategy however has two serious drawbacks: Firstly, days with erroneous outliers tend to be over-weighted. Secondly, the maxima of the similarity matrix could be at neighboring phases for different days which would falsify the results extensively as illustrated by figure 5.6. Here, the mean of correlation coefficients at the stretching factors ϵ_{mod} is simply maximized to avoid such cycle skipping:

$$\mathrm{cc}_{\mathrm{mean}} = \frac{1}{N} \sum_{i=1}^{N} \mathrm{cc}(\epsilon_{\mathrm{mod}}(t_i)) \ . \tag{5.5}$$

This basically finds the model curve which runs along the highest ridge of the similarity matrix. The optimization uses the Nelder-Mead simplex algorithm (*Nelder and Mead*, 1965; *Wright*, 1996) implemented in the SciPy library (*Jones et al.*, 2001–) with reasonable starting values. The estimated long-term velocity changes ϵ_{mod} are used for the a posteriori calculation of the reference trace introduced in section 5.2 ($\epsilon_{\mathrm{prel}} = \epsilon_{\mathrm{mod}}$). The calculation of the similarity matrix and the fitting is then repeated with the preliminary values. For the plot in figure 5.14a the final optimal parameters are

$$\begin{aligned}&\epsilon_{\mathrm{P}} = 0.19\,\%, && \epsilon_{\mathrm{EQ}} = 0.68\,\%, \quad \epsilon_0 = -0.10\,\%, \\ &t_{\mathrm{P}} = 61\,\mathrm{d} \qquad \text{and} \quad && t_{\mathrm{EQ}} = 770\,\mathrm{d}\,.\end{aligned}$$

5.4.3. Shaking induced velocity changes and their relationship to peak ground acceleration

Here short-term velocity changes are analyzed which are not contained in the above model. Removing the long-term trend at station PATCX as provided by the function in equation (5.4) produces the plot in figure 5.14b. An additional short-term velocity decrease at the time of the Tocopilla earthquake shows an overlap of different effects with different time scales. At other days velocity drops can be observed, too, recovering in the course of several days to one month. Such days show a high peak ground acceleration caused by regional earthquakes as indicated in the bottom of figure 5.14b. The bar plot shows the peak ground acceleration on the vertical component of each day as it was sensed by an accelerometer right next to the seismometer. The exceptional high sensitivity of the environment at station PATCX allows for an investigation of the question if the amplitude of the velocity decrease correlates better to the sensed peak ground acceleration or the dynamic strain, which constrains the physics behind the velocity decreases. The amplitude of the short-term velocity decreases is measured by taking the difference of mean velocity during the 10 days prior to the event and minimum velocity with reasonable correlation after the event. Maxima of dynamic strain are estimated with the ratio of peak ground velocity and average shear velocity $\overline{v}_S$ of the uppermost 30 m. In the case of a single station dynamic strain is proportional to the peak ground velocity with the proportionality factor $1/\overline{v}_S$.

Hobiger et al. (2012) analyzed peak ground accelerations and coseismic velocity changes observed with cross-correlations for the 2008 M6.9 Iwate earthquake at different stations. They found a trend linking strong acceleration to high velocity drops. Considering the scatter and the averaging of station sensitivities inherent to their inversion procedure the relation is not very clear. Both *Takagi and Okada* (2012) and *Sawazaki and Snieder* (2013) found for the M9.0 Tohoku earthquake, that amplitudes of coseismic changes are in a better agreement with dynamic strain data than peak ground acceleration.

Here I compare the correlation of velocity drops of different earthquakes with a) dynamic strain at station PATCX and b) peak ground acceleration at station PATCX and c) the correlation of velocity drops by the Tocopilla event with the peak ground acceleration at different stations (each IPOC seismometer is accompanied by a low-gain accelerometer). The amplitude of the short-term velocity decreases are measured by taking the difference of mean velocity before the event and minimum velocity with reasonable correlation in the similarity matrix immediately after the event. Peak ground accelerations are calculated from the Z component of the response-corrected accelerometer

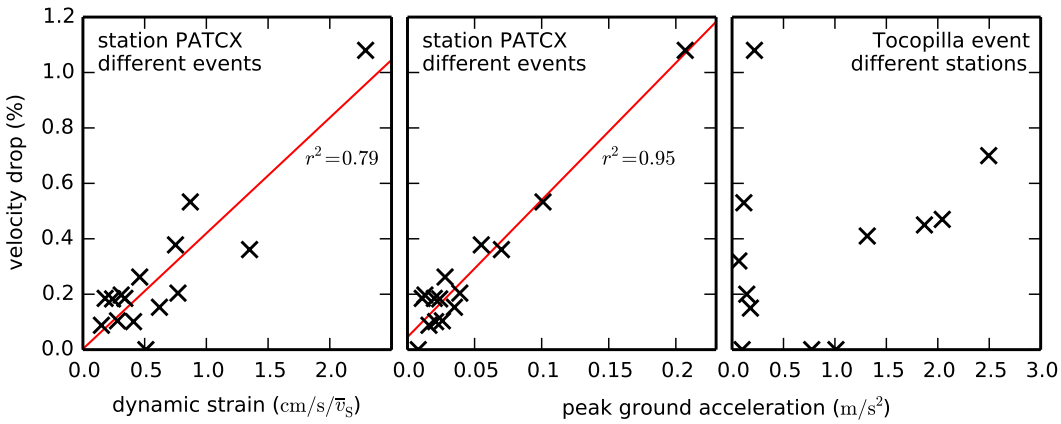

Figure 5.15.: Seismic velocity decrease as a function of dynamic strain (left) and peak ground acceleration for different events at station PATCX (middle) and for the Tocopilla event at different stations (right). The linear regressions favor a correlation between peak ground acceleration and velocity drop over a correlation between dynamic strain and velocity drop at station PATCX. This relationship does not hold true when considering different stations because of different environmental settings.

data at the different sites. Peak ground velocities at station PATCX are calculated from Z component of the response-corrected seismograms. Maxima of dynamic strains are expressed in terms of peak ground velocities and unknown average shear velocity $\overline{v}_S$. Figure 5.15 displays the results of the investigation. Notice that the data point for the Tocopilla earthquake and station PATCX consists of the long-term velocity decrease ϵ_{EQ} and the additional short-term velocity decrease. A linear relationship between the amplitude of the velocity drops and the peak ground acceleration of corresponding days for station PATCX is revealed (middle panel). In contrast a linear relationship does not exist when comparing the velocity decrease caused by the Tocopilla earthquake at different stations (right panel). Obviously the media around different stations have different sensitivity to velocity changes caused by ground acceleration. Dynamic strain shows a good correlation to the coseismic velocity changes, too, but its coefficient of determination r^2 is just 0.79 compared to 0.95 for the correlation to peak ground acceleration. Thus, the results presented here favor a linear relationship to peak ground acceleration over dynamic strain.

5.4.4. Velocity changes in the course of one day

Section 5.4.2 indicates that the long-term periodic velocity changes at station PATCX are caused by the temperature. Still, other factors showing a similar annual periodicity as

temperature could result in a similar effect. Precipitation or ground water level changes can be excluded in the Atacama desert because of very dry conditions. Here daily velocity changes are analyzed at station PATCX to test the hypothesis that velocity changes are temperature related. For calculating the daily velocity changes the autocorrelation of the 4 to 6 Hz data is performed in bunches of one hour with an overlap of half an hour. Then the stretching procedure is performed for the 48 autocorrelations for each day using the mean of all functions of this day as a reference. The result is demeaned and days with less than 48 data points because of missing data are discarded. Finally, the stretching factors with the highest correlation coefficient and of the same hour of day are stacked for all remaining 1570 days. Figure 5.16 shows the resulting velocity changes together with error bars of a length of twice the standard error of the mean. The mean of the correlation coefficients of each hour of the day are displayed in a second panel. A daily relative velocity change is observed with a peak-to-peak value of around 0.18 % for 5 to 10 s lag time and a peak-to-peak value of 0.04 % for the later two time windows. For larger lag times the errors tend to be higher and the correlation coefficient tends to be lower. The mean air temperature over all available days is plotted in the same panel as the daily velocity changes. The temperature data comes from a creepmeter installation (station CHO2) 32 km south of station PATCX with a similar distance to the coast and a similar elevation as PATCX. The velocity change measurements show the same pattern as the air temperature. The only difference is a phase shift of 1.5 h, 3.3 h and 14.5 h between the two measurements for the lag time windows 5 s−10 s, 10 s−15 s and 15 s−20 s, respectively. This result clearly indicates that the daily velocity change is caused by air temperature changes, especially for the first two time windows, and supports the idea that temperature changes are responsible for the annual variations of subsurface velocities. Amplitude and phase of the periodic velocity variations are discussed in section 5.5.

5.4.5. Frequency and lapse-time dependence of long-term velocity changes

Now long-term velocity changes at station PATCX are analyzed as a function of frequency and lag time. Therefore the data are filtered in the preparation-step (before autocorrelation and normalizations) with different frequency bands ranging from 2 Hz to 12 Hz. The rest of the processing is the same as described in section 5.2 except that lag-time windows of 2 s length are chosen as input into the stretching procedure (equation (5.1)) to increase the resolution in lapse time.

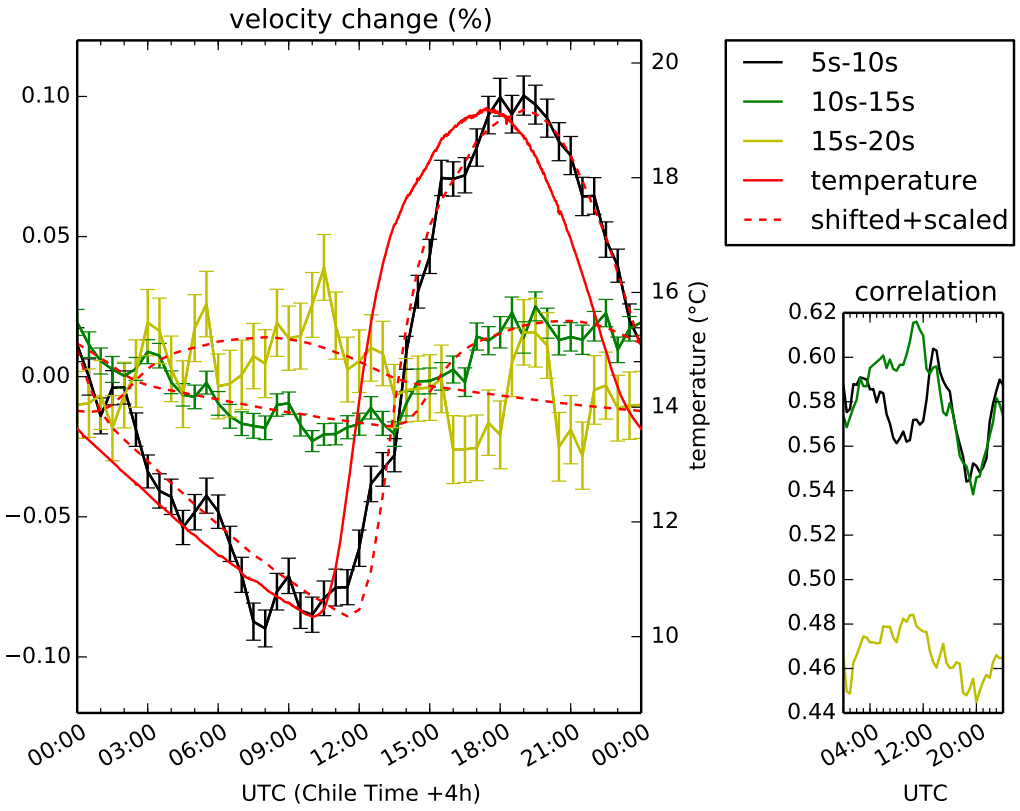

Figure 5.16.: Velocity change at station PATCX in the course of one day for three different time windows of the autocorrelation function compared to air temperature (red line). Additionally a fit (stretched on y-axis and delayed on x-axis) of the temperature curve to the observations is shown (dashed red lines). The velocity changes follow clearly the course of the temperature with a time delay of 1.5 h, 3.3 h and 14.5 h for the 5 s−10 s, 10 s−15 s and 15 s−20 s window, respectively. Data for the last time window has a low correlation and high error bars as compared to the first two time windows, and fits the temperature least well.

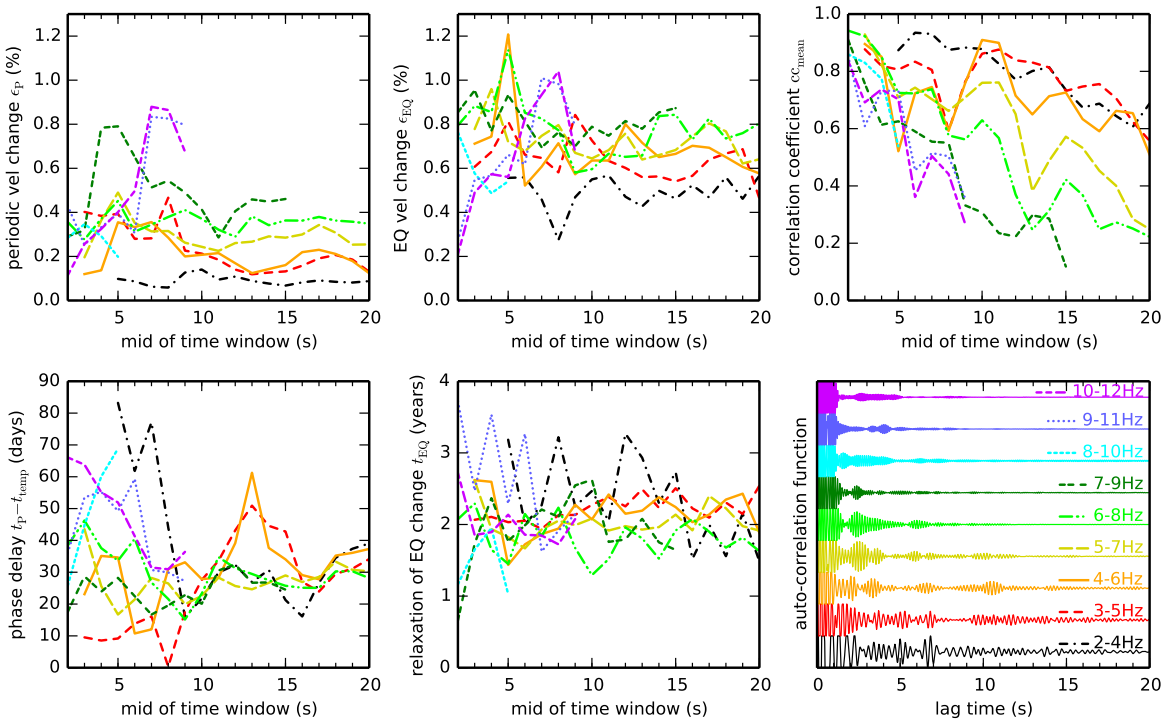

Figure 5.17.: Fitting parameters of equation (5.4) corresponding to the thick arrows in figure 5.14 and the optimized mean correlation coefficients cc_{mean} as a function of lag time window and frequency band for station PATCX. The width of the time windows is 2 s and the data is filtered in the frequency band before performing the autocorrelation and normalization. Lower left panel displays the phase delay of the periodic change against the phase of the temperature course. Lower right panel shows the legend and the mean autocorrelation functions with values above 0.02 clipped.

To easily compare the long-term velocity changes the parameters of the fit function ϵ_{mod} are compared. Figure 5.17 displays the velocity drop due to the Tocopilla event ϵ_{EQ}, the recovery time of this drop to 10 % t_{EQ}, the amplitude of the annual periodic velocity change ϵ_P and the phase delay against temperature of this change $t_P - t_{temp}$ together with the parameter that was maximized during the optimization process – the mean correlation at the different stretching factors ϵ_{mod} – all as a function of lag time and frequency. The phase of the temperature $t_{temp} = 30$ d was determined from a sensor at the creepmeter station CHO2 in around 50 cm depth. The following features are observed:

1. The mean correlation generally decreases with higher lag time, because the fraction of waves contributing to the Green's function is decreasing compared to random energy in the autocorrelation function. This effect is even larger for high frequencies.

The coherence is therefore completely lost for late lag times and high frequencies.

2. The amplitude of the periodic velocity change ϵ_{P} ranges from 0.1 % for low frequencies to 0.8 % for high frequencies. Observed trends are higher amplitudes for higher frequencies and slightly lower amplitudes for later lag times.

3. The amplitude of the Tocopilla earthquake related velocity change ϵ_{EQ} ranges from 0.5 % to 1.2 %. The same trend – higher amplitudes for higher frequencies – is observed as for ϵ_{P}. The magnitude of frequency dependency, however, is much smaller. It is just a factor of around 1.6 for amplitudes between 7 to 9 Hz and 2 to 4 Hz compared to a factor of 4 for ϵ_{P}. The amplitude is constant with lag time for most frequencies.

4. The phase delay between periodic velocity changes and the course of the temperature $t_{\mathrm{P}} - t_{\mathrm{temp}}$ is around 30 days for late lag times and most frequencies. For earlier lag times the phase tends to be smaller for low frequencies (except 2 to 4 Hz) and higher for high frequencies.

5. The recovery time t_{EQ} is nearly independent of lag time and frequency and is around 2 years.

The different apparent velocity changes of the autocorrelation signal of different frequency contents indicate that both the earthquake and periodical effects are near-surface effects. Therefore waves with higher frequencies sampling the near surface region show generally higher apparent velocity changes than low frequency waves. Because the periodical effect is even more dependent on frequency I suspect that this effect is even more shallow, which confirms again the indications of section 5.4.4, that the periodic velocity changes are caused by the atmospheric temperature. The phase delay of around 30 days could illustrate the fact that the temperature field in the subsurface is delayed due to diffusion. Finally, the duration of the recovery process of the earthquake related velocity changes is independent of frequency and therefore independent of depth.

5.5. Model for periodic velocity variations

5.5.1. Temperature fluctuations in the subsurface

Data from station PATCX show a velocity variation of the subsurface with annual and daily period. Section 5.4.3 indicates that these changes are caused by the change of the subsurface temperature. Furthermore, station PATCX shows, contrary to all other stations, velocity drops at low ground accelerations. The environment of station PATCX is strongly influenced by sedimented salt in the whole area including the nearby Salar Grande (figure 5.18). This is not the case for the other IPOC stations, even for PB02 which is at a similar distance but upslope from the Salar Grande. Therefore the particular geological conditions at station PATCX are suspected to be the reason for the medium's superior sensitivity to ground acceleration and temperature changes.

To improve the understanding of the periodic velocity changes, the effect of temperature changes with periods of one day and one year is modeled. The aim is to demonstrate that temperature changes are able to explain the observed velocity changes with reasonable medium parameters. This is specifically motivated by the fact, that studies of elastic constants and their temperature derivatives generally show a negative correlation between seismic velocity and temperature for constant pressure (e.g. *Anderson et al.*, 1968, table 1), opposite to the presented observations, which show a positive correlation. A possible process explaining this discrepancy is thermally induced stressing. Increased temperature can lead to stress build up. This again changes elastic properties and the velocity of the medium (*Toupin and Bernstein*, 1961, and references therein).

A model based on thermal stressing which explains the observations has to consider:

1. the distribution of temperature fluctuation in the subsurface,
2. thermally induced stress,
3. its implications on local velocity changes and finally
4. autocorrelation sensitivity kernels to model the phase delay and amplitude of velocity changes observed in the autocorrelation function.

For modeling the subsurface temperature fluctuations T, a temperature fluctuation field at the surface of

$$T(x, z{=}0, t) = T_0 \frac{1 + \cos kx}{2} e^{i\omega t} \tag{5.6}$$

is assumed as similarly described by *Berger* (1975). T_0 is the amplitude, ω the angular frequency and k the wavenumber of the spatial fluctuations. Cartesian coordinates x,

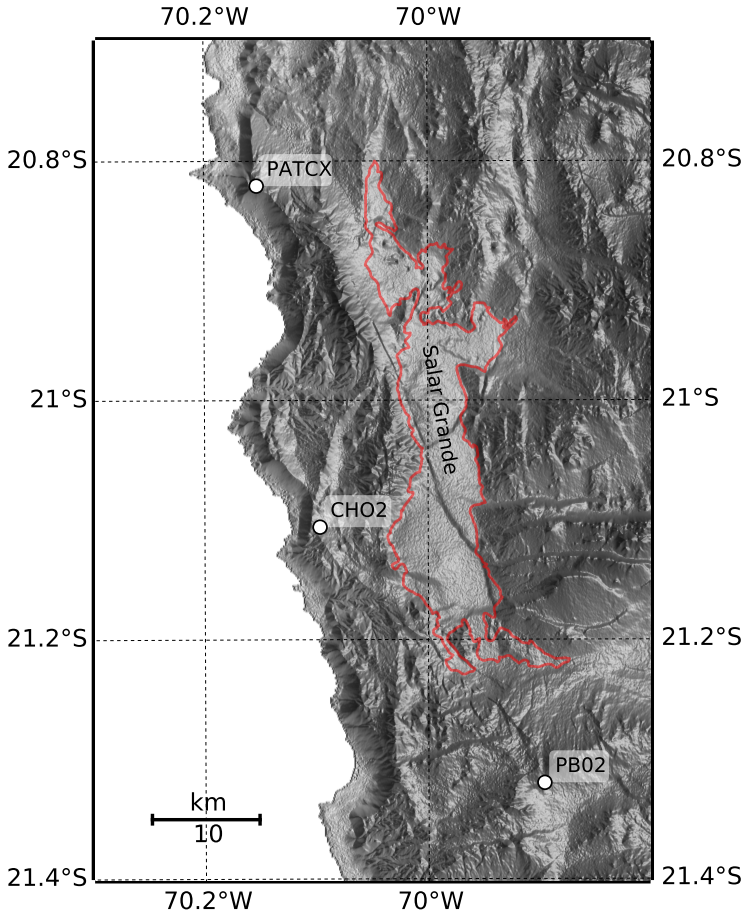

Figure 5.18.: Shaded relief map with seismic stations PATCX, PB02 and creepmeter installation CHO2. Contour of Salar Grande is from *Reijs and McClay* (1998). The environment of station PATCX is dominated by salar sediment, unlike PB02, which is at a similar distance but upslope from the Salar Grande.

y and z point eastern, southern and downwards, respectively. The term $(1 + \cos kx)/2$ represents the influence of topography and the ocean (*Berger*, 1975). Its wavelength $2\pi/k$ is in the order of several kilometers. Station PATCX is located around 3 km away from the ocean. Assuming $k = 2\pi/10\,\mathrm{km}$ and a station near $x = 0$, temperature fluctuations over the ocean are small with no fluctuations 2 km away from the coast. Horizontal heat conduction is ignored with the approximation $k^2 \ll \omega/\kappa$ valid for typical values of k, ω and thermal diffusivity κ. The solution of the heat conduction equation then reads

$$\begin{aligned} T(x,z,t) &= T_0 \frac{1+\cos kx}{2} e^{i(\omega t-\gamma z)-\gamma z} \\ &= T(x, z{=}0, t)\, e^{-(1+i)\gamma z} \quad \text{with } \gamma = \sqrt{\frac{\omega}{2\kappa}}\,. \end{aligned} \tag{5.7}$$

The resulting temperature fluctuations are exponentially decreasing with depth and they are subject to a phase delay increasing with depth. At the skin depth $z = 1/\gamma$ the amplitude of the signal is $1/e$ compared to the amplitude at the surface and the phase delay is 1 rad.

κ and T_0 for daily and annual temperature fluctuations can be determined with the help of temperature sensors installed at the creepmeter station CHO2 32 km south of PATCX. *Bach* (2010) describes an experiment with 4 temperature sensors installed at different depth for a period of 4 days. The absolute values of the daily temperature fluctuation are taken from table 3.1 and the phase shifts are estimated from figure 3.5 of *Bach* (2010). The data point for annual temperature fluctuation is taken from the temperature sensor installed directly at the creepmeter buried at around 50 cm depth. These data points and the expected temperature variation with depth for annual and daily periods are displayed in figure 5.19. The expected temperature variation is calculated as a weighted least-squares fit of function $T(x, z, t)$ from equation (5.7) with $\omega = 2\pi/1\,\mathrm{d}$, $x = 0$ and $t = 0$ to the data points. The weights are $1/2\pi$ for phase delays and $1/19\,\mathrm{K}$ for absolute daily temperature fluctuations. The misfit function is defined as

$$\mathrm{mf} = \sum_{i=1}^{4} \frac{\left(T_\mathrm{m}(z_i) - T_{0\mathrm{d}} e^{-\gamma_\mathrm{d} z_i}\right)^2}{(19\,\mathrm{K})^2} + \frac{\left(\mathrm{ph}_\mathrm{m}(z_i) + \gamma_\mathrm{d} z_i\right)^2}{(2\pi)^2} \tag{5.8}$$

with T_m and ph_m representing the 4 data points of *Bach* (2010). The best fit is obtained for values of $\gamma_\mathrm{d} = 10.4\,\mathrm{m}^{-1}$ and $2T_{0\mathrm{d}} = 38\,\mathrm{K}$ for daily temperature fluctuations with a misfit value of $\mathrm{mf} = 0.008$. The resulting thermal diffusivity is $\kappa = 0.3\,\mathrm{mm}^2/\mathrm{s}$. The amplitude of the annual temperature fluctuation can be derived from the single data point for yearly fluctuations and is $2T_{0\mathrm{a}} = 12\,\mathrm{K}$. The resulting skin depth is 1.9 m for annual and just 10 cm for daily changes (table 5.1). The daily temperature fluctuations

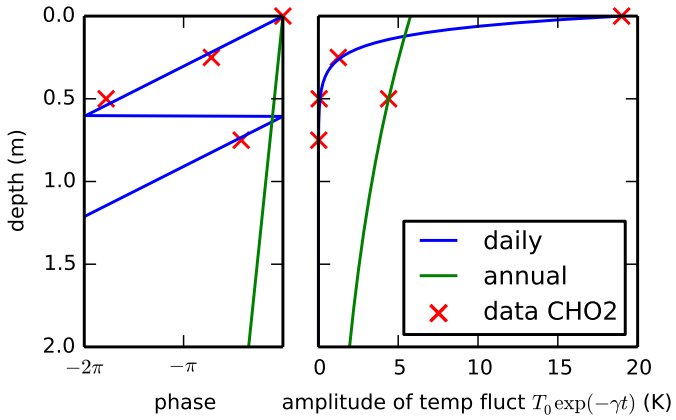

Figure 5.19.: Phase and absolute value of daily and annual temperature fluctuations as a function of depth. The skin depth is 1.9 m for annual and just 10 cm for daily changes. The respective peak-to-peak amplitudes are 12 K and 38 K. Data points of daily temperature fluctuations are from *Bach* (2010).

Table 5.1.: Thermal diffusivity, resulting skin depth and delay time of a periodical surface temperature field for daily and annual periods. Thermal diffusivity is derived from the temperature data in figure 5.19.

κ in mm^2/s	period	γ in m^{-1}	skin depth $1/\gamma$ in m	delay time $1/\omega$ at depth $1/\gamma$
0.3	1 a	0.54	1.9	58 d
	1 d	10.4	0.10	3.8 h

directly at the surface are larger than the daily air temperature variations of around 9 K because of heating by absorption of radiation.

5.5.2. Thermally induced stress

The next step is the calculation of stress changes induced by the fluctuating temperature. *Berger* (1975) thoroughly analyzed the relation between these two quantities with a 'plane strain' assumption. *Ben-Zion and Leary* (1986) added unconsolidated cover at the surface to Berger's model. The unconsolidated layer takes part in the diffusion of heat, but does not support stress. This leads to a larger time delay between surface temperature and strain which better fits their data. *Tsai* (2011) tried to explain periodic velocity variations observed by *Meier et al.* (2010) in Southern California with these models.

Berger (1975) describes thermally induced stress by supplying the stress-strain relationship with an additional term to allow for thermal expansion :

$$\varepsilon_{ij} = \frac{1+\nu}{E}\sigma_{ij} - \left(\frac{\nu}{E}\sum_k \sigma_{kk} - \alpha T\right)\delta_{ij} \,. \tag{5.9}$$

Here ε is strain, σ stress, E the Young's modulus, ν Poisson's ratio, α the linear expansion coefficient, T temperature variation and δ_{ij} is the Kronecker delta which yields 1 for $i = j$ and 0 otherwise. In this thesis the stress change is estimated as a linear superposition of the principal stresses in all 3 directions

$$\sigma = \sigma_{xx} + \sigma_{yy} + \sigma_{zz} \,. \tag{5.10}$$

Using equation (5.9) and the plane strain assumption $\varepsilon_{yy} = 0$ stress can be expressed as a function of strains and temperature fluctuation:

$$\sigma = \frac{E}{1-2\nu}\left(\varepsilon_{xx} + \varepsilon_{zz} - 3\alpha T\right) \,. \tag{5.11}$$

Finally, the solution of equation (5.9) for the approximation $k \ll \gamma$ from *Berger* (1975, equation (8), reproduced in appendix C.5) is inserted and leads together with the temperature field from the previous section to

$$\sigma = \frac{\alpha E T(z{=}0)}{1-\nu}\left(-2e^{-(1+i)\gamma z} + (1+\nu)\,(1-i)\,\frac{k}{\gamma}e^{-kz}\right) \,. \tag{5.12}$$

One term with k^2/γ^2 is neglected in the process because of $k \ll \gamma$. Higher velocities are expected for compressional stress, which corresponds to negative (extensional) stress σ. The compressional stresses $-\sigma_{xx}$, $-\sigma_{yy}$, $-\sigma_{zz}$ and $-\sigma$ are plotted in figure 5.20 at location $x = 0$ and time $t = 0$ for periods of one year. The solution for stress includes two exponential terms decreasing with depth: one decreasing with $e^{-\gamma z}$ and the other with e^{-kz} as illustrated in top and bottom of figure 5.20. The first term is directly proportional to the temperature fluctuation field in the subsurface and clearly dominates near the surface when z is in the order of the temperature skin depth $1/\gamma$. The second term originates from the spatial fluctuation of the temperature field and dominates for larger z. The phase for compressional stresses of the first term is the same as for the subsurface temperature field. The phase delay for the second term compared to the surface temperature is constant and $-5\pi/4$. When comparing with Berger's publication one has to keep in mind that compressional stress $-\sigma$ and extensional strain ε show the

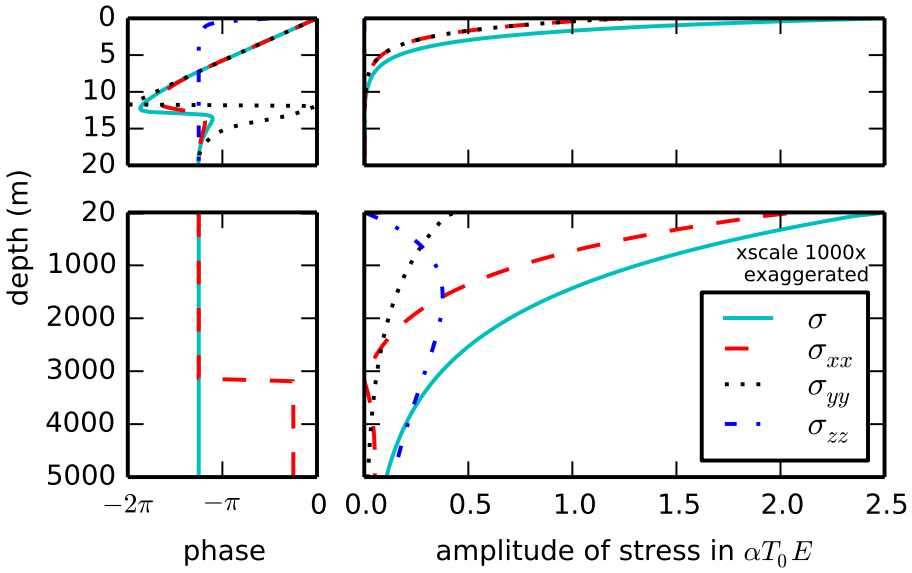

Figure 5.20.: Stress in the subsurface due to temperature changes for a period of one year and for $t = 0$, $x = 0$ and $\nu = 0.2$. The y-axis of the upper panels scales from 0 to $\approx 10/\gamma$ for $\gamma = 0.54\,\mathrm{m}^{-1}$. The lower panel's scale ranges up to a depth of π/k for $k = 2\pi/10\,\mathrm{km}$. The scale of the x-axis of the lower right panel is exaggerated by a factor of 1000 compared to the displayed scale. The phases are displayed for compressional stresses. In the lower left panel, phases of stresses in y and z direction are the same as for the stress invariant. The upper panels are dominated by the first term, the lower panels by the second term of equation (5.12).

same variation with depth. The phase delay for the first near surface term is also the same for $-\sigma$ and ε. However the phase delays of the second term are different being $-5\pi/4$ for $-\sigma$ and $-\pi/4$ for ε. When assuming a constant sensitivity with depth the integrated first term for stress is proportional to $(-1+i)/2\gamma$ (phase delay $-\pi/4$) while the second term integrates to a value proportional to $(1-i)/\gamma$ being by a factor of $1+\nu$ larger than the first term but with opposite phase.

I expect that the first term dominates the data, because autocorrelations were analyzed with a small lag time. Furthermore, the observed values and the second term have a different phase shift between surface temperature and velocity change.

5.5.3. Relationship between compressional stress and relative velocity change

Before illustrating the last statement of the previous section the relationship between stress and velocity needs to be discussed. Velocity variations induced by stress can be caused by opening and closing of (micro-)cracks and the pore space in the material. Therefore, rheology models on microscopic scale were developed by different authors (e.g. *Budiansky and O'Connell*, 1976; *Lyakhovsky et al.*, 1997). *Shapiro* (2003) and *Shapiro and Kaselow* (2005) introduced the elastic piezosensitivity and the tensor of stress sensitivity to describe stress-dependent changes in the elastic constants of isotropic material under isotropic load and of anisotropic rocks under a load of arbitrary shape, respectively. They find that compliant pores (compare with figure 3 of *Shapiro and Kaselow*, 2005) play the most important role in the stress-velocity relationship. Following the principles of poroelasticity they derive and interpret the phenomenologically established (e.g. *Zimmerman et al.*, 1986; *Khaksar et al.*, 1999) stress-velocity relationship

$$v(p) = A + Kp - B\exp(-pD) \tag{5.13}$$

with seismic velocity v, differential stress p between confining pressure and pore pressure and constants A, K, B, D. Equation (5.13) describes a positive correlation between changes in confining pressure and changes of seismic velocity.

Independent from the possible underlying mechanisms I follow here a macroscopic approach which is based on the expansion of the energy-strain function to cubic terms in strain leading to the third-order elastic constants. By measuring velocity variations due to uniaxial tension or hydrostatic pressure the third-order elastic (TOE) constants can be determined for different materials (*Hughes and Kelly*, 1953; *Toupin and Bernstein*,

1961; *Thurston and Brugger*, 1964). TOE constants of rocks are found to be very high compared to the second-order elastic Lamé constants (*Winkler and Liu*, 1996; *Winkler and McGowan*, 2004). This means seismic velocities in rock are relatively sensitive to stress changes as indicated by the increase of velocity with depth in the subsurface. The relative velocity change due to compressional stress σ_c is estimated with the help of experimentally determined values of $\partial\rho v^2/\partial\sigma_c$:

$$\frac{\Delta v}{v} = \frac{\partial v}{v\partial\sigma_c}\Delta\sigma_c = \frac{\partial\rho v^2}{2\rho v^2\partial\sigma_c}\Delta\sigma_c = b\frac{\partial\rho v^2}{\partial\sigma_c}\frac{(1-\nu)\,\Delta\sigma_c}{E}\,. \tag{5.14}$$

ρv^2 is the shear modulus for S-waves and the P-wave modulus for P-waves. When using the relationships between different elastic moduli $\rho v_s^2 = E/2\,(1+\nu)$ and $\rho v_p^2 = E\,(1-\nu)/(1+\nu)\,(1-2\nu)$ (*Birch*, 1961, table 4) constant b can be expressed as

$$b = \begin{cases} \frac{(1+\nu)(1-2\nu)}{2(1-\nu)^2} \approx 0.6 & \text{for P-waves and } \nu = 0.2\,, \\ \frac{(1+\nu)}{(1-\nu)} \approx 1.5 & \text{for S-waves and } \nu = 0.2\,. \end{cases}$$

Moreover $\partial\rho = 0$ is assumed in equation (5.14) because the effect of density change is negligibly small compared to the effects of stressing due to $\partial\rho v^2/\partial\sigma_c \gg 1$ (table 5.2). Combining equations (5.12) and (5.14) with $\Delta\sigma_c = -\sigma$ leads to:

$$\frac{\Delta v}{v}(x,z,t) = b\alpha\frac{\partial\rho v^2}{\partial\sigma_c}T(x,z{=}0,t)\left[2e^{-(1+i)\gamma z} - (1+\nu)\,(1-i)\,\frac{k}{\gamma}e^{-kz}\right]. \tag{5.15}$$

When only considering the first term, which is reasonable for a sensitivity kernel decreasing rapidly with depth, the equation further simplifies to

$$\frac{\Delta v}{v}(x,z,t) = 2b\alpha\frac{\partial\rho v^2}{\partial\sigma_c}T(x,z,t)\;. \tag{5.16}$$

The temperature effect on seismic velocities due to the $\exp(-\gamma z)$ term is roughly estimated in table 5.2. These values seem to become very high for temperature fluctuations up to 30 K, but such velocity variations are only observed very close to the surface. The local velocity changes in the subsurface still need to be linked to the observed velocity changes by determining sensitivity kernels of the measurements. Although equation (5.16) is a reasonable approximation, equation (5.15) with both terms will be used for calculating the local velocity changes in the following.

Table 5.2.: $\partial\rho v^2/\partial\sigma_c$ as an expression of third-order elastic constants, linear thermal expansion coefficient and the resulting relative velocity change due to temperature change predicted by the model using equation (5.16) for different rock materials. Reproduced are the values for P-waves and the two horizontal modes of S-waves for uniaxial stress. $\partial\rho v^2/\partial\sigma_c$ for hydrostatic stress is even higher up to a factor of 10.

material	$\frac{\partial\rho v^2}{\partial\sigma_c}$	α in $1\times10^{-6}\,\mathrm{K}^{-1}$	$\frac{\Delta v}{vT}$ in $\%\mathrm{K}^{-1}$
Berea sandstone #1	320, 480, 160[a]	10[b]	0.36, 1.44, 0.48
Indiana limestone	240, 160, 80[a]	8[b]	0.22, 0.38, 0.20
Westerly granite	670, 160, 40[c]	8[b]	0.60, 0.38, 0.10

[a] *Winkler and McGowan* (2004)
[b] *Skinner* (1966)
[c] *Winkler and Liu* (1996)

5.5.4. Autocorrelation sensitivity kernels

I assume here that the scattered waves recorded by the autocorrelation function are mainly body waves. This assumption is supported by simulations of *Obermann et al.* (2013) accentuating the dominance of body waves against surface waves for late times and high heterogeneity. In the long-time limit the scattered waves can be described in the diffusion regime with the normalized energy distribution in the absence of absorption

$$P_{\mathrm{diff}}(\boldsymbol{r},t)=\frac{1}{(4\pi Dt)^{3/2}}\exp\left(-\frac{r^2}{4Dt}\right) \tag{5.17}$$

with distance to the source $r=|\boldsymbol{r}|$, travel time t and diffusion coefficient $D=cl/3$ with velocity c and mean free path l. Because the travel times of the waves in the observations are quite small in the order of the mean free time l/c, this approximation is not strictly valid anymore and low-order scattered waves have to be considered, too. For this the analytic approximation of the solution for 3-dimensional radiative transfer by *Paasschens* (1997) is used:

$$\begin{aligned}P_{\mathrm{rt}}(\boldsymbol{r},t)\approx\exp\left(-\frac{ct}{l}\right)\Bigg[&\frac{\delta(r-ct)}{4\pi r^2}+\left(\frac{4}{3}\pi lc\right)^{-\frac{3}{2}}\\&\cdot\left(1-\frac{r^2}{c^2t^2}\right)^{\frac{1}{8}}t^{-\frac{3}{2}}G\left(\frac{ct}{l}\left(1-\frac{r^2}{c^2t^2}\right)^{\frac{3}{4}}\right)H(ct-r)\Bigg]\\ \text{with } G(x)=e^x&\sqrt{1+\frac{2.026}{x}}\,.\end{aligned} \tag{5.18}$$

The term with the Dirac delta function δ describes the direct wave, while the other term describes scattered waves. In the limit case $r, l \ll ct$ equation (5.18) transforms to equation (5.17) for the diffusion approximation. The travel time kernel for the autocorrelation in the diffusion approximation is a special case of the kernel for the cross correlation function for co-located source and receiver (*Pacheco and Snieder*, 2005) and given by

$$K_{3\mathrm{D}}(\boldsymbol{r}, t) = \frac{1}{P_0(t)} \int_0^t P(\boldsymbol{r}, t - t')\ P(\boldsymbol{r}, t')\ \mathrm{d}t' \,. \tag{5.19}$$

Planès et al. (2013) derived this equation independently based on scattering theory. $P_0(t)$ is a normalization constant. In the diffusion approximation it is given as $P(\mathbf{0}, t)$, the energy of the wave field at the position of the receiver at time t. $K_{3\mathrm{D}}(\boldsymbol{r}, t)$ represents the time of multiple scattered waves spent inside an infinitesimal volume at location $\boldsymbol{r}$ – under the condition that the waves start at the receiver and are detected by the receiver after the travel time t. According to the definition of $K_{3\mathrm{D}}$ the travel time can be expressed as the integral

$$t = \int_V K_{3\mathrm{D}}(\boldsymbol{r}, t)\ \mathrm{d}\boldsymbol{r}^3 \tag{5.20}$$

over the whole volume V (*Pacheco and Snieder*, 2005). *Pacheco and Snieder* (2005, equation (19)) show how to calculate the travel time change as a function of slowness perturbation in the medium with the help of equation (5.20). The result, rewritten, connects the observed velocity changes ϵ from section 5.4.2 with the local velocity changes $\Delta v / v(\boldsymbol{r})$:

$$\epsilon(t) = \frac{1}{t} \int_V K_{3\mathrm{D}}(\boldsymbol{r}, t)\, \frac{\Delta v}{v}(\boldsymbol{r})\, \mathrm{d}\boldsymbol{r}^3 \,. \tag{5.21}$$

Furthermore *Pacheco and Snieder* (2005) give the solution for the autocorrelation kernel in the diffusion approximation as

$$K_{3\mathrm{D,diff}}(\boldsymbol{r}, t) = \frac{1}{2\pi D r} \exp\left(\frac{-r^2}{Dt}\right) \,. \tag{5.22}$$

Equation (5.22) can be derived by inserting equation (5.17) into equation (5.19). For calculating the kernel in the radiative transfer approximation, the definition of the kernel in the diffusion approximation in equation (5.19) is used as done by *Planès et al.* (2013). This neglects the sensitivity of direct waves because equation (5.19) has been derived in the diffusion approximation but the radiative transfer allows adding sensitivity of low-ordered scattered waves. A disadvantage of this approach is that $P_0(t) = P(\mathbf{0}, t)$ is not valid anymore under the condition that equation (5.20) holds true. This problem is

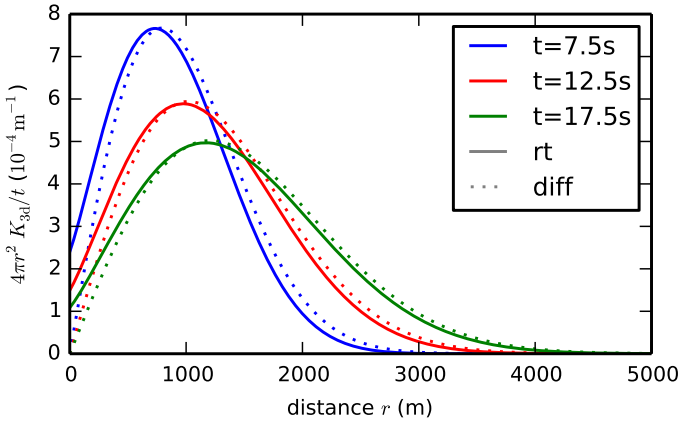

Figure 5.21.: Sensitivity kernel K_{3d} as a function of distance for travel times $t = 7.5\,\mathrm{s}$, $12.5\,\mathrm{s}$ and $17.5\,\mathrm{s}$ with $c = 1\,\mathrm{km/s}$ and $l = 500\,\mathrm{m}$. The kernels diverge for $r \to 0$ and are therefore multiplied by $4\pi r^2$ to represent the sensitivity to an infinitesimal spherical shell volume. Furthermore the kernels are divided by t.

circumvented by a renormalization of the kernel. $P_0(t)$ is then given by

$$P_0(t) = \frac{1}{t} \int_V \int_0^t P(\boldsymbol{r}, t - t')\; P(\boldsymbol{r}, t')\; \mathrm{d}t' \mathrm{d}\boldsymbol{r}^3\,. \tag{5.23}$$

Finally, the 3D autocorrelation kernel is calculated in the radiative transfer approximation by inserting equation (5.18) and (5.23) into equation (5.19). The kernel calculated in this way is not exact even in the radiative transfer approximation, because firstly the analytic approximation given by equation (5.18) is used and secondly the sensitivity of the direct wave term is not considered. Still, the kernel is more reliable than the kernel in the diffusion approximation because it includes correction terms for low-order scattering.

The integration is performed partly analytically for terms involving the Dirac delta function and partly numerically (appendix C.6). The 3D solution for the autocorrelation kernels are displayed in figure 5.21 for $c = 1\,\mathrm{km/s}$ and $l = 500\,\mathrm{m}$ and three different travel times. With the approximation that the temperature T does not vary laterally in the main scope of the sensitivity kernel ($\cos kx \approx 1$ in equation (5.15)), $\Delta v/v$ becomes a function of just z and t. Therefore, the kernel is further integrated in x and y directions to isolate the depth dependence. A cylindrical coordinate system with radius ρ and depth z is chosen for this purpose. Equation (5.21) then reads

$$\epsilon(t) = \frac{1}{t} \int_0^\infty K_z(z, t)\, \frac{\Delta v}{v}(z)\, \mathrm{d}z \tag{5.24}$$

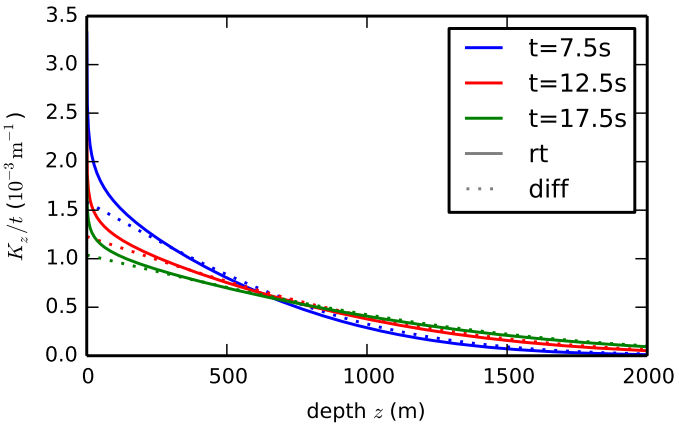

Figure 5.22.: Sensitivity kernel K_z divided by t for travel times $t = 7.5\,\mathrm{s}$, $12.5\,\mathrm{s}$ and $17.5\,\mathrm{s}$ with $c = 1\,\mathrm{km/s}$ and $l = 500\,\mathrm{m}$ as a function of depth. Only the regularized version of the kernel is shown. The contribution of the irregular part of the kernel to the modeled velocity change is negligible (appendix C.6).

with

$$\begin{aligned} K_z(z,t) &= 2\int_0^\infty 2\pi\rho K_{3\mathrm{D}}\left(\sqrt{\rho^2+z^2},t\right)\mathrm{d}\rho \\ &= 2\int_z^\infty 2\pi r K_{3\mathrm{D}}(r,t)\,\mathrm{d}r\,. \end{aligned} \tag{5.25}$$

Insertion of equation (5.22) and rewriting the integral with the substitution $r = r'\sqrt{Dt}$ gives the analytic solution in the diffusion approximation

$$K_{z,\mathrm{diff}}(z,t) = \sqrt{\frac{\pi t}{D}}\left(1-\mathrm{erf}\left(\frac{z}{\sqrt{Dt}}\right)\right) \tag{5.26}$$

with the error function $\mathrm{erf}(x) = 2/\sqrt{\pi}\cdot\int_0^x \exp(-x'^2)\,\mathrm{d}x'$. Figure 5.22 compares this solution with the numerical integration for radiative transfer. As expected waves arriving at earlier times have a higher sensitivity to velocity changes at shallow depth than later arriving waves. Low-order scattered waves in the radiative transfer solution further intensify the sensitivity close to the receiver.

5.5.5. Periodic velocity changes – observed and modeled

Finally, the fruits can be reaped and relative velocity changes predicted by the model can be calculated. Parameters defining the model are summarized in table 5.3. The parameters of the temperature field determine its spatial characteristics namely the phase and amplitude. They are determined from temperature data from station CHO2 as described in section 5.5.1. The wavenumber k of the temperature field is chosen as

Table 5.3.: Model parameters and assumed values

temperature field		
angular frequencies	ω_d, ω_a	$2\pi/1\,\mathrm{d}$, $2\pi/1\,\mathrm{a}$
amplitudes	$T_{0\mathrm{d}}$, $T_{0\mathrm{a}}$	6 K, 19 K
skin depths	$1/\gamma_\mathrm{d}$, $1/\gamma_\mathrm{a}$	10 cm, 1.9 m
wave number	k	$2\pi/10\,\mathrm{km}$
elastic properties of the medium		
Poison's ratio	ν	0.2
factor (Poison's ratio)	$b(\nu)$	0.6 – 1.5
linear thermal expansion	α	$1 \times 10^{-6}\,\mathrm{m}^{-1}$ – $1 \times 10^{-5}\,\mathrm{m}^{-1}$
velocity change due to stress	$\partial\rho v^2/\partial\sigma_\mathrm{c}$	200 – 1000 (uniaxial) 500 – 5000 (hydrostatic)
scattering parameters for sensitivity kernel		
velocity	c	1 km/s
mean free path	l	500 m

$2\pi/10\,\mathrm{km}$ to reflect the influence of the ocean remaining at constant temperature. The stress field in the subsurface can be determined with the elastic properties of the medium. The relative change of seismic velocities is inferred from equation (5.15). The spatial characteristics of the local velocity change are just controlled by the parameters of the temperature field. Poisson's ratio is set to 0.2 resulting in values of b in equation (5.14) equal to 0.6 for P-waves and 1.5 for S-waves. For the scattered mixture of wave types that is analyzed in the autocorrelation function, b is between these two values. The velocity change due to stress $\partial\rho v^2/\partial\sigma_\mathrm{c}$ is not very well determined even if the material and the polarization properties of the contributing waves were known. $b = 1.5$, $\alpha = 1 \times 10^{-5}\,\mathrm{m}^{-1}$ and $\partial\rho v^2/\partial\sigma_\mathrm{c} = 5000$ (hydrostatic pressure changes) form the upper end of the possible intervals are chosen to maximize the estimate of the temperature-dependent velocity changes. Together with the autocorrelation depth sensitivity kernels that are determined by the scattering parameters and equation (5.24), finally predicted velocity changes can be calculated. Here I choose $c = 1\,\mathrm{km/s}$ as a near surface velocity and $l = 500\,\mathrm{m}$ for the scattering mean free path. This is a rough guess based on information from volcanoes (*Wegler and Lühr*, 2001; *Yamamoto and Sato*, 2010) as there is no information available from this area or one with similar conditions.

A comparison of the modeled and observed daily and annual periodic velocity changes is presented in table 5.4 for 4 to 6 Hz. The modeled values are calculated for the lag times 7.5 s, 12.5 s and 17.5 s. These lag times represent the middle of the 5 second long lag time intervals used for the observations of velocity changes of daily periodicity. For

Table 5.4.: Comparison of modeled and observed daily and annual periodic velocity changes (amplitude ϵ_P and phase delay $t_P - t_{temp}$) for 4 to 6 Hz and different lag times.

period	lag time	model		observation	
		phase d.	amplitude	phase d.	amplitude
1 day	7.5 s	2.8 h	0.058 %	1.5 h	0.09 %
	12.5 s	2.8 h	0.037 %	3.3 h	0.02 %
	17.5 s	2.8 h	0.028 %	14.5 h	0.02 %
1 year	7.5 s	41 d	0.26 %	(25 ± 11) d	(0.29 ± 0.06) %
	12.5 s	41 d	0.17 %	(38 ± 12) d	(0.17 ± 0.03) %
	17.5 s	41 d	0.13 %	(33 ± 4) d	(0.19 ± 0.04) %

annual periodicity 6 observed values from the overlapping 2 second long time windows from figure 5.17 are averaged to determine the mean value and its sample standard deviation for each of the 5 second long time windows. The first-order observation that amplitudes decrease with lag time both for daily and annual periods can be reproduced by the model. The amplitude values roughly agree within a factor of 2. The modeled annual phase delay is 41 days and therefore just between 3 and 16 days away from the mean of the observed phase delays in the three lag time windows. The modeled daily phase delay is 2.8 h and near the observed value at 12.5 s lag time. The phase delays for the two other lag times are not predicted well.

Despite the poor fit of some observations the model shows that the measured daily and annual temperature variations are within the range of values that are to be expected for thermally induced stress changes. It is reasonable to assume that the temperature field is well determined from the data of the nearby station CHO2. There are three sources of uncertainty in the model that could cause discrepancies. First and foremost the assumption of the horizontal confinement that directly relates expansion to stress might be inappropriate. *Ben-Zion and Leary* (1986) included an unconsolidated surface layer in their model that takes part in the heat conduction but does not transfer stresses and would thus not influence velocities. The choice not to include such a layer is based on the observation of sediment that is firmly cemented by salt crystals at the surface. The second assumption of the model that is not well constrained is the wavelength of the spatial temperature variation. Changing k affects mostly the ratio between the terms in equation (5.15). But as the model is dominated by the first term the results will not change significantly for a large range of k. Finally, the third assumption with considerable uncertainty is that information about velocity changes is carried by body

waves that propagate in a medium with depth independent mean free path. The choice of body wave kernels was motivated by the observed lapse time dependence of the velocity changes. Surface wave propagation would not be consistent with this observation but could in turn explain the frequency dependence. (The frequency dependency of the velocity changes can also be explained by a frequency-dependent scattering mean free path.) In fact *Obermann et al.* (2013) showed that the sensitivity of measurements with scattered coda waves is a combination of surface and body wave sensitivity with time dependent partitioning that gradually transitions from surface to body wave sensitivity with increasing lapse time. Such an effect would indeed allow to explain the small phase delays at early lag times for daily periods as well as for annual periods in some frequencies bands. The exceptionally high phase delay of 14.5 h for 17.5 s lag time and daily periods could be explained by a reduced sensitivity for the topmost layer ($\approx$10 cm). Then the second term in equation (5.15) would dominate for daily periods, but the first term for annual periods. This would explain, why the observed lag time has the same phase delay of $5\pi/4$ (corresponding to 15 h) as the second term of the stress distribution. However, the measurement at 17.5 s lapse time has a significant uncertainty. The relatively strong fluctuations of the frequency and lapse time characteristics of the measurements (figure 5.17) partly result from deterministic arrivals in the autocorrelations. This could be responsible for the extraordinary high phase delay of low-frequency autocorrelations at 13 s that appear as outliers in the model that is valid for an ensemble average only.

To summarize, key features and rough amplitudes of the observations can be reproduced by the model. Periodic velocity variations result from thermal stresses in the uppermost 10 m. Even high deviations from average observations for some lag times and frequencies could be explained by sensitivity kernels, resulting from direct reflections, surface wave contributions or locally varying scattering parameters.

6. Conclusions

Different methods are used to analyze temporal variations of seismic velocities in the north Chilean crust. With the receiver function method shifts in the converted phases at the time of the Tocopilla earthquake can be observed. However, a conclusion on a distinct velocity change can not be drawn because of the methods high statistical errors. To monitor velocity variations in the deeper crust I suggest to use body waves constructed from ambient noise in a future study. This combines the advantage of the depth sensitivity of receiver functions with the advantages of ambient noise based methods. Recent studies successfully demonstrate the construction of body waves from ambient noise cross-correlations (e.g. *Boué et al.*, 2013). *Lin and Tsai* (2013) show, that the late coda of large deep earthquakes is most suitable to construct teleseismic body waves between two stations. Because the virtual source location equals the position of one station, the disadvantage of changing source parameters of the receiver function method can be circumvented. A data point for monitoring can then be obtained for each sufficient big and deep earthquake without limiting the event region as in this study.

The second method that I use for the monitoring of velocity changes is noise correlation interferometry. No distinct velocity change is observed by analyzing the stacked daily cross-correlation functions. Several factors influence this observation. Firstly, velocity variations are only induced at the shallow subsurface. Compared to the whole depth range which low-frequency waves are sampling the contribution of the shallow layers to the observed apparent velocity change is minor. Secondly, the variability of the microseismic noise sources is not completely suppressed by using a time window in the coda of the constructed Green's function. Long-term velocity changes under 0.2 % are therefore difficult to discriminate from the changes in the apparent velocity induced by the variability of noise sources. And finally, the applied stacking limits the temporal resolution of the method and prevents the observation of possible short-term velocity variations.

By using autocorrelations the above factors do not apply and seismic noise velocity variations are observed that correspond to changes in rheological properties caused by temperature variations and ground shaking. As previously reported for other earthquakes

(e.g. *Wegler et al.*, 2009) a coseismic decrease of seismic velocities is observed in and around the fault zone of the Tocopilla earthquake. The amplitude of this drop decreases with distance but shows large scatter. Velocity changes and peak ground acceleration (PGA) measured at different seismometer locations are not correlated in any simple way.

At station PATCX a strong coseismic decrease with the Tocopilla event is observed despite the comparatively large distance from the fault area and the small peak ground acceleration (PGA). This indicates a high sensitivity of the subsurface velocity to shaking. The observation of velocity changes coincident with other regional earthquakes confirms the high sensitivity and allows to investigate the relation between PGA and the amplitude of the velocity decrease without the need to involve different stations. A linear correlation between PGA and the observed velocity changes at PATCX can be identified. This means that the coseismic changes are due to shaking and consequent damage of the near surface material and not related to changes of the ambient static stress. Previous attempts to establish a relation of $\Delta v/v$ with PGA or dynamic strain suffered from the necessity to include data from different stations as usually the distribution of changes following a single event is analyzed (e.g. *Sawazaki and Snieder*, 2013). This shows that the local subsurface conditions have a major effect on the amplitude of the velocity changes. As the velocity changes are due to changes in the elastic moduli that are an important quantity in earthquake engineering, the slope of the PGA-$\Delta v/v$ relation might add important information to the site characterization in seismic hazard analysis. A high sensitivity of the subsurface material at station PATCX is also found for compressional stress. Periodic daily and annual velocity changes are observed and modeled with stress induced by atmospheric temperature changes. This model takes into account the chain from the subsurface temperature field $\rightarrow$ subsurface stresses $\rightarrow$ local velocity variations $\rightarrow$ observed velocity changes. The central relation between stress and velocity uses third order elastic constants as a mathematical description of the physical process that introduces non-linearity in the elastic behavior.

The third observation that is important for understanding the physical origin of the velocity changes is the recovery process of the coseismic changes. Following the Tocopilla earthquake an exponentially decreasing recovery process of the seismic velocity is observed with a duration of 2 years at station PATCX. Recovery following the smaller regional events is faster in the order of days to one month. These three observations – high sensitivity of velocity to shaking (PGA), pronounced velocity changes due to thermal stress, and postseismic recovery integrate in a model that relates the elastic moduli to compliant porosity and microcracks. The outstanding property of the material at station PATCX is the firm cementation of salt at the surface resulting in an above-average

consolidated layer at shallow depth supporting stress. The temperature changes therefore change the seismic velocity through the straining of compliant pores as described by *Shapiro* (2003) and *Shapiro and Kaselow* (2005) and as is reflected in the third order elastic constants. Shaking causes damage and the opening of compliant pores and microcracks. Healing is the process of gradually closing these cracks again. The salt content in the sediments at PATCX is therefore likely to be the major reason for the high sensitivity of the velocity changes to stress and shaking.

A. Supplement station data

A.1. IPOC station coordinates

station	network	latitude	longitude	elevation (m)	seismometer
PB01	CX	21.04323°S	69.48740°W	900	STS2
PB02	CX	21.31973°S	69.89603°W	1015	STS2
PB03	CX	22.04847°S	69.75310°W	1460	STS2
PB04	CX	22.33369°S	70.14918°W	1530	STS2
PB05	CX	22.85283°S	70.20235°W	1150	STS2
PB06	CX	22.70580°S	69.57188°W	1440	STS2
PB07	CX	21.72667°S	69.88618°W	1560	STS2
PB08	CX	20.14112°S	69.15340°W	3070	STS2
PB09	CX	21.79638°S	69.24192°W	1530	STS2
PB10	CX	23.51343°S	70.55408°W	250	STS2
PB11	CX	19.76096°S	69.65582°W	1410	STS2
PB12	CX	18.61406°S	70.32808°W	908	STS2
PB13	CX	18.33585°S	69.50160°W	4730	STS2
PB14	CX	24.62597°S	70.40379°W	2620	STS2
PB15	CX	23.20833°S	69.47092°W	1830	STS2
PB16	CX	18.33510°S	69.50767°W	4480	STS2
PB17	CX	21.53414°S	68.73017°W	3650	STS2
HMBCX	CX	20.27822°S	69.88791°W	1152	STS2
MNMCX	CX	19.13108°S	69.59553°W	2304	STS2
PSGCX	CX	19.59717°S	70.12305°W	966	STS2
PATCX	CX	20.82071°S	70.15288°W	830	STS2
LVC	GE	22.6182°S	68.9113°W	2915	CMG3T

STS2: Steckeisen STS-2/N or Steckeisen STS-2.5/N (station PB17)
CMG3T: Güralp CMG-3T/120F

A.2. Probabilistic power spectral densities for IPOC stations

Probability density functions of power spectral densities (PSDs) for the different IPOC stations are calculated with the method of *McNamara and Buland* (2004). Data segments are divided in 13 windows overlapping by 75 % and the PSD for this data segment is calculated by averaging PSDs of the 13 individual windows. The PSDs are converted to decibels with respect to acceleration ($m^2/s^4/Hz$). Finally a lot of PSDs from different data segments overlapping by 50 % are accumulated in a histogram to generate a probability density function. *McNamara and Buland* (2004) processed 1-hour segments of data and accumulated the PSDs in 1 dB bins. In contrast I choose 6-hour data segments to extend the plot for higher periods and accumulate the PSDs in 0.5 dB bins to enhance the resolution of the power axis. Because of the smaller power bins the color scale of the plots differs from the one used by *McNamara and Buland* (2004). The black lines indicate the 0, 25, 50, 75, and 100 percentiles. The new low and new high noise models of *Peterson* (1993) are indicated by gray lines. The calculations were performed under usage of the Python package ObsPy (*Beyreuther et al.*, 2010).

Apart from characterizing ambient noise power spectra with the typical appearance of the double-frequency microseism peak at around 7 s, the plots are useful for characterizing station sites. Transients for long periods at all stations except PB01, PB04, PB06, PB10, PB13, PB15, HMBCX and LVC are caused by problems with the adjustment of the mass center in most cases. For station LVC 20 Hz data were analyzed and therefore the short period part of the PSDs are missing. Furthermore some PSDs of station LVC are smaller than for the new low noise model and form a second maxima. This is, because the response information of LVC changed multiple times in the analyzed time period and obviously some data segments have not been corrected accordingly in the processing. Station PB14 plays a special role, because it is not located inside a cavern as all other stations. Therefore it shows partially higher power levels for periods above 20 s.

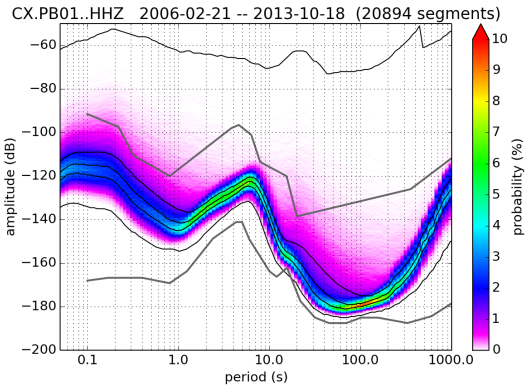
CX.PB01..HHZ 2006-02-21 -- 2013-10-18 (20894 segments)
amplitude (dB)
period (s)
probability (%)

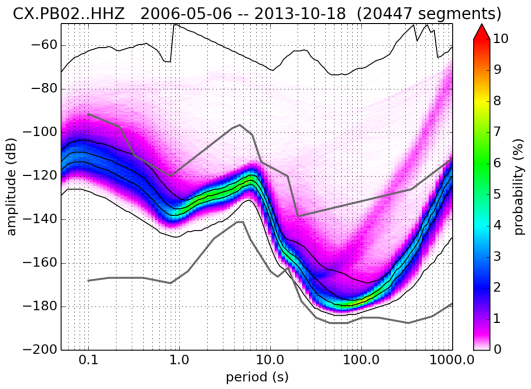
CX.PB02..HHZ 2006-05-06 -- 2013-10-18 (20447 segments)
amplitude (dB)
period (s)
probability (%)

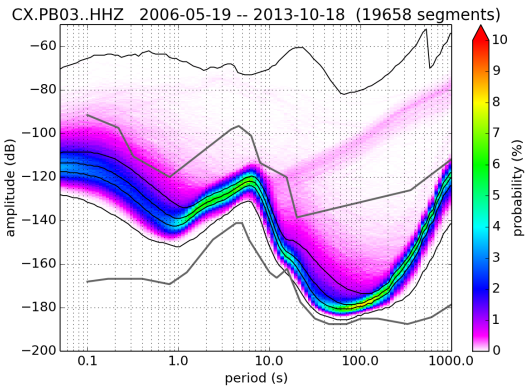
CX.PB03..HHZ 2006-05-19 -- 2013-10-18 (19658 segments)
amplitude (dB)
period (s)
probability (%)

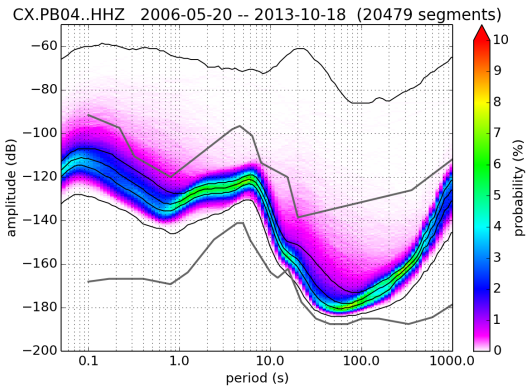
CX.PB04..HHZ 2006-05-20 -- 2013-10-18 (20479 segments)
amplitude (dB)
period (s)
probability (%)

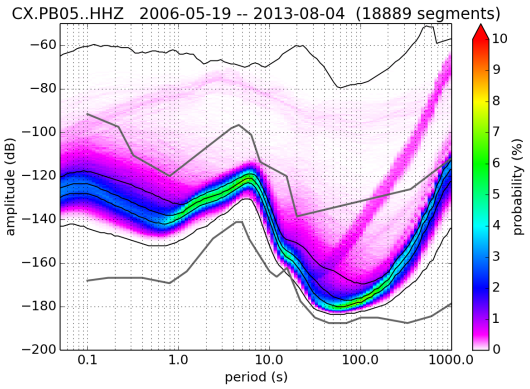
CX.PB05..HHZ 2006-05-19 -- 2013-08-04 (18889 segments)
amplitude (dB)
period (s)
probability (%)

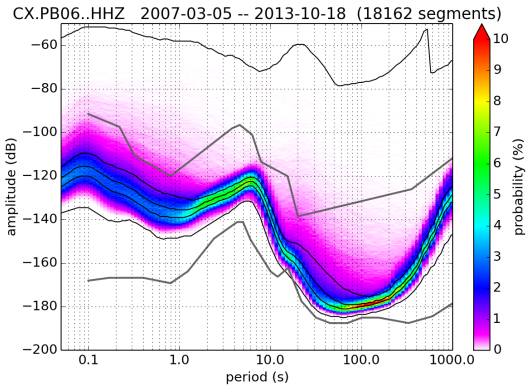
CX.PB06..HHZ 2007-03-05 -- 2013-10-18 (18162 segments)
amplitude (dB)
period (s)
probability (%)

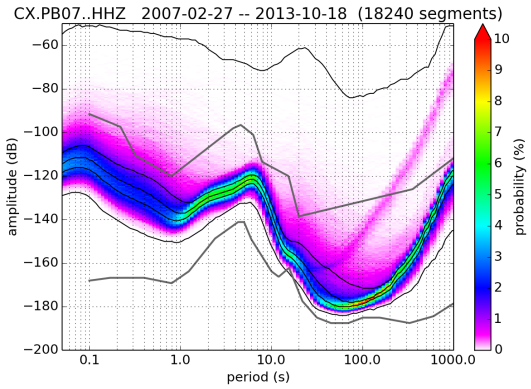
CX.PB07..HHZ 2007-02-27 -- 2013-10-18 (18240 segments)
amplitude (dB)
period (s)
probability (%)

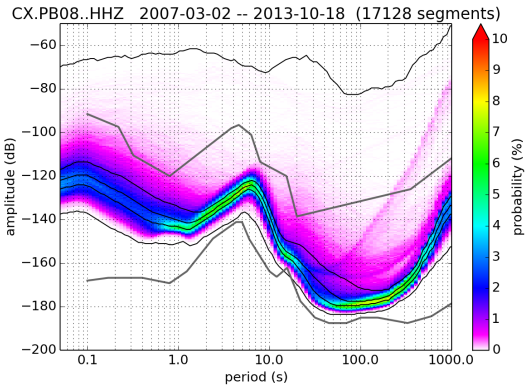
CX.PB08..HHZ 2007-03-02 -- 2013-10-18 (17128 segments)
amplitude (dB)
period (s)
probability (%)

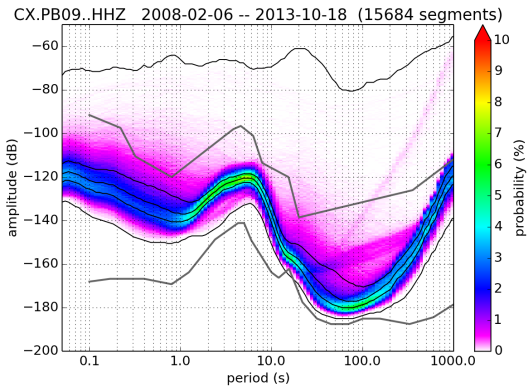
CX.PB09..HHZ 2008-02-06 -- 2013-10-18 (15684 segments)
amplitude (dB)
period (s)
probability (%)

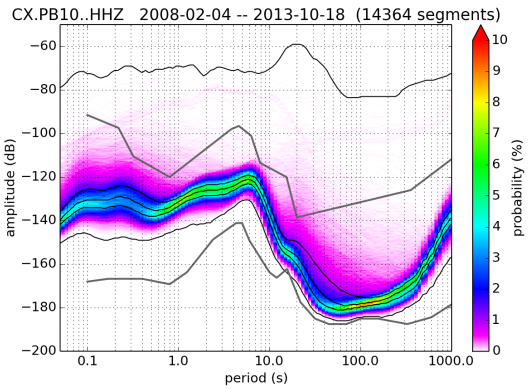
CX.PB10..HHZ 2008-02-04 -- 2013-10-18 (14364 segments)
amplitude (dB)
period (s)
probability (%)

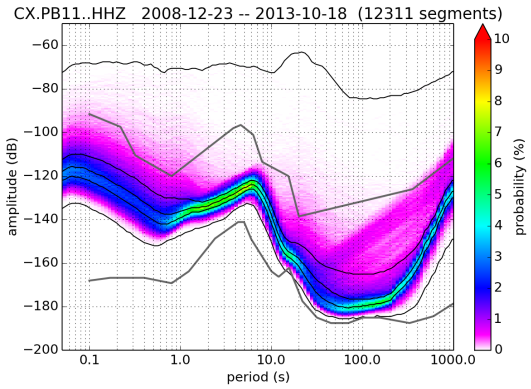
CX.PB11..HHZ 2008-12-23 -- 2013-10-18 (12311 segments)
amplitude (dB)
period (s)
probability (%)

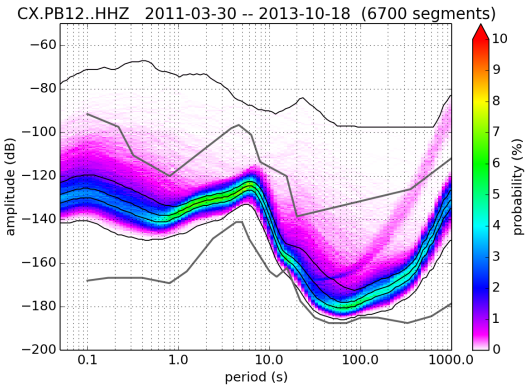
CX.PB12..HHZ 2011-03-30 -- 2013-10-18 (6700 segments)
amplitude (dB)
period (s)
probability (%)

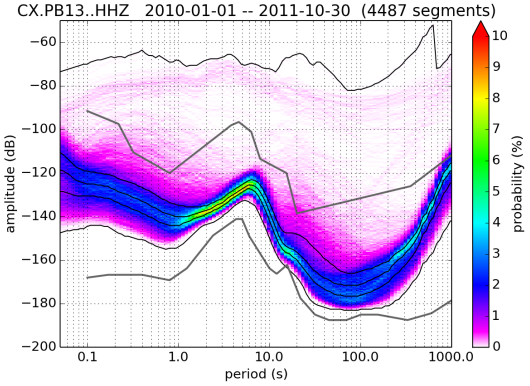
CX.PB13..HHZ 2010-01-01 -- 2011-10-30 (4487 segments)
amplitude (dB)
period (s)
probability (%)

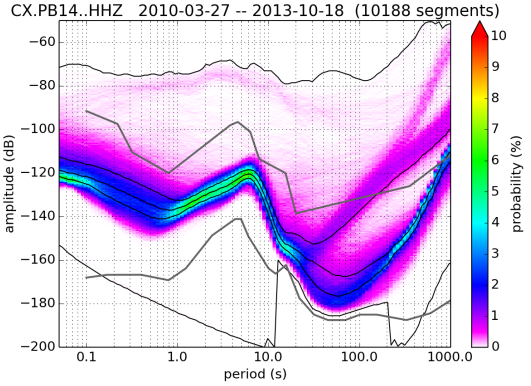
CX.PB14..HHZ 2010-03-27 -- 2013-10-18 (10188 segments)
amplitude (dB)
period (s)
probability (%)

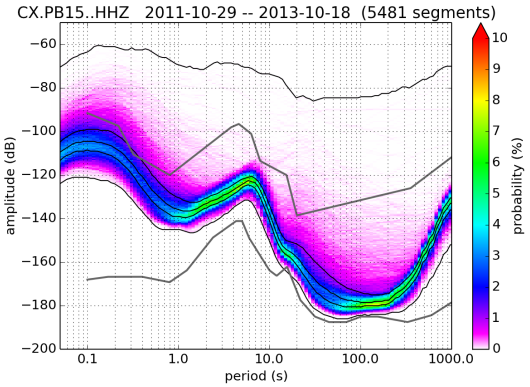
CX.PB15..HHZ 2011-10-29 -- 2013-10-18 (5481 segments)
amplitude (dB)
period (s)
probability (%)

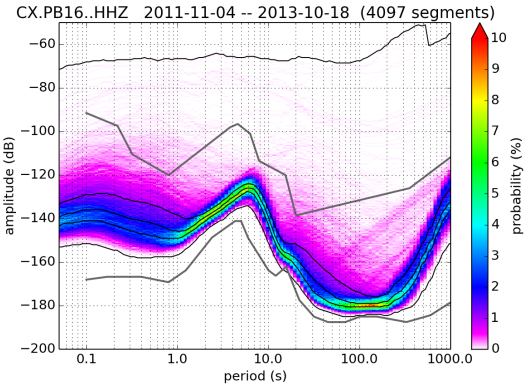
CX.PB16..HHZ 2011-11-04 -- 2013-10-18 (4097 segments)
amplitude (dB)
period (s)
probability (%)

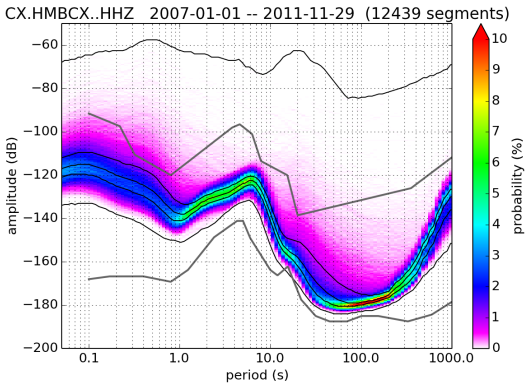
CX.HMBCX..HHZ 2007-01-01 -- 2011-11-29 (12439 segments)
amplitude (dB)
period (s)
probability (%)

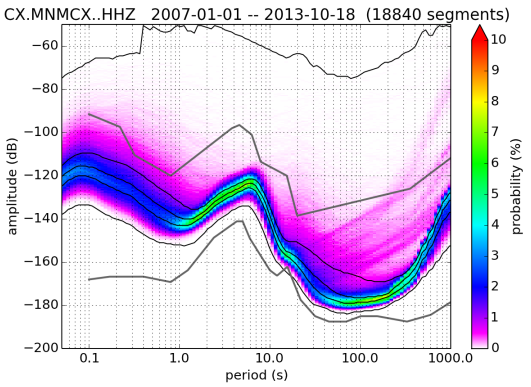
CX.MNMCX..HHZ 2007-01-01 -- 2013-10-18 (18840 segments)
amplitude (dB)
period (s)
probability (%)

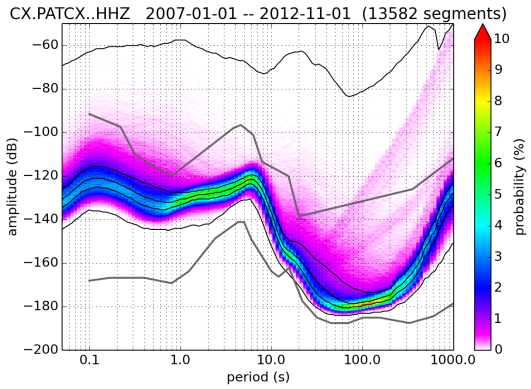
CX.PATCX..HHZ 2007-01-01 -- 2012-11-01 (13582 segments)
amplitude (dB)
period (s)
probability (%)

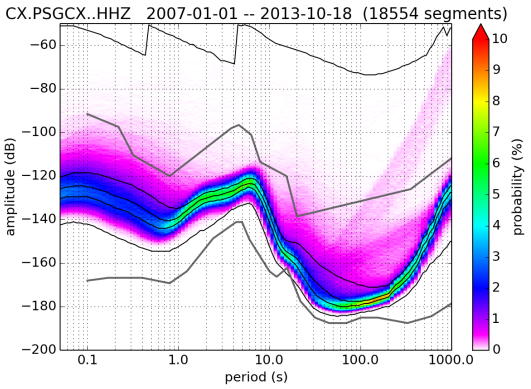
CX.PSGCX..HHZ 2007-01-01 -- 2013-10-18 (18554 segments)
amplitude (dB)
period (s)
probability (%)

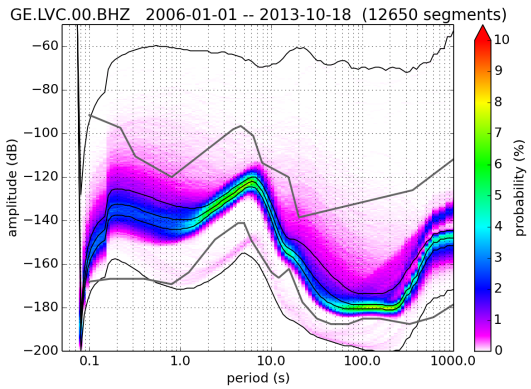
GE.LVC.00.BHZ 2006-01-01 -- 2013-10-18 (12650 segments)
amplitude (dB)
period (s)
probability (%)

B. Supplement receiver functions

B.1. Events used for calculation of receiver functions

It follows a table with 542 teleseismic events above magnitude 5.5 used for the receiver function study. The receiver function usage column indicates which events are discarded because of the criteria presented in section 4.1 (quality control). The numbers 1 to 9 stand for stations PB01 to PB09, letters A to G for stations PB10 to PB16, H, M, P, S for HMBCX, MNMCX, PATCX, PSGCX and L for station LVC. A dot indicates that the event is discarded for this station, a cross indicates that the event is used.

date and time	latitude (°)	longitude (°)	depth (km)	magnitude	RF usage 123456789ABCDEFGHMPSL	Flinn-Engdahl region
2006-02-23 04:04:05	−54.669	1.765	10	6.2	.....	Bouvet Island Region
2006-03-02 23:35:44	19.358	−63.787	24	5.6	x.....	Leeward Islands
2006-03-03 23:36:27	−55.695	−4.232	10	6.0	.....	Southern Mid Atlantic Ridge
2006-03-04 00:53:31	1.133	−27.879	10	5.6	.....	Central Mid Atlantic Ridge
2006-03-04 08:11:37	12.598	−89.356	27	5.7	.....	Off Coast of Central America
2006-03-09 09:59:53	−59.542	−29.660	10	5.9	.....	South Sandwich Islands Region
2006-03-09 17:55:55	0.791	−26.125	10	6.0	.....	Central Mid Atlantic Ridge
2006-03-10 10:12:18	−60.419	−46.505	10	6.1	.....	Scotia Sea
2006-03-19 04:31:55	−58.051	−25.263	58	5.5	x.....	South Sandwich Islands Region
2006-03-23 13:57:41	−62.470	165.168	10	5.7	.....	Balleny Islands Region
2006-03-27 01:10:32	7.075	−34.216	10	5.5	.....	Central Mid Atlantic Ridge
2006-04-04 02:30:28	18.716	−106.992	33	6.0	x	Off Coast of Jalisco, Mexico
2006-04-10 06:26:13	7.511	−36.930	10	5.7	.....	Central Mid Atlantic Ridge
2006-05-01 07:47:59	8.165	−82.882	13	5.9	x.....	Panama-Costa Rica Border Region
2006-05-01 09:13:31	8.115	−82.874	10	5.5	.....	Panama-Costa Rica Border Region
2006-05-01 20:13:28	2.205	−99.035	10	5.7	.....	West of Galapagos Islands
2006-05-04 02:08:54	−58.259	157.926	10	5.9	.....	Macquarie Island Region
2006-05-21 02:07:36	1.550	−85.311	10	6.0	x.....	Off Coast of Ecuador
2006-05-24 00:32:32	−27.565	−112.793	10	5.6	.x..x.....	Easter Island Region
2006-05-29 05:20:39	−59.590	−26.235	44	5.7	xxxx.....x	South Sandwich Islands Region
2006-06-05 06:27:07	1.175	−28.065	10	6.0	....x.....	Central Mid Atlantic Ridge
2006-06-05 06:34:31	1.018	−28.162	10	5.7	.....	Central Mid Atlantic Ridge
2006-06-09 23:17:27	−47.750	32.612	22	5.9	....x.....	Prince Edward Islands Region
2006-06-18 18:28:02	33.028	−39.702	9	6.0	....x.....	Northern Mid Atlantic Ridge
2006-06-20 10:02:07	51.582	−130.473	10	5.6	.....	Queen Charlotte Islands Region
2006-06-27 09:15:20	−60.428	153.711	10	5.7	.....	West of Macquarie Island
2006-06-27 13:03:09	14.986	−94.140	9	5.8	x...x.....	Off Coast of Chiapas, Mexico
2006-07-03 02:04:44	−56.529	−142.489	10	5.8	.....	Pacific Antarctic Ridge
2006-07-10 07:21:37	−11.627	−13.432	10	5.5	x.....	Ascension Island Region
2006-07-13 19:13:40	−60.942	−36.471	10	5.7	xxxxx.....	Scotia Sea
2006-07-29 19:53:43	23.589	−63.923	10	5.8	xx..x.....	North Atlantic Ocean
2006-07-30 01:20:59	26.864	−111.209	10	5.9	..x.....	Gulf of California
2006-07-31 01:24:15	10.166	−103.863	10	5.5	.....	Northern East Pacific Rise
2006-08-11 14:30:40	18.541	−101.048	56	6.1	xxx.x.....x	Guerrero, Mexico
2006-08-14 04:03:55	−55.503	−124.349	10	5.6	.....	Southern East Pacific Rise
2006-08-19 05:41:28	16.231	−97.257	32	5.6	.....	Oaxaca, Mexico
2006-08-20 03:41:48	−61.029	−34.371	13	7.0	xxxxx.....x	Scotia Sea
2006-08-20 13:34:59	−60.913	−34.057	10	5.9	.xxx.....	Scotia Sea
2006-09-01 07:09:50	−54.678	−128.537	10	5.5	.....	Pacific Antarctic Ridge

date and time	latitude	longitude	depth	magnitude	123456789ABCDEFGHMPSL	Flynn region
2006-09-06 11:42:41	−60.844	−34.166	10	5.7	xxxxx.....	Scotia Sea
2006-09-10 14:56:08	26.319	−86.606	14	5.9	xxx.x.....	Gulf of Mexico
2006-09-29 13:08:26	10.876	−61.756	53	6.1	xxxxx.....x	Trinidad
2006-09-29 18:23:05	10.814	−61.758	52	5.5	xx.....x	Trinidad
2006-09-30 12:47:22	7.283	−34.658	10	5.5	....x.....x	Central Mid Atlantic Ridge
2006-10-06 16:25:27	−50.105	−114.598	10	5.7	.....	Southern East Pacific Rise
2006-10-09 18:19:33	−51.030	29.024	10	5.7	..xx.....	South of Africa
2006-10-10 08:02:51	−56.101	−122.373	10	6.0	.....	Southern East Pacific Rise
2006-10-11 06:00:48	8.405	−103.165	10	5.8	.....	Northern East Pacific Rise
2006-10-18 21:15:49	4.820	−82.652	20	5.7	.....	South of Panama
2006-11-15 10:44:17	−25.088	−112.161	10	5.5	.....	Easter Island Region
2006-11-16 00:18:10	−62.707	−160.905	10	5.7	.....	Pacific Antarctic Ridge
2006-11-18 10:05:44	11.111	−87.810	30	5.5	.....	Near Coast of Nicaragua
2006-11-19 01:55:05	−55.584	−24.871	10	5.7	xx.....	South Sandwich Islands Region
2006-11-19 06:59:07	18.463	−104.489	18	5.5	.....	Near Coast of Jalisco, Mexico
2006-11-19 18:57:33	−4.521	−104.832	10	6.1	x.x.....	Central East Pacific Rise
2006-11-29 15:38:44	53.741	−35.438	10	5.6	.....	Reykjanes Ridge
2006-11-30 21:20:11	−53.844	−134.359	10	6.2	xxxxx.....	Pacific Antarctic Ridge
2006-11-30 23:38:12	−29.761	−111.958	10	5.6	.....	Easter Island Region
2006-12-03 08:19:51	−0.538	−19.738	10	5.6	.....	Central Mid Atlantic Ridge
2006-12-03 20:52:15	13.994	−91.207	61	6.0	xxx.x.....	Near Coast of Guatemala
2006-12-05 15:58:54	11.397	−86.411	35	5.5	.....	Near Coast of Nicaragua
2006-12-05 20:14:30	−35.342	−104.546	10	5.8	.x.....	Southeast of Easter Island
2006-12-15 23:57:10	−35.327	−105.745	10	5.8	.....	Southern East Pacific Rise
2006-12-30 14:33:10	5.496	−82.489	16	5.5	.....	South of Panama
2006-12-31 22:48:54	−28.591	−112.330	10	5.6	.....	Easter Island Region
2007-01-15 07:58:11	−60.915	−34.069	10	5.5	.....	Scotia Sea
2007-01-15 21:19:40	−4.609	−105.145	10	5.6	.....	Central East Pacific Rise
2007-01-17 18:34:14	−57.911	−64.528	6	5.6	xxxxx.....	Drake Passage
2007-01-20 06:21:04	−55.419	−29.533	10	6.2	xxxxx.....	South Sandwich Islands Region
2007-01-21 15:03:16	−55.764	−27.016	47	5.6	xxxxx.....	South Sandwich Islands Region
2007-01-23 04:16:07	−43.139	41.647	10	5.5	.....	Prince Edward Islands Region
2007-01-23 22:46:25	−55.305	−29.382	35	5.6	xxx.x.....	South Sandwich Islands Region
2007-02-04 03:33:19	35.344	−35.944	10	5.6	.....	Northern Mid Atlantic Ridge
2007-02-04 20:56:59	19.372	−78.518	10	6.2	xxxxx.....	Cuba Region
2007-02-04 21:17:46	−55.883	−122.721	10	6.2	.....	Southern East Pacific Rise
2007-02-04 22:52:54	−55.791	−123.448	10	5.6	.....	Southern East Pacific Rise
2007-02-12 10:35:22	35.804	−10.312	20	6.0	xxxxx.....	Azores Cape St. Vincent Ridge
2007-02-14 01:29:07	−29.590	−112.051	10	5.9	xxxxx.....	Easter Island Region
2007-02-18 21:37:44	6.336	−82.706	26	5.7	.....	South of Panama
2007-02-25 15:00:41	26.146	−110.421	10	5.9	.x.....	Gulf of California
2007-02-26 23:49:53	−44.770	35.495	10	5.7	.....	Prince Edward Islands Region
2007-02-28 23:13:15	−55.245	−29.142	10	6.2	xxxxx.x.....	South Sandwich Islands Region
2007-03-01 23:11:52	26.581	−44.594	10	6.0	x.x.....	Northern Mid Atlantic Ridge
2007-03-03 20:52:08	−55.252	−129.337	10	5.7	..x.....	Pacific Antarctic Ridge
2007-03-04 11:26:11	33.790	−38.473	10	5.6	.....	Northern Mid Atlantic Ridge
2007-03-07 23:01:24	3.018	−31.819	10	5.5	...x.....	Central Mid Atlantic Ridge
2007-03-08 11:14:31	−58.217	−7.615	10	6.2	x.xxxxx.....	East of South Sandwich Islands
2007-03-09 21:01:37	13.261	−87.387	226	5.6	x....x.....	Honduras
2007-03-13 02:59:04	26.261	−110.537	26	6.0	......x.....	Gulf of California
2007-03-14 21:59:13	11.514	−86.590	35	5.5	.....	Near Coast of Nicaragua
2007-03-17 22:43:09	4.551	−78.536	10	6.0	xxxxxxxx.....	South of Panama
2007-03-18 02:11:05	4.585	−78.494	7	6.2	xxxxxxxx.....	South of Panama
2007-03-19 21:20:38	−60.695	154.090	10	5.7	.....	West of Macquarie Island
2007-03-31 12:49:03	−56.083	−123.270	10	6.2	xx...x.....	Southern East Pacific Rise
2007-04-05 03:56:50	37.306	−24.621	14	6.3	x......x.....	Azores Islands Region
2007-04-05 21:27:00	1.507	−84.669	10	5.5	.....	Off Coast of Ecuador
2007-04-06 05:54:20	−55.373	−123.645	10	5.9	.x....x.....	Southern East Pacific Rise
2007-04-07 07:09:25	37.306	−24.494	8	6.1	xx....x.....	Azores Islands Region
2007-04-12 18:24:49	−61.828	160.960	10	6.0	.....	Balleny Islands Region
2007-04-13 05:42:23	17.302	−100.198	34	6.0	xx.xxxxx.....	Guerrero, Mexico
2007-04-13 18:24:19	−35.051	−108.836	10	6.1	xxxxxxx.....	Southern East Pacific Rise
2007-04-16 01:24:07	−63.337	169.919	10	5.8	....x.....	Balleny Islands Region
2007-04-28 14:02:37	−60.789	−20.208	10	6.1	xxxxxxxx.....	East of South Sandwich Islands
2007-04-30 15:38:52	−53.999	6.081	10	5.6	.....	Bouvet Island Region
2007-05-04 12:06:51	−1.410	−14.921	7	6.2	xxxx.x.....x..	North of Ascension Island
2007-05-15 01:14:55	−55.477	−127.989	10	5.6	..x.....	Pacific Antarctic Ridge
2007-05-23 04:41:46	52.352	−31.814	10	5.7	.....	Northern Mid Atlantic Ridge
2007-05-23 19:09:15	21.892	−96.359	10	5.6	....x.....	Gulf of Mexico
2007-05-26 02:44:46	−35.928	−103.097	10	5.5	..x...x.....	Southeast of Easter Island
2007-05-30 19:35:21	−59.972	−26.457	35	5.5	.x.x..x.....	South Sandwich Islands Region
2007-06-05 15:27:02	−60.182	−26.728	10	5.7	.xxxxx.....	South Sandwich Islands Region

date and time	latitude	longitude	depth	magnitude	123456789ABCDEFGHMPSL	Flynn region
2007-06-08 13:32:00	13.835	−90.766	47	5.8	x...x..x.....	Near Coast of Guatemala
2007-06-08 15:08:38	13.639	−90.802	38	5.5	x.....	Near Coast of Guatemala
2007-06-11 17:13:44	−35.687	−16.143	10	5.5	.....	Southern Mid Atlantic Ridge
2007-06-13 19:29:40	13.554	−90.618	23	6.7	xxxxxx.x.....x.x	Near Coast of Guatemala
2007-06-14 13:37:40	−36.208	−100.152	10	5.9	xxx.xxx.....x..	Southeast of Easter Island
2007-06-15 03:48:34	−58.596	−26.244	146	5.5	.....	South Sandwich Islands Region
2007-06-24 00:25:18	−55.645	−2.626	10	6.5	.....x.....	Southern Mid Atlantic Ridge
2007-07-03 08:26:00	0.715	−30.272	10	6.3	xxxxxxx.....x..	Central Mid Atlantic Ridge
2007-07-06 01:09:19	16.350	−93.990	113	6.1	xxxx.xxx.....x.x	Chiapas, Mexico
2007-07-13 16:33:35	−55.604	−128.519	10	5.7	.....x.....	Pacific Antarctic Ridge
2007-07-21 20:40:53	−55.091	−129.418	10	5.7	.....	Pacific Antarctic Ridge
2007-07-23 06:00:35	−4.109	−104.235	10	5.5	.....	Central East Pacific Rise
2007-07-23 06:03:52	−3.942	−104.029	10	5.7	.....	Central East Pacific Rise
2007-07-23 22:30:08	14.381	−90.954	113	5.5	.....	Guatemala
2007-07-24 18:33:00	−56.351	−142.499	10	5.8	.....	Pacific Antarctic Ridge
2007-07-26 18:12:39	−62.693	155.707	10	5.7	.....	Balleny Islands Region
2007-07-28 16:13:43	−54.130	7.881	10	5.5	.....	Bouvet Island Region
2007-07-30 06:06:50	−35.519	−103.846	10	5.5	.....	Southeast of Easter Island
2007-07-31 02:42:48	−56.058	−27.733	104	5.6	xxxxx.x.....x.x	South Sandwich Islands Region
2007-07-31 22:55:31	−0.162	−17.795	11	6.2	xxxxxxx.....x.x	North of Ascension Island
2007-08-02 07:19:23	−52.444	17.647	10	5.5	....x.....	Southwest of Africa
2007-08-03 00:41:14	−62.973	145.306	6	5.9	.....x.....	South of Australia
2007-08-04 14:24:51	−4.797	−105.406	10	6.1	xx.....	Central East Pacific Rise
2007-08-09 17:25:05	25.918	−45.001	10	5.6	..x.....	Northern Mid Atlantic Ridge
2007-08-13 10:27:23	−60.549	153.785	10	6.1	......x.....	West of Macquarie Island
2007-08-13 22:23:04	−30.994	−13.408	10	5.5	.xxxxx.....x..	Southern Mid Atlantic Ridge
2007-08-16 14:18:24	−3.522	−12.153	10	5.5	.....	North of Ascension Island
2007-08-19 00:04:31	−60.390	−26.863	30	5.5	.x....x.....	South Sandwich Islands Region
2007-08-20 12:37:06	−0.256	−18.175	10	5.7	.....	Central Mid Atlantic Ridge
2007-08-20 22:42:28	8.036	−39.251	6	6.5	xxxxxxx.....x.x	Central Mid Atlantic Ridge
2007-09-01 19:14:22	24.902	−109.689	9	6.1	x.....x	Gulf of California
2007-09-07 04:46:45	−56.081	−123.314	10	5.9	x.....	Southern East Pacific Rise
2007-09-11 06:21:15	−9.120	−109.434	10	5.5	....x.....	Central East Pacific Rise
2007-09-13 20:06:38	−57.625	−147.303	10	6.0	.....x.....	Pacific Antarctic Ridge
2007-09-26 18:39:34	−7.074	−11.713	10	5.6	x.....	Ascension Island Region
2007-10-13 03:58:22	4.922	−82.565	10	5.5	.....x...	South of Panama
2007-10-17 01:05:49	−6.409	−107.307	10	5.5	.....	Central East Pacific Rise
2007-10-18 16:13:14	30.132	−42.594	10	5.7	.x.....x...	Northern Mid Atlantic Ridge
2007-10-31 03:04:54	37.434	−121.774	10	5.6	.....	Central California
2007-11-02 21:20:13	−55.172	−129.214	10	5.6	.....	Pacific Antarctic Ridge
2007-11-02 22:31:43	−55.466	−128.966	10	6.1	xx..xxx.....xx...	Pacific Antarctic Ridge
2007-11-04 20:35:37	−67.034	111.199	10	5.7	......x.....	Antarctica
2007-11-19 20:32:48	43.542	−127.414	10	5.8	.....	Off Coast of Oregon
2007-11-23 19:18:47	−53.270	9.426	10	5.5	.....	Southwest of Africa
2007-11-26 17:41:40	15.280	−93.363	87	5.7	.xx.xxx.....xx...	Near Coast of Chiapas, Mexico
2007-11-26 21:56:12	18.654	−101.703	53	5.8	xxxxxxx.....xxxxx	Guerrero, Mexico
2007-11-29 03:26:22	−36.756	−97.404	10	6.3	xxx.xxx.....xx...	West Chile Rise
2007-11-29 19:00:20	14.944	−61.274	156	7.4	xxxxxxx.....xxxx.	Windward Islands
2007-12-06 17:12:03	22.692	−45.113	10	5.8	..x....x.....x..xx	Northern Mid Atlantic Ridge
2007-12-07 06:19:35	−56.205	−139.294	10	5.5	.....	Pacific Antarctic Ridge
2007-12-08 03:54:46	−60.508	−52.382	10	5.8	x.x..x.x.....x..	South Shetland Islands
2007-12-11 17:20:54	−62.063	−65.835	10	5.9	xxxxx.x.....xx.x	Southern Pacific Ocean
2007-12-12 23:39:59	52.102	−131.554	10	5.8	.....	Queen Charlotte Islands Region
2007-12-20 07:55:15	−39.011	178.291	20	6.6	xxxxxxx.....xxxxx	Off E. Coast of N. Island, N.Z.
2007-12-21 03:10:57	−57.720	−141.447	10	5.6	.....	Pacific Antarctic Ridge
2008-01-05 01:56:45	14.129	−91.479	66	5.6	.x.....x.x.	Guatemala
2008-01-05 10:39:14	51.324	−130.390	10	5.7	.....x...	Queen Charlotte Islands Region
2008-01-05 11:01:06	51.254	−130.746	15	6.6	....xx.....xx...	Queen Charlotte Islands Region
2008-01-05 11:44:48	51.163	−130.542	10	6.4	.....x...	Queen Charlotte Islands Region
2008-01-05 19:55:31	−62.139	−155.695	10	5.7	.x.....x....	Pacific Antarctic Ridge
2008-01-09 14:40:00	51.649	−131.183	10	6.1	x.....	Queen Charlotte Islands Region
2008-01-10 01:37:19	43.785	−127.264	13	6.3	xxx.xxx.....xx..x	Off Coast of Oregon
2008-01-20 06:08:56	−35.017	−112.019	10	5.6	..x...x.....x...	Southern East Pacific Rise
2008-01-21 12:24:27	−34.863	−111.851	10	5.8	xxxxx.x.....xxx.	Southern East Pacific Rise
2008-01-23 05:49:32	14.278	−94.037	13	5.5	..x.....	Off Coast of Chiapas, Mexico
2008-01-24 04:12:13	6.943	−82.383	10	5.9	.x..xxx.....xx...	South of Panama
2008-01-29 14:57:26	−58.735	−25.240	35	5.6	..x.....	South Sandwich Islands Region
2008-02-03 14:24:37	−56.272	−27.043	99	5.6	xx..x.xx.....x...	South Sandwich Islands Region
2008-02-04 07:43:56	19.028	−66.902	14	5.5	x...x.xx.....x...	Puerto Rico Region
2008-02-08 09:38:14	10.671	−41.899	9	6.9	xxxxxxxxxx.....xxxxx	Northern Mid Atlantic Ridge
2008-02-10 12:22:02	−60.797	−25.586	8	6.6	xx.xxxxxxx.....xxxxx	South Sandwich Islands Region
2008-02-12 12:50:18	16.357	−94.304	83	6.5	xxxxxxxxxx.....xxxxx	Oaxaca, Mexico

date and time	latitude	longitude	depth	magnitude	123456789ABCDEFGHMPSL	Flynn region
2008-02-15 22:00:55	−61.294	154.249	10	5.7	.....	Balleny Islands Region
2008-02-20 12:11:20	−52.917	−46.492	10	5.5	.....	South Atlantic Ocean
2008-02-20 12:49:44	−53.015	−46.542	10	5.6	........x........x...	South Atlantic Ocean
2008-02-21 14:16:02	41.153	−114.867	6	6.0	xxx.xxx.x.......xx.x.	Nevada
2008-02-23 15:57:20	−57.335	−23.433	14	6.8	xxxxxxxxxx......xxxx.	South Sandwich Islands Region
2008-02-27 04:54:27	−34.625	−178.966	44	5.5	.....	South of Kermadec Islands
2008-02-29 02:38:29	−35.074	−108.968	10	5.7	.xx.............x...	Southern East Pacific Rise
2008-03-01 23:06:44	−35.379	−179.299	24	5.6	....x.....	East of North Island, N.Z.
2008-03-13 13:28:44	−45.492	35.008	10	6.0	.....	Prince Edward Islands Region
2008-03-13 23:01:18	14.463	−93.462	10	5.7	.....	Near Coast of Chiapas, Mexico
2008-03-15 14:44:36	42.412	−126.835	10	5.7	x...xx.........x...	Off Coast of Oregon
2008-03-17 19:06:12	−54.324	−136.082	10	5.6	.....	Pacific Antarctic Ridge
2008-03-26 06:29:50	−56.712	−141.903	10	5.5	.....	Pacific Antarctic Ridge
2008-03-27 09:42:57	17.199	−84.835	10	5.6	..x.....	North of Honduras
2008-03-29 15:12:03	−41.055	42.525	10	5.5	......x.....	Prince Edward Islands Region
2008-04-12 12:05:14	43.648	−127.621	10	5.5	.....	Off Coast of Oregon
2008-04-14 09:45:19	−56.022	−28.035	140	6.0	xxxx.xxx........xxxx.	South Sandwich Islands Region
2008-04-15 03:03:04	13.564	−90.599	33	6.1	.x..xxx........xxxx.	Near Coast of Guatemala
2008-04-24 12:14:49	−1.182	−23.471	10	6.5	.xx.....x.......x....	Central Mid Atlantic Ridge
2008-04-27 14:35:29	−35.464	−16.597	10	5.6	x.....	Southern Mid Atlantic Ridge
2008-04-28 00:06:28	17.846	−100.171	56	5.8	xxxxxxxxxx......xx.xx	Guerrero, Mexico
2008-04-28 15:57:55	−58.739	−24.714	35	6.1	..x..xx.........xx...	South Sandwich Islands Region
2008-05-14 21:47:40	−56.771	−142.309	10	5.7	........x.....	Pacific Antarctic Ridge
2008-05-15 14:23:28	−57.911	−25.483	35	5.9	xx...x..x.....	South Sandwich Islands Region
2008-05-19 03:16:13	−47.781	31.965	10	5.9	.x.....	South of Africa
2008-05-23 19:35:34	7.313	−34.897	8	6.5	xxxxxxxxxx......xx.x.	Central Mid Atlantic Ridge
2008-05-24 04:58:18	42.386	−30.515	10	5.5	........x........x...	Azores Islands Region
2008-05-26 15:01:33	8.423	−82.968	13	5.6	..x.....	Panama-Costa Rica Border Region
2008-05-27 11:27:55	13.616	−91.020	26	5.7	..x.x.....	Near Coast of Guatemala
2008-05-29 15:46:00	64.004	−21.013	9	6.3	.....	Iceland
2008-05-30 10:44:11	−54.744	0.987	10	5.7	....x.....	Bouvet Island Region
2008-05-31 23:16:04	−28.919	−112.258	10	5.8	..x.xx..x.......x....	Easter Island Region
2008-06-01 00:31:14	−54.816	0.979	10	5.5	.....x.....	Bouvet Island Region
2008-06-06 20:02:56	35.883	−0.658	4	5.5	.x..x.x.....	Northern Algeria
2008-06-12 05:30:43	−50.157	−114.169	10	5.9	..............x...	Southern East Pacific Rise
2008-06-15 08:37:17	−36.623	−107.450	10	6.0	........x.....	Southern East Pacific Rise
2008-06-17 17:42:09	5.008	−82.652	10	5.9	xxxxx.xx.x......xx...	South of Panama
2008-06-29 09:42:19	14.178	−92.718	6	5.5	x.....	Near Coast of Chiapas, Mexico
2008-06-30 06:17:43	−58.227	−22.099	8	7.0	xxxxxxxxxx......xx.x.	South Sandwich Islands Region
2008-07-01 01:54:41	−58.121	−21.882	10	5.6	xxxx.xx.x........x...	East of South Sandwich Islands
2008-07-03 06:34:53	10.281	−60.442	33	5.8	xxxx.xxxx.......x....	Trinidad
2008-07-15 05:07:11	−47.366	−12.170	10	5.7	..x.............x...	Southern Mid Atlantic Ridge
2008-07-17 22:36:18	44.367	−129.356	10	5.5	.....	Off Coast of Oregon
2008-07-17 22:51:55	44.371	−129.417	10	5.7	.....	Off Coast of Oregon
2008-07-27 21:15:42	−0.252	−18.287	17	5.9	.....x..x.....	Central Mid Atlantic Ridge
2008-07-29 18:42:15	33.953	−117.761	14	5.5	.......x........xx...	Southern California
2008-07-29 20:56:22	−54.727	−118.783	10	5.8	x...x...x.....	Southern East Pacific Rise
2008-07-30 20:15:11	−59.644	−27.806	136	5.6	x.x.x.x.........xx...	South Sandwich Islands Region
2008-08-07 02:18:13	26.640	−111.000	10	5.5	........x.....	Gulf of California
2008-08-07 22:58:33	−9.139	−109.518	10	5.6	x.......x.....	Central East Pacific Rise
2008-08-09 06:01:48	−60.648	153.771	10	6.5	.....x..x.....	West of Macquarie Island
2008-08-09 16:36:38	−60.693	153.826	10	6.3	..x.....	West of Macquarie Island
2008-08-11 23:38:38	−1.020	−21.843	13	6.0	.x....x.....	Central Mid Atlantic Ridge
2008-08-13 01:32:45	−13.382	−111.281	10	5.7	.xx.x.x.....	Central East Pacific Rise
2008-08-14 22:55:47	7.292	−82.726	6	5.5	..x.....x.......x...	South of Panama
2008-08-17 15:39:08	−52.873	−4.453	10	5.6	.....x.....	Southern Mid Atlantic Ridge
2008-08-19 08:33:55	−8.201	−13.449	10	5.5	.....	Ascension Island Region
2008-08-19 10:58:00	−28.545	−112.842	9	5.7	.......xx.....	Easter Island Region
2008-08-28 12:37:35	50.165	−129.628	12	5.9	x.....	Vancouver Island, Canada Region
2008-08-28 15:22:23	−0.252	−17.358	12	6.3	x.x.xxx.x.......x...	North of Ascension Island
2008-08-31 01:15:25	−61.233	−67.738	10	5.5	xxxx.xx.x.......x...	Drake Passage
2008-09-05 19:07:38	−1.171	−13.955	10	5.8	.x.....	North of Ascension Island
2008-09-10 13:08:14	8.093	−38.705	9	6.6	.xxxxxxxxx......xx.x.	Central Mid Atlantic Ridge
2008-09-16 07:28:25	0.902	−28.998	10	5.8	x..xx...x.....	Central Mid Atlantic Ridge
2008-09-18 01:41:03	−4.554	−105.999	11	6.0	xxxxx.xxx.......xx...	Central East Pacific Rise
2008-09-24 02:33:05	17.612	−105.497	12	6.4	xxxxxxxxxx......xx.x.	Off Coast of Jalisco, Mexico
2008-10-03 05:26:20	7.517	−36.758	5	5.7	.....	Central Mid Atlantic Ridge
2008-10-03 05:30:24	7.561	−36.882	10	5.6	.....	Central Mid Atlantic Ridge
2008-10-04 07:56:52	−59.340	−25.903	35	5.7	xxx.xxx.xx......xx...	South Sandwich Islands Region
2008-10-11 10:40:14	19.161	−64.833	23	6.1	xxxxxxx.xx......xx.x.	Virgin Islands
2008-10-16 19:41:25	14.423	−92.364	24	6.7	xxxxx.x.xx......xx.x.	Near Coast of Chiapas, Mexico
2008-10-16 19:43:37	14.256	−92.554	23	5.8	.........x.....	Near Coast of Chiapas, Mexico

date and time	latitude	longitude	depth	magnitude	123456789ABCDEFGHMPSL	Flynn region
2008-10-29 01:35:58	−8.896	−108.395	10	5.7	....xx.....x...	Central East Pacific Rise
2008-10-30 15:15:41	−9.020	−108.246	10	6.1	xxxxx.x.x.....xx...	Central East Pacific Rise
2008-11-13 15:10:15	−55.961	−27.234	87	5.6	.....x...	South Sandwich Islands Region
2008-11-13 16:02:08	−56.920	−140.801	10	5.5	.x.....x....	Pacific Antarctic Ridge
2008-11-14 02:05:09	−53.794	8.727	12	5.9	..x..x.....x....	Bouvet Island Region
2008-11-15 23:03:16	13.050	−88.750	48	5.8	xxx.xxx.x.....x...	El Salvador
2008-11-19 06:11:20	8.267	−82.967	32	6.3	xxxxxxx.xx.....xx.x.	Panama-Costa Rica Border Region
2008-11-21 22:35:01	−55.033	−129.565	10	5.6	.x.....	Pacific Antarctic Ridge
2008-11-22 18:49:42	−1.230	−13.933	10	6.3	.xxxxxx.xx.....x.x.	North of Ascension Island
2008-11-22 23:06:47	−37.244	−95.065	10	5.7	.x..xxx.....	Southeast of Easter Island
2008-11-28 13:42:18	40.348	−126.978	10	5.9	.....	Off Coast of N. California
2008-12-07 06:23:09	13.350	−44.826	10	5.6	xxx..xx...x....xx...	Northern Mid Atlantic Ridge
2008-12-08 01:51:01	13.415	−44.795	10	5.5	..xx.x.....	Northern Mid Atlantic Ridge
2008-12-14 20:36:29	−60.078	−18.762	10	5.5	xxxxxxx.xxx.....xx.x.	East of South Sandwich Islands
2008-12-19 08:31:51	47.006	−27.290	5	5.9	xxx.xxxxx.x.....xx...	Northern Mid Atlantic Ridge
2008-12-20 21:05:16	−31.193	−13.338	4	5.8	xxxxxxxxxxx.....xx.x.	Southern Mid Atlantic Ridge
2008-12-25 08:11:58	49.128	−128.621	10	5.8	.....	Vancouver Island, Canada Region
2009-01-01 06:27:51	−34.840	−107.647	10	5.8	....x...x.x....xx...	Southern East Pacific Rise
2009-01-02 19:42:27	0.624	−26.661	10	5.6	.....	Central Mid Atlantic Ridge
2009-01-02 20:14:30	0.791	−27.118	10	5.5	.....x....	Central Mid Atlantic Ridge
2009-01-05 10:59:30	23.808	−108.757	10	5.5	xxx..xxx..x.....xx...	Gulf of California
2009-01-08 19:21:35	10.165	−84.197	14	6.1	xx.xxxx.x.x.....xx.x.	Costa Rica
2009-01-17 02:57:31	15.739	−92.744	169	5.8	x....x.x..x.....xx.x.	Mexico-Guatemala Border Region
2009-02-18 03:07:50	−52.966	20.909	10	5.9	xx..x.x.x.x.....	South of Africa
2009-02-18 03:30:34	−61.706	154.752	10	5.6	x.....	Balleny Islands Region
2009-02-28 14:33:06	−60.525	−24.796	15	6.3	xxxxxx.xxxx.....xx.x.	South Sandwich Islands Region
2009-03-11 17:24:36	8.504	−83.219	14	5.9	.x....x.....x...	Costa Rica
2009-03-11 21:03:58	8.493	−83.206	17	5.9	......xxx.....x...	Costa Rica
2009-03-12 05:18:08	−60.861	−23.810	10	5.5	.....x.....	South Sandwich Islands Region
2009-03-12 23:23:34	5.686	−82.767	9	6.3	xxx.x.x.x.....xx...	South of Panama
2009-03-15 03:14:31	2.429	−95.124	10	5.8	xxxx.xx.x.x.....xx.xx	Galapagos Islands Region
2009-03-16 07:13:36	−55.144	−129.700	10	5.9	.....	Pacific Antarctic Ridge
2009-04-04 07:19:41	−62.599	155.117	10	5.9	.....	Balleny Islands Region
2009-04-04 18:39:17	−55.976	−27.727	87	5.5	x.....	South Sandwich Islands Region
2009-04-08 06:26:54	−58.096	−6.263	10	5.6	.....	Southern Mid Atlantic Ridge
2009-04-16 14:57:06	−60.203	−26.858	20	6.7	xxxxxxxxxxx.....xx.xx	South Sandwich Islands Region
2009-04-27 16:46:28	17.032	−99.446	35	5.8	xxx.xxxxx.x.....x...	Guerrero, Mexico
2009-04-28 19:54:35	52.666	−35.028	10	5.6	.....x.....	Reykjanes Ridge
2009-05-03 16:21:45	14.546	−91.143	108	6.3	xxxxxxxxxxx.....xx.xx	Guatemala
2009-05-04 09:10:20	10.200	−67.010	6	5.5	xx.x.xxx..x.....xx...	Near Coast of Venezuela
2009-05-07 22:28:52	−55.713	−124.577	10	5.5	.....	Southern East Pacific Rise
2009-05-10 01:16:06	1.393	−85.169	6	6.1	xxx.xxx.x.x.....xx.x.	Off Coast of Ecuador
2009-05-22 00:24:21	13.875	−90.742	69	5.5	.....	Near Coast of Guatemala
2009-05-22 19:24:18	18.114	−98.457	62	5.6	......x.....xx...	Central Mexico
2009-05-24 09:57:11	−4.050	−103.969	6	5.6	xx.x..x...x.....xx..x	Central East Pacific Rise
2009-05-25 06:40:14	−62.316	165.062	10	5.5	.....	Balleny Islands Region
2009-05-28 08:24:46	16.731	−86.217	19	7.3	xxxxxxxxxxx.....xx.xx	North of Honduras
2009-05-29 01:04:38	18.374	−106.535	11	5.5	.....	Off Coast of Jalisco, Mexico
2009-05-30 06:47:54	−60.424	−26.111	10	5.5	.....x....	South Sandwich Islands Region
2009-06-02 06:27:03	−62.834	−158.432	10	5.5	.....	Pacific Antarctic Ridge
2009-06-03 21:37:37	19.553	−109.165	6	5.6	.....x.....	Revilla Gigedo Islands Region
2009-06-04 17:25:25	−45.833	35.139	16	6.0	x.....x.....	Prince Edward Islands Region
2009-06-05 13:39:10	−35.418	−104.398	15	5.7	..x.....x...	Southeast of Easter Island
2009-06-06 20:33:28	23.864	−46.105	14	6.0	xxxxxxxxx.x.....x..xx	Northern Mid Atlantic Ridge
2009-06-09 22:42:38	−55.061	−126.655	10	5.6	x.x..xx.x.x.....xx...	Southern East Pacific Rise
2009-06-16 20:05:56	−54.366	5.871	10	6.1	.....xx.x.....x...	Bouvet Island Region
2009-06-27 15:45:49	−33.201	−15.935	13	5.6	xxxxxxxxxxx.....xx.x.	Southern Mid Atlantic Ridge
2009-07-03 11:00:14	25.131	−109.754	10	6.0	.....	Gulf of California
2009-07-04 06:49:35	9.590	−78.966	38	6.1	xxxxxxxxxxx.....xx.x.	Panama
2009-07-06 14:37:22	11.383	−86.496	76	5.5	.....	Near Coast of Nicaragua
2009-07-08 19:23:37	−36.004	−102.686	12	6.0	xxx.x.xxxx.....xx..x	Southeast of Easter Island
2009-07-31 10:09:46	−56.504	−143.181	10	5.7	.....x...	Pacific Antarctic Ridge
2009-08-01 13:33:29	−56.234	−124.296	10	6.1	..x.....x...	Southern East Pacific Rise
2009-08-03 17:55:22	28.904	−112.997	10	5.5	...x.....x...	Gulf of California
2009-08-03 17:59:56	29.039	−112.903	10	6.9	xxxxxxxxxx...x..xx.xx	Gulf of California
2009-08-03 18:40:50	29.310	−113.728	10	6.2	....x.....	Gulf of California
2009-08-05 09:13:12	29.615	−113.789	10	5.8	..x.....	Gulf of California
2009-08-12 14:50:14	−57.660	−25.250	28	5.5	.....	South Sandwich Islands Region
2009-08-13 03:46:53	−26.760	−114.261	10	5.5	.....	Easter Island Region
2009-08-13 09:37:35	7.948	−85.633	10	5.8	x.....x.....	Off Coast of Costa Rica
2009-08-15 13:22:43	18.183	−100.366	56	5.5	.....	Guerrero, Mexico
2009-09-10 19:46:03	−29.926	−111.824	10	5.5	x.....	Easter Island Region

date and time	latitude	longitude	depth	magnitude	123456789ABCDEFGHMPSL	Flynn region
2009-09-12 20:06:25	10.709	−67.927	14	6.4	xxxx.xxxxx...x..xx..x	Near Coast of Venezuela
2009-09-17 23:21:38	−29.144	−112.267	10	6.2	..x..x.........x....	Easter Island Region
2009-09-18 18:46:08	19.269	−108.481	10	5.6	.....	Revilla Gigedo Islands Region
2009-09-24 07:16:20	18.829	−107.339	13	6.4	xxx.xxxxxx.....xx.xx	Off Coast of Jalisco, Mexico
2009-10-06 01:59:39	−4.533	−104.912	10	5.7	.x..x.x.x.....	Central East Pacific Rise
2009-10-06 17:22:50	18.796	−107.527	10	5.5	.....	Off Coast of Jalisco, Mexico
2009-10-15 03:34:28	1.111	−85.322	10	5.5	.....	Off Coast of Ecuador
2009-10-15 17:48:21	3.272	−103.823	10	6.0	xxx..xxxx.....xx.xx	Galapagos Triple Junction Region
2009-10-22 00:51:39	6.729	−82.579	18	6.0	xxx.xxxxx.....xx.x.	South of Panama
2009-10-27 00:04:46	−59.955	−65.163	10	6.0	xxxxxxxxxxx.....xx.xx	Drake Passage
2009-10-29 10:52:56	18.911	−95.538	16	5.7	xxxxxxxxx.x.....xx.xx	Veracruz, Mexico
2009-11-04 18:41:43	36.155	−33.878	2	5.9	x.x..xx.x.....xx...	Azores Islands Region
2009-11-09 00:21:38	−43.462	39.613	10	5.5	.....	Prince Edward Islands Region
2009-11-17 15:30:47	52.123	−131.395	17	6.6	xxxxxxx.x.x.....	Queen Charlotte Islands Region
2009-11-17 15:37:42	52.102	−131.572	10	5.8	.....	Queen Charlotte Islands Region
2009-11-18 01:42:47	−53.965	6.484	10	5.5	x.....x.....	Bouvet Island Region
2009-11-20 19:31:26	−0.180	−18.002	5	5.5	.....x....	Central Mid Atlantic Ridge
2009-11-23 06:08:39	18.083	−105.597	34	5.6	.....x.....	Off Coast of Jalisco, Mexico
2009-11-26 19:08:11	13.514	−89.907	56	5.9	xxxxxxxxxxx.....xx.xx	El Salvador
2009-12-03 06:12:32	−56.476	−122.321	10	6.0	x.x...x.x.....	Southern East Pacific Rise
2009-12-09 07:48:13	−54.709	−135.814	10	5.6	..x.....	Pacific Antarctic Ridge
2009-12-09 16:00:43	−0.642	−21.072	10	6.4	.xx.xx.....	Central Mid Atlantic Ridge
2009-12-16 03:40:23	−55.488	−26.898	10	5.5	xx.xxx.xxxx.....xx.xx	South Sandwich Islands Region
2009-12-17 01:37:48	36.463	−9.900	19	5.6	.....	West of Gibraltar
2009-12-17 14:55:36	42.447	−30.565	4	5.5	.....	Azores Islands Region
2009-12-30 18:48:57	32.437	−115.165	9	5.9	.x...xxxx.x.....xx..x	Calif.-Baja Calif. Border Region
2009-12-31 09:23:24	−59.401	−150.975	10	6.0	..x..x.....	Pacific Antarctic Ridge
2009-12-31 09:29:44	−59.395	−151.034	10	5.6	.....	Pacific Antarctic Ridge
2010-01-05 04:55:39	−58.173	−14.695	13	6.8	xxxxxxxxxxx.x...xxxxx	East of South Sandwich Islands
2010-01-06 16:38:35	−41.605	−16.568	10	5.6	xxx.xxxx..x.....x...	Southern Mid Atlantic Ridge
2010-01-10 00:27:39	40.652	−124.692	29	6.5	xxx.xxxxxxx.x....xxxx	Near Coast of N. California
2010-01-12 21:53:10	18.443	−72.571	13	7.0	xxxxxxxxxxx.x...xxxxx	Haiti Region
2010-01-12 22:00:41	18.387	−72.784	10	6.0	.....	Haiti Region
2010-01-12 22:12:04	18.452	−72.513	10	5.7	.....	Haiti Region
2010-01-13 01:32:44	18.420	−72.861	10	5.6	......xx..x.....	Haiti Region
2010-01-13 01:36:31	18.404	−72.826	10	5.6	.....	Haiti Region
2010-01-13 05:02:57	18.367	−72.903	10	5.8	x......x..x.....xx.x.	Haiti Region
2010-01-15 18:00:46	10.454	−63.475	8	5.6	.x.....	Near Coast of Venezuela
2010-01-17 12:00:01	−57.664	−65.879	5	6.3	xxxxxxxxxxx.x...xxxxx	Drake Passage
2010-01-18 15:40:26	13.728	−90.132	54	5.9	xxx.xx.xx.x.....xx..x	Near Coast of Guatemala
2010-01-19 14:23:38	19.004	−80.804	10	5.9	x.x.x.xxx.x.....xxxxx	Cuba Region
2010-01-20 11:03:43	18.423	−72.823	10	5.9	xxxxxxxxxxx.x...xxxxx	Haiti Region
2010-01-21 08:03:23	8.268	−110.357	12	5.6	xxxxxxxxxxx.x...xxxxx	East Central Pacific Ocean
2010-01-27 17:42:45	−14.100	−14.554	10	5.8	xxxxxxx..x......xxxx.	Southern Mid Atlantic Ridge
2010-01-29 13:16:26	1.634	−90.281	10	5.5	.....x...	Galapagos Islands Region
2010-01-29 20:47:53	1.585	−90.602	10	5.6	x.....	Galapagos Islands Region
2010-01-30 19:21:27	−57.638	−141.462	10	5.6	.x.....	Pacific Antarctic Ridge
2010-02-04 20:20:21	40.412	−124.961	23	5.9	.....x.....	Near Coast of N. California
2010-02-09 00:47:40	15.893	−96.861	39	5.7	.x.....x.x....x...	Near Coast of Oaxaca, Mexico
2010-02-11 11:51:53	−40.593	−16.769	10	5.5	x..xx.....	Southern Mid Atlantic Ridge
2010-02-23 15:16:00	15.967	−91.260	10	5.6	....x...x.x.....	Mexico-Guatemala Border Region
2010-02-25 03:15:03	11.176	−86.126	24	5.7	.....x....x.x....x...	Near Coast of Nicaragua
2010-02-26 00:11:50	−55.758	−4.758	6	5.6	x...xx.....x	Southern Mid Atlantic Ridge
2010-02-27 06:34:16	−54.027	−133.640	10	5.6	.....	Pacific Antarctic Ridge
2010-02-27 19:54:28	10.840	−43.406	10	5.8	.xx...x.x.....x..	Northern Mid Atlantic Ridge
2010-03-07 07:05:24	−16.236	−115.296	18	6.3	xxxxxxxxxxx.x...xxx.x	Southern East Pacific Rise
2010-03-11 06:22:18	−57.285	−27.931	307	5.6	xxxxx.x...x.....xx.x	South Sandwich Islands Region
2010-03-14 22:33:20	−58.417	−23.567	40	5.6	.....	South Sandwich Islands Region
2010-03-20 18:08:08	19.674	−75.331	14	5.6	xx..xxxx.xx.....xxxxx	Cuba Region
2010-03-28 20:01:05	−55.139	−128.373	10	5.7	.....x.....	Pacific Antarctic Ridge
2010-04-01 15:46:51	−61.203	153.875	10	5.6	.....	Balleny Islands Region
2010-04-04 22:40:43	32.297	−115.278	4	7.2	xxxxxxxxxxx.xx..xxxxx	Calif.-Baja Calif. Border Region
2010-04-11 22:08:12	36.965	−3.542	609	6.3	..x.xxx.x.....x...	Strait of Gibraltar
2010-04-13 20:27:00	−56.331	−27.311	100	5.5	x.xxx.xxx.x.....x.xx	South Sandwich Islands Region
2010-04-15 20:52:31	−13.451	−112.167	10	5.6	.....	Central East Pacific Rise
2010-04-17 20:52:42	11.678	−86.813	33	5.5	.....x...	Near Coast of Nicaragua
2010-04-18 13:30:58	14.514	−91.987	63	5.6	......x.....	Guatemala
2010-04-25 21:09:44	−55.606	−27.730	7	5.6	xxxxxxx.x.x.....xxx.x	South Sandwich Islands Region
2010-05-05 09:38:23	−35.949	−103.058	10	5.9	x.....x..x..x...	Southeast of Easter Island
2010-05-06 11:35:29	−55.725	−127.942	10	5.8	..x.x.....	Pacific Antarctic Ridge
2010-05-07 17:46:13	44.362	−129.466	10	5.5	.....	Off Coast of Oregon
2010-05-16 05:16:10	18.400	−67.070	113	5.8	xxxxxxxxxx..x....xxx	Mona Passage

date and time	latitude	longitude	depth	magnitude	123456789ABCDEFGHMPSL	Flynn region
2010-05-19 10:30:10	−54.800	−135.252	10	6.0	.....	Pacific Antarctic Ridge
2010-05-19 10:51:03	−54.843	−135.398	10	6.0	x.....	Pacific Antarctic Ridge
2010-05-20 00:44:58	−56.870	−143.132	10	5.6	.....	Pacific Antarctic Ridge
2010-05-20 22:16:30	9.247	−84.302	21	5.9	.....x.x.x.....x	Costa Rica
2010-05-22 06:15:17	−56.236	−139.157	15	5.7	.x.....x...	Pacific Antarctic Ridge
2010-05-25 09:19:32	−65.425	179.875	10	5.5	.....	Balleny Islands Region
2010-05-25 10:09:05	35.336	−35.924	10	6.3	..x.....	Northern Mid Atlantic Ridge
2010-06-01 03:26:15	9.331	−84.206	18	6.0	.xx.xxx.x.....x..x	Costa Rica
2010-06-02 01:49:03	−57.369	−26.446	127	5.9	xxx.....x.....x...	South Sandwich Islands Region
2010-06-15 04:26:58	32.700	−115.921	5	5.8	.....	Calif.-Baja Calif. Border Region
2010-06-20 21:08:51	−36.129	−100.176	23	5.6	.x.....x...x...	Southeast of Easter Island
2010-06-30 07:22:27	16.396	−97.782	20	6.3	x.....x.....	Oaxaca, Mexico
2010-07-07 23:53:33	33.420	−116.489	14	5.5	.....x.....	Southern California
2010-07-20 17:19:50	−29.031	−13.096	10	5.8	xxxxxxxxxx..x...xxxx	Southern Mid Atlantic Ridge
2010-07-31 11:36:56	−0.763	−16.025	10	5.5	.....	North of Ascension Island
2010-08-02 03:30:02	7.103	−34.206	10	5.8	.....	Central Mid Atlantic Ridge
2010-08-24 02:11:59	18.795	−107.193	10	6.1	.....	Off Coast of Jalisco, Mexico
2010-09-14 23:32:01	21.487	−105.930	16	5.6	.....	Near Coast of Central Mexico
2010-09-27 00:08:45	57.688	−32.762	11	5.5	.....x.....	Reykjanes Ridge
2010-10-09 01:54:04	10.211	−84.293	91	5.8	xxx.xxx...x.xx...x.xx	Costa Rica
2010-10-20 04:09:42	24.540	−109.098	10	5.8	.x.....x.....	Gulf of California
2010-10-20 04:15:34	24.466	−109.144	10	5.9	.....x.....x.....	Gulf of California
2010-10-20 06:58:13	24.471	−109.026	10	5.8	x.....x.....x.....	Gulf of California
2010-10-21 17:53:13	24.690	−109.159	10	6.7	xxx.xxx.xxx..x..xx..x	Gulf of California
2010-10-23 03:09:15	−56.700	−141.952	10	5.7	x.....	Pacific Antarctic Ridge
2010-10-28 02:22:25	23.084	−108.454	10	5.6	..x.....	Gulf of California
2010-10-30 15:18:33	−56.586	−142.292	10	6.4	.....x...	Pacific Antarctic Ridge
2010-11-01 23:16:46	16.738	−93.793	167	5.6	.....x...	Chiapas, Mexico
2010-11-10 23:48:38	5.946	−82.571	19	5.7	..x.....	South of Panama
2010-11-12 19:01:29	−35.958	−102.210	10	5.8	xx...x..x.x.....xx...	Southeast of Easter Island
2010-11-21 04:36:31	−54.967	−131.479	10	6.0	xxx.x.xxx.x.....xx..x	Pacific Antarctic Ridge
2010-11-27 02:44:52	10.293	−43.128	10	5.8	.....	Northern Mid Atlantic Ridge
2010-12-05 21:44:35	−36.231	−100.826	12	5.9	.x.....x..x	Southeast of Easter Island
2010-12-07 04:27:22	−57.932	−7.474	10	5.9	xxxxxxxxxx..x...x.xx	East of South Sandwich Islands
2010-12-07 05:31:03	−58.019	−7.503	10	5.7	...x.x..x.....x..x	East of South Sandwich Islands
2010-12-08 05:24:35	−56.412	−25.741	29	6.3	xxxxxxxxxx.xx...x.x.	South Sandwich Islands Region
2010-12-20 15:15:08	10.171	−103.977	10	5.9	xxx.xxxx..x.....xx.xx	Northern East Pacific Rise
2010-12-20 17:21:26	12.995	−88.640	72	5.7	xxxxxxxxxx.xx..xx..x	Off Coast of Central America
2010-12-24 05:48:52	−63.592	−167.354	4	6.0	xx..x.x.....xx...	Pacific Antarctic Ridge
2011-01-22 01:27:29	15.216	−104.474	10	5.5	.....x.....	Off Coast of Michoacan, Mexico
2011-01-29 11:58:17	−62.964	−164.221	10	5.5	x.....x.....	Pacific Antarctic Ridge
2011-02-12 02:53:15	0.079	−17.018	10	5.6	.xx..x.....x.....xx.	North of Ascension Island
2011-02-23 03:01:36	12.388	−87.815	41	5.7	x.....x...xx...x...	Near Coast of Nicaragua
2011-02-25 13:07:26	17.843	−95.007	122	5.9	xxxxxxxx.xxxx..xx.x.	Oaxaca, Mexico
2011-02-28 11:04:16	−59.233	−17.012	10	5.6	.....	East of South Sandwich Islands
2011-02-28 23:42:17	−29.474	−112.061	9	5.5	x.....	Easter Island Region
2011-03-01 00:53:46	−29.701	−111.981	10	6.0	xxx.xxx.x.xx.x...x...	Easter Island Region
2011-03-02 18:50:49	8.596	−76.855	44	5.7	xxxxxxxxxxx.x..xx.x.	Near North Coast of Colombia
2011-03-06 14:32:36	−56.422	−27.063	87	6.5	xxxxxxxxxxx.x..xx.x.	South Sandwich Islands Region
2011-03-11 00:14:48	−53.210	−117.837	10	5.7	.....xx.....x...	Southern East Pacific Rise
2011-03-12 13:25:59	25.209	−109.820	12	5.5	.....	Gulf of California
2011-03-22 13:31:28	−33.096	−15.977	10	5.8	xxxxxxxxxxxxx..xx.x.	Southern Mid Atlantic Ridge
2011-03-27 06:20:56	14.374	−92.347	35	5.6	.....x.....x.....	Near Coast of Chiapas, Mexico
2011-04-07 13:11:22	17.208	−94.338	166	6.6	xxxxxxxxxxxx..xx.x.	Chiapas, Mexico
2011-04-07 20:41:51	17.107	−85.078	7	5.8	.....x...xx...	North of Honduras
2011-04-14 20:50:16	11.172	−86.352	35	5.7	xxx.xxx.x.xx.x..xx...	Near Coast of Nicaragua
2011-04-24 21:09:32	−35.704	−16.994	10	5.6	.....x.....	Southern Mid Atlantic Ridge
2011-04-24 22:44:15	−35.420	−16.958	10	5.6	.....	Southern Mid Atlantic Ridge
2011-04-26 11:07:27	16.851	−99.471	11	5.5	.....	Near Coast of Guerrero, Mexico
2011-04-28 13:07:43	10.129	−103.614	10	5.8	x.x....xx.x..x...x..x	Northern East Pacific Rise
2011-04-30 08:19:16	6.851	−82.333	8	6.1	x.....x.x....x...	South of Panama
2011-05-05 13:24:07	16.784	−98.618	24	5.7	.xx..x..x.x.....x.x.	Near Coast of Guerrero, Mexico
2011-05-10 15:05:22	−4.742	−105.594	10	5.5	.....	Central East Pacific Rise
2011-05-10 16:45:45	−4.702	−105.515	10	5.5	x.....	Central East Pacific Rise
2011-05-13 03:36:50	−59.438	−151.353	10	5.7	.....x...	Pacific Antarctic Ridge
2011-05-13 22:47:54	9.954	−84.313	72	5.9	xxxxxxxx.xxxxx..x.xx	Costa Rica
2011-05-15 13:08:13	0.569	−25.647	10	6.1	....x.x.....	Central Mid Atlantic Ridge
2011-05-21 00:16:25	−56.074	−27.110	48	5.9	x.x..xxxx.xx.....x..x	South Sandwich Islands Region
2011-06-07 05:18:32	−44.176	−16.039	10	5.6	xx.x.x.....x.....	Southern Mid Atlantic Ridge
2011-06-10 15:32:48	−6.730	−122.738	10	5.5	....x.....	South Pacific Ocean
2011-06-18 17:30:19	14.021	−91.640	32	5.5	.....	Guatemala
2011-06-19 11:05:29	−54.889	−129.493	10	5.5	..x.....x.....	Pacific Antarctic Ridge

date and time	latitude	longitude	depth	magnitude	123456789ABCDEFGHMPSL	Flynn region
2011-06-27 20:04:16	−63.577	170.802	10	5.5	..x.....	Balleny Islands Region
2011-07-03 06:34:39	12.410	−87.584	59	5.7	.........x......x...	Near Coast of Nicaragua
2011-07-08 05:53:03	0.961	−26.419	10	5.6	....xx.....	Central Mid Atlantic Ridge
2011-07-11 15:51:23	−49.928	−114.076	10	5.7	..............x...	Southern East Pacific Rise
2011-07-14 08:52:31	−38.237	−93.772	10	5.5	xxx.xxx......xx.....x	West Chile Rise
2011-07-15 13:26:02	−60.762	−23.523	10	6.1	xx..x......x.x...x..x	South Sandwich Islands Region
2011-07-21 23:01:42	−62.496	164.452	10	6.0	..............x...	Balleny Islands Region
2011-07-26 17:44:20	25.101	−109.525	12	6.0	........x.....	Gulf of California
2011-07-27 23:00:30	10.801	−43.393	10	5.9	xxxxxxx..x...xx.xx...	Northern Mid Atlantic Ridge
2011-08-10 23:45:43	−7.040	−12.618	10	6.0	............x.....	Ascension Island Region
2011-08-13 07:33:06	14.394	−94.674	6	5.8	.....x..x.....	Off Coast of Chiapas, Mexico
2011-08-14 01:29:39	−1.337	−14.653	10	5.6	....x........x.....	North of Ascension Island
2011-08-16 20:24:03	−57.229	−25.452	44	5.7	..x....x........x..x	South Sandwich Islands Region
2011-08-21 12:38:53	−56.428	−27.494	130	5.6	xxxxx.xxx.xx.....x..x	South Sandwich Islands Region
2011-08-23 17:51:04	37.936	−77.933	6	5.8	xxxxxxxxxxxx.x..xx.xx	Virginia
2011-08-28 10:10:19	−24.535	−115.945	10	5.6	....xx.......x.....	Southern East Pacific Rise
2011-08-31 12:17:27	43.589	−28.902	10	5.5	.....	Northern Mid Atlantic Ridge
2011-09-03 04:48:57	−56.451	−26.847	84	6.4	xxxxxxxxxxxxx..xx.xx	South Sandwich Islands Region
2011-09-05 11:21:36	6.564	−82.358	24	5.8	..............x...	South of Panama
2011-09-09 19:41:34	49.535	−126.893	22	6.4	xx.x.xxx..xx....xx...	Vancouver Island, Canada Region
2011-09-13 04:49:35	5.617	−77.471	10	5.7	xx.....x..xx....x..x.	Near West Coast of Colombia
2011-09-14 13:36:34	−35.111	−178.991	13	5.7	.........x.....	East of North Island, N.Z.
2011-09-15 07:53:18	−35.366	−179.039	10	6.1	x..xxxxxx.x......x..x	East of North Island, N.Z.
2011-09-19 18:33:55	14.186	−90.238	9	5.6	..........x.....x...	Guatemala
2011-09-20 02:40:22	−4.532	−105.207	10	5.7	.....	Central East Pacific Rise
2011-09-23 19:02:48	−9.051	−109.440	10	5.9	xxxxxxxxx.xx.x..xx...	Central East Pacific Rise
2011-10-06 00:39:32	57.890	−32.492	10	5.5	....x...x.xx....xx...	Reykjanes Ridge
2011-10-09 18:01:47	−50.076	−115.958	10	5.6	.....	Southern East Pacific Rise
2011-10-10 05:18:10	−25.459	−116.219	10	5.5	..x........x.....	Southern East Pacific Rise
2011-10-13 04:14:00	43.462	−127.135	20	5.6	.....	Off Coast of Oregon
2011-10-31 04:45:43	−23.346	−114.963	10	5.5	.....	Easter Island Region
2011-11-01 12:32:00	19.831	−109.205	10	6.3	x	Revilla Gigedo Islands Region
2011-11-02 14:59:27	−55.294	−128.843	10	6.1	..........x.x.....	Pacific Antarctic Ridge
2011-11-06 03:53:10	35.532	−96.765	5	5.6	..................x.	Oklahoma
2011-11-07 16:51:25	−63.245	170.735	5	5.8	x.....	Balleny Islands Region
2011-11-07 22:35:25	11.560	−85.861	177	6.0	xxxxxxxxxxx.xxx.x.xx	Nicaragua
2011-11-11 10:41:37	−55.981	−124.439	10	6.0	......x.....	Southern East Pacific Rise
2011-11-11 22:50:40	−55.707	−124.327	10	5.6	.....	Southern East Pacific Rise
2011-11-13 03:15:16	−55.508	−125.015	10	5.5	.....	Southern East Pacific Rise
2011-11-17 06:52:41	8.415	−103.158	10	5.6	.xx.....	Northern East Pacific Rise
2011-11-17 13:30:58	13.973	−91.718	34	5.8	.....	Near Coast of Guatemala
2011-11-18 04:34:03	−37.423	179.989	33	5.6	.....	Off E. Coast of N. Island, N.Z.
2011-11-18 06:00:53	33.704	−38.495	10	5.7	..............x...	Northern Mid Atlantic Ridge
2011-11-18 07:51:24	−37.806	179.418	12	5.8	...x.xx.x.x...x..x...	Off E. Coast of N. Island, N.Z.
2011-11-29 00:30:29	−1.602	−15.450	10	5.9	xxxxxxx.x..x.xx.xx.x.	North of Ascension Island
2011-12-03 09:27:11	17.900	−59.808	10	5.6	xxxxxxxxx.xx..x..x.xx	Leeward Islands
2011-12-11 01:47:25	17.844	−99.963	54	6.5	xxxxxxxxx.xx.xxx.x.x.	Guerrero, Mexico
2011-12-11 09:54:55	−56.009	−28.184	116	6.2	xxxxxxxxxxxx.xxx.x.x.	South Sandwich Islands Region
2011-12-23 10:52:07	−33.815	−178.344	10	5.5	.....	South of Kermadec Islands
2011-12-23 19:12:34	−52.120	27.958	10	5.9	.....	South of Africa
2011-12-31 00:19:18	−56.958	−142.457	10	5.7	.....	Pacific Antarctic Ridge
2012-01-05 09:35:32	18.332	−70.350	41	5.5	......x.........x...	Dominican Republic Region
2012-01-06 18:54:39	−6.341	−107.312	10	5.5	x.........x.........	Central East Pacific Rise
2012-01-12 14:11:08	−52.113	28.152	10	5.5	x.........x.........	South of Africa
2012-01-13 16:02:23	−60.548	−27.073	10	5.6	............x.....	South Sandwich Islands Region
2012-01-15 13:40:16	−60.990	−56.109	10	5.9	xx.x.xxxxxxx.xxx.x.x.	South Shetland Islands
2012-01-15 13:40:19	−60.948	−56.113	8	6.6	xx.x.xxxxxxx.xxx.x.x.	South Shetland Islands
2012-01-15 14:21:31	−60.879	−55.969	10	6.0	x..x..x.x..x.....x.	South Shetland Islands
2012-01-16 03:59:44	−60.721	−56.055	10	5.6	.......xx.x...xx.....	South Shetland Islands
2012-01-21 18:47:11	14.873	−93.005	45	6.2	xx.x.xxxxxxx.xxx.x.x.	Near Coast of Chiapas, Mexico
2012-01-22 05:53:42	−56.748	−25.223	13	6.0	xx.x.xxxx.xx.x.x.x.x.	South Sandwich Islands Region
2012-01-22 06:00:05	−56.633	−24.906	10	5.5	.....x..x.....	South Sandwich Islands Region
2012-01-24 16:31:07	−56.336	−27.723	7	5.5	xx.x.xx.xxxx.....x...	South Sandwich Islands Region
2012-01-28 04:43:41	−36.793	−110.509	10	5.6	......x...x.....	Southern East Pacific Rise
2012-02-04 20:05:30	48.879	−127.956	11	5.6	.....	Vancouver Island, Canada Region
2012-02-09 08:49:24	−56.371	−25.836	9	5.5	xx...xxxx.xx.....x...	South Sandwich Islands Region
2012-02-09 18:52:47	−58.325	157.870	3	5.9	.....	Macquarie Island Region
2012-02-13 10:55:09	9.180	−84.101	16	5.9	xx...x..x.xx.xxx.x...	Costa Rica
2012-02-13 21:07:02	41.153	−123.818	32	5.6	.x....x.x.xx.....	Northern California
2012-02-15 03:31:20	43.536	−127.381	10	5.8	............x.....	Off Coast of Oregon
2012-02-20 19:09:43	14.394	−92.882	63	5.6	.........x......x...	Near Coast of Chiapas, Mexico

B.2. Calculated Q component receiver functions

For each station follows a plot with the Q component receiver function for the selected events (see previous section). In the top panel the mean of all receiver functions is displayed. On the right panel the event back azimuth (azi) and the epicentral distance of the event (dist) is displayed in degrees. The receiver functions are sorted by back azimuth.

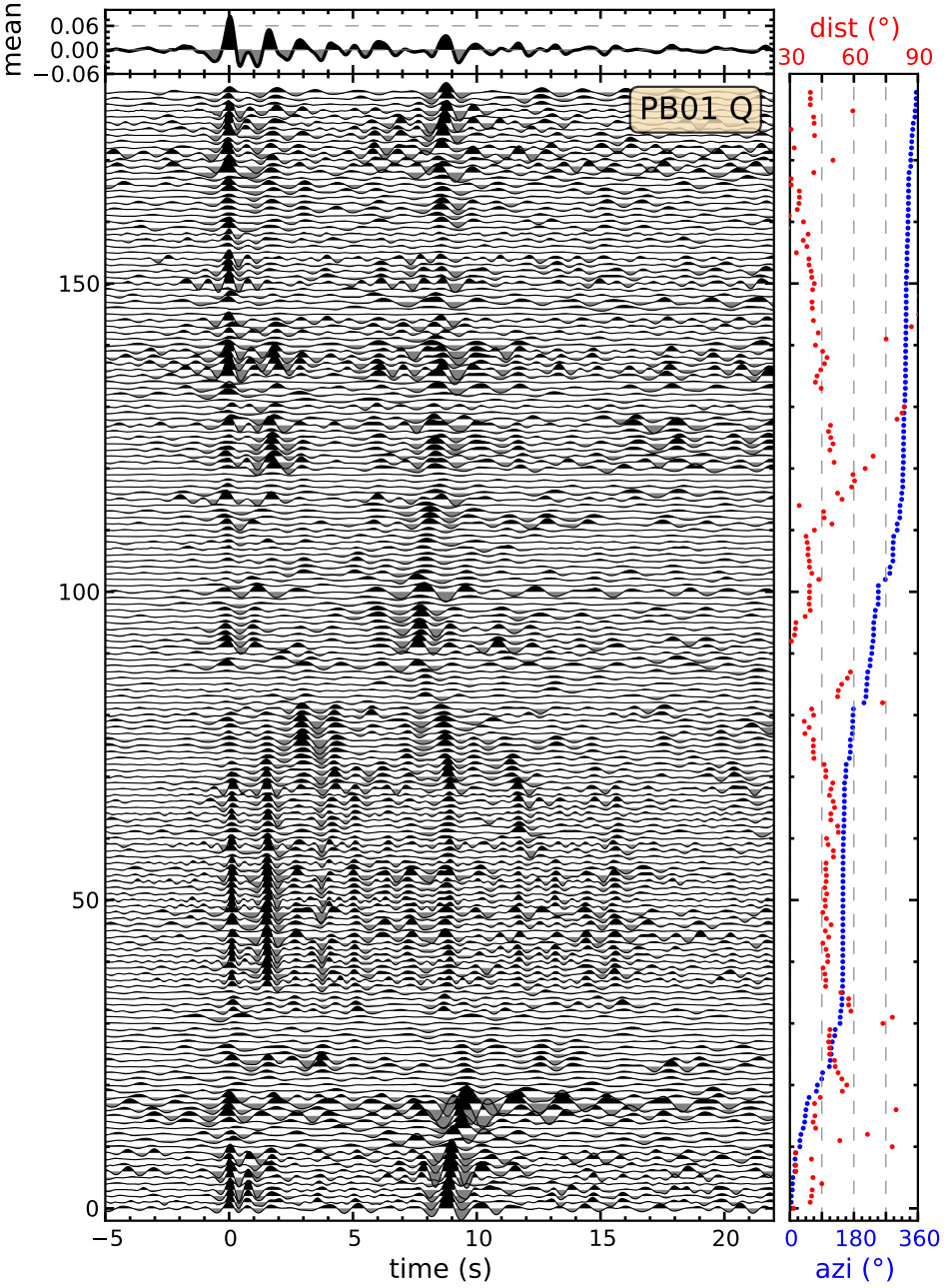

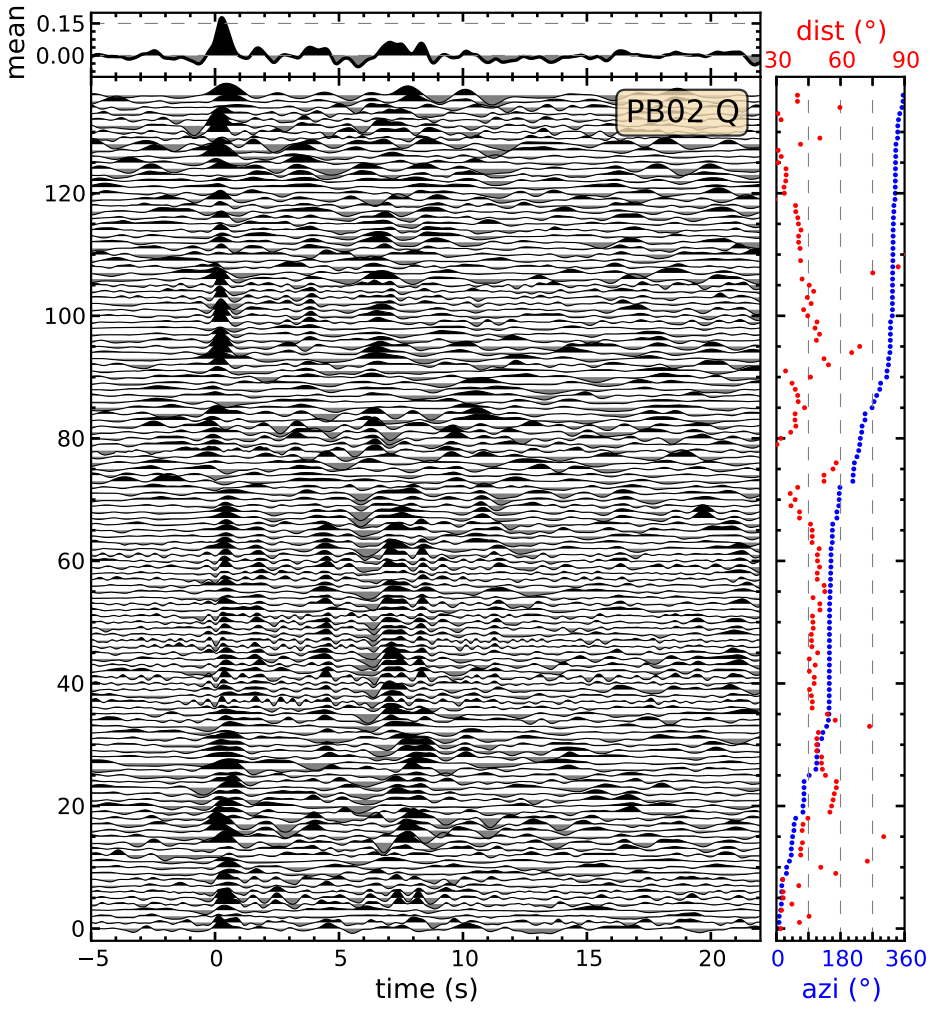
mean
0.15
0.00
PB02 Q
dist (°)
30
60
90
120
100
80
60
40
20
0
−5
0
5
10
15
20
time (s)
0
180
360
azi (°)

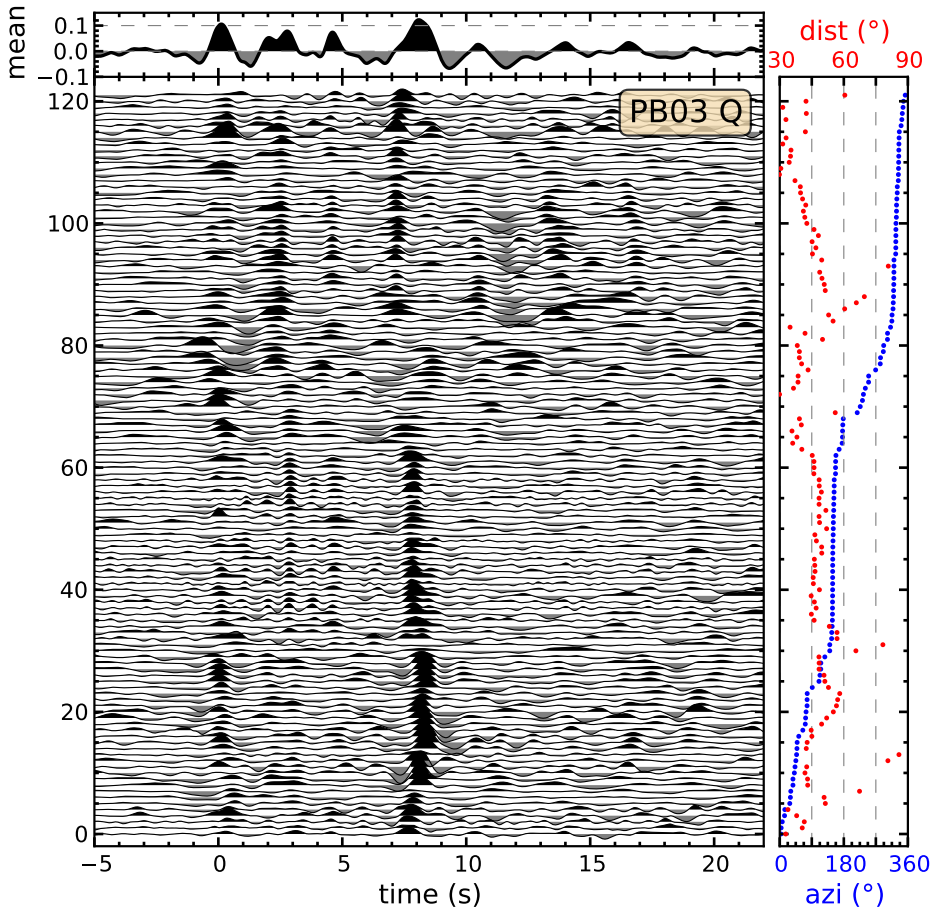
mean
0.1
0.0
−0.1
PB03 Q
dist (°)
30
60
90
120
100
80
60
40
20
0
−5
0
5
10
15
20
time (s)
0
180
360
azi (°)

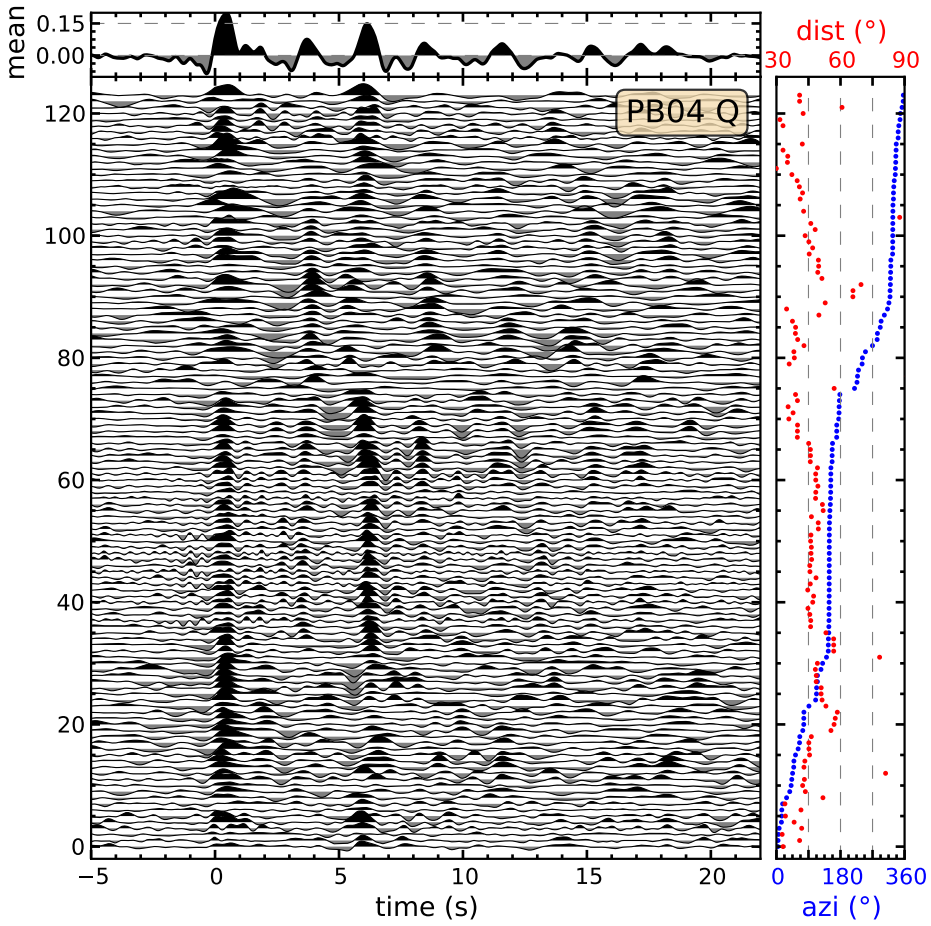
mean
0.15
0.00
PB04 Q
dist (°)
30
60
90
120
100
80
60
40
20
0
−5
0
5
10
15
20
time (s)
0
180
360
azi (°)

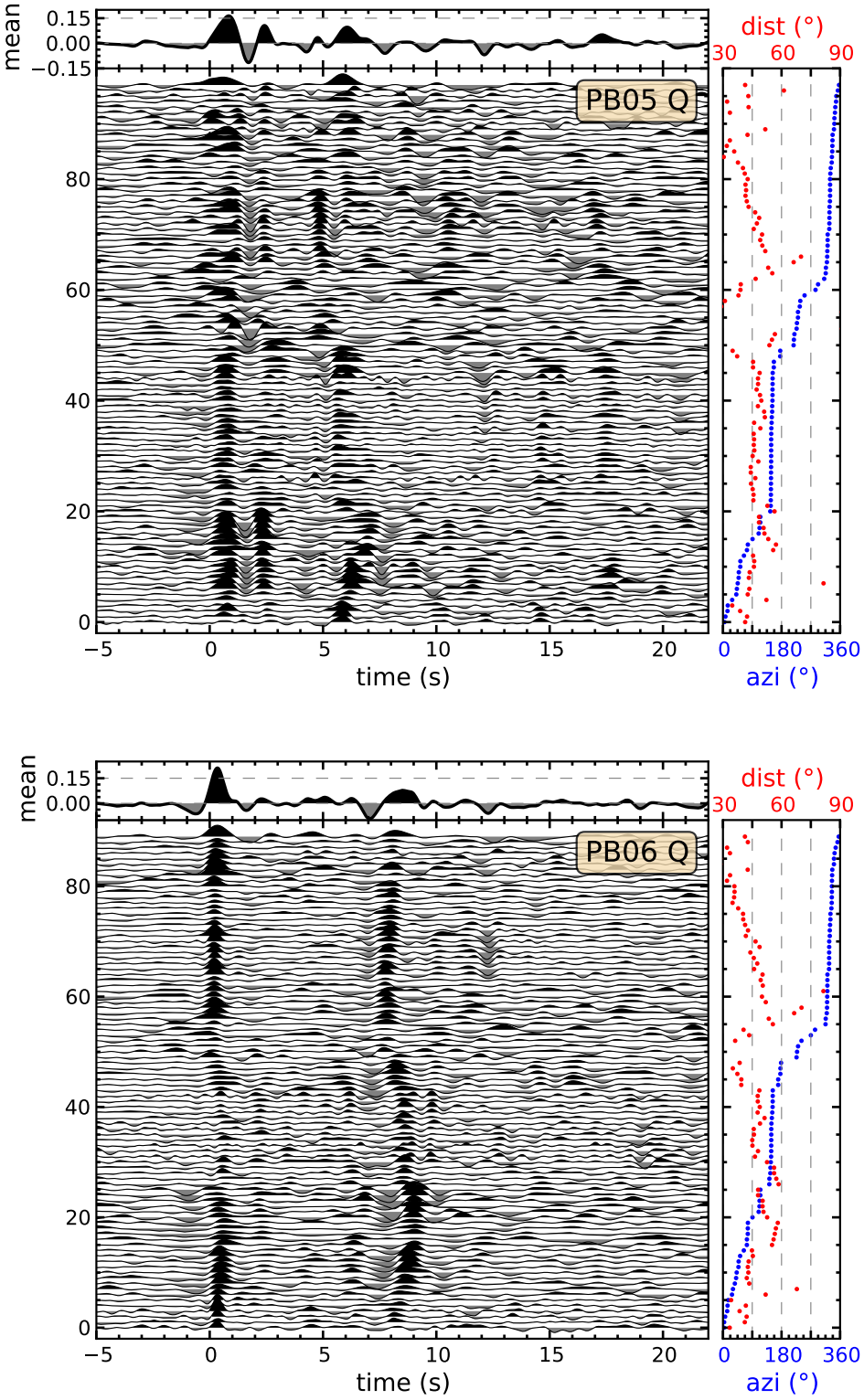
mean
0.15
0.00
−0.15
PB05 Q
dist (°)
30
60
90
0
20
40
60
80
−5
0
5
10
15
20
time (s)
0
180
360
azi (°)
mean
0.15
0.00
PB06 Q
dist (°)
30
60
90
0
20
40
60
80
−5
0
5
10
15
20
time (s)
0
180
360
azi (°)

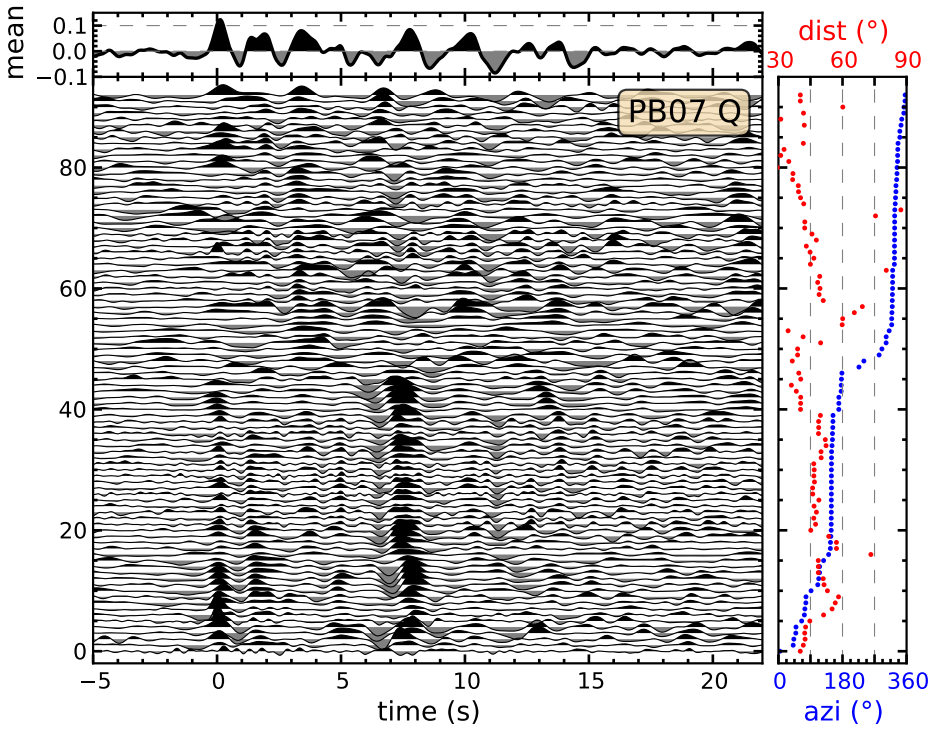
mean
0.1
0.0
−0.1
PB07 Q
dist (°)
30
60
90
0
20
40
60
80
−5
0
5
10
15
20
time (s)
0
180
360
azi (°)

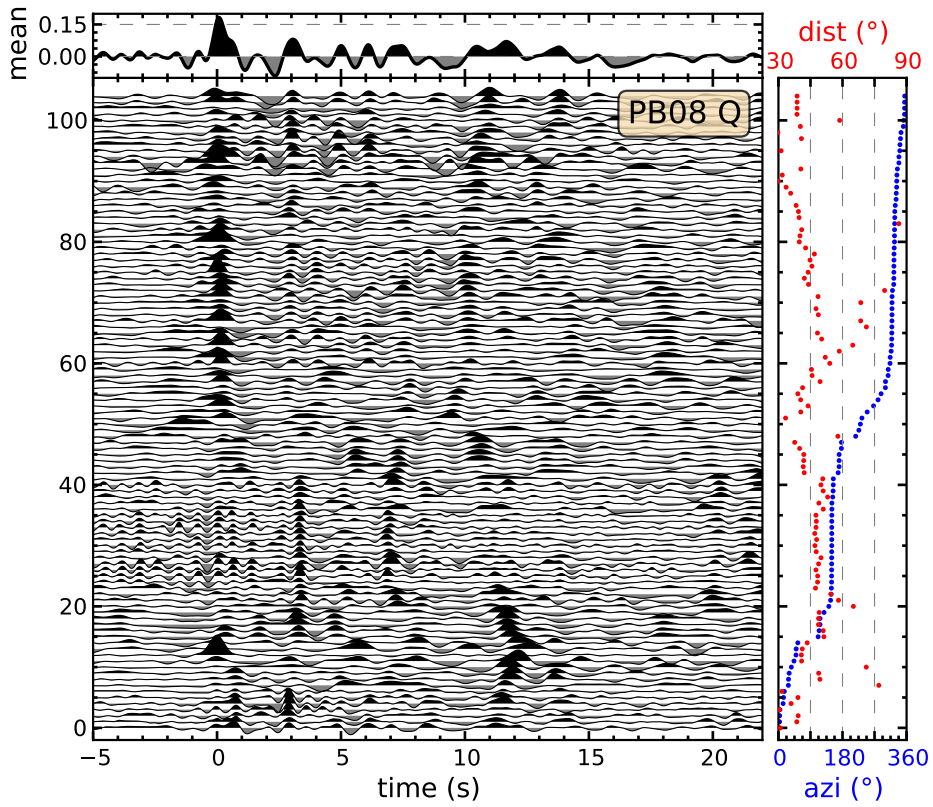
mean
0.15
0.00
PB08 Q
dist (°)
30
60
90
0
20
40
60
80
100
−5
0
5
10
15
20
time (s)
0
180
360
azi (°)

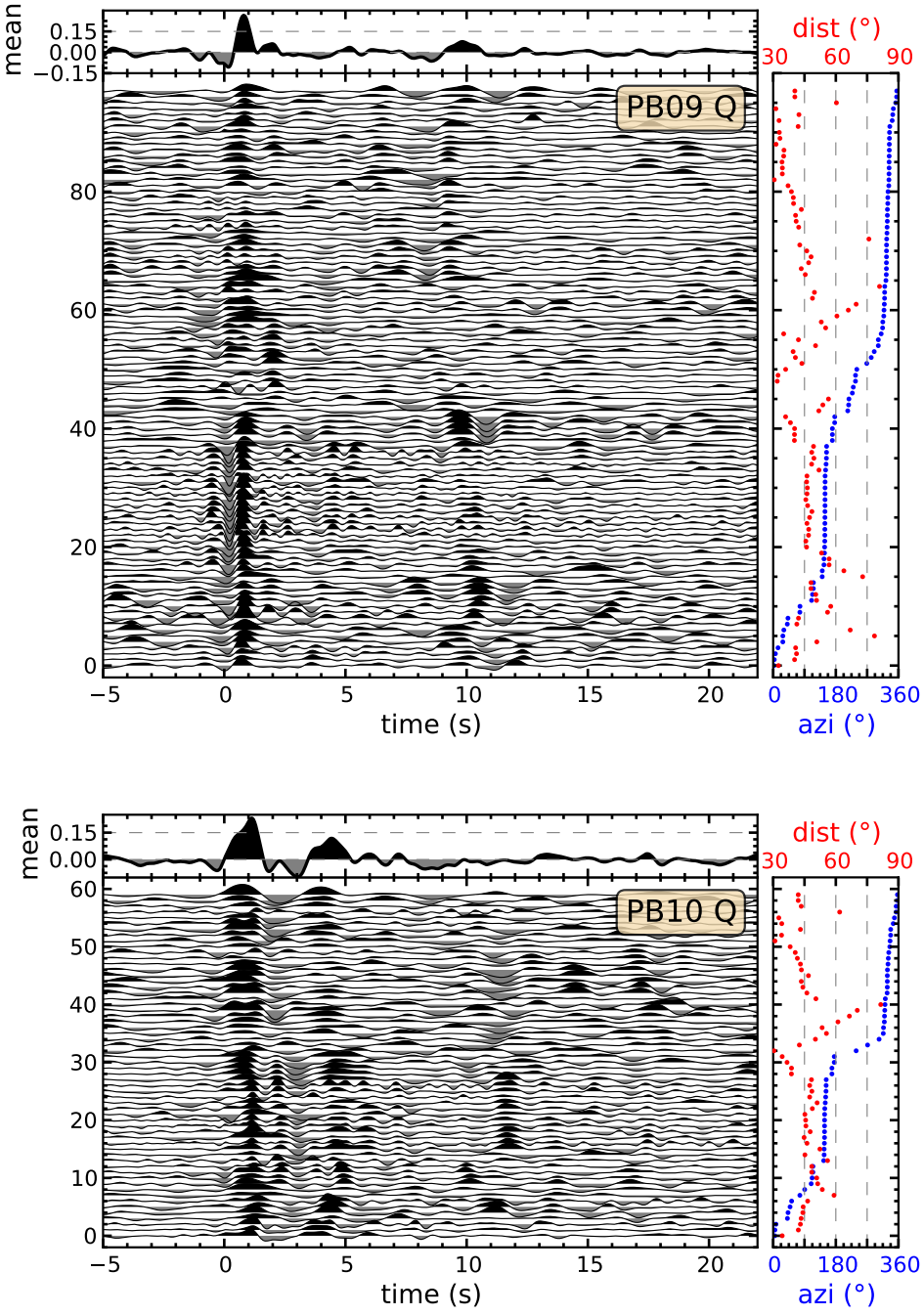
mean
0.15
0.00
−0.15
PB09 Q
dist (°)
30
60
90
80
60
40
20
0
−5
0
5
10
15
20
time (s)
0
180
360
azi (°)
mean
0.15
0.00
PB10 Q
dist (°)
30
60
90
60
50
40
30
20
10
0
−5
0
5
10
15
20
time (s)
0
180
360
azi (°)

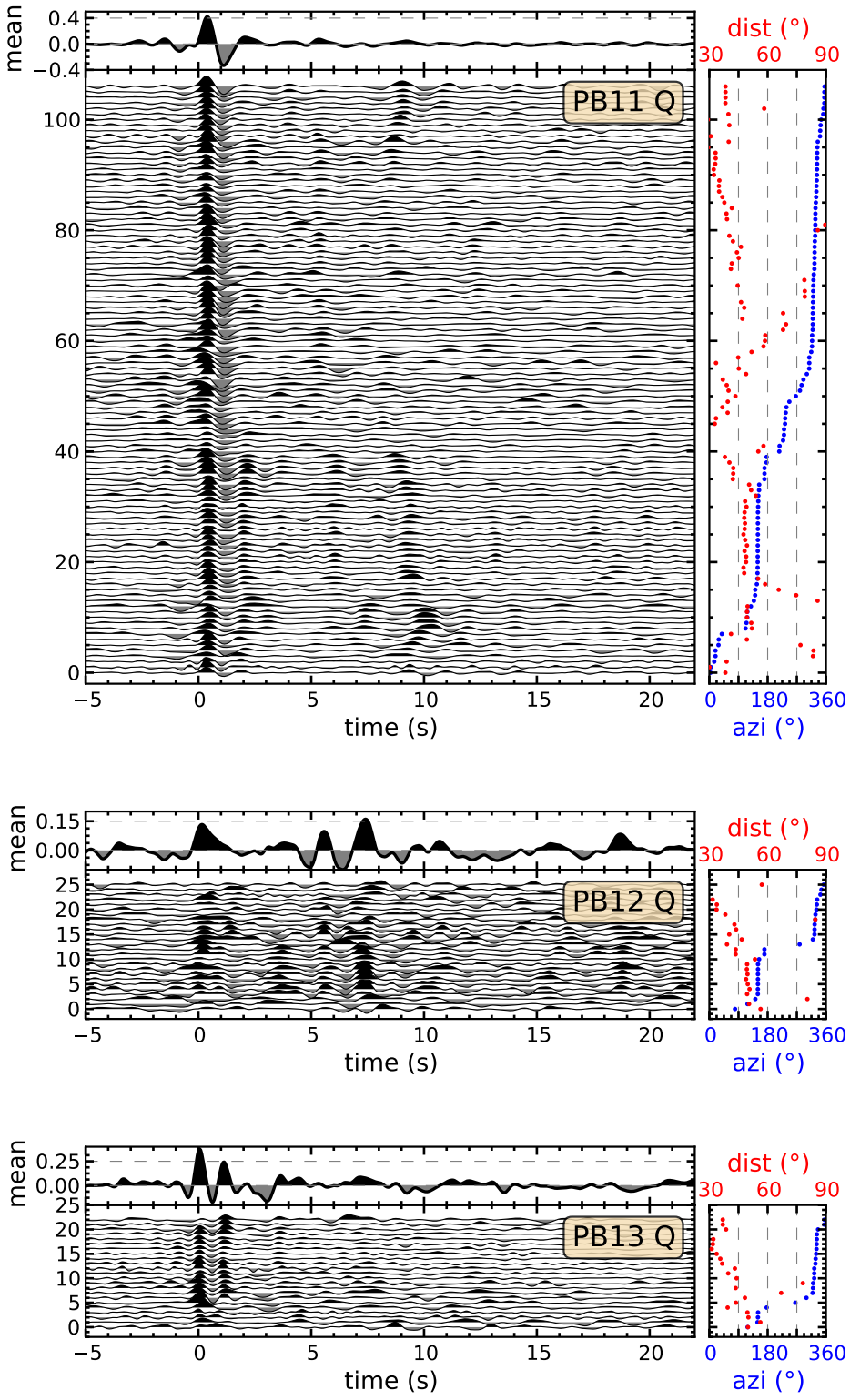
mean
0.4
0.0
−0.4
PB11 Q
100
80
60
40
20
0
−5
0
5
10
15
20
time (s)
dist (°)
30
60
90
0
180
360
azi (°)
mean
0.15
0.00
PB12 Q
25
20
15
10
5
0
time (s)
dist (°)
azi (°)
mean
0.25
0.00
PB13 Q
time (s)
dist (°)
azi (°)

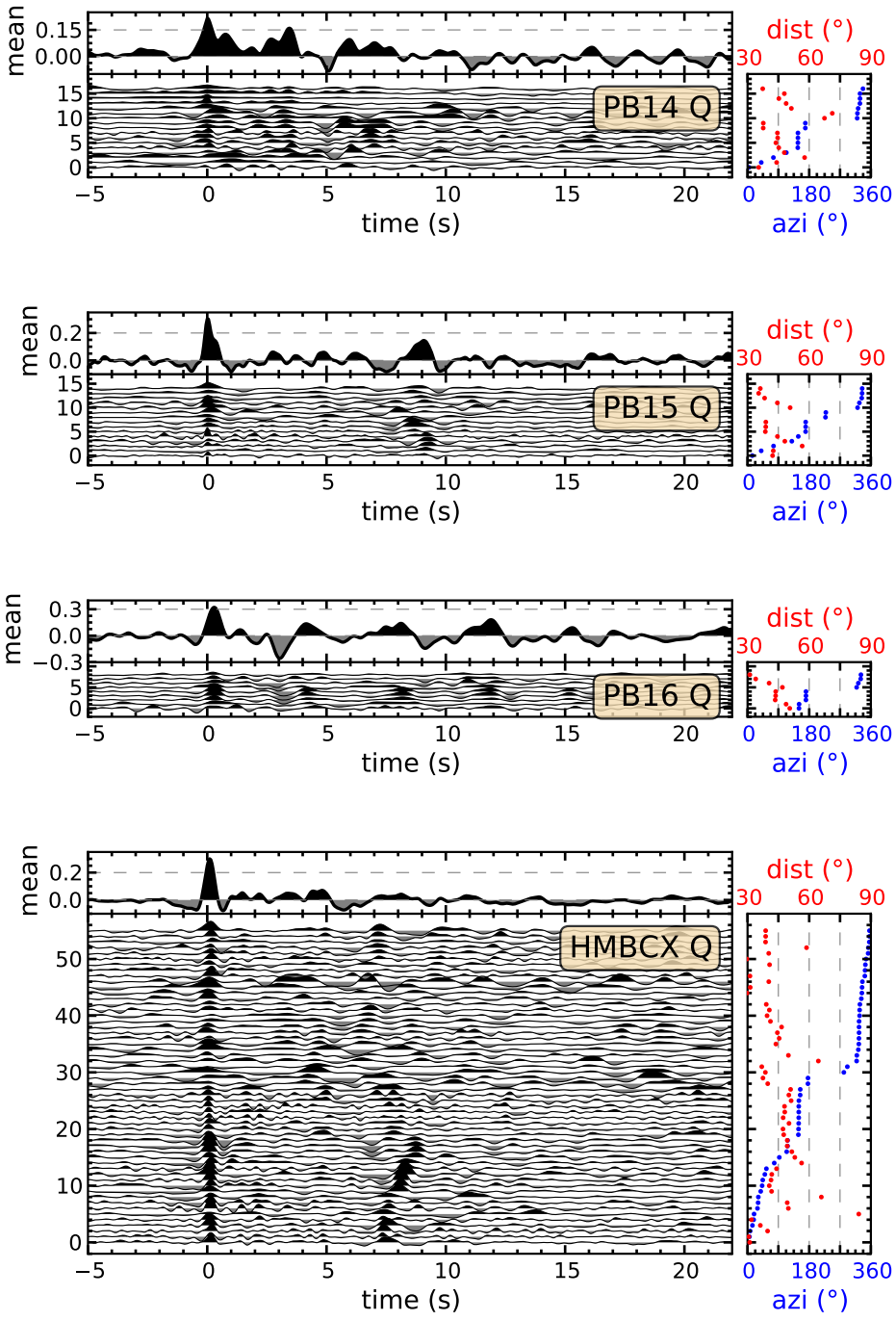
mean
0.15
0.00
15
10
5
0
PB14 Q
−5
0
5
10
15
20
time (s)
dist (°)
30
60
90
0
180
360
azi (°)
mean
0.2
0.0
15
10
5
0
PB15 Q
−5
0
5
10
15
20
time (s)
dist (°)
30
60
90
0
180
360
azi (°)
mean
0.3
0.0
−0.3
5
0
PB16 Q
−5
0
5
10
15
20
time (s)
dist (°)
30
60
90
0
180
360
azi (°)
mean
0.2
0.0
50
40
30
20
10
0
HMBCX Q
−5
0
5
10
15
20
time (s)
dist (°)
30
60
90
0
180
360
azi (°)

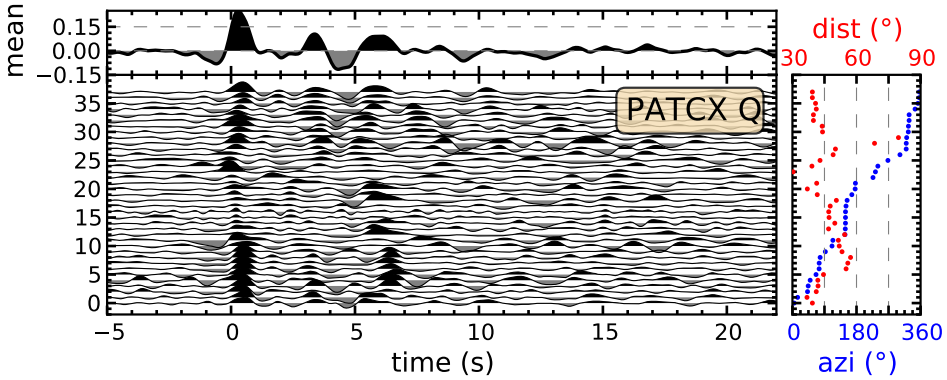
mean
0.15
0.00
−0.15
PATCX Q
dist (°)
30 60 90
35
30
25
20
15
10
5
0
−5 0 5 10 15 20
time (s)
0 180 360
azi (°)

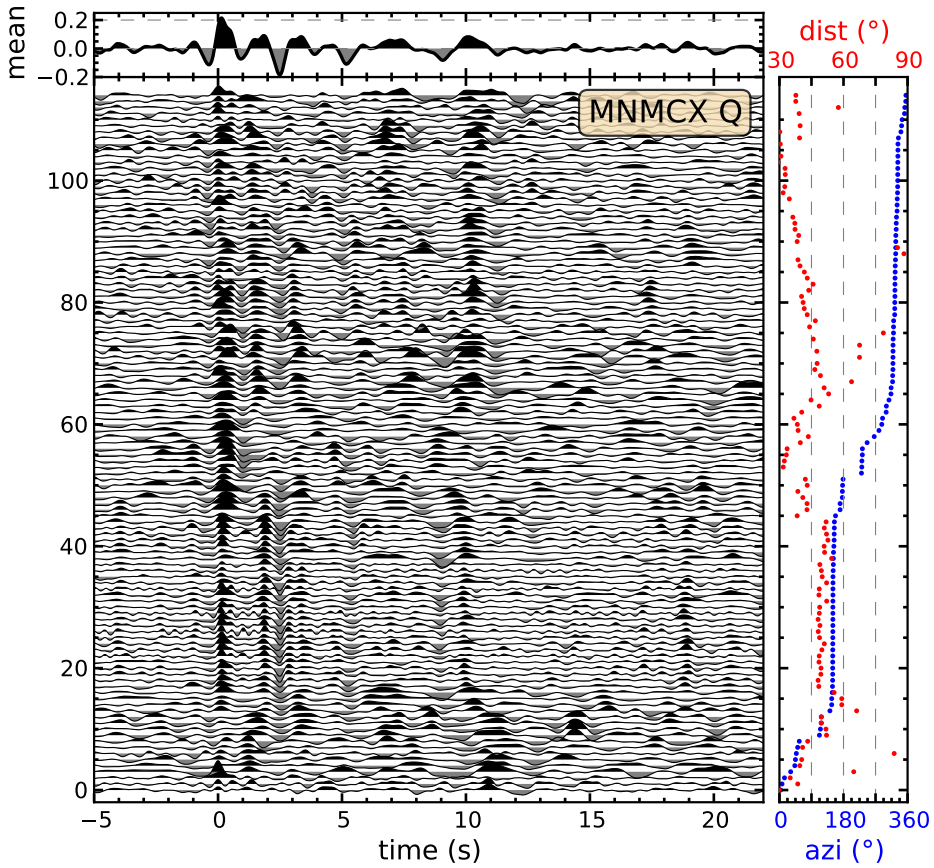
mean
0.2
0.0
−0.2
MNMCX Q
dist (°)
30 60 90
100
80
60
40
20
0
−5 0 5 10 15 20
time (s)
0 180 360
azi (°)

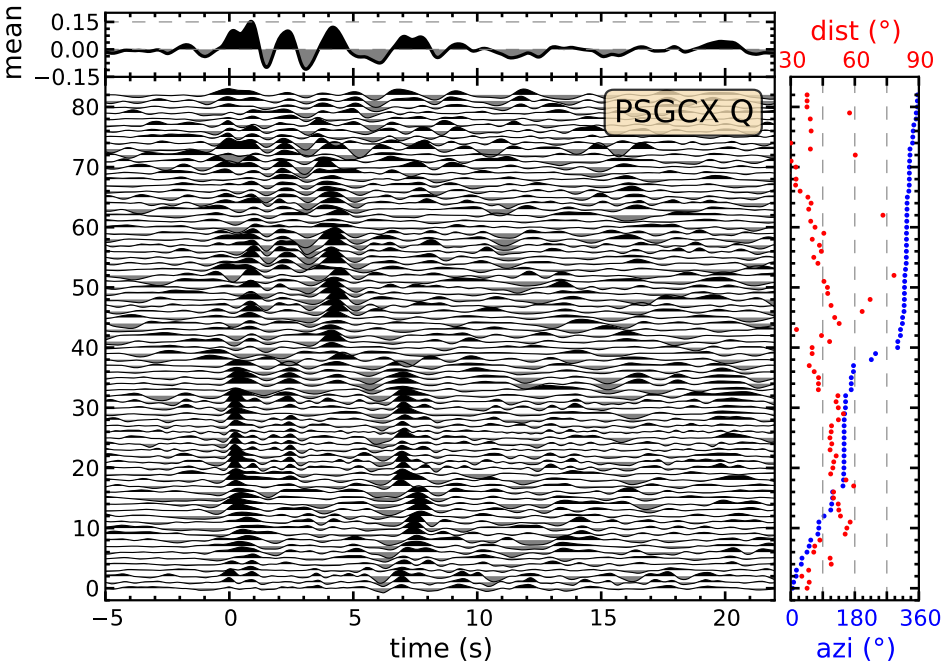
mean
0.15
0.00
−0.15
PSGCX Q
dist (°)
30
60
90
80
70
60
50
40
30
20
10
0
−5
0
5
10
15
20
time (s)
0
180
360
azi (°)

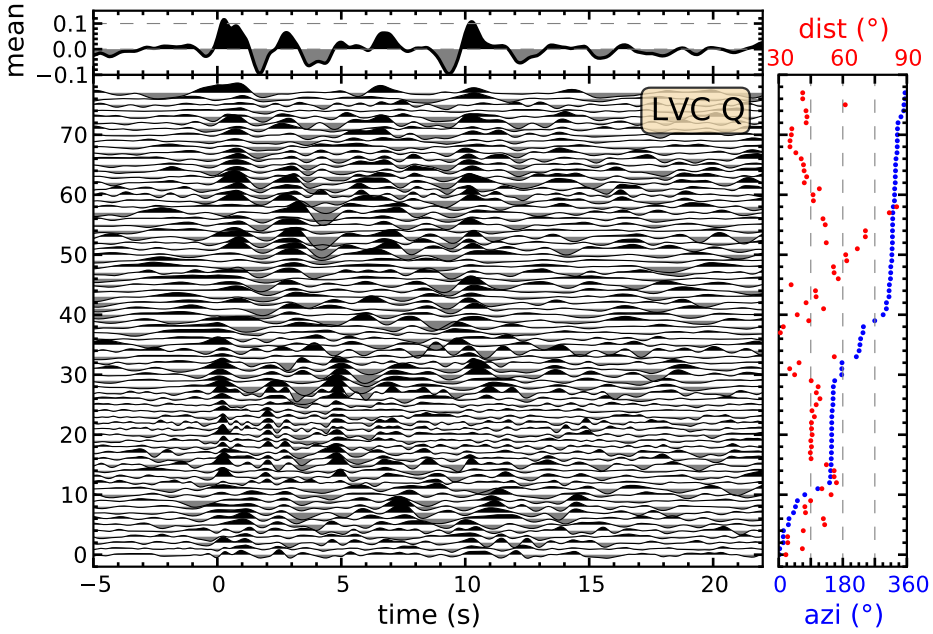
mean
0.1
0.0
−0.1
LVC Q
dist (°)
30
60
90
70
60
50
40
30
20
10
0
−5
0
5
10
15
20
time (s)
0
180
360
azi (°)

B.3. Q component receiver functions from specific regions

For each station there are the following three plots with just the events originating from a specific region. In the top panel the mean of all receiver functions is displayed. On the first right panel the event back azimuth (azi) and the event epicentral distance (dist) are displayed in degrees. The receiver functions are sorted by event time which is displayed in the most right panel. The occurrence of the Tocopilla earthquake is indicated by a red star in this panel. The phases which were analyzed for time shifts are marked with a yellow bar. The results of the analysis for the different phases are displayed in the lower left of each analyzed plot. The three symbols represent the methods used (circle: maximum, square: correlation, triangle: correlation above score). Following the figures I present a table with the numerical results of the analysis.

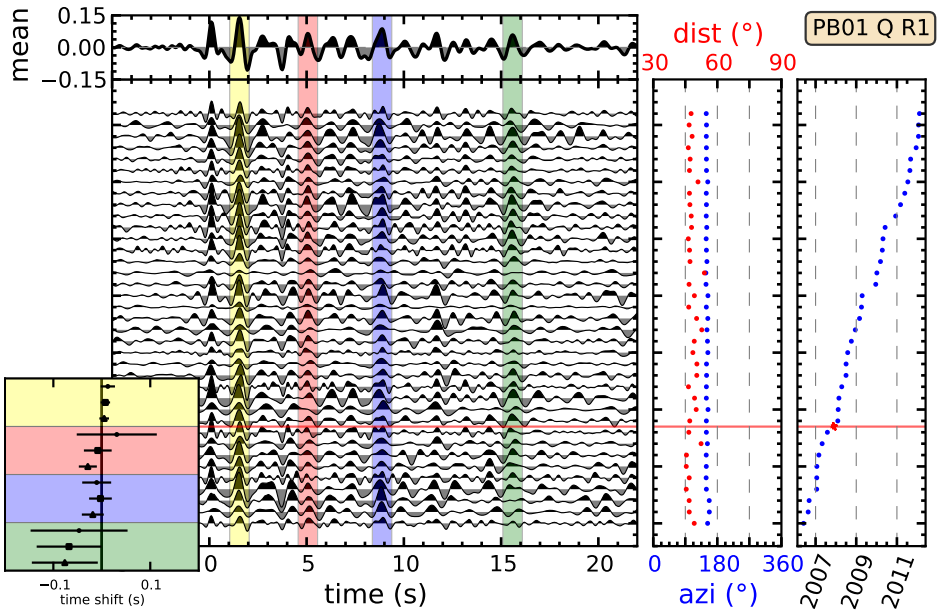

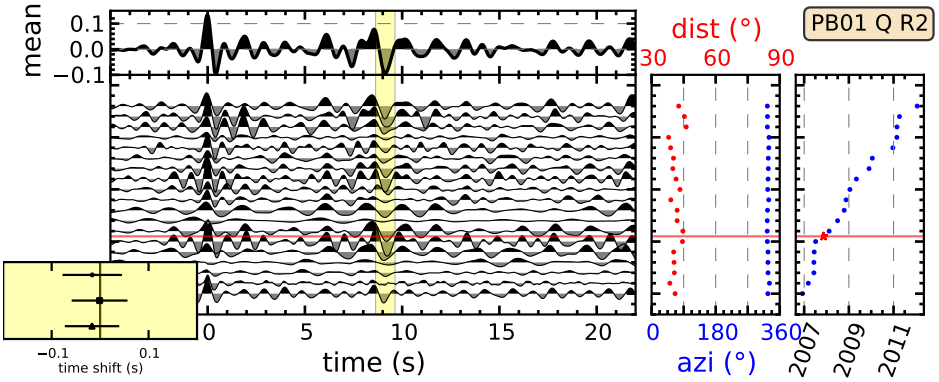
mean
0.1
0.0
−0.1
dist (°)
30
60
90
PB01 Q R2
0
5
10
15
20
time (s)
−0.1
0.1
time shift (s)
0
180
360
azi (°)
2007
2009
2011

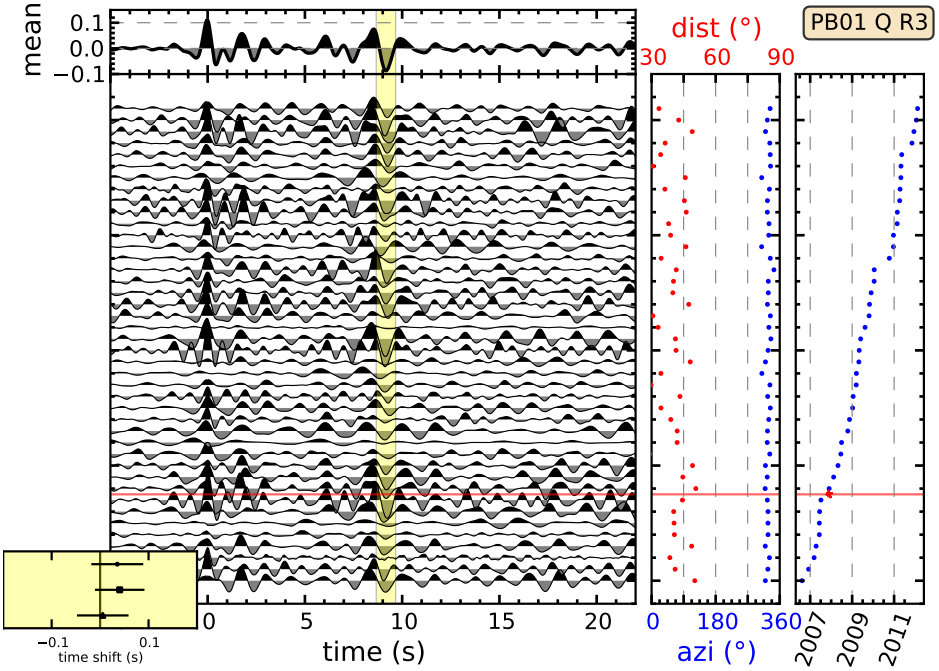
mean
0.1
0.0
−0.1
dist (°)
30
60
90
PB01 Q R3
0
5
10
15
20
time (s)
−0.1
0.1
time shift (s)
0
180
360
azi (°)
2007
2009
2011

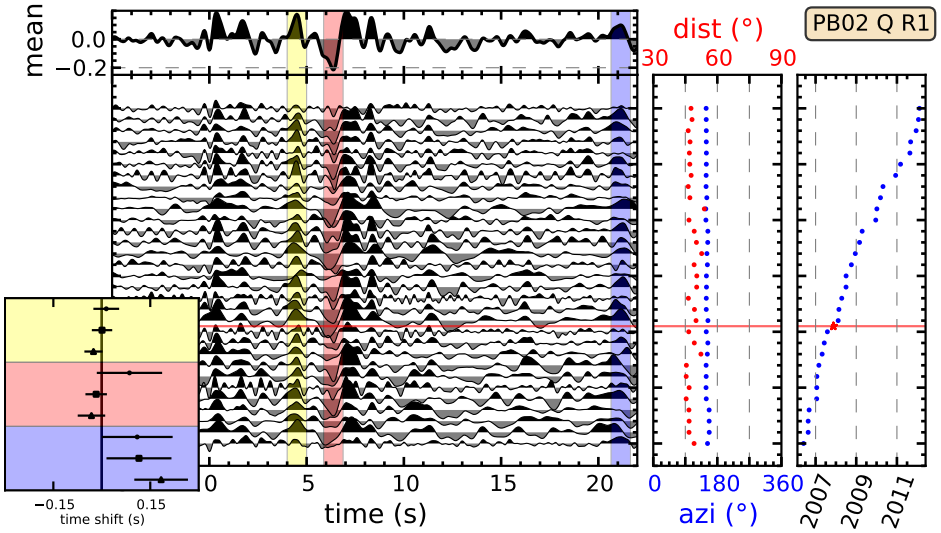
mean
0.0
−0.2
PB02 Q R1
dist (°)
30
60
90
0
5
10
15
20
time (s)
−0.15
0.15
time shift (s)
0
180
360
azi (°)
2007
2009
2011

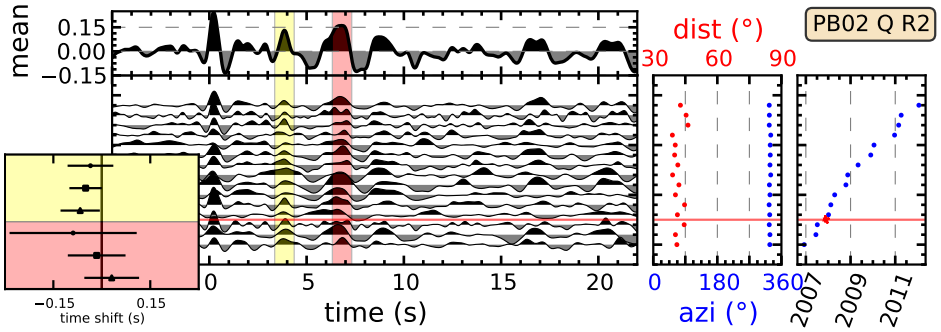
mean
0.15
0.00
−0.15
PB02 Q R2
dist (°)
30
60
90
0
5
10
15
20
time (s)
−0.15
0.15
time shift (s)
0
180
360
azi (°)
2007
2009
2011

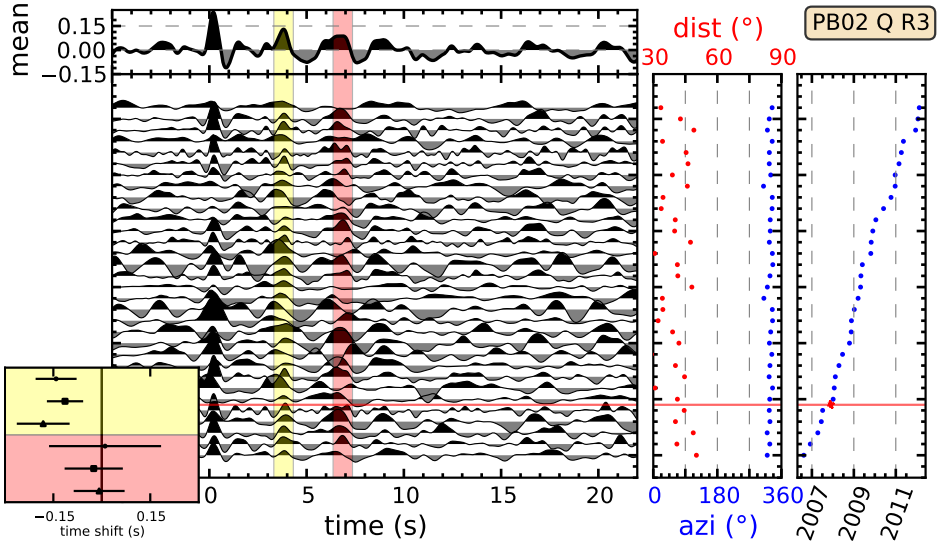
mean
0.15
0.00
−0.15
PB02 Q R3
dist (°)
30
60
90
0
5
10
15
20
time (s)
−0.15
0.15
time shift (s)
0
180
360
azi (°)
2007
2009
2011

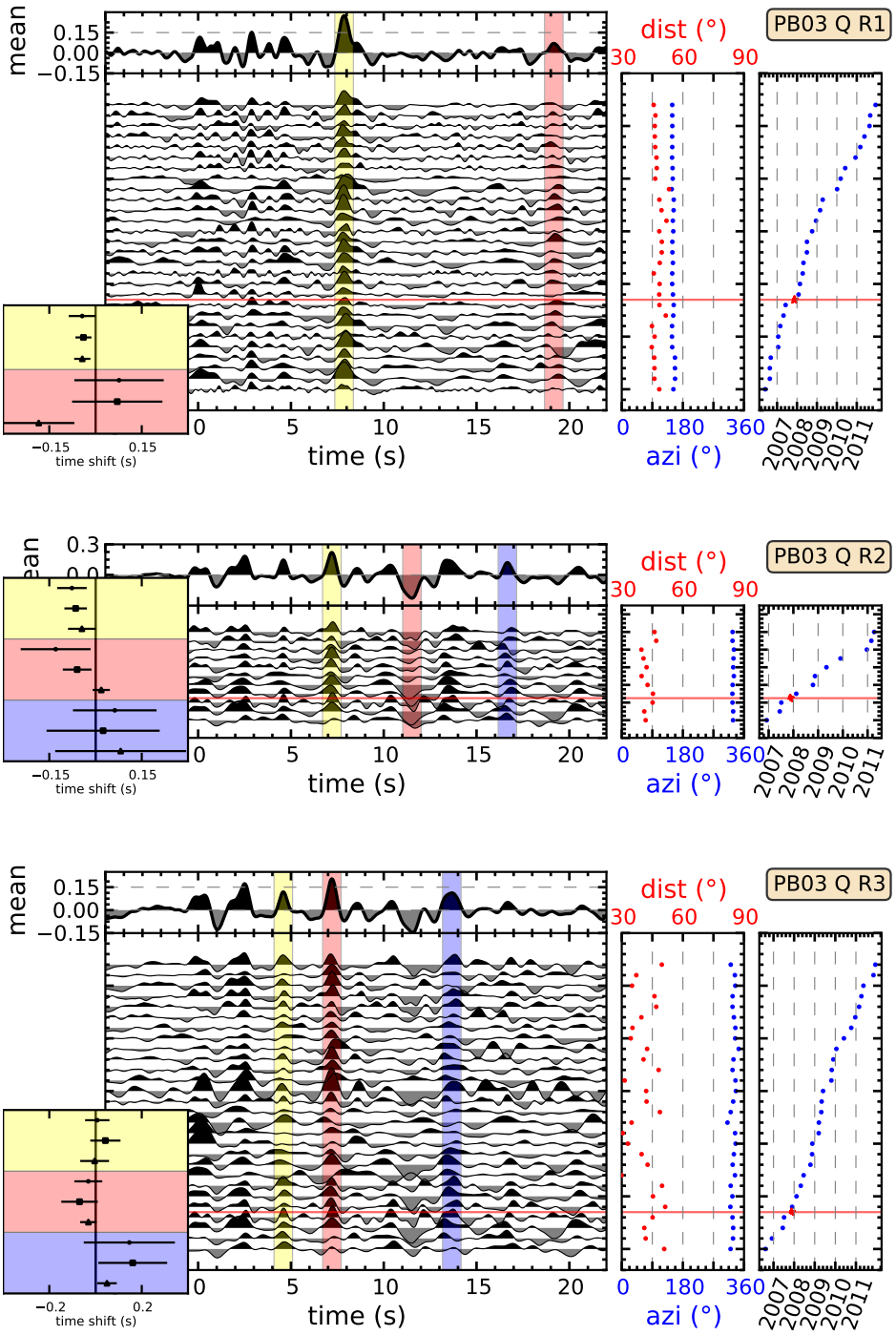
mean
0.15
0.00
−0.15
dist (°)
30 60 90
PB03 Q R1
0 5 10 15 20
time (s)
0 180 360
azi (°)
2007 2008 2009 2010 2011
−0.15 0.15
time shift (s)
PB03 Q R2
PB03 Q R3
−0.2 0.2

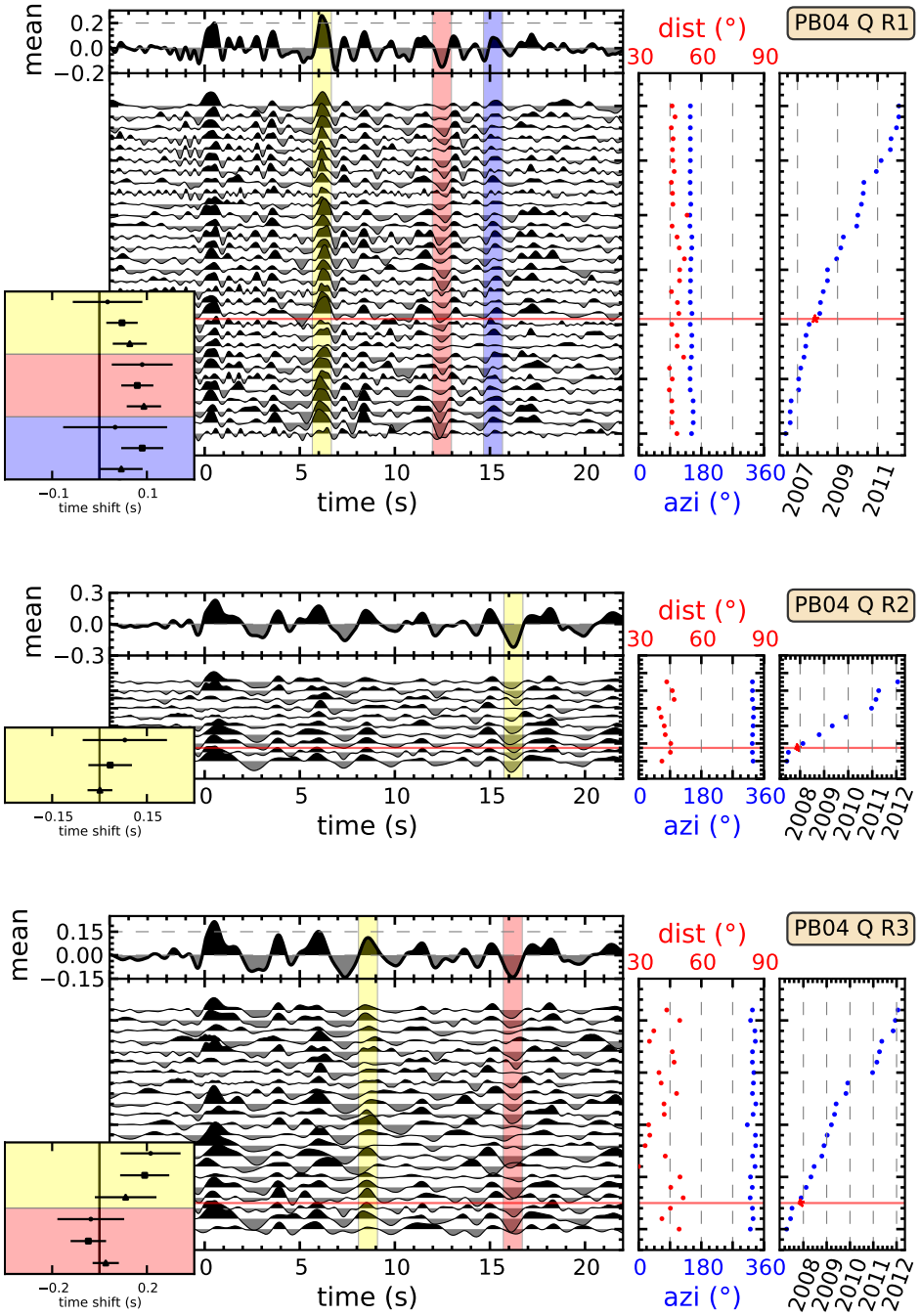
mean
0.2
0.0
−0.2
dist (°)
30
60
90
PB04 Q R1
0
5
10
15
20
time (s)
−0.1
0.1
time shift (s)
0
180
360
azi (°)
2007
2009
2011
mean
0.3
0.0
−0.3
dist (°)
30
60
90
PB04 Q R2
0
5
10
15
20
time (s)
−0.15
0.15
time shift (s)
0
180
360
azi (°)
2008
2009
2010
2011
2012
mean
0.15
0.00
−0.15
dist (°)
30
60
90
PB04 Q R3
0
5
10
15
20
time (s)
−0.2
0.2
time shift (s)
0
180
360
azi (°)
2008
2009
2010
2011
2012

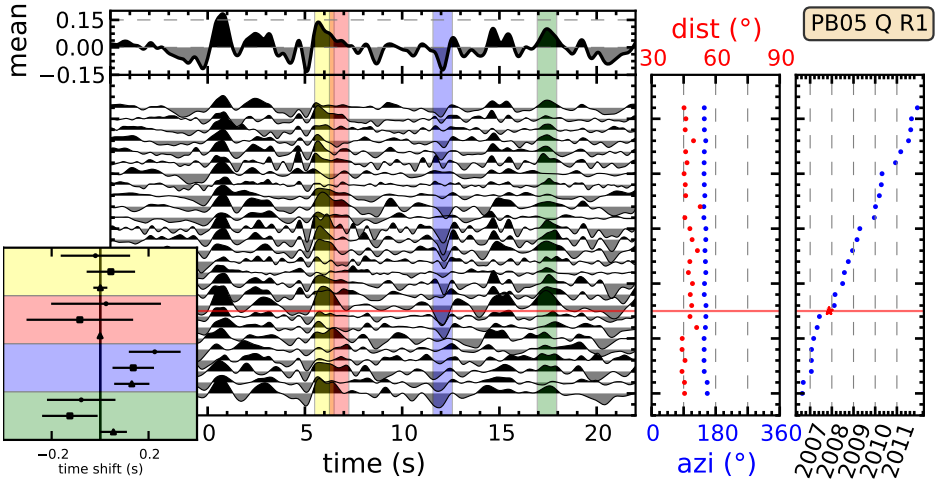
mean
0.15
0.00
−0.15
dist (°)
30 60 90
PB05 Q R1
0 5 10 15 20
time (s)
0 180 360
azi (°)
2007 2008 2009 2010 2011
−0.2 0.2
time shift (s)

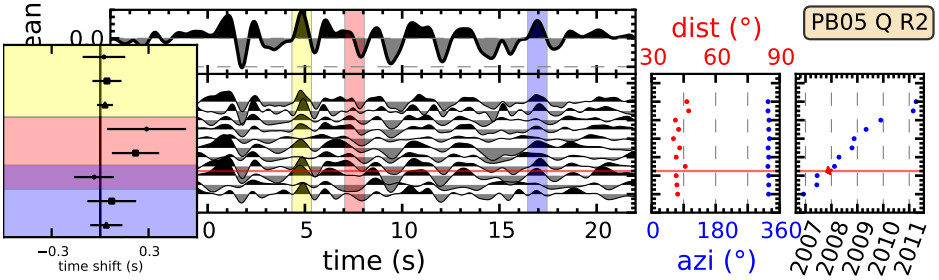
dist (°)
30 60 90
PB05 Q R2
0 5 10 15 20
time (s)
0 180 360
azi (°)
2007 2008 2009 2010 2011
−0.3 0.3
time shift (s)

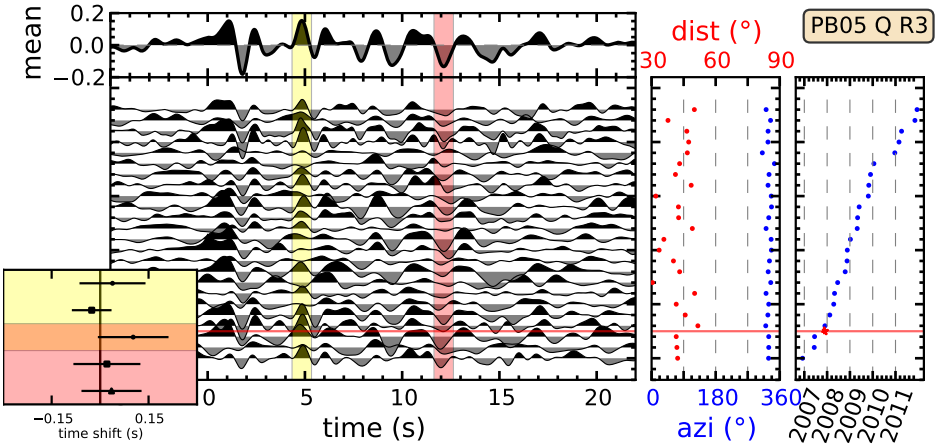
mean
0.2
0.0
−0.2
dist (°)
30 60 90
PB05 Q R3
0 5 10 15 20
time (s)
0 180 360
azi (°)
2007 2008 2009 2010 2011
−0.15 0.15
time shift (s)

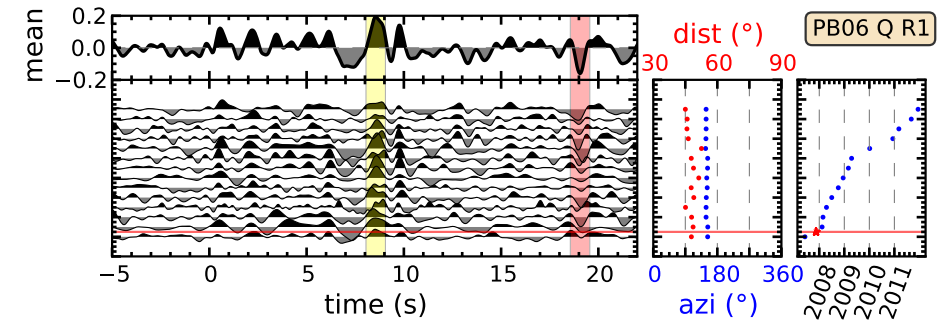
mean
0.2
0.0
−0.2
dist (°)
30
60
90
PB06 Q R1
−5
0
5
10
15
20
time (s)
0
180
360
azi (°)
2008
2009
2010
2011

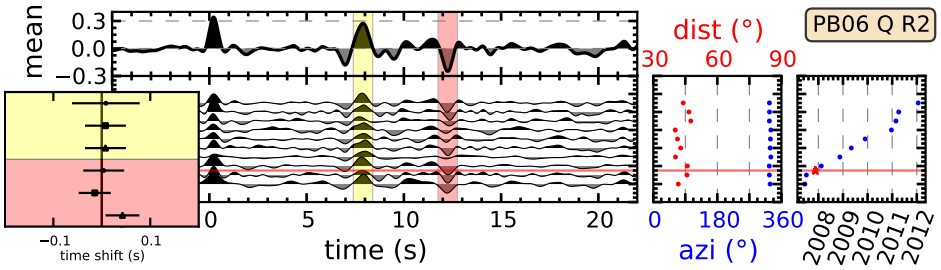
mean
0.3
0.0
−0.3
dist (°)
30
60
90
PB06 Q R2
−0.1
0.1
time shift (s)
0
5
10
15
20
time (s)
0
180
360
azi (°)
2008
2009
2010
2011
2012

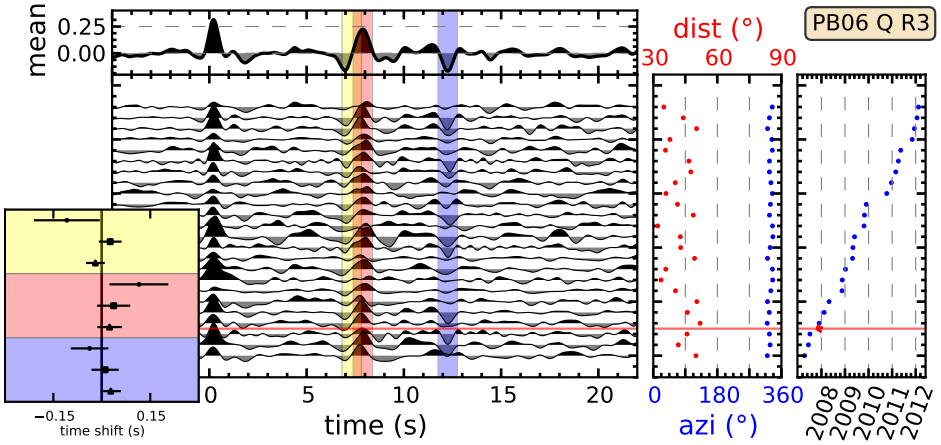
mean
0.25
0.00
dist (°)
30
60
90
PB06 Q R3
−0.15
0.15
time shift (s)
0
5
10
15
20
time (s)
0
180
360
azi (°)
2008
2009
2010
2011
2012

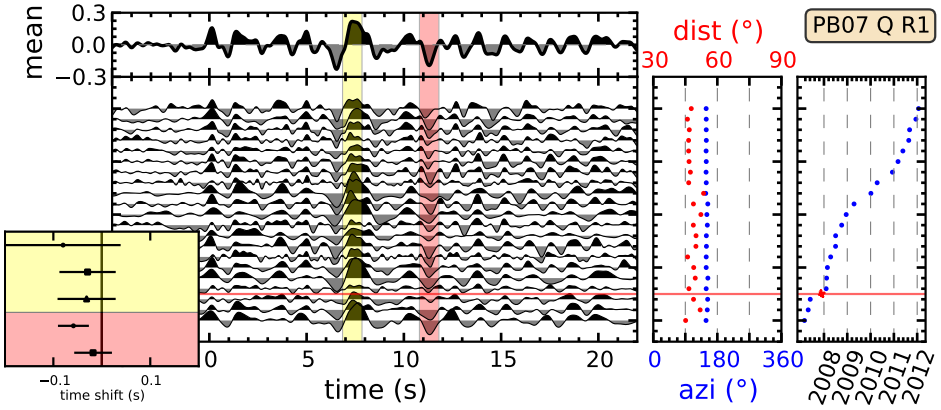
mean
0.3
0.0
−0.3
dist (°)
30
60
90
PB07 Q R1
−0.1
0.1
time shift (s)
0
5
10
15
20
time (s)
0
180
360
azi (°)
2008
2009
2010
2011
2012

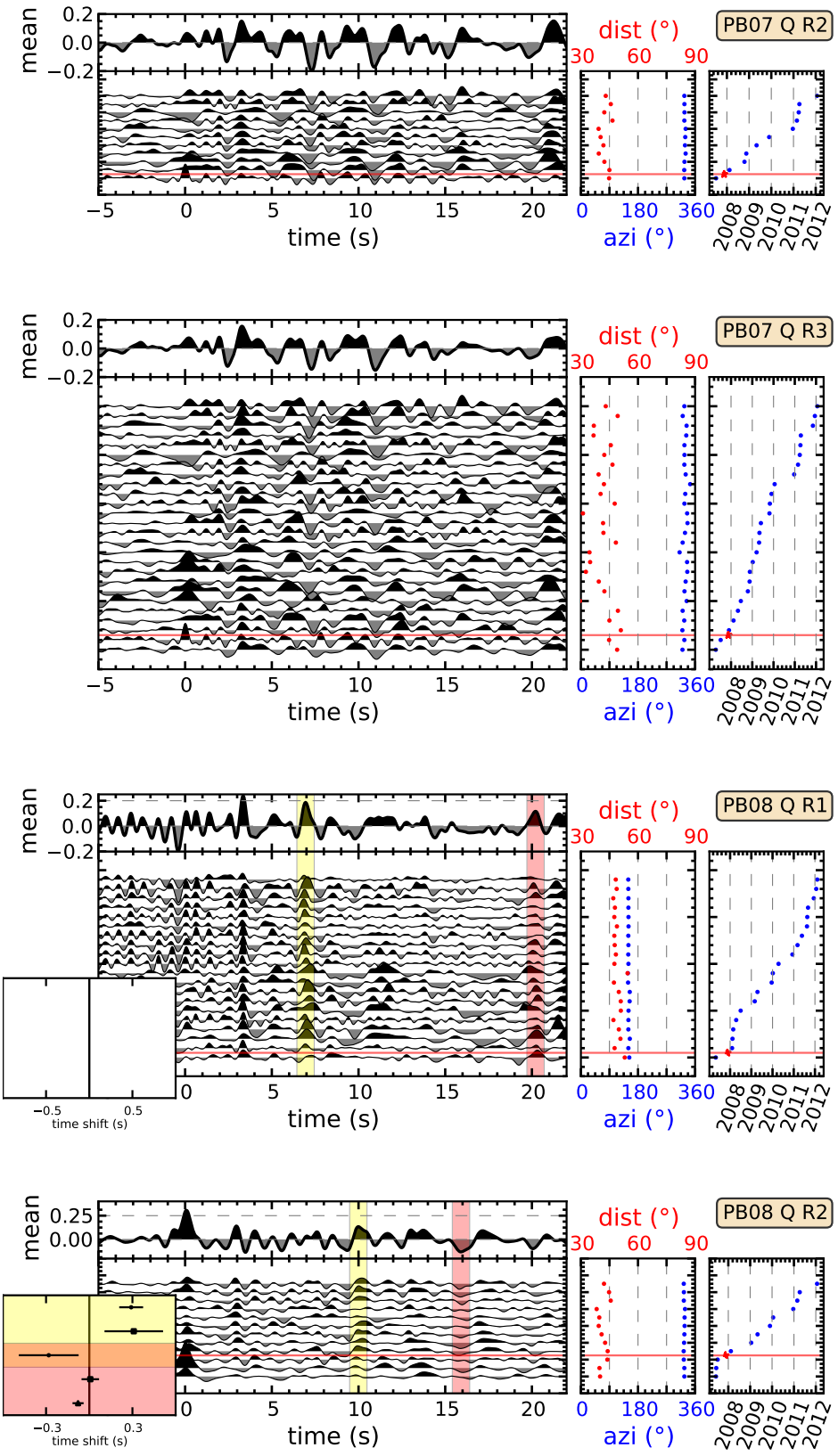
PB07 Q R2
PB07 Q R3
PB08 Q R1
PB08 Q R2
mean
time (s)
dist (°)
azi (°)
time shift (s)

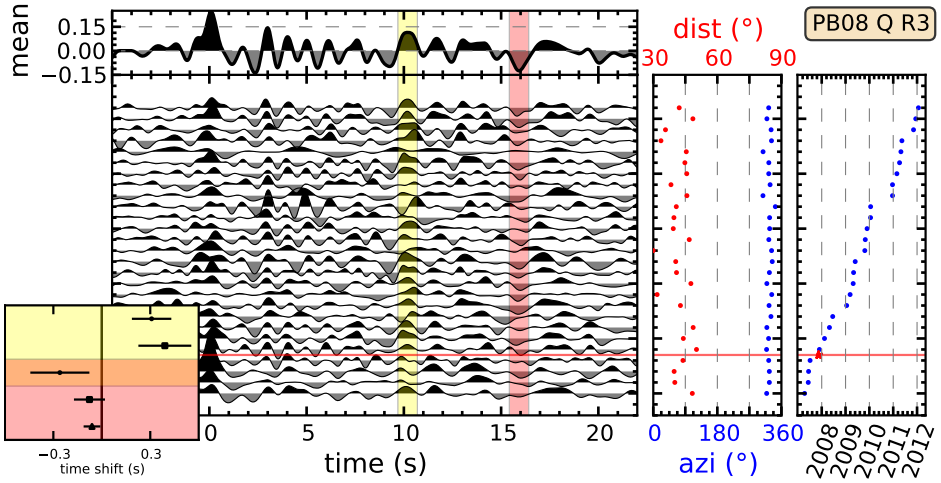

station region	phase	method	time shift (s) and number of traces before Tocopilla event	after Tocopilla event	difference	rel. diff. (%)
PB01 R1	1.55 s (+)	maxima	-0.009 ± 0.009 (9)	0.004 ± 0.006 (28)	0.012 ± 0.015	0.80 ± 0.95
		correlation	-0.006 ± 0.006 (9)	0.001 ± 0.003 (28)	0.007 ± 0.010	0.47 ± 0.63
		cor. above 0.95	-0.006 ± 0.006 (9)	-0.001 ± 0.003 (24)	0.005 ± 0.010	0.32 ± 0.64
	5.07 s (+)	maxima	-0.027 ± 0.061 (9)	0.004 ± 0.022 (28)	0.031 ± 0.083	0.61 ± 1.63
		correlation	-0.020 ± 0.016 (9)	-0.028 ± 0.012 (28)	-0.008 ± 0.029	-0.16 ± 0.57
		cor. above 0.80	-0.012 ± 0.013 (6)	-0.041 ± 0.006 (20)	-0.029 ± 0.019	-0.57 ± 0.37
	8.88 s (+)	maxima	-0.033 ± 0.015 (9)	-0.044 ± 0.015 (28)	-0.011 ± 0.030	-0.12 ± 0.34
		correlation	0.002 ± 0.013 (9)	-0.001 ± 0.010 (28)	-0.003 ± 0.023	-0.03 ± 0.26
		cor. above 0.85	0.017 ± 0.010 (7)	-0.001 ± 0.013 (22)	-0.019 ± 0.023	-0.21 ± 0.25
	15.59 s (+)	maxima	0.058 ± 0.080 (9)	0.011 ± 0.020 (28)	-0.047 ± 0.100	-0.30 ± 0.64
		correlation	0.078 ± 0.054 (9)	0.011 ± 0.013 (28)	-0.068 ± 0.067	-0.43 ± 0.43
		cor. above 0.90	0.093 ± 0.055 (5)	0.017 ± 0.013 (22)	-0.076 ± 0.068	-0.49 ± 0.44
PB01 R2	9.13 s (−)	maxima	-0.002 ± 0.042 (6)	-0.018 ± 0.020 (13)	-0.016 ± 0.061	-0.18 ± 0.67
		correlation	0.015 ± 0.035 (6)	0.013 ± 0.023 (13)	-0.001 ± 0.058	-0.01 ± 0.63
		cor. above 0.80	0.030 ± 0.031 (4)	0.013 ± 0.025 (12)	-0.017 ± 0.056	-0.18 ± 0.61
PB01 R3	9.16 s (−)	maxima	-0.013 ± 0.032 (8)	0.023 ± 0.022 (34)	0.035 ± 0.054	0.39 ± 0.58
		correlation	-0.019 ± 0.029 (8)	0.022 ± 0.022 (34)	0.040 ± 0.051	0.44 ± 0.56
		cor. above 0.80	0.021 ± 0.030 (4)	0.026 ± 0.023 (32)	0.005 ± 0.053	0.06 ± 0.58
PB02 R1	4.50 s (+)	maxima	-0.021 ± 0.021 (11)	-0.008 ± 0.018 (20)	0.014 ± 0.040	0.31 ± 0.89
		correlation	0.007 ± 0.015 (11)	0.008 ± 0.017 (20)	0.001 ± 0.032	0.02 ± 0.70
		cor. above 0.90	0.018 ± 0.018 (8)	-0.008 ± 0.011 (12)	-0.026 ± 0.028	-0.57 ± 0.63
	6.38 s (−)	maxima	-0.193 ± 0.064 (11)	-0.107 ± 0.037 (20)	0.086 ± 0.101	1.34 ± 1.59
		correlation	-0.013 ± 0.015 (11)	-0.031 ± 0.018 (20)	-0.017 ± 0.033	-0.27 ± 0.52
		cor. above 0.85	-0.011 ± 0.016 (10)	-0.043 ± 0.026 (13)	-0.032 ± 0.043	-0.50 ± 0.67
	21.15 s (+)	maxima	-0.163 ± 0.073 (11)	-0.053 ± 0.037 (20)	0.110 ± 0.110	0.52 ± 0.52
		correlation	-0.087 ± 0.063 (11)	0.028 ± 0.037 (20)	0.115 ± 0.101	0.54 ± 0.48
		cor. above 0.90	-0.152 ± 0.047 (6)	0.032 ± 0.036 (14)	0.184 ± 0.083	0.87 ± 0.39
PB02 R2	3.86 s (+)	maxima	0.028 ± 0.039 (3)	-0.007 ± 0.032 (12)	-0.035 ± 0.071	-0.91 ± 1.83
		correlation	0.049 ± 0.018 (3)	-0.001 ± 0.032 (12)	-0.050 ± 0.050	-1.30 ± 1.30
		cor. above 0.85	0.049 ± 0.018 (3)	-0.018 ± 0.042 (8)	-0.067 ± 0.061	-1.73 ± 1.58
	6.82 s (+)	maxima	0.049 ± 0.137 (3)	-0.040 ± 0.059 (12)	-0.089 ± 0.197	-1.30 ± 2.88
		correlation	0.031 ± 0.055 (3)	0.015 ± 0.035 (12)	-0.016 ± 0.089	-0.23 ± 1.31
		cor. above 0.95	0.031 ± 0.055 (3)	0.062 ± 0.030 (8)	0.031 ± 0.085	0.45 ± 1.24
PB02 R3	3.82 s (+)	maxima	0.063 ± 0.024 (5)	-0.079 ± 0.040 (27)	-0.141 ± 0.063	-3.71 ± 1.66
		correlation	0.084 ± 0.026 (5)	-0.030 ± 0.030 (27)	-0.114 ± 0.056	-2.98 ± 1.47
		cor. above 0.90	0.079 ± 0.045 (3)	-0.102 ± 0.037 (14)	-0.181 ± 0.082	-4.75 ± 2.14
	6.86 s (+)	maxima	-0.115 ± 0.108 (5)	-0.105 ± 0.066 (27)	0.010 ± 0.173	0.15 ± 2.53
		correlation	0.038 ± 0.027 (5)	0.013 ± 0.064 (27)	-0.025 ± 0.090	-0.36 ± 1.31
		cor. above 0.85	0.039 ± 0.034 (4)	0.031 ± 0.044 (14)	-0.008 ± 0.079	-0.12 ± 1.15

stat./reg.	phase	method	before event (s)	after event (s)	difference (s)	rel. diff. (%)
PB03 R1	7.86 s (+)	maxima	0.036 ± 0.026 (9)	−0.007 ± 0.018 (19)	−0.043 ± 0.044	−0.55 ± 0.56
		correlation	0.021 ± 0.015 (9)	−0.018 ± 0.011 (19)	−0.039 ± 0.026	−0.50 ± 0.33
		cor. above 0.95	0.021 ± 0.015 (9)	−0.021 ± 0.012 (17)	−0.043 ± 0.026	−0.55 ± 0.34
	19.16 s (+)	maxima	0.014 ± 0.080 (9)	0.091 ± 0.065 (19)	0.076 ± 0.145	0.40 ± 0.76
		correlation	−0.045 ± 0.087 (9)	0.026 ± 0.059 (19)	0.070 ± 0.147	0.37 ± 0.76
		cor. above 0.90	0.098 ± 0.049 (4)	−0.086 ± 0.066 (10)	−0.184 ± 0.116	−0.96 ± 0.60
PB03 R2	7.20 s (+)	maxima	0.058 ± 0.034 (3)	−0.019 ± 0.014 (8)	−0.077 ± 0.048	−1.06 ± 0.67
		correlation	0.021 ± 0.017 (3)	−0.043 ± 0.019 (8)	−0.064 ± 0.037	−0.89 ± 0.51
		cor. above 0.90	0.012 ± 0.025 (2)	−0.032 ± 0.020 (5)	−0.044 ± 0.045	−0.61 ± 0.63
	11.52 s (−)	maxima	0.097 ± 0.056 (3)	−0.033 ± 0.057 (8)	−0.129 ± 0.113	−1.12 ± 0.98
		correlation	0.037 ± 0.012 (3)	−0.022 ± 0.035 (8)	−0.060 ± 0.047	−0.52 ± 0.40
		cor. above 0.95	0.047 ± 0.012 (2)	0.066 ± 0.016 (4)	0.019 ± 0.028	0.16 ± 0.24
	16.66 s (+)	maxima	−0.024 ± 0.072 (3)	0.039 ± 0.064 (8)	0.062 ± 0.136	0.37 ± 0.81
		correlation	−0.026 ± 0.107 (3)	−0.001 ± 0.077 (8)	0.025 ± 0.183	0.15 ± 1.10
		cor. above 0.90	−0.110 ± 0.113 (2)	−0.029 ± 0.100 (6)	0.082 ± 0.212	0.49 ± 1.27
PB03 R3	4.59 s (+)	maxima	−0.003 ± 0.021 (4)	0.004 ± 0.032 (24)	0.008 ± 0.053	0.17 ± 1.15
		correlation	0.005 ± 0.028 (4)	0.048 ± 0.037 (24)	0.043 ± 0.065	0.93 ± 1.42
		cor. above 0.85	0.005 ± 0.028 (4)	0.001 ± 0.034 (12)	−0.004 ± 0.062	−0.08 ± 1.36
	7.21 s (+)	maxima	0.044 ± 0.028 (4)	0.012 ± 0.033 (24)	−0.031 ± 0.060	−0.43 ± 0.84
		correlation	0.063 ± 0.050 (4)	−0.006 ± 0.029 (24)	−0.069 ± 0.079	−0.96 ± 1.09
		cor. above 0.90	0.014 ± 0.010 (3)	−0.017 ± 0.026 (19)	−0.031 ± 0.035	−0.43 ± 0.49
	13.67 s (+)	maxima	−0.154 ± 0.147 (4)	−0.008 ± 0.050 (24)	0.146 ± 0.197	1.07 ± 1.44
		correlation	−0.137 ± 0.101 (4)	0.024 ± 0.048 (24)	0.161 ± 0.149	1.18 ± 1.09
		cor. above 0.95	−0.010 ± 0.019 (2)	0.039 ± 0.023 (15)	0.049 ± 0.042	0.36 ± 0.31
PB04 R1	6.16 s (+)	maxima	0.042 ± 0.055 (11)	0.059 ± 0.018 (20)	0.017 ± 0.073	0.28 ± 1.19
		correlation	−0.023 ± 0.024 (11)	0.025 ± 0.009 (20)	0.047 ± 0.033	0.77 ± 0.54
		cor. above 0.85	−0.038 ± 0.025 (9)	0.026 ± 0.011 (15)	0.064 ± 0.036	1.04 ± 0.58
	12.48 s (−)	maxima	−0.094 ± 0.032 (11)	−0.004 ± 0.032 (20)	0.090 ± 0.064	0.72 ± 0.51
		correlation	−0.068 ± 0.017 (11)	0.011 ± 0.017 (20)	0.080 ± 0.034	0.64 ± 0.27
		cor. above 0.85	−0.084 ± 0.016 (9)	0.010 ± 0.020 (14)	0.094 ± 0.036	0.75 ± 0.29
	15.16 s (+)	maxima	0.041 ± 0.077 (11)	0.074 ± 0.032 (20)	0.033 ± 0.110	0.22 ± 0.72
		correlation	−0.052 ± 0.033 (11)	0.038 ± 0.012 (20)	0.090 ± 0.044	0.59 ± 0.29
		cor. above 0.80	−0.010 ± 0.032 (5)	0.036 ± 0.013 (17)	0.046 ± 0.045	0.30 ± 0.30
PB04 R2	16.23 s (−)	maxima	−0.062 ± 0.064 (2)	0.018 ± 0.069 (8)	0.080 ± 0.133	0.49 ± 0.82
		correlation	0.029 ± 0.011 (2)	0.062 ± 0.058 (8)	0.034 ± 0.069	0.21 ± 0.43
		cor. above 0.95	0.029 ± 0.011 (2)	0.030 ± 0.028 (5)	0.001 ± 0.039	0.01 ± 0.24
PB04 R3	8.59 s (+)	maxima	−0.127 ± 0.075 (3)	0.088 ± 0.052 (19)	0.216 ± 0.126	2.51 ± 1.47
		correlation	−0.089 ± 0.047 (3)	0.102 ± 0.057 (19)	0.191 ± 0.104	2.22 ± 1.21
		cor. above 0.95	−0.087 ± 0.081 (2)	0.023 ± 0.049 (13)	0.110 ± 0.130	1.28 ± 1.51
	16.20 s (−)	maxima	0.048 ± 0.070 (3)	0.011 ± 0.071 (19)	−0.037 ± 0.141	−0.23 ± 0.87
		correlation	0.010 ± 0.023 (3)	−0.037 ± 0.052 (19)	−0.047 ± 0.075	−0.29 ± 0.46
		cor. above 0.90	0.010 ± 0.023 (3)	0.036 ± 0.033 (10)	0.026 ± 0.055	0.16 ± 0.34
PB05 R1	6.00 s (+)	maxima	−0.193 ± 0.089 (8)	−0.212 ± 0.054 (19)	−0.019 ± 0.143	−0.32 ± 2.39
		correlation	−0.026 ± 0.064 (8)	0.018 ± 0.037 (19)	0.044 ± 0.100	0.74 ± 1.67
		cor. above 0.85	0.033 ± 0.018 (4)	0.034 ± 0.011 (13)	0.001 ± 0.029	0.02 ± 0.48
	6.76 s (/)	maxima	0.030 ± 0.159 (8)	0.054 ± 0.067 (19)	0.025 ± 0.227	0.36 ± 3.35
		correlation	0.419 ± 0.131 (8)	0.335 ± 0.089 (19)	−0.084 ± 0.220	−1.24 ± 3.25
		cor. above 0.85	0.550 ± 0.000 (4)	0.550 ± 0.000 (12)	−0.000 ± 0.000	−0.00 ± 0.00
	12.08 s (−)	maxima	−0.225 ± 0.064 (8)	0.000 ± 0.043 (19)	0.225 ± 0.107	1.87 ± 0.88
		correlation	−0.124 ± 0.043 (8)	0.012 ± 0.042 (19)	0.137 ± 0.086	1.13 ± 0.71
		cor. above 0.90	−0.105 ± 0.045 (7)	0.025 ± 0.028 (9)	0.131 ± 0.073	1.08 ± 0.60
	17.45 s (+)	maxima	0.065 ± 0.088 (8)	−0.013 ± 0.053 (19)	−0.078 ± 0.141	−0.45 ± 0.81
		correlation	0.057 ± 0.080 (8)	−0.068 ± 0.035 (19)	−0.125 ± 0.115	−0.72 ± 0.66
		cor. above 0.90	−0.088 ± 0.033 (5)	−0.033 ± 0.023 (14)	0.055 ± 0.056	0.31 ± 0.32
PB05 R2	4.83 s (+)	maxima	−0.012 ± 0.048 (3)	0.012 ± 0.084 (8)	0.024 ± 0.132	0.49 ± 2.73
		correlation	−0.039 ± 0.017 (3)	0.003 ± 0.073 (8)	0.042 ± 0.090	0.87 ± 1.86
		cor. above 0.85	−0.041 ± 0.030 (2)	−0.011 ± 0.019 (6)	0.030 ± 0.049	0.62 ± 1.02
	7.55 s (−)	maxima	0.093 ± 0.217 (3)	0.380 ± 0.028 (8)	0.288 ± 0.245	3.81 ± 3.25
		correlation	−0.205 ± 0.125 (3)	0.014 ± 0.021 (8)	0.219 ± 0.146	2.90 ± 1.94
		cor. above 0.85	−0.028 ± 0.000 (1)	−0.016 ± 0.024 (5)	0.012 ± 0.024	0.16 ± 0.32
	16.95 s (+)	maxima	−0.080 ± 0.036 (3)	−0.117 ± 0.088 (8)	−0.037 ± 0.124	−0.22 ± 0.73
		correlation	−0.116 ± 0.091 (3)	−0.044 ± 0.060 (8)	0.072 ± 0.151	0.43 ± 0.89
		cor. above 0.90	−0.025 ± 0.022 (2)	0.013 ± 0.078 (5)	0.039 ± 0.100	0.23 ± 0.59
PB05 R3	4.84 s (+)	maxima	−0.012 ± 0.048 (3)	0.026 ± 0.054 (21)	0.038 ± 0.102	0.79 ± 2.11
		correlation	−0.037 ± 0.017 (3)	−0.063 ± 0.045 (21)	−0.026 ± 0.061	−0.54 ± 1.27
		cor. above 0.90	−0.012 ± 0.000 (1)	−0.028 ± 0.026 (11)	−0.017 ± 0.026	−0.35 ± 0.53
	12.14 s (−)	maxima	−0.107 ± 0.068 (3)	−0.004 ± 0.041 (21)	0.102 ± 0.109	0.84 ± 0.90

stat./reg.	phase	method	before event (s)	after event (s)	difference (s)	rel. diff. (%)
		correlation	-0.026 ± 0.064 (3)	-0.005 ± 0.040 (21)	0.021 ± 0.104	0.17 ± 0.85
		cor. above 0.95	-0.026 ± 0.064 (3)	0.010 ± 0.029 (14)	0.035 ± 0.093	0.29 ± 0.77
PB06 R1	8.55 s (+)	maxima	-0.025 ± 0.000 (1)	0.094 ± 0.056 (13)	0.119 ± 0.056	1.39 ± 0.65
		correlation	-0.005 ± 0.000 (1)	0.007 ± 0.024 (13)	0.013 ± 0.024	0.15 ± 0.29
		cor. above 0.90	-0.005 ± 0.000 (1)	-0.028 ± 0.018 (10)	-0.023 ± 0.018	-0.27 ± 0.20
	19.06 s (−)	maxima	0.071 ± 0.000 (1)	0.013 ± 0.027 (13)	-0.058 ± 0.027	-0.31 ± 0.14
		correlation	0.001 ± 0.000 (1)	-0.003 ± 0.029 (13)	-0.004 ± 0.029	-0.02 ± 0.15
		cor. above 0.90	0.001 ± 0.000 (1)	0.028 ± 0.033 (8)	0.027 ± 0.033	0.14 ± 0.17
PB06 R2	7.90 s (+)	maxima	-0.009 ± 0.033 (2)	-0.001 ± 0.037 (8)	0.008 ± 0.070	0.11 ± 0.88
		correlation	-0.013 ± 0.015 (2)	-0.005 ± 0.027 (8)	0.007 ± 0.042	0.09 ± 0.53
		cor. above 0.95	-0.013 ± 0.015 (2)	-0.005 ± 0.027 (8)	0.007 ± 0.042	0.09 ± 0.53
	12.26 s (−)	maxima	-0.008 ± 0.016 (2)	-0.004 ± 0.027 (8)	0.004 ± 0.042	0.03 ± 0.34
		correlation	0.002 ± 0.002 (2)	-0.013 ± 0.031 (8)	-0.015 ± 0.033	-0.12 ± 0.27
		cor. above 0.95	0.002 ± 0.002 (2)	0.044 ± 0.032 (4)	0.043 ± 0.035	0.35 ± 0.29
PB06 R3	7.32 s (/)	maxima	0.173 ± 0.072 (3)	0.065 ± 0.030 (21)	-0.108 ± 0.102	-1.48 ± 1.39
		correlation	-0.085 ± 0.011 (3)	-0.059 ± 0.024 (21)	0.026 ± 0.035	0.36 ± 0.48
		cor. above 0.85	-0.085 ± 0.011 (3)	-0.105 ± 0.018 (14)	-0.020 ± 0.029	-0.27 ± 0.40
	7.89 s (+)	maxima	-0.058 ± 0.053 (3)	0.056 ± 0.038 (21)	0.115 ± 0.091	1.46 ± 1.15
		correlation	-0.002 ± 0.015 (3)	0.034 ± 0.036 (21)	0.037 ± 0.051	0.46 ± 0.65
		cor. above 0.95	-0.002 ± 0.015 (3)	0.022 ± 0.022 (16)	0.024 ± 0.038	0.30 ± 0.48
	12.25 s (−)	maxima	0.022 ± 0.031 (3)	-0.016 ± 0.027 (21)	-0.038 ± 0.058	-0.31 ± 0.48
		correlation	-0.010 ± 0.011 (3)	0.001 ± 0.031 (21)	0.010 ± 0.042	0.08 ± 0.34
		cor. above 0.90	-0.010 ± 0.011 (3)	0.018 ± 0.020 (13)	0.028 ± 0.031	0.23 ± 0.26
PB07 R1	7.35 s (+)	maxima	0.135 ± 0.084 (3)	0.055 ± 0.035 (18)	-0.080 ± 0.119	-1.09 ± 1.62
		correlation	0.009 ± 0.042 (3)	-0.020 ± 0.016 (18)	-0.029 ± 0.058	-0.40 ± 0.79
		cor. above 0.90	0.009 ± 0.042 (3)	-0.022 ± 0.018 (15)	-0.031 ± 0.060	-0.43 ± 0.82
	11.30 s (−)	maxima	0.050 ± 0.014 (3)	-0.009 ± 0.017 (18)	-0.059 ± 0.032	-0.52 ± 0.28
		correlation	0.008 ± 0.024 (3)	-0.010 ± 0.015 (18)	-0.018 ± 0.039	-0.16 ± 0.34
		cor. above 0.90	-0.000 ± 0.000 (1)	-0.017 ± 0.018 (13)	-0.017 ± 0.018	-0.15 ± 0.16
PB08 R1	6.95 s (+)	maxima	0.328 ± 0.000 (1)	0.036 ± 0.034 (19)	-0.292 ± 0.034	-4.21 ± 0.49
		correlation	0.015 ± 0.000 (1)	0.011 ± 0.024 (19)	-0.004 ± 0.024	-0.06 ± 0.34
		cor. above 0.85	0.015 ± 0.000 (1)	0.008 ± 0.029 (12)	-0.007 ± 0.029	-0.10 ± 0.42
	20.21 s (+)	maxima	0.115 ± 0.000 (1)	-0.058 ± 0.047 (19)	-0.173 ± 0.047	-0.86 ± 0.23
		correlation	-0.017 ± 0.000 (1)	-0.024 ± 0.038 (19)	-0.007 ± 0.038	-0.03 ± 0.19
		cor. above 0.85	-0.017 ± 0.000 (1)	-0.063 ± 0.028 (11)	-0.046 ± 0.028	-0.23 ± 0.14
PB08 R2	9.99 s (+)	maxima	-0.157 ± 0.014 (3)	0.135 ± 0.069 (9)	0.291 ± 0.083	2.92 ± 0.83
		correlation	-0.226 ± 0.151 (3)	0.083 ± 0.052 (9)	0.309 ± 0.203	3.10 ± 2.03
		cor. above 0.90	0.021 ± 0.000 (1)	0.040 ± 0.027 (7)	0.019 ± 0.027	0.19 ± 0.27
	15.91 s (−)	maxima	0.389 ± 0.136 (3)	0.108 ± 0.072 (9)	-0.281 ± 0.208	-1.77 ± 1.31
		correlation	-0.044 ± 0.016 (3)	-0.036 ± 0.045 (9)	0.007 ± 0.061	0.05 ± 0.38
		cor. above 0.95	-0.038 ± 0.026 (2)	-0.116 ± 0.013 (5)	-0.078 ± 0.039	-0.49 ± 0.24
PB08 R3	10.19 s (+)	maxima	-0.291 ± 0.066 (4)	0.017 ± 0.056 (23)	0.308 ± 0.122	3.03 ± 1.20
		correlation	-0.353 ± 0.118 (4)	0.038 ± 0.046 (23)	0.390 ± 0.164	3.83 ± 1.61
		cor. above 0.90	-0.005 ± 0.000 (1)	0.017 ± 0.046 (17)	0.022 ± 0.046	0.22 ± 0.46
	15.92 s (−)	maxima	0.296 ± 0.134 (4)	0.037 ± 0.049 (23)	-0.260 ± 0.183	-1.63 ± 1.15
		correlation	0.070 ± 0.054 (4)	-0.007 ± 0.042 (23)	-0.076 ± 0.096	-0.48 ± 0.60
		cor. above 0.95	0.018 ± 0.034 (2)	-0.043 ± 0.017 (13)	-0.061 ± 0.052	-0.38 ± 0.33

C. Supplement passive image interferometry

C.1. Examples of daily cross-correlation functions

Some examples of daily cross-correlation functions of the 208 station pairs are plotted here. Data were filtered between 0.01 Hz and 0.5 Hz and prepared as described in section 5.2 before performing the cross-correlation. Daily cross-correlation functions are sorted from early times (bottom) to later times (top). The top panel shows the stack over all daily cross-correlations. The color scale has its maximum at the respective maxima of the stacked cross-correlation multiplied by 1.5 and rounded to the first significant digit. Therefore the color scale is different for each plot. The x-scale (lag time) is also different to account for different interstation distances.

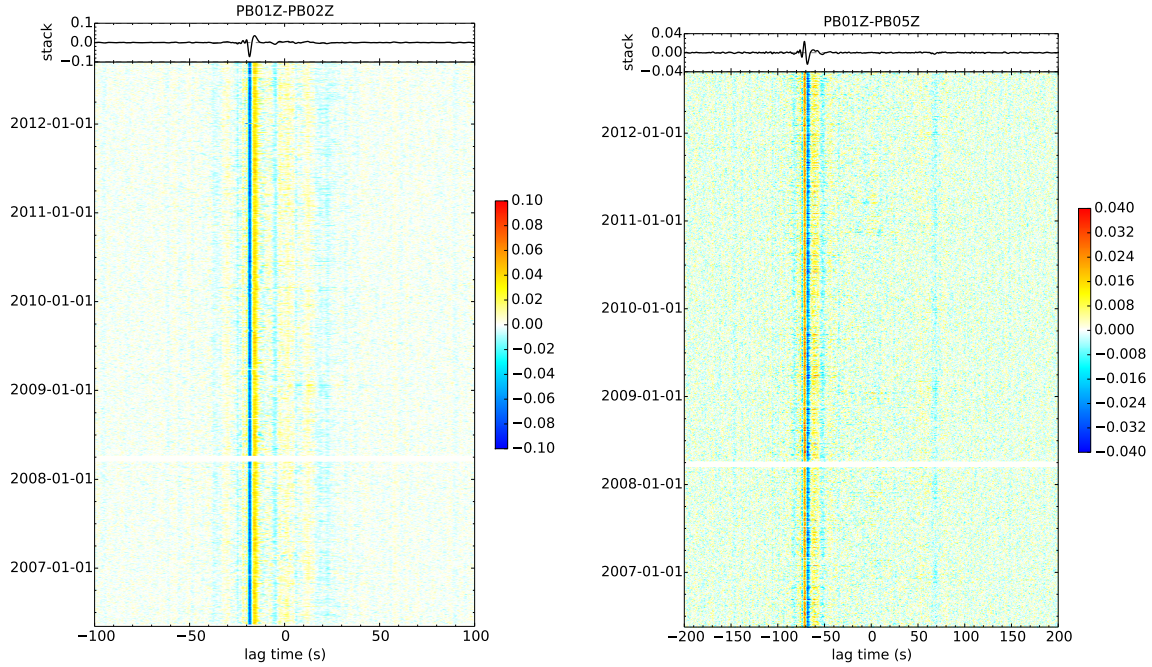

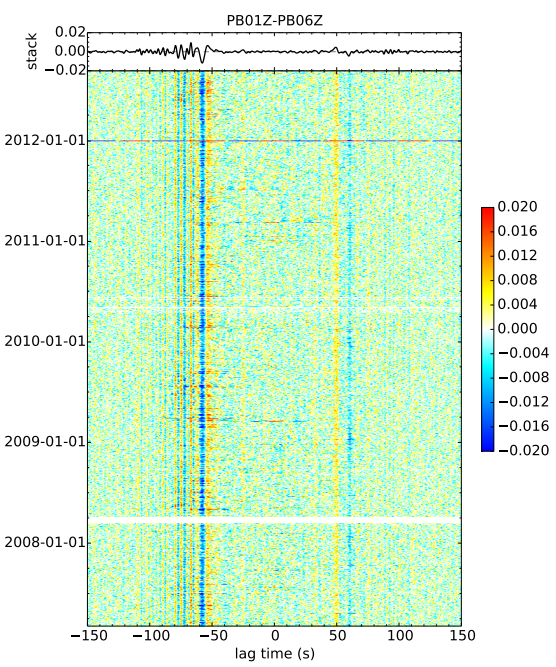
PB01Z-PB06Z
stack
0.02
0.00
−0.02
2012-01-01
2011-01-01
2010-01-01
2009-01-01
2008-01-01
−150 −100 −50 0 50 100 150
lag time (s)
0.020
0.016
0.012
0.008
0.004
0.000
−0.004
−0.008
−0.012
−0.016
−0.020

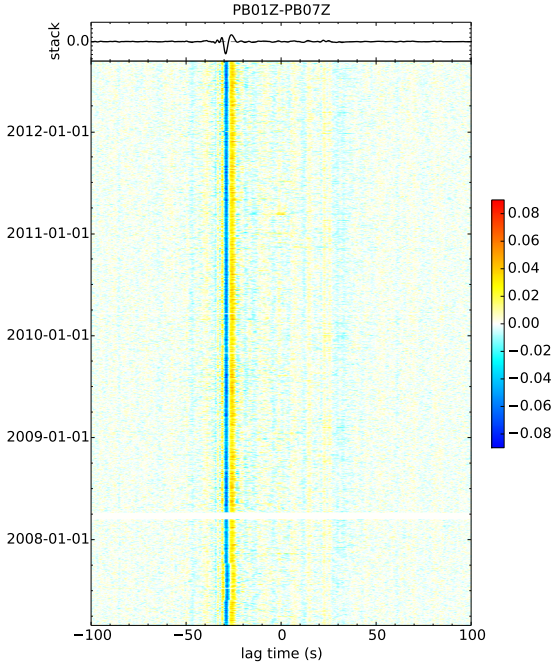
PB01Z-PB07Z
stack
0.0
2012-01-01
2011-01-01
2010-01-01
2009-01-01
2008-01-01
−100 −50 0 50 100
lag time (s)
0.08
0.06
0.04
0.02
0.00
−0.02
−0.04
−0.06
−0.08

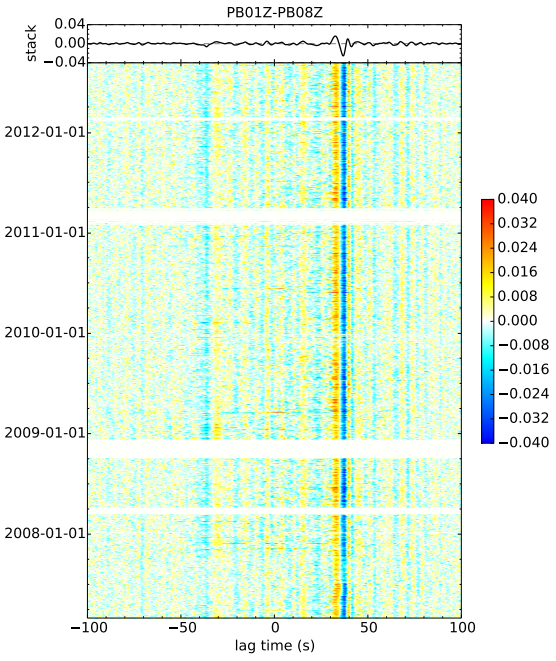
PB01Z-PB08Z
stack
0.04
0.00
−0.04
2012-01-01
2011-01-01
2010-01-01
2009-01-01
2008-01-01
−100 −50 0 50 100
lag time (s)
0.040
0.032
0.024
0.016
0.008
0.000
−0.008
−0.016
−0.024
−0.032
−0.040

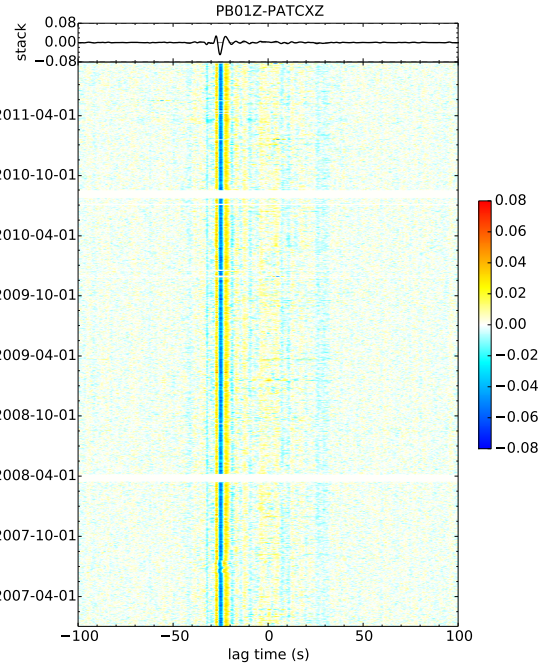
PB01Z-PATCXZ
stack
0.08
0.00
−0.08
2011-04-01
2010-10-01
2010-04-01
2009-10-01
2009-04-01
2008-10-01
2008-04-01
2007-10-01
2007-04-01
−100 −50 0 50 100
lag time (s)
0.08
0.06
0.04
0.02
0.00
−0.02
−0.04
−0.06
−0.08

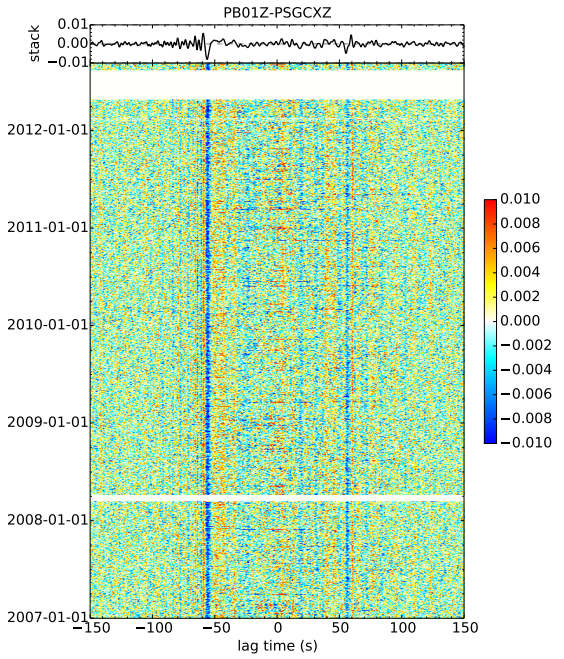
PB01Z-PSGCXZ
stack
0.01
0.00
−0.01
2012-01-01
2011-01-01
2010-01-01
2009-01-01
2008-01-01
2007-01-01
−150 −100 −50 0 50 100 150
lag time (s)
0.010
0.008
0.006
0.004
0.002
0.000
−0.002
−0.004
−0.006
−0.008
−0.010

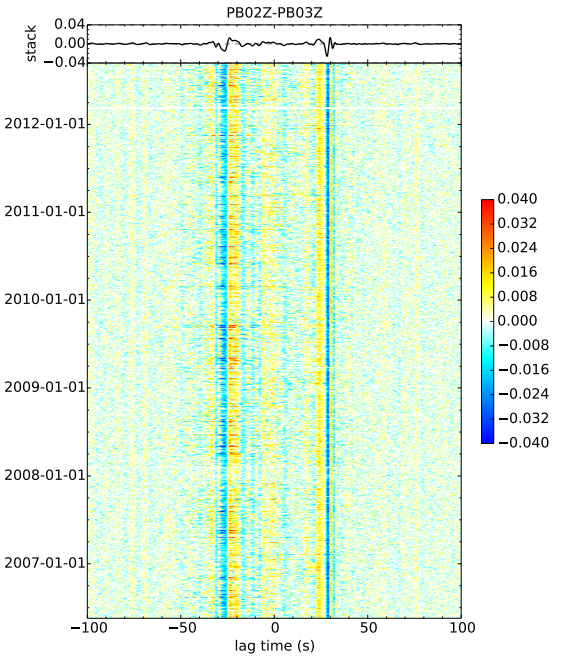
PB02Z-PB03Z
stack
0.04
0.00
−0.04
2012-01-01
2011-01-01
2010-01-01
2009-01-01
2008-01-01
2007-01-01
−100 −50 0 50 100
lag time (s)
0.040
0.032
0.024
0.016
0.008
0.000
−0.008
−0.016
−0.024
−0.032
−0.040

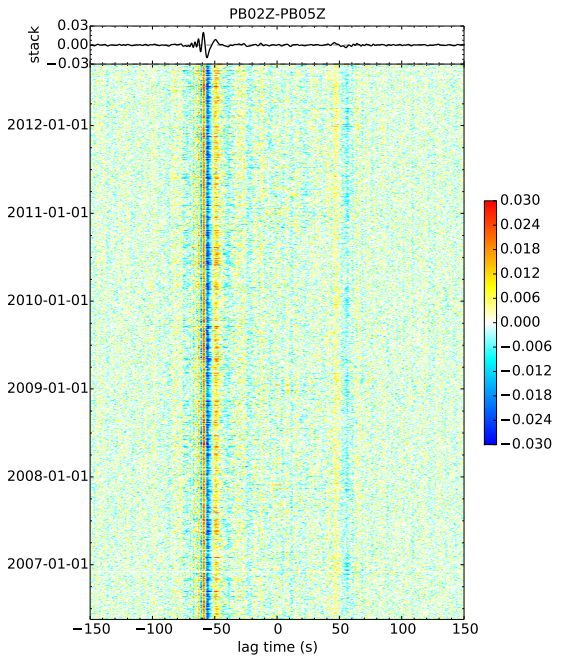
PB02Z-PB05Z
stack
0.03
0.00
−0.03
2012-01-01
2011-01-01
2010-01-01
2009-01-01
2008-01-01
2007-01-01
−150 −100 −50 0 50 100 150
lag time (s)
0.030
0.024
0.018
0.012
0.006
0.000
−0.006
−0.012
−0.018
−0.024
−0.030

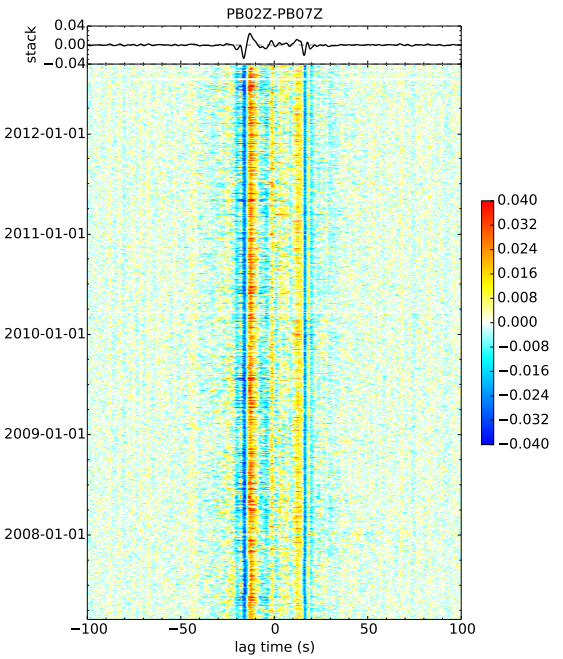
PB02Z-PB07Z
stack
0.04
0.00
−0.04
2012-01-01
2011-01-01
2010-01-01
2009-01-01
2008-01-01
−100 −50 0 50 100
lag time (s)
0.040
0.032
0.024
0.016
0.008
0.000
−0.008
−0.016
−0.024
−0.032
−0.040

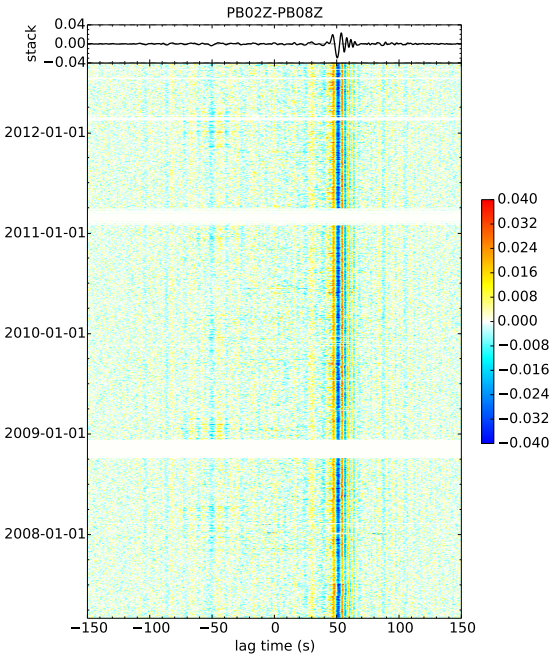
PB02Z-PB08Z
stack
0.04
0.00
−0.04
2012-01-01
2011-01-01
2010-01-01
2009-01-01
2008-01-01
−150
−100
−50
0
50
100
150
lag time (s)
0.040
0.032
0.024
0.016
0.008
0.000
−0.008
−0.016
−0.024
−0.032
−0.040

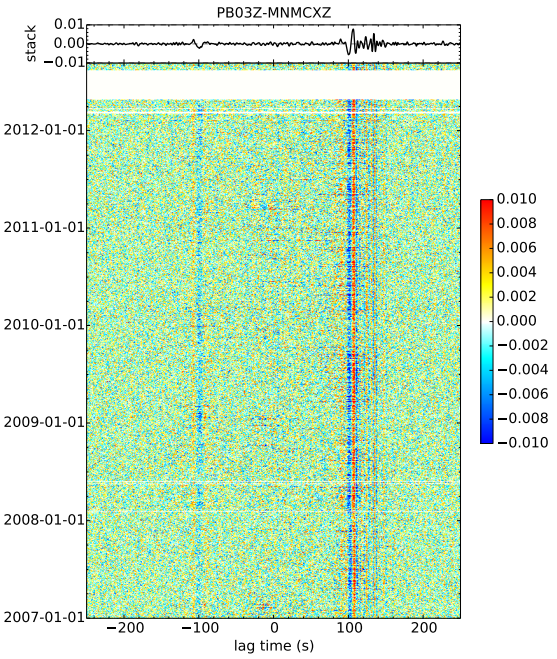
PB03Z-MNMCXZ
stack
0.01
0.00
−0.01
2012-01-01
2011-01-01
2010-01-01
2009-01-01
2008-01-01
2007-01-01
−200
−100
0
100
200
lag time (s)
0.010
0.008
0.006
0.004
0.002
0.000
−0.002
−0.004
−0.006
−0.008
−0.010

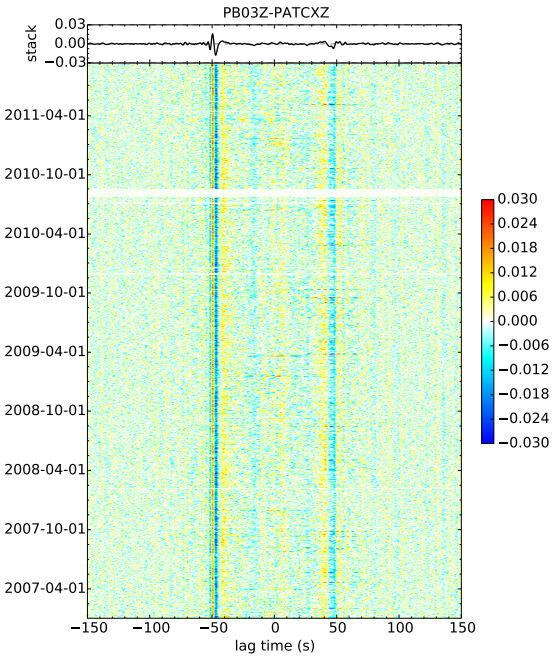
PB03Z-PATCXZ
stack
0.03
0.00
−0.03
2011-04-01
2010-10-01
2010-04-01
2009-10-01
2009-04-01
2008-10-01
2008-04-01
2007-10-01
2007-04-01
−150
−100
−50
0
50
100
150
lag time (s)
0.030
0.024
0.018
0.012
0.006
0.000
−0.006
−0.012
−0.018
−0.024
−0.030

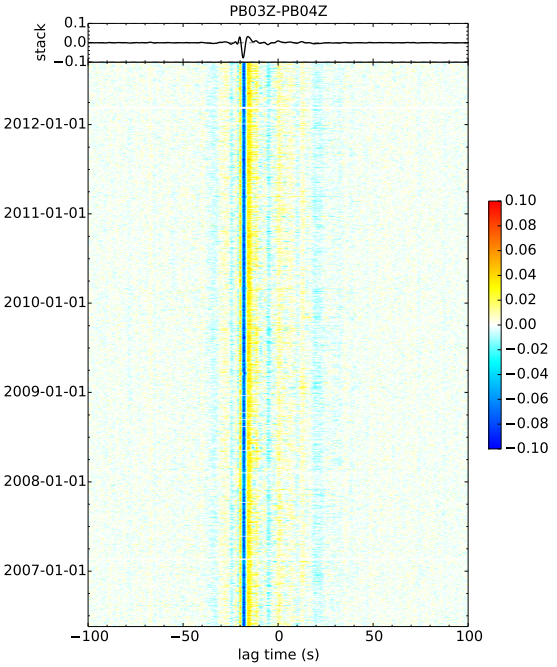
PB03Z-PB04Z
stack
0.1
0.0
−0.1
2012-01-01
2011-01-01
2010-01-01
2009-01-01
2008-01-01
2007-01-01
−100
−50
0
50
100
lag time (s)
0.10
0.08
0.06
0.04
0.02
0.00
−0.02
−0.04
−0.06
−0.08
−0.10

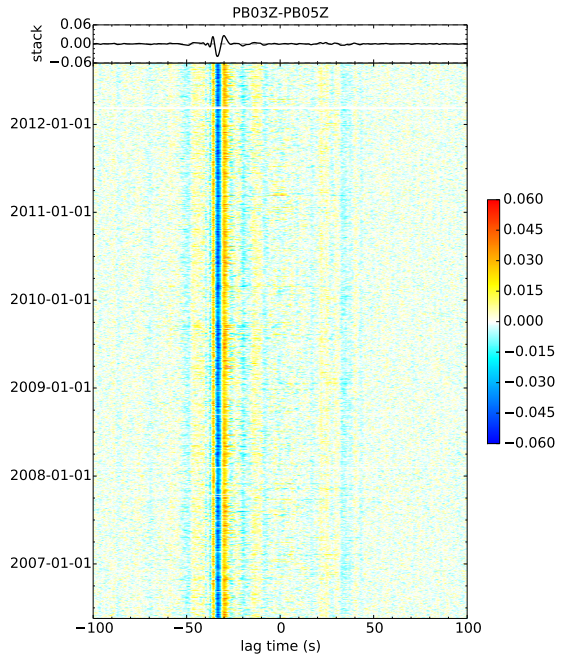
PB03Z-PB05Z
stack
0.06
0.00
−0.06
2012-01-01
2011-01-01
2010-01-01
2009-01-01
2008-01-01
2007-01-01
−100
−50
0
50
100
lag time (s)
0.060
0.045
0.030
0.015
0.000
−0.015
−0.030
−0.045
−0.060

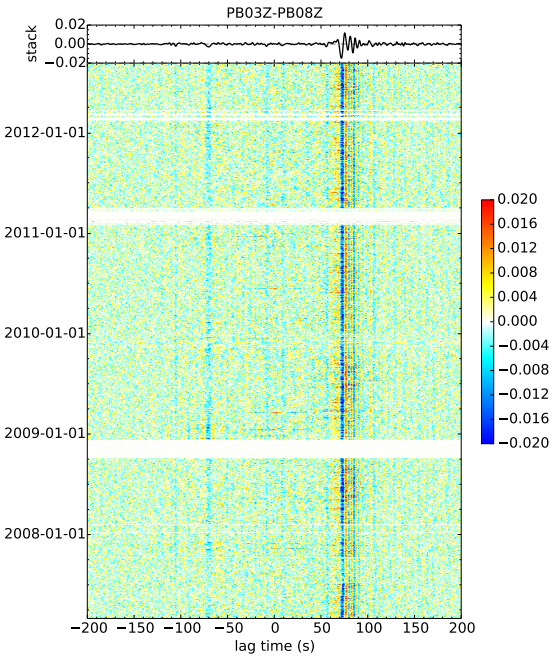
PB03Z-PB08Z
stack
0.02
0.00
−0.02
2012-01-01
2011-01-01
2010-01-01
2009-01-01
2008-01-01
−200
−150
−100
−50
0
50
100
150
200
lag time (s)
0.020
0.016
0.012
0.008
0.004
0.000
−0.004
−0.008
−0.012
−0.016
−0.020

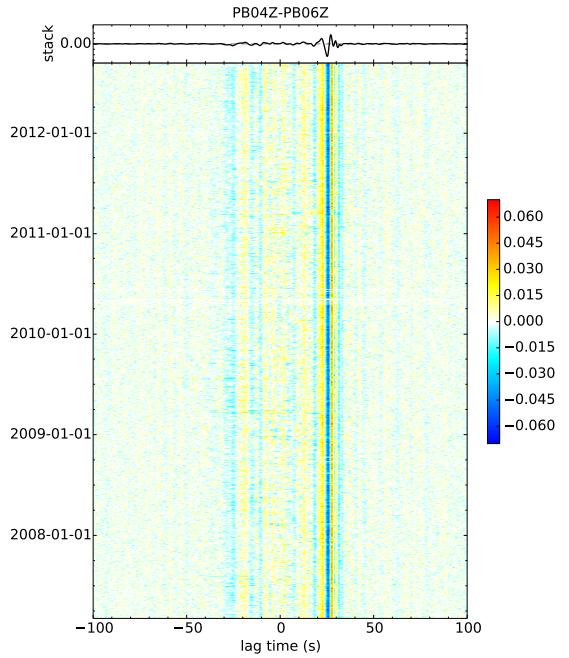
PB04Z-PB06Z
stack
0.00
2012-01-01
2011-01-01
2010-01-01
2009-01-01
2008-01-01
−100
−50
0
50
100
lag time (s)
0.060
0.045
0.030
0.015
0.000
−0.015
−0.030
−0.045
−0.060

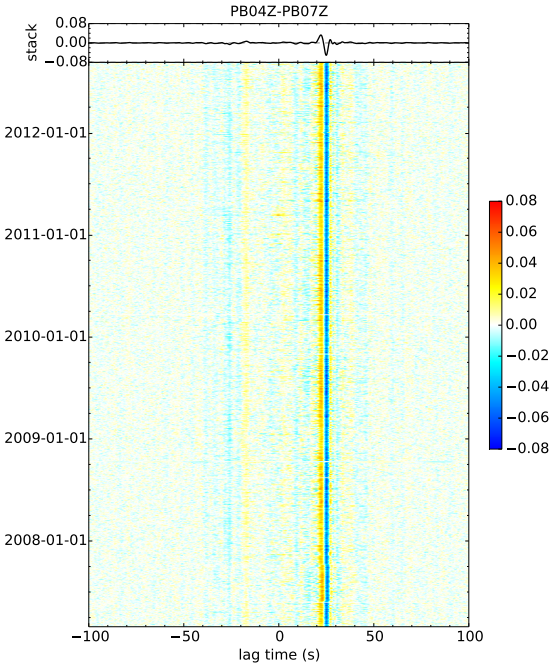
PB04Z-PB07Z
stack
0.08
0.00
−0.08
2012-01-01
2011-01-01
2010-01-01
2009-01-01
2008-01-01
−100
−50
0
50
100
lag time (s)
0.08
0.06
0.04
0.02
0.00
−0.02
−0.04
−0.06
−0.08

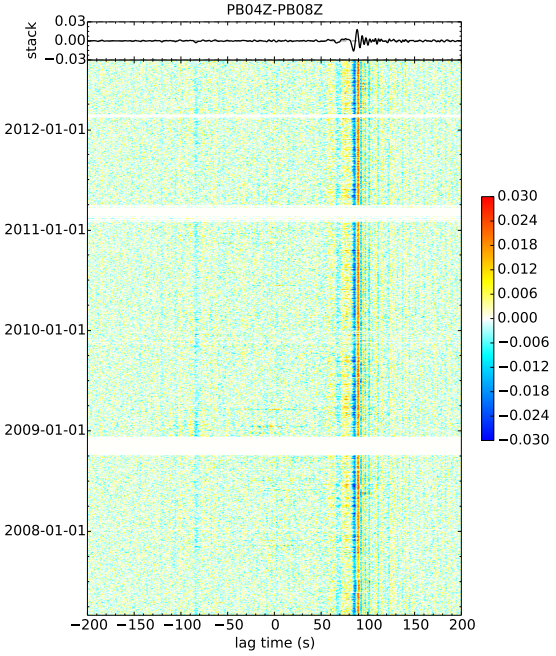
PB04Z-PB08Z
stack
0.03
0.00
−0.03
2012-01-01
2011-01-01
2010-01-01
2009-01-01
2008-01-01
0.030
0.024
0.018
0.012
0.006
0.000
−0.006
−0.012
−0.018
−0.024
−0.030
−200 −150 −100 −50 0 50 100 150 200
lag time (s)

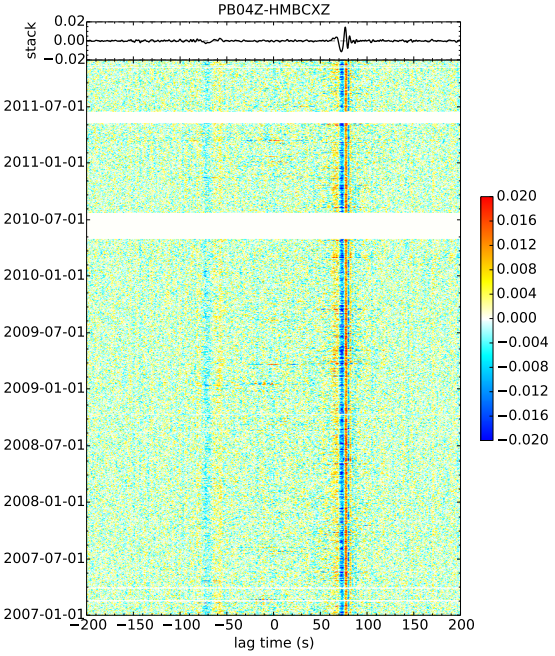
PB04Z-HMBCXZ
stack
0.02
0.00
−0.02
2011-07-01
2011-01-01
2010-07-01
2010-01-01
2009-07-01
2009-01-01
2008-07-01
2008-01-01
2007-07-01
2007-01-01
0.020
0.016
0.012
0.008
0.004
0.000
−0.004
−0.008
−0.012
−0.016
−0.020
−200 −150 −100 −50 0 50 100 150 200
lag time (s)

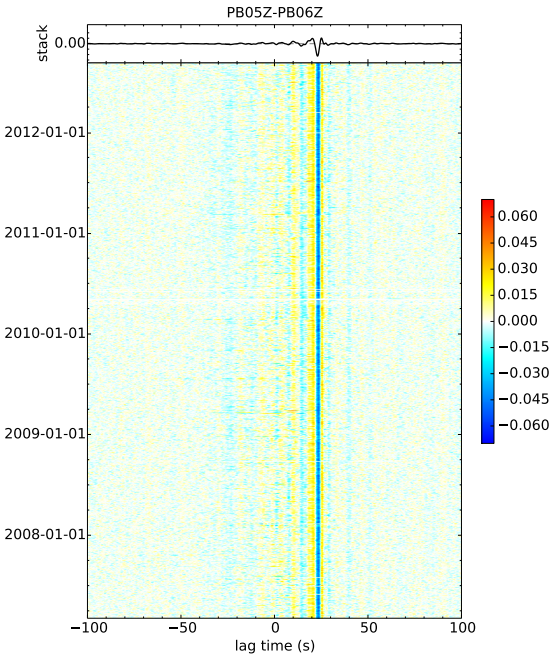
PB05Z-PB06Z
stack
0.00
2012-01-01
2011-01-01
2010-01-01
2009-01-01
2008-01-01
0.060
0.045
0.030
0.015
0.000
−0.015
−0.030
−0.045
−0.060
−100 −50 0 50 100
lag time (s)

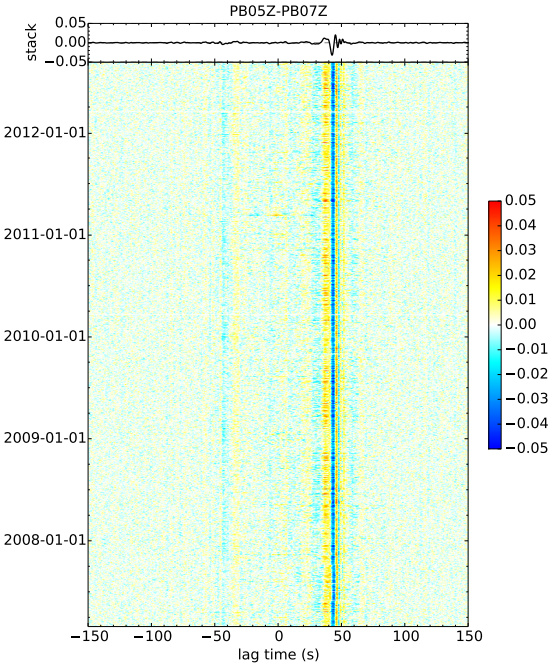
PB05Z-PB07Z
stack
0.05
0.00
−0.05
2012-01-01
2011-01-01
2010-01-01
2009-01-01
2008-01-01
0.05
0.04
0.03
0.02
0.01
0.00
−0.01
−0.02
−0.03
−0.04
−0.05
−150 −100 −50 0 50 100 150
lag time (s)

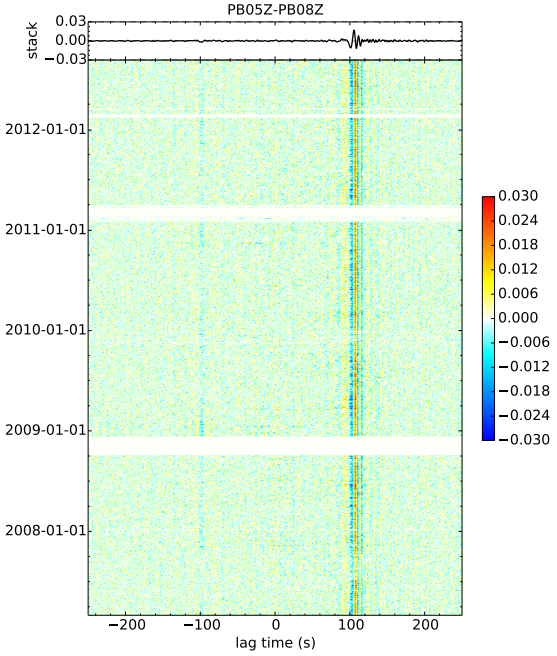
PB05Z-PB08Z
stack
0.03
0.00
−0.03
2012-01-01
2011-01-01
2010-01-01
2009-01-01
2008-01-01
−200
−100
0
100
200
lag time (s)
0.030
0.024
0.018
0.012
0.006
0.000
−0.006
−0.012
−0.018
−0.024
−0.030

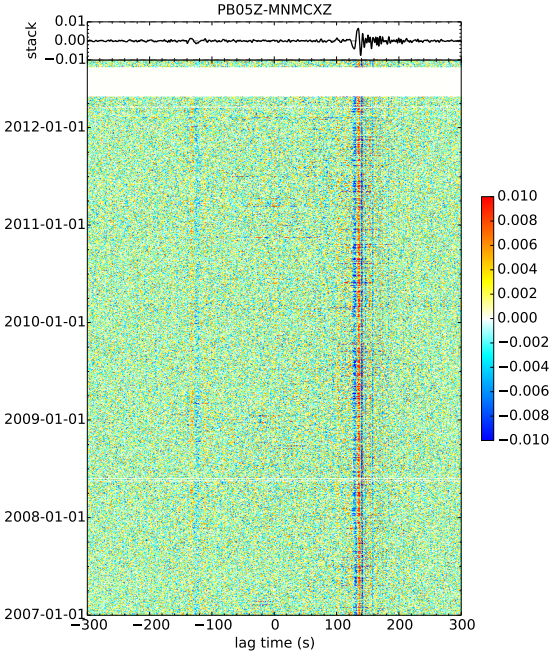
PB05Z-MNMCXZ
stack
0.01
0.00
−0.01
2012-01-01
2011-01-01
2010-01-01
2009-01-01
2008-01-01
2007-01-01
−300
−200
−100
0
100
200
300
lag time (s)
0.010
0.008
0.006
0.004
0.002
0.000
−0.002
−0.004
−0.006
−0.008
−0.010

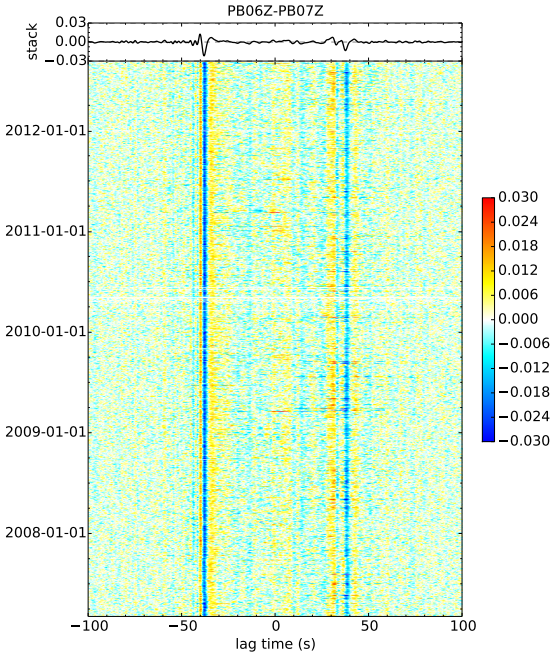
PB06Z-PB07Z
stack
0.03
0.00
−0.03
2012-01-01
2011-01-01
2010-01-01
2009-01-01
2008-01-01
−100
−50
0
50
100
lag time (s)
0.030
0.024
0.018
0.012
0.006
0.000
−0.006
−0.012
−0.018
−0.024
−0.030

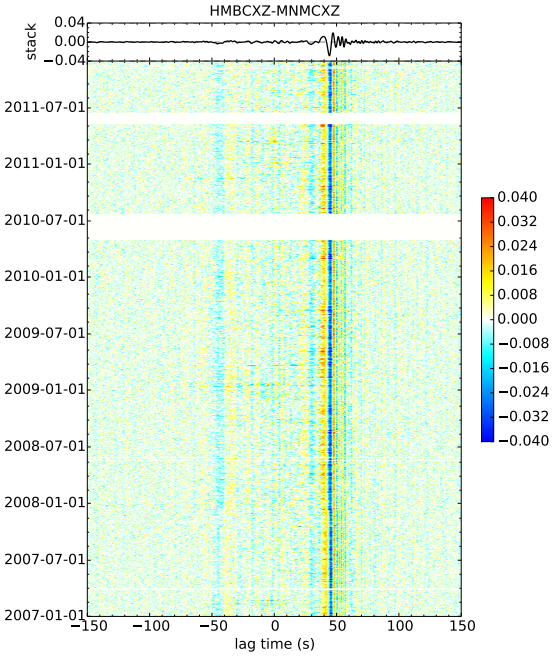
HMBCXZ-MNMCXZ
stack
0.04
0.00
−0.04
2011-07-01
2011-01-01
2010-07-01
2010-01-01
2009-07-01
2009-01-01
2008-07-01
2008-01-01
2007-07-01
2007-01-01
−150
−100
−50
0
50
100
150
lag time (s)
0.040
0.032
0.024
0.016
0.008
0.000
−0.008
−0.016
−0.024
−0.032
−0.040

C.2. Examples of similarity matrices for cross-correlation functions

Similarity matrices for the cross-correlations displayed in appendix C.1 for the time window from 30 s to 110 s behind the direct surface wave for the years 2007 and 2008. They were calculated with the stretching method described in section 5.2. The similarity matrix shows the correlation coefficients for the different stretching factors for every second day. Each column represents a stack over 10 subsequent days. The maxima over time allow to determine the observed apparent velocity change (blue line). Each plot consists of a top panel for the time window of the acausal part of the correlation function and a bottom panel for the causal part. The gray vertical line is drawn at the time of the Tocopilla earthquake. Notice that the plots show velocity decrease $-\epsilon$.

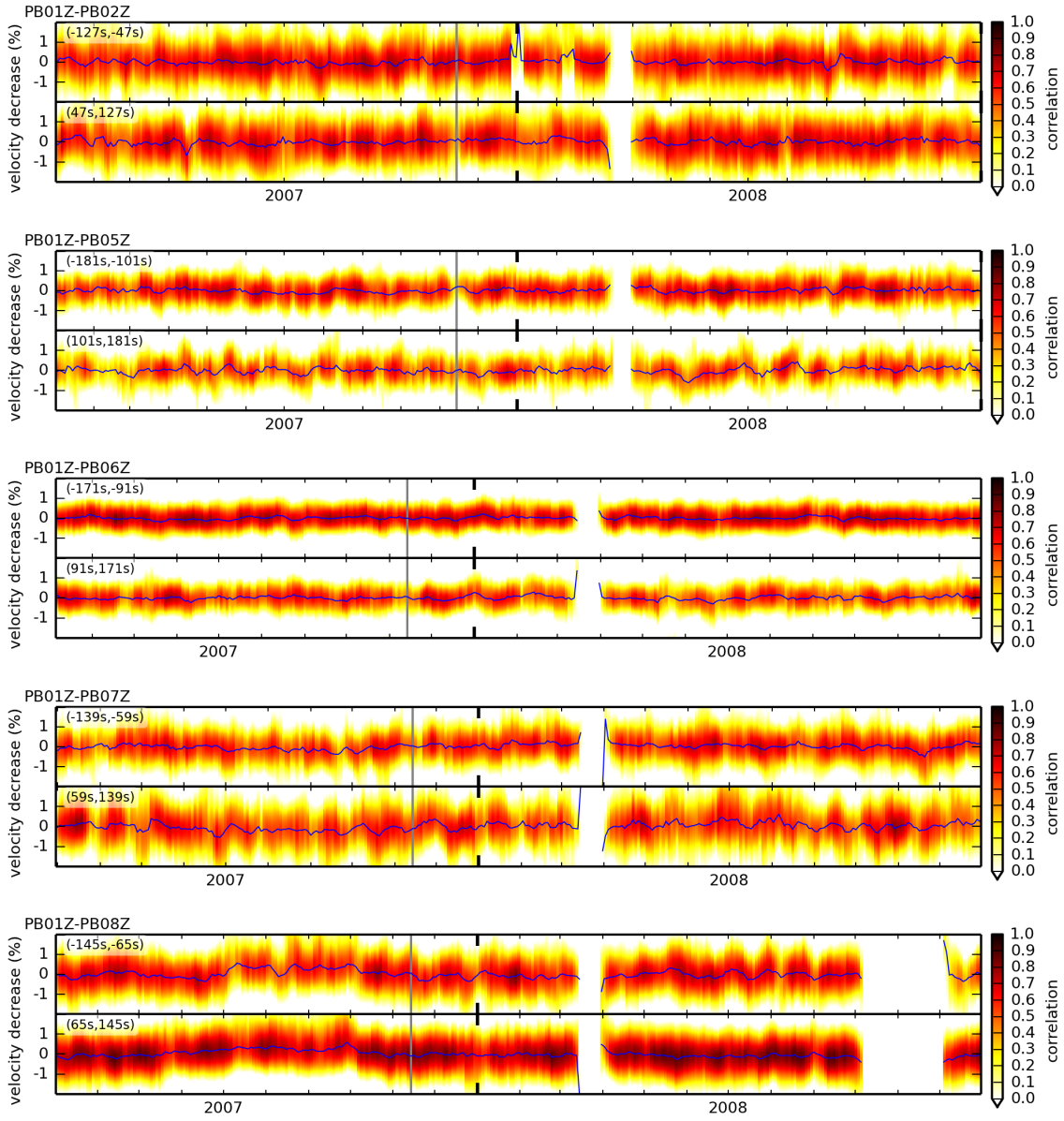

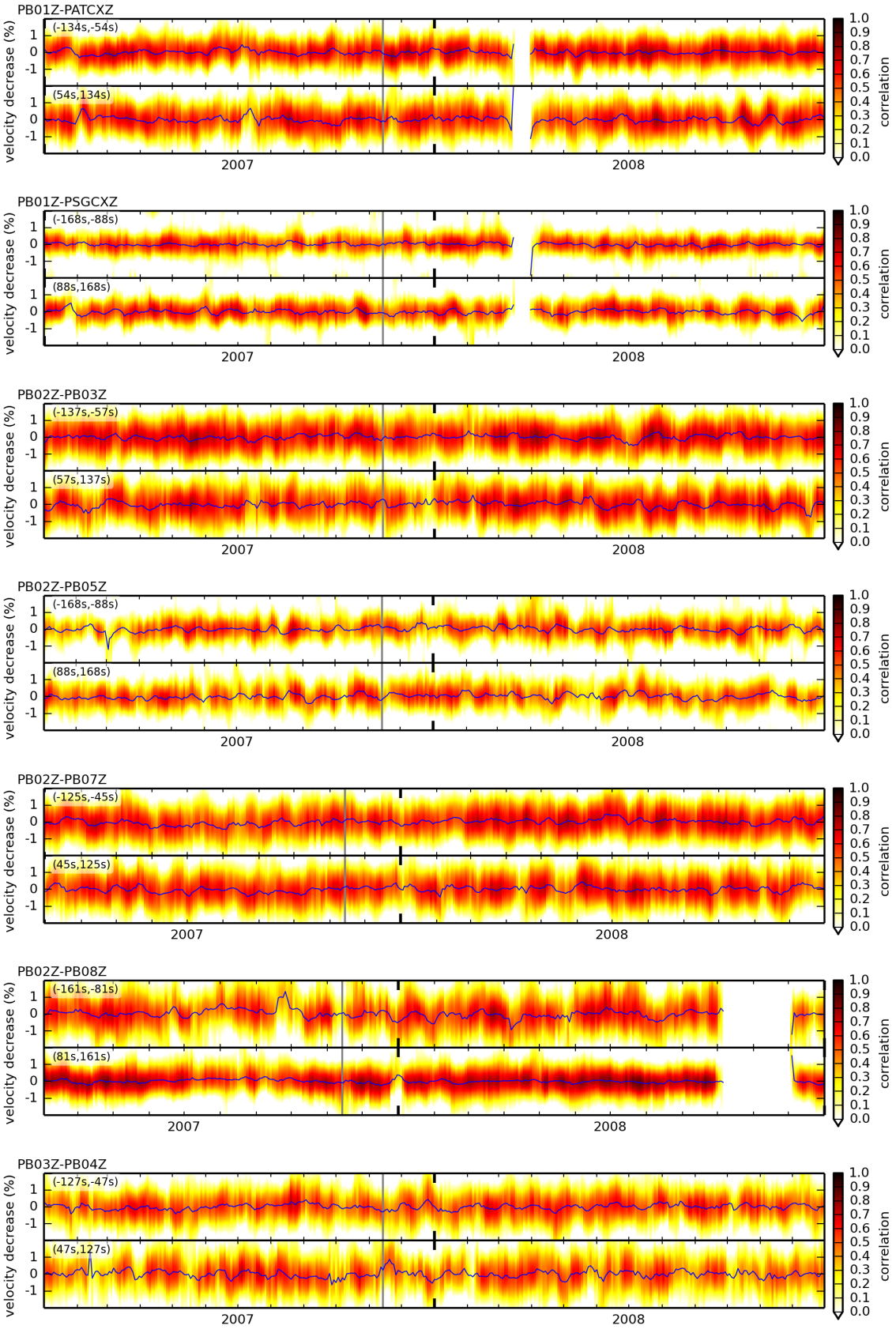
PB01Z-PATCXZ
(-134s,-54s)
(54s,134s)
PB01Z-PSGCXZ
(-168s,-88s)
(88s,168s)
PB02Z-PB03Z
(-137s,-57s)
(57s,137s)
PB02Z-PB05Z
(-168s,-88s)
(88s,168s)
PB02Z-PB07Z
(-125s,-45s)
(45s,125s)
PB02Z-PB08Z
(-161s,-81s)
(81s,161s)
PB03Z-PB04Z
(-127s,-47s)
(47s,127s)
velocity decrease (%)
correlation
2007
2008

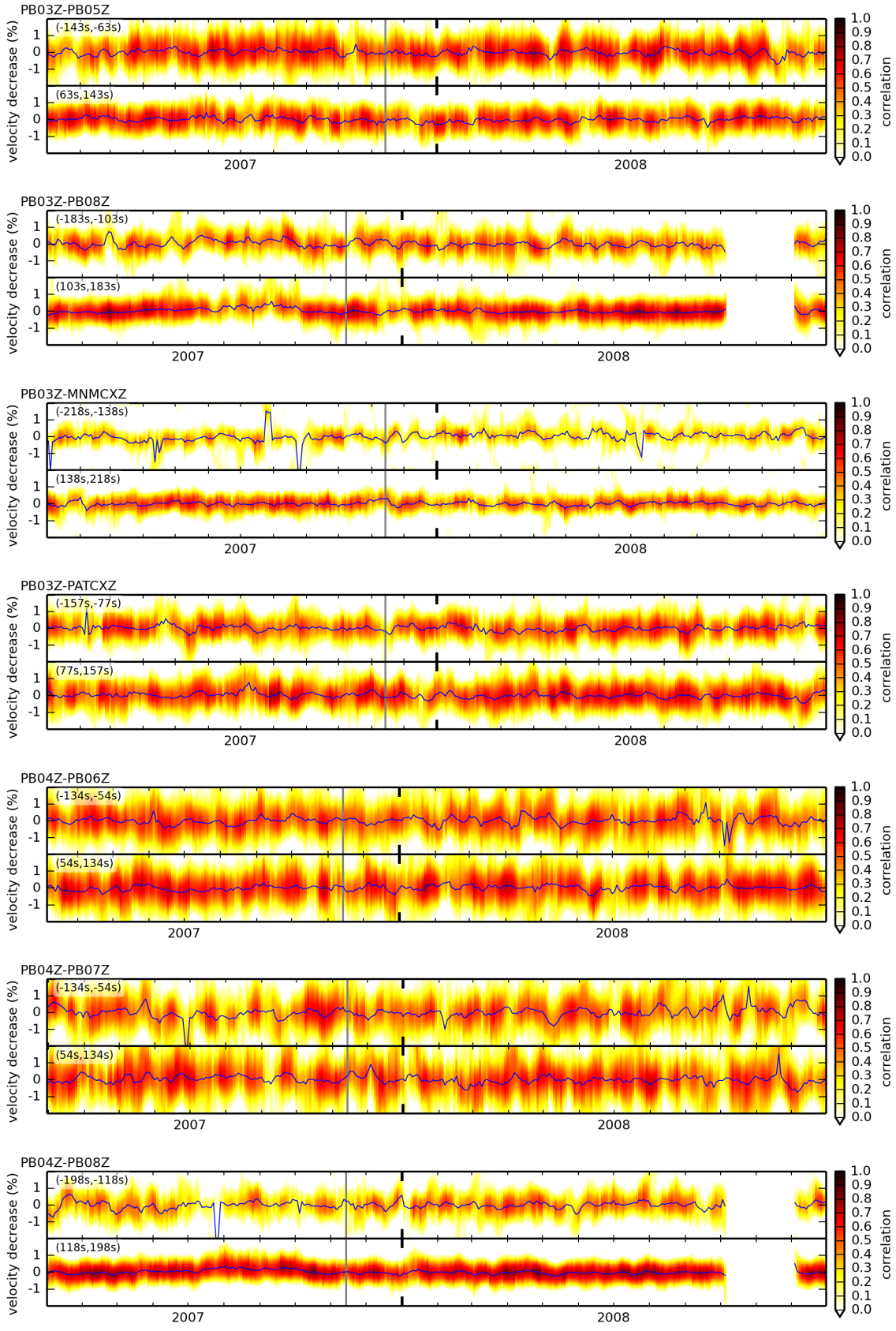
PB03Z-PB05Z
(-143s,-63s)
(63s,143s)
PB03Z-PB08Z
(-183s,-103s)
(103s,183s)
PB03Z-MNMCXZ
(-218s,-138s)
(138s,218s)
PB03Z-PATCXZ
(-157s,-77s)
(77s,157s)
PB04Z-PB06Z
(-134s,-54s)
(54s,134s)
PB04Z-PB07Z
(-134s,-54s)
(54s,134s)
PB04Z-PB08Z
(-198s,-118s)
(118s,198s)
velocity decrease (%)
correlation
2007
2008

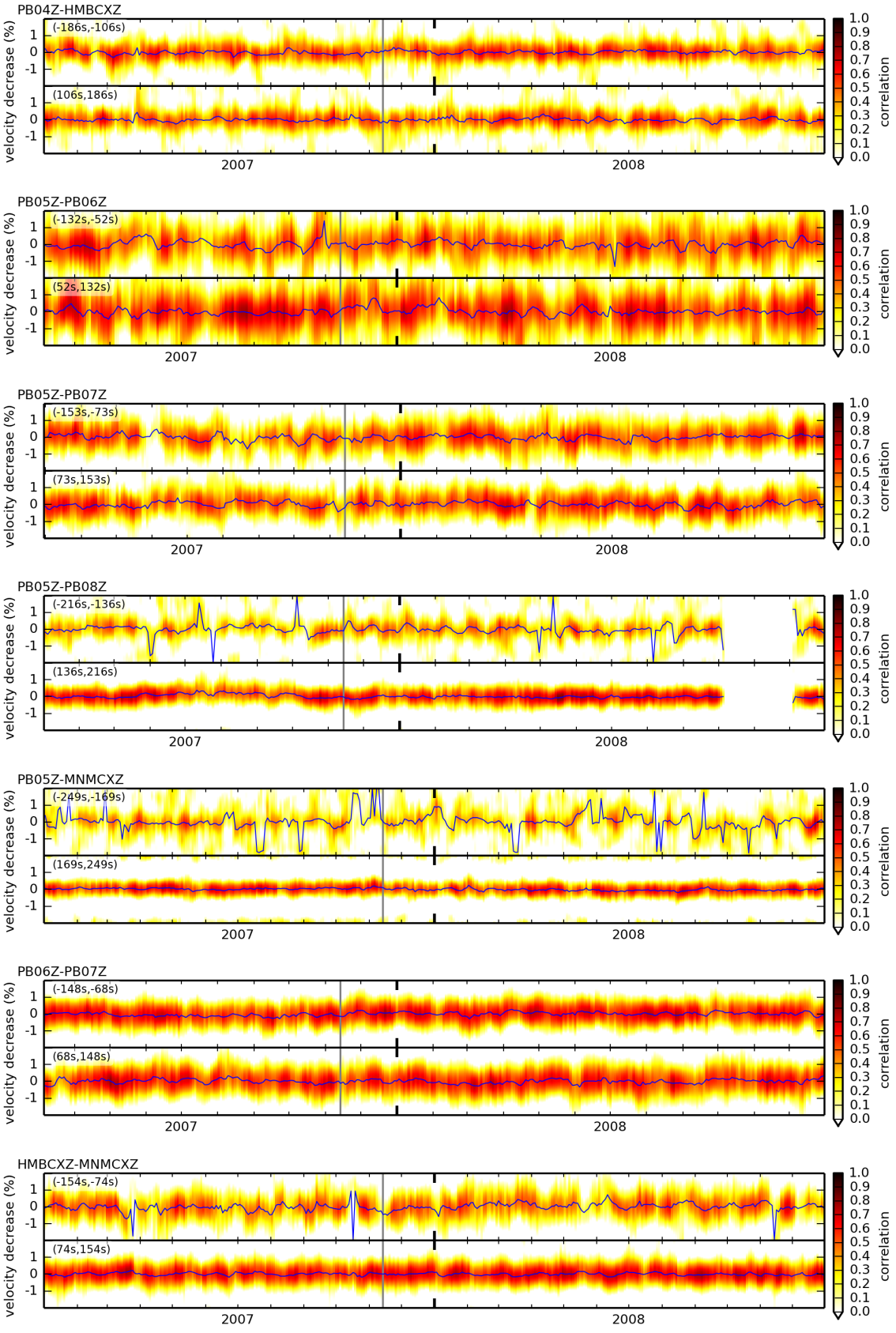
PB04Z-HMBCXZ
(-186s,-106s)
(106s,186s)
PB05Z-PB06Z
(-132s,-52s)
(52s,132s)
PB05Z-PB07Z
(-153s,-73s)
(73s,153s)
PB05Z-PB08Z
(-216s,-136s)
(136s,216s)
PB05Z-MNMCXZ
(-249s,-169s)
(169s,249s)
PB06Z-PB07Z
(-148s,-68s)
(68s,148s)
HMBCXZ-MNMCXZ
(-154s,-74s)
(74s,154s)
velocity decrease (%)
correlation
2007
2008

C.3. Daily autocorrelation functions for different stations in two frequency bands

Daily autocorrelation functions from the 12 IPOC stations installed at the time of the Tocopilla earthquake (PB01-PB08, HMBCX, MNMCX, PATCX and PSGCX) are plotted. The data was filtered in the 1 Hz−3 Hz and 4 Hz−6 Hz frequency bands and prepared as described in section 5.2 before performing the autocorrelation. Daily autocorrelation functions are sorted from early times (bottom) to later times (top). The top panel shows the stack over all daily autocorrelations. The color scale has its maximum at a value of 0.1 to embrace the signal at later lag times.

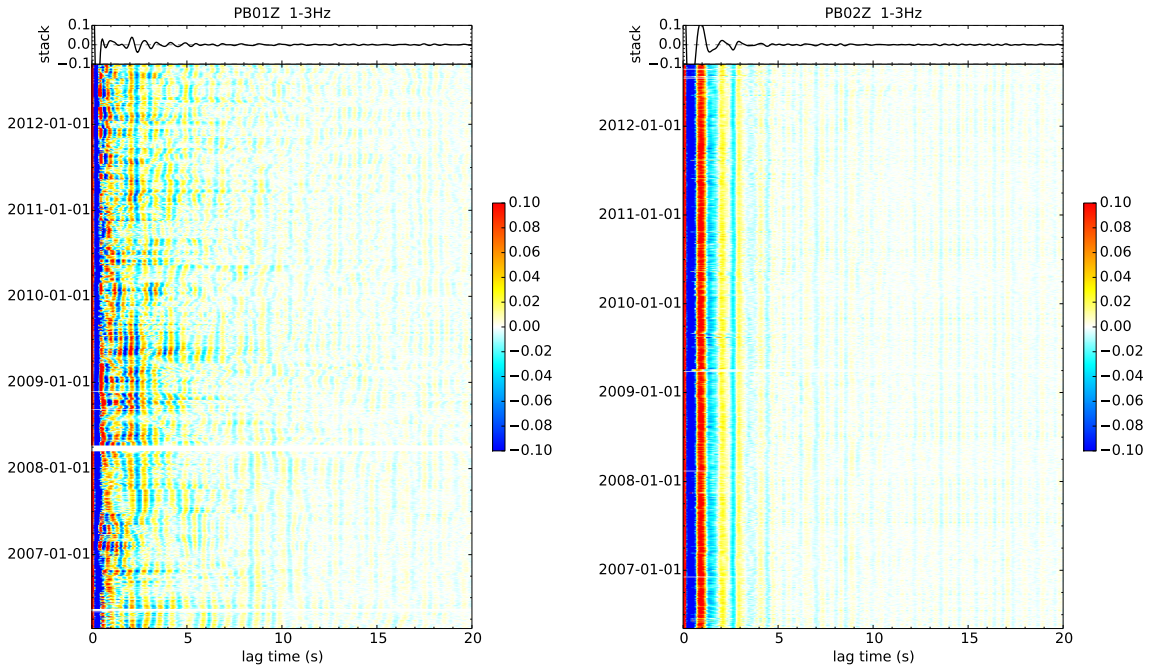

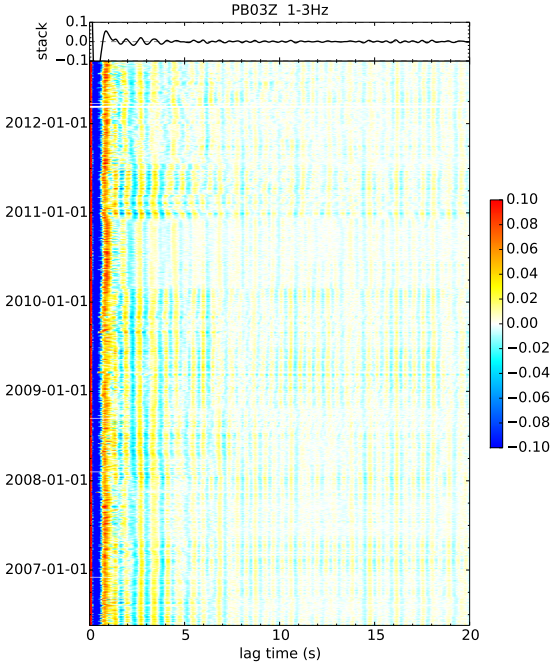
PB03Z 1-3Hz
stack
0.1
0.0
−0.1
2012-01-01
2011-01-01
2010-01-01
2009-01-01
2008-01-01
2007-01-01
0
5
10
15
20
lag time (s)
0.10
0.08
0.06
0.04
0.02
0.00
−0.02
−0.04
−0.06
−0.08
−0.10

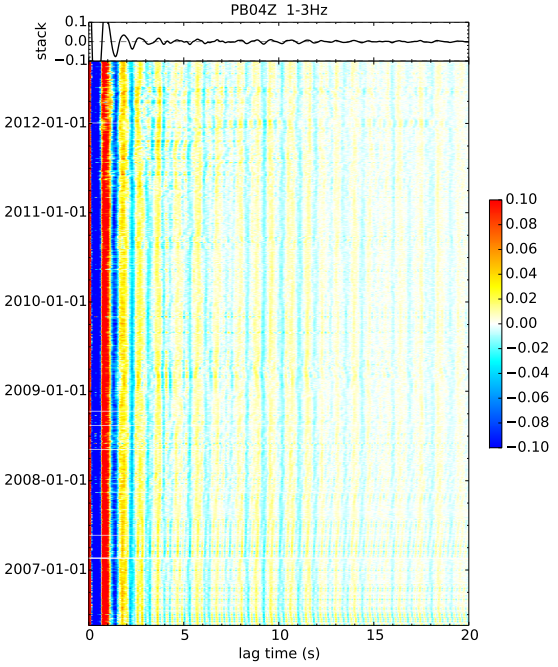
PB04Z 1-3Hz
stack
0.1
0.0
−0.1
2012-01-01
2011-01-01
2010-01-01
2009-01-01
2008-01-01
2007-01-01
0
5
10
15
20
lag time (s)
0.10
0.08
0.06
0.04
0.02
0.00
−0.02
−0.04
−0.06
−0.08
−0.10

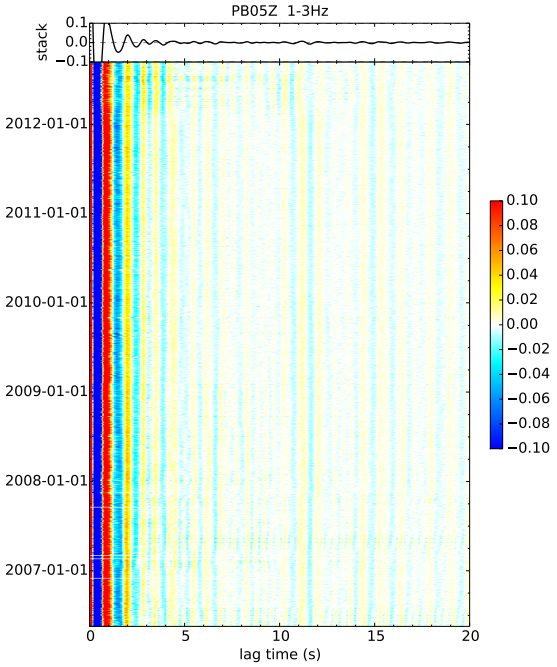
PB05Z 1-3Hz
stack
0.1
0.0
−0.1
2012-01-01
2011-01-01
2010-01-01
2009-01-01
2008-01-01
2007-01-01
0
5
10
15
20
lag time (s)
0.10
0.08
0.06
0.04
0.02
0.00
−0.02
−0.04
−0.06
−0.08
−0.10

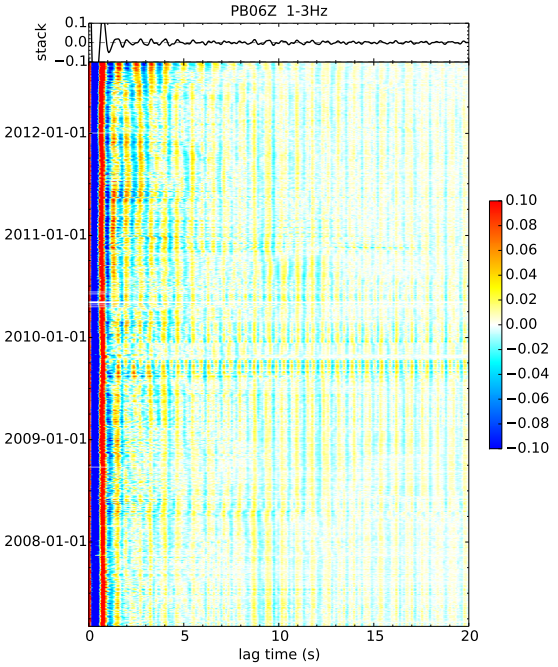
PB06Z 1-3Hz
stack
0.1
0.0
−0.1
2012-01-01
2011-01-01
2010-01-01
2009-01-01
2008-01-01
0
5
10
15
20
lag time (s)
0.10
0.08
0.06
0.04
0.02
0.00
−0.02
−0.04
−0.06
−0.08
−0.10

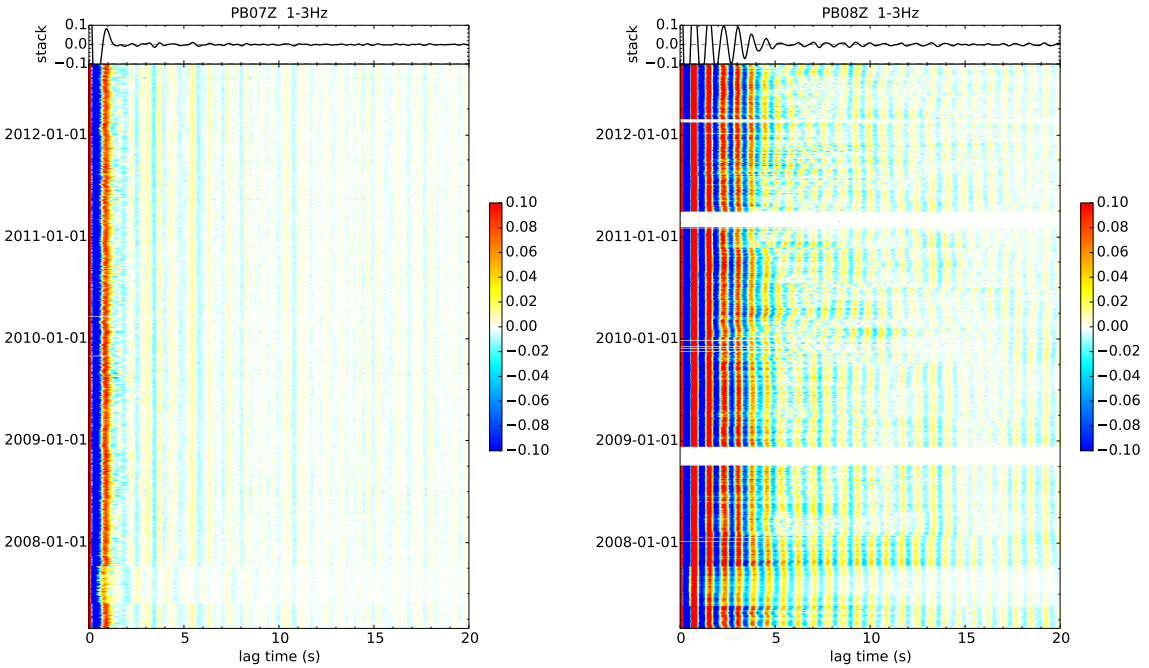
PB07Z 1-3Hz
stack
0.1
0.0
−0.1
2012-01-01
2011-01-01
2010-01-01
2009-01-01
2008-01-01
0
5
10
15
20
lag time (s)
0.10
0.08
0.06
0.04
0.02
0.00
−0.02
−0.04
−0.06
−0.08
−0.10

PB08Z 1-3Hz
stack
0.1
0.0
−0.1
2012-01-01
2011-01-01
2010-01-01
2009-01-01
2008-01-01
0
5
10
15
20
lag time (s)
0.10
0.08
0.06
0.04
0.02
0.00
−0.02
−0.04
−0.06
−0.08
−0.10

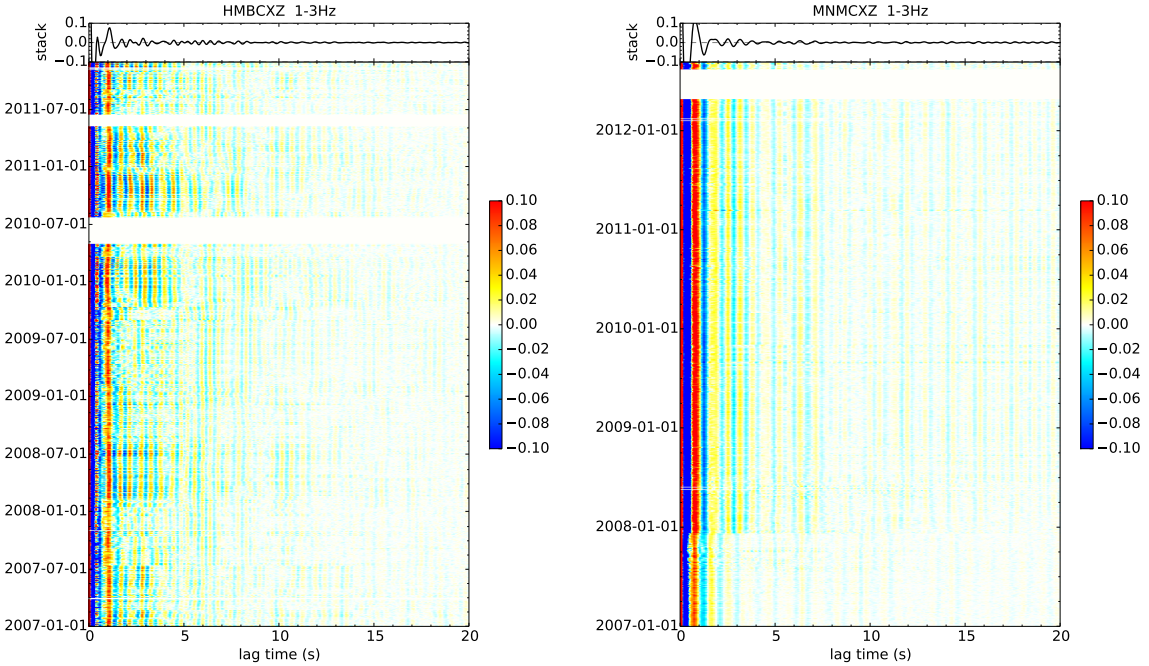
HMBCXZ 1-3Hz
stack
0.1
0.0
−0.1
2011-07-01
2011-01-01
2010-07-01
2010-01-01
2009-07-01
2009-01-01
2008-07-01
2008-01-01
2007-07-01
2007-01-01
0
5
10
15
20
lag time (s)
0.10
0.08
0.06
0.04
0.02
0.00
−0.02
−0.04
−0.06
−0.08
−0.10

MNMCXZ 1-3Hz
stack
0.1
0.0
−0.1
2012-01-01
2011-01-01
2010-01-01
2009-01-01
2008-01-01
2007-01-01
0
5
10
15
20
lag time (s)
0.10
0.08
0.06
0.04
0.02
0.00
−0.02
−0.04
−0.06
−0.08
−0.10

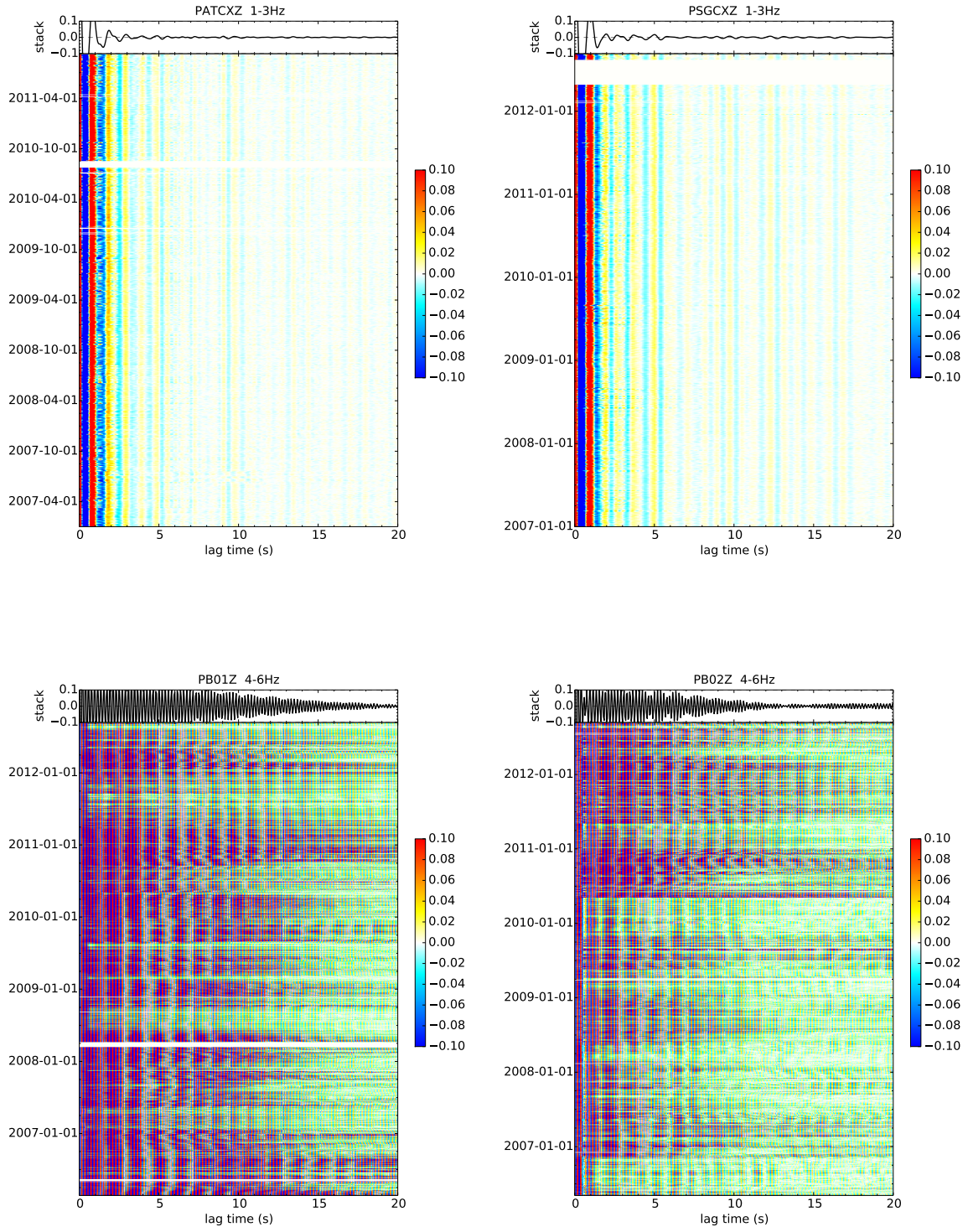
PATCXZ 1-3Hz
PSGCXZ 1-3Hz
PB01Z 4-6Hz
PB02Z 4-6Hz
stack
lag time (s)

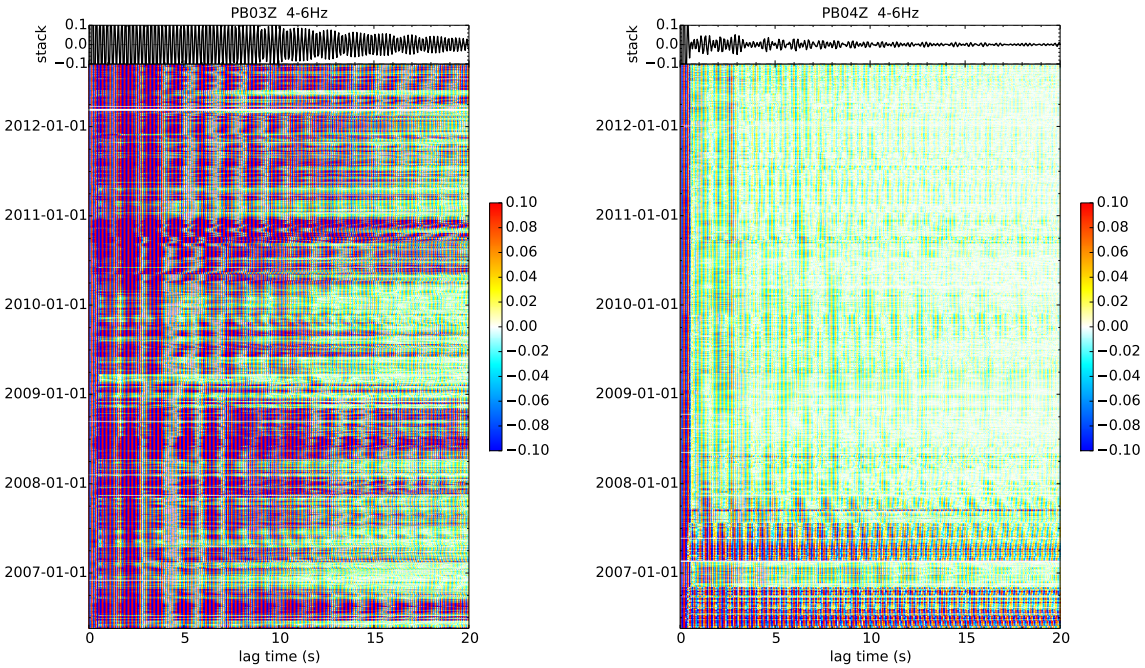
PB03Z 4-6Hz
PB04Z 4-6Hz
stack
0.1
0.0
−0.1
2012-01-01
2011-01-01
2010-01-01
2009-01-01
2008-01-01
2007-01-01
0
5
10
15
20
lag time (s)
0.10
0.08
0.06
0.04
0.02
0.00
−0.02
−0.04
−0.06
−0.08
−0.10

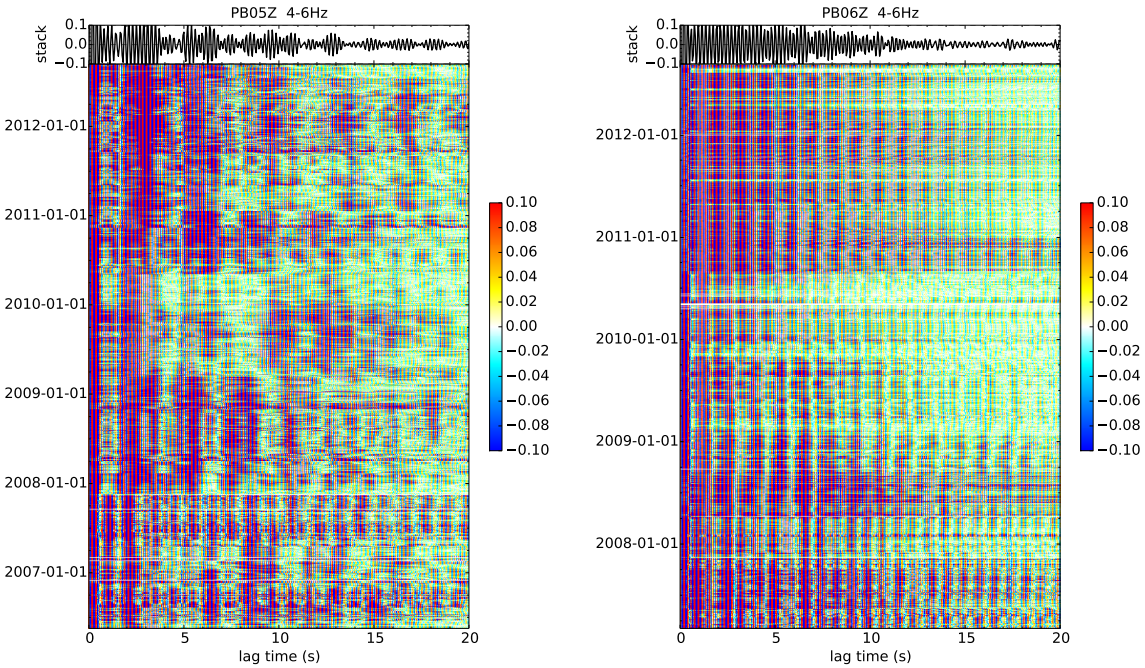
PB05Z 4-6Hz
PB06Z 4-6Hz
stack
0.1
0.0
−0.1
2012-01-01
2011-01-01
2010-01-01
2009-01-01
2008-01-01
2007-01-01
0
5
10
15
20
lag time (s)
0.10
0.08
0.06
0.04
0.02
0.00
−0.02
−0.04
−0.06
−0.08
−0.10

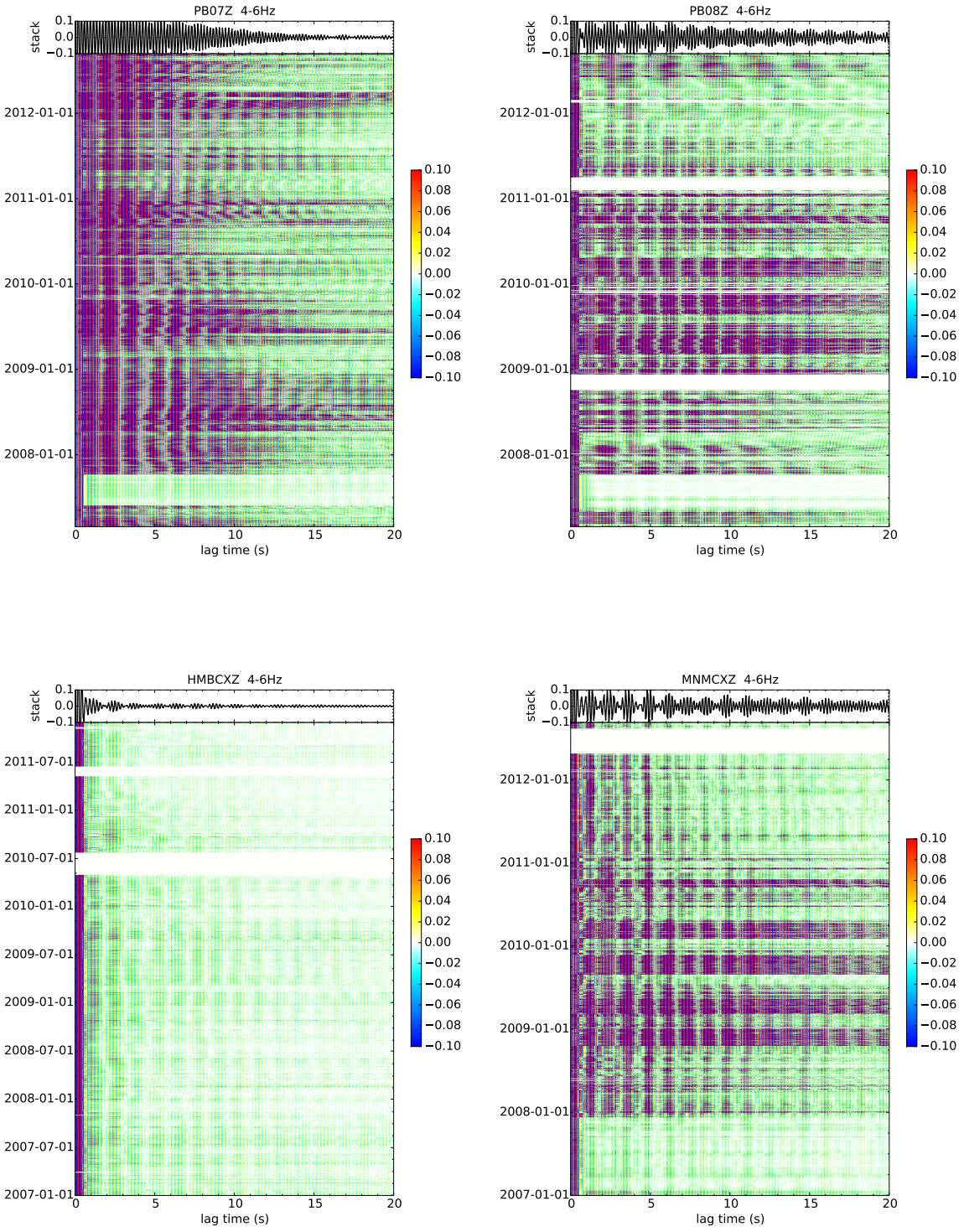
PB07Z 4-6Hz
PB08Z 4-6Hz
HMBCXZ 4-6Hz
MNMCXZ 4-6Hz
stack
lag time (s)

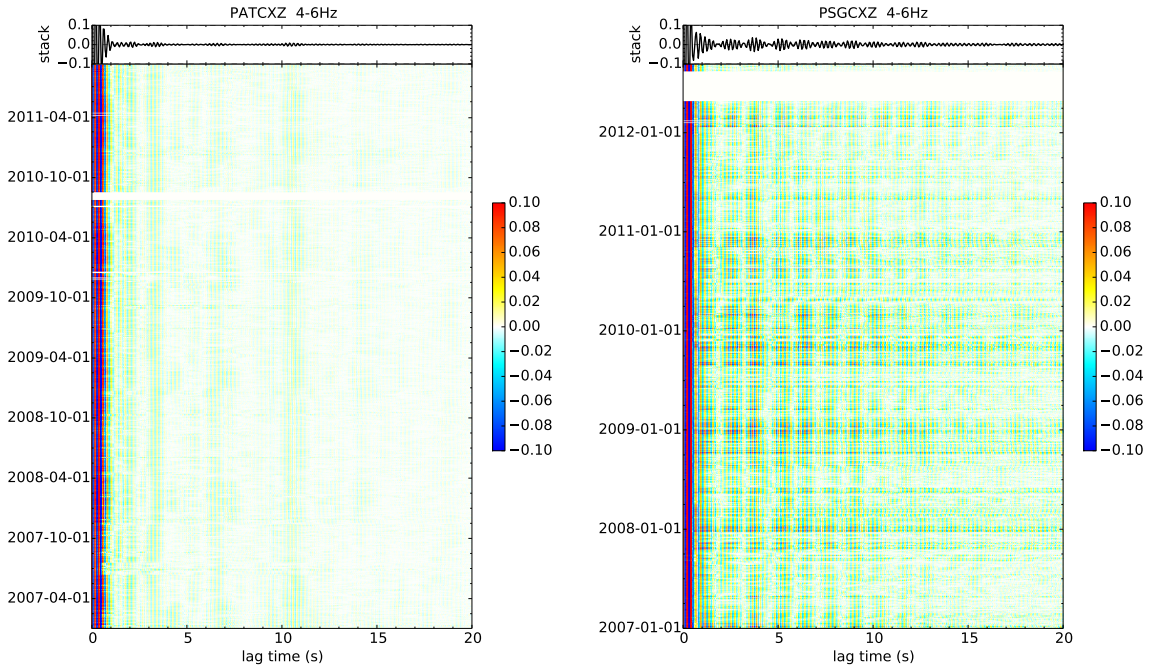
PATCXZ 4-6Hz
stack
0.1
0.0
−0.1
2011-04-01
2010-10-01
2010-04-01
2009-10-01
2009-04-01
2008-10-01
2008-04-01
2007-10-01
2007-04-01
0
5
10
15
20
lag time (s)
0.10
0.08
0.06
0.04
0.02
0.00
−0.02
−0.04
−0.06
−0.08
−0.10
PSGCXZ 4-6Hz
stack
0.1
0.0
−0.1
2012-01-01
2011-01-01
2010-01-01
2009-01-01
2008-01-01
2007-01-01
0
5
10
15
20
lag time (s)
0.10
0.08
0.06
0.04
0.02
0.00
−0.02
−0.04
−0.06
−0.08
−0.10

C.4. Similarity matrices for autocorrelation functions in two frequency bands

Similarity matrices for the autocorrelations displayed in appendix C.3 for the three lapse time windows 5 s−10 s, 10 s−15 s and 15 s−20 s are shown. They were calculated with the stretching method described in section 5.2. The similarity matrix shows the correlation coefficients for the different stretching factors for each day. The maxima over time represent the observed apparent velocity change. The gray vertical line is drawn at the time of the Tocopilla earthquake. Notice that the plots show velocity decrease $-\epsilon$.

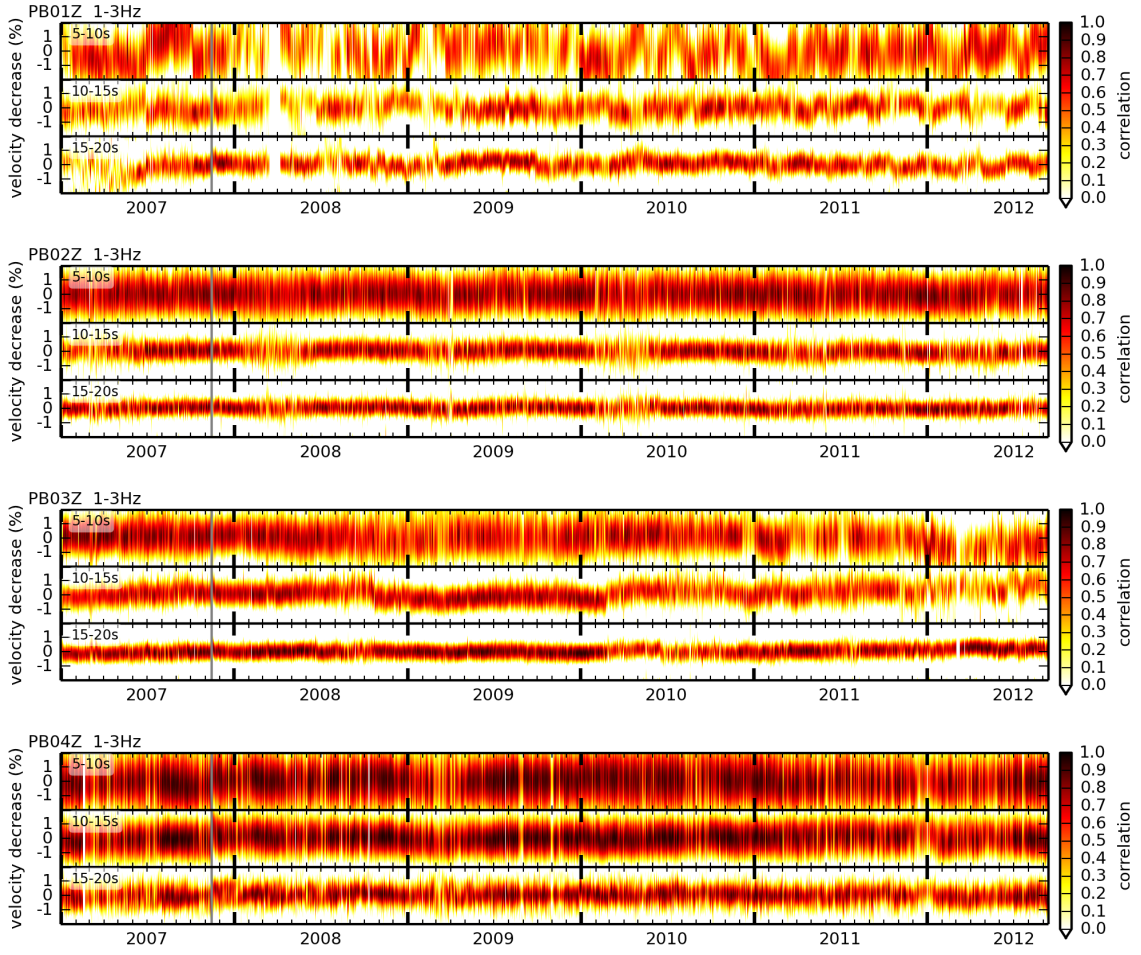

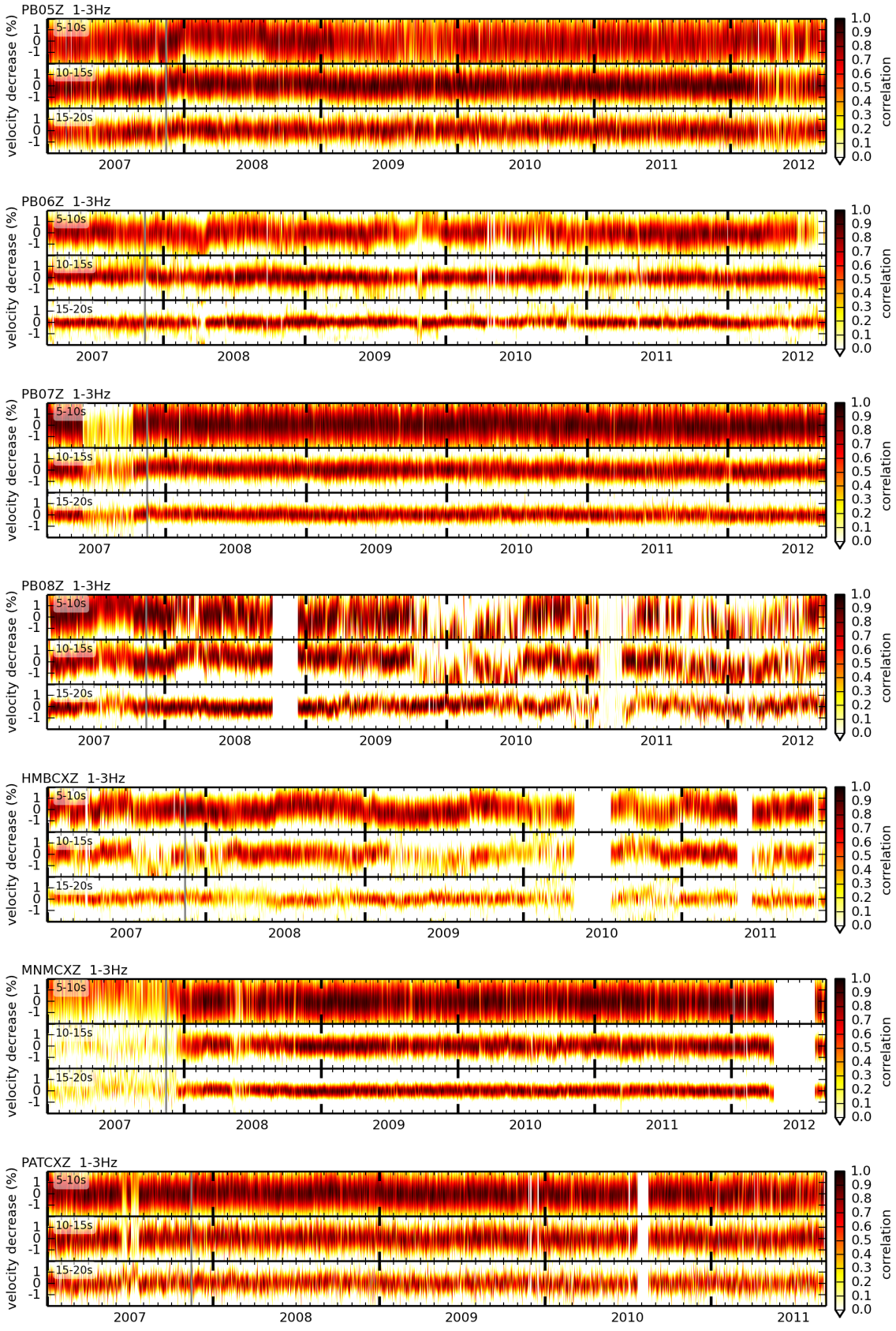
PB05Z 1-3Hz
PB06Z 1-3Hz
PB07Z 1-3Hz
PB08Z 1-3Hz
HMBCXZ 1-3Hz
MNMCXZ 1-3Hz
PATCXZ 1-3Hz
5-10s
10-15s
15-20s
velocity decrease (%)
correlation
2007
2008
2009
2010
2011
2012

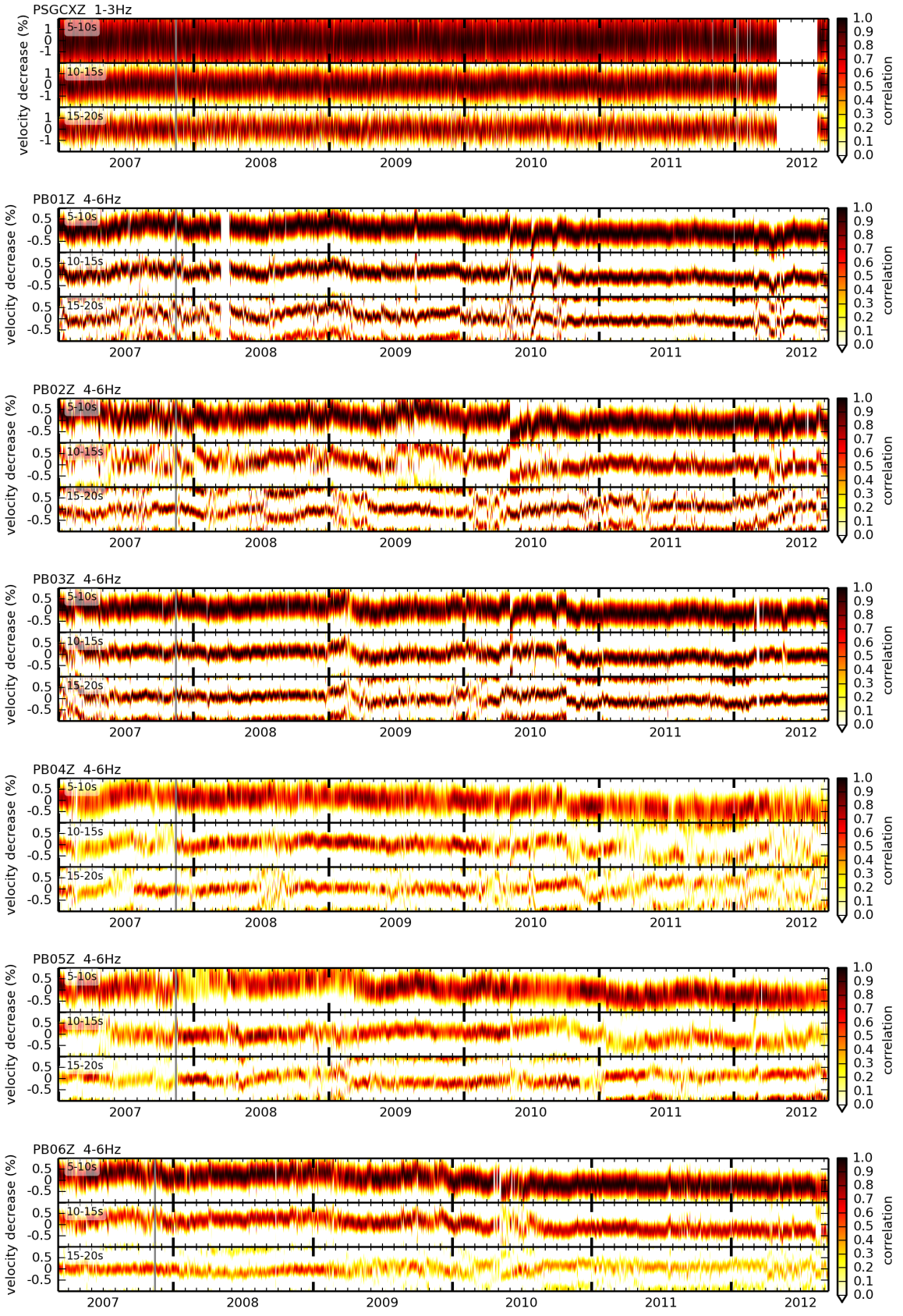
PSGCXZ 1-3Hz
PB01Z 4-6Hz
PB02Z 4-6Hz
PB03Z 4-6Hz
PB04Z 4-6Hz
PB05Z 4-6Hz
PB06Z 4-6Hz
5-10s
10-15s
15-20s
velocity decrease (%)
correlation
2007
2008
2009
2010
2011
2012

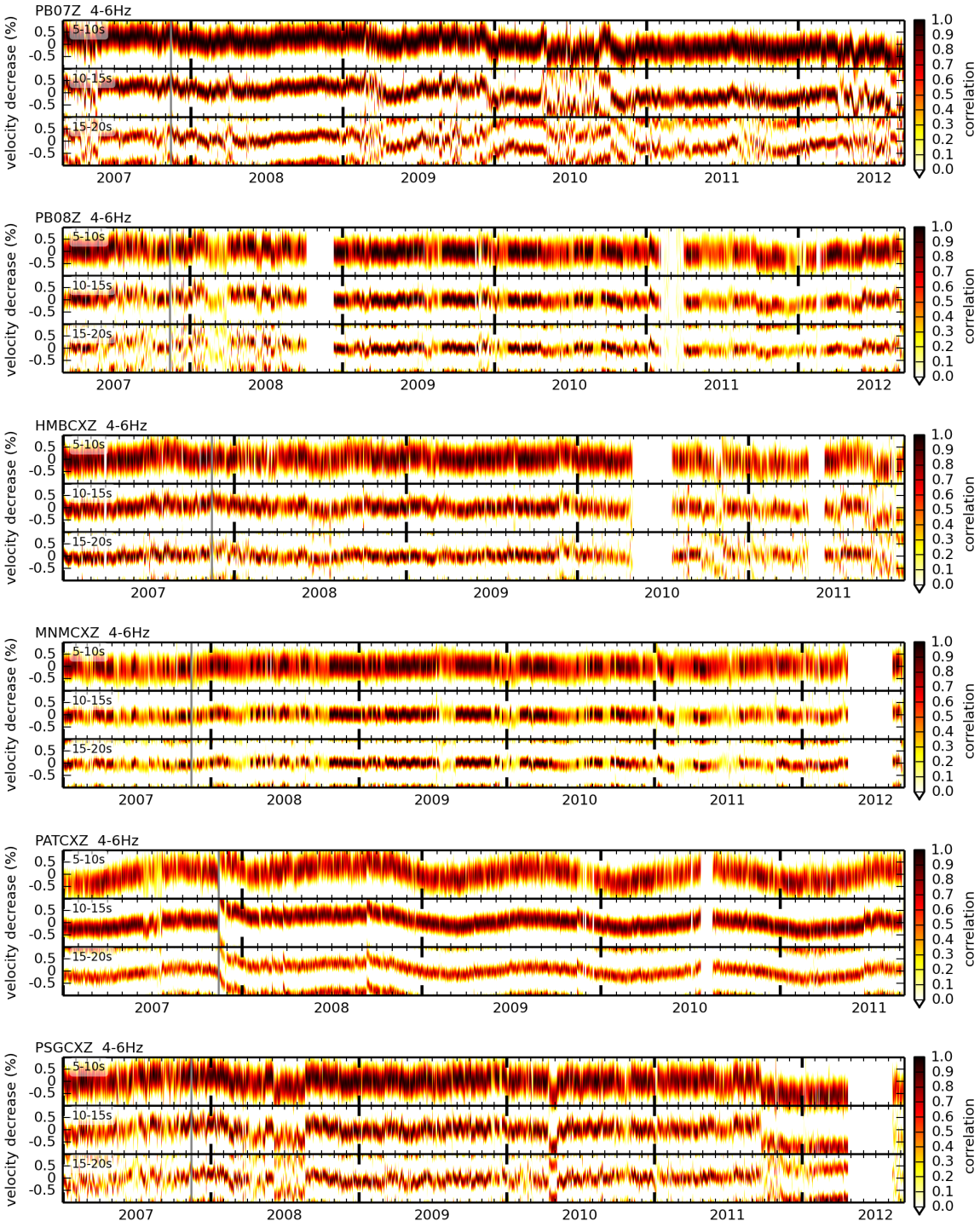
PB07Z 4-6Hz
PB08Z 4-6Hz
HMBCXZ 4-6Hz
MNMCXZ 4-6Hz
PATCXZ 4-6Hz
PSGCXZ 4-6Hz
5-10s
10-15s
15-20s
velocity decrease (%)
correlation
2007
2008
2009
2010
2011
2012

C.5. Berger's solution for thermoelastic strain

Berger's solution of equation (5.9) for a periodic surface temperature field with the approximation $k \ll \gamma$ and under consideration of the plane strain assumption is reproduced here. *Berger* (1975, equation (8)) used a different coordinate system, a different definition of γ and a different surface temperature field $T(x, z{=}0, t)$. His equations rewritten for the principal strains with the definitions used in this work are:

$$\begin{aligned} \varepsilon_{xx} &= \frac{1+\nu}{1-\nu}\frac{k}{(1+i)\,\gamma}\left\{(2\,(1-\nu)-kz)\,e^{-kz} - \frac{k}{(1+i)\,\gamma}e^{-(1+i)\gamma z}\right\}\alpha T(x, z{=}0, t) \\ \varepsilon_{zz} &= \frac{1+\nu}{1-\nu}\left\{-\frac{k}{(1+i)\,\gamma}\,(2\nu-kz)\,e^{-kz} + e^{-(1+i)\gamma z}\right\}\alpha T(x, z{=}0, t)\ . \end{aligned} \tag{C.1}$$

C.6. Radiative transfer kernel for autocorrelation

I want to insert equation (5.18) into equation (5.19) and (5.25) and perform the integrations to derive the 3D and depth sensitivity kernels for autocorrelation functions in the radiative transfer approximation. I define three terms A, B, C in the energy distribution given by

$$P(\boldsymbol{r}, t) = \overbrace{\exp\!\left(-\frac{ct}{l}\right)}^{A(t)}\left[\overbrace{\frac{\delta(r-ct)}{4\pi r^2}}^{B(t,r)} + \overbrace{\left(\frac{4}{3}\pi l c\right)^{-\frac{3}{2}}\left(1-\frac{r^2}{c^2t^2}\right)^{\frac{1}{8}} t^{-\frac{3}{2}} G\!\left(\frac{ct}{l}\left(1-\frac{r^2}{c^2t^2}\right)^{\frac{3}{4}}\right) H(ct-r)}^{C(t,r)}\right]$$

which leads to

$$\begin{aligned} K_{\mathrm{3D,rt}}(\boldsymbol{r}, t) &= \frac{1}{P_0(t)}\int_0^t P(\boldsymbol{r}, t-t')\ P(\boldsymbol{r}, t')\ \mathrm{d}t' \\ &= \frac{A(t)}{P_0(t)}\int_0^t B(t-t')\,B(t') + \Big[B(t-t')\,C(t') + B(t')\,C(t-t')\Big] + C(t-t')\,C(t')\ \mathrm{d}t'\,. \end{aligned} \tag{C.2}$$

There are three contributions to the kernel. Firstly waves scattered just one time at position $\boldsymbol{r}$ (term BB), then waves not scattered while traveling to $\boldsymbol{r}$ but scattered while traveling back or vice versa (terms BC) and finally waves scattered on the way to $\boldsymbol{r}$ and back (term CC). The resulting contributions to the kernel are named K_1, K_2 and K_3. The last term can be integrated numerically without problems to get K_3 and $K_{z,3}$:

$$K_3\,(\boldsymbol{r}, t) = \frac{A(t)}{P_0(t)}\int_0^t C(t-t', r)\,C(t', r)\ \mathrm{d}t'\,.$$

The first integration for the BC terms collapses because of the Dirac delta function:

$$K_2(\boldsymbol{r}, t) = \frac{A(t)}{2\pi r^2 c P_0(t)} C\Big(t - \frac{r}{c}, r\Big) .$$

Inserting into equation (5.25) gives

$$K_{z,2}(z, t) = \frac{2A(t)}{cP_0(t)} \int_z^\infty \frac{C\Big(t - \frac{r}{c}, r\Big)}{r} \,\mathrm{d}r .$$

Numerical integration can be performed again with a careful consideration because of the diverging kernel at $z \to 0$. There a small hemispherical proximity with radius ϵ' is excluded when integrating. The kernel without the hemispherical proximity

$$K'_{z,2}(z, t) = \frac{2A(t)}{cP_0(t)} \int_{\max(z,\epsilon')}^\infty \frac{C\Big(t - \frac{r}{c}, r\Big)}{r} \,\mathrm{d}r$$

can be integrated without problems. The observed velocity change ϵ_2 due to K_2 is then be calculated with equations (5.21) and (5.24) as

$$\epsilon_2(t) = \frac{1}{t} \left[\frac{2A(t)}{cP_0(t)} \epsilon' C(t, 0) \frac{\Delta v}{v}(\mathbf{0}) + \int_0^\infty K'_{z,2}(z, t) \frac{\Delta v}{v}(z) \,\mathrm{d}z \right] .$$

The first term will have a vanishing contribution if ϵ' is chosen small enough. This leaves the first term in equation (C.2) which includes two Dirac delta functions. The first integration leaves one Dirac delta:

$$K_1(\boldsymbol{r}, t) = \frac{A(t)\, \delta(r - ct/2)}{P_0(t) \left(4\pi r^2\right)^2 c} .$$

Under the assumption of validity of equation (5.19) the calculated 3D kernel for single scattering is sensitive only to a spherical shell volume at a distance of $ct/2$ – the location where it is scattered. This is obviously not correct. The kernel should be sensitive to the whole spherical volume with a radius of $ct/2$. This fact reflects the trade-off of using the definition of the kernel given by equation (5.19) which is strictly valid only in the diffusion approximation. Performing the second integration over depth gives a non-zero, constant depth kernel for all $z \leq ct/2$

$$K_{z,1}(\boldsymbol{z}, t) = \frac{2A(t)\, H(ct/2 - z)}{\pi P_0(t)\, c^4 t^3} .$$

For reasonable scattering parameters c and l the contribution of K_1 and $K_{z,1}$ to the whole kernels is insignificant. The contributing terms for the 3D and depth kernels for radiative transfer and autocorrelation are

$$K_{\mathrm{3D,rt}} = K_2 + K_3 \,,$$
$$K_{z,\mathrm{rt}} = K'_{z,2} + K_{z,3} \,.$$

List of figures

List of tables

References

Allmendinger, R. W., T. E. Jordan, S. M. Kay, and B. L. Isacks (1997). The evolution of the Altiplano-Puna plateau of the Central Andes. *Annual Review of Earth and Planetary Sciences*, 25(1):139–174. doi:10.1146/annurev.earth.25.1.139. Cited on page 5.

Ammon, C. J., G. E. Randall, and G. Zandt (1990). On the Nonuniqueness of Receiver Function Inversions. *Journal of Geophysical Research*, 95(B10):15,303–15,318. doi:10.1029/jb095ib10p15303. Cited on page 16.

Anderson, O. L., E. Schreiber, R. C. Liebermann, and N. Soga (1968). Some elastic constant data on minerals relevant to geophysics. *Reviews of Geophysics*, 6(4):491–524. doi:10.1029/rg006i004p00491. Cited on page 58.

Ando, M., K. Sudo, T. Hashida, K. Irikura, and C. Igarashi (1980). A precise continuous measurement of in situ seismic velocity near the Obaku fault, Kyoto. *Zishin II*, 33:501–15. Cited on page 1.

Angermann, D., J. Klotz, and C. Reigber (1999). Space-geodetic estimation of the Nazca-South America euler vector. *Earth and Planetary Science Letters*, 171(3):329–334. doi:10.1016/s0012-821x(99)00173-9. Cited on pages 5, 6, and 9.

Arushanian, O. B., M. K. Samarin, V. V. Voevodin, E. E. Tyrtyshnikov, B. S. Garbow, J. M. Boyle, W. R. Cowell, and K. W. Dritz (1983). TOEPLITZ package users' guide. Technical Report ANL-83-16, Moskovskij Gosudarstvennyj University, Argonne National Laboratory. Cited on page 18.

Audet, P. (2010). Temporal Variations in Crustal Scattering Structure near Parkfield, California, Using Receiver Functions. *Bulletin of the Seismological Society of America*, 100(3):1356–1362. doi:10.1785/0120090299. Cited on page 2.

Bach, C. (2010). *Sub-millimeter displacement measurements: creepmeter instrumentation and first results in the central Andean forearc*. Diploma thesis, Universität Potsdam, Institut für Geowissenschaften. Cited on pages 60 and 61.

Beck, S. L., G. Zandt, S. C. Myers, T. C. Wallace, P. G. Silver, and L. Drake (1996). Crustal-thickness variations in the central Andes. *Geology*, 24(5):407–410. doi:10.1130/0091-7613(1996)024%3C0407:ctvitc%3E2.3.co;2. Cited on page 7.

Béjar-Pizarro, M., D. Carrizo, A. Socquet, R. Armijo, S. Barrientos, F. Bondoux, S. Bonvalot, J. Campos, D. Comte, J. B. de Chabalier, O. Charade, A. Delorme, G. Gabalda, J. Galetzka, J. Genrich, A. Nercessian, M. Olcay, F. Ortega, I. Ortega, D. Remy, J. C. Ruegg, M. Simons, C. Valderas, and C. Vigny (2010). Asperities and barriers on the seismogenic zone in North Chile: state-of-the-art after the 2007 Mw 7.7 Tocopilla earthquake inferred by GPS and InSAR data. *Geophysical Journal International*, 183(1):390–406. doi:10.1111/j.1365-246x.2010.04748.x. Cited on pages 7, 8, and 9.

Ben-Zion, Y. and P. Leary (1986). Thermoelastic strain in a half-space covered by unconsolidated material. *Bulletin of the Seismological Society of America*, 76(5):1447–1460. Cited on pages 61 and 71.

Bensen, G. D., M. H. Ritzwoller, M. P. Barmin, A. L. Levshin, F. Lin, M. P. Moschetti, N. M. Shapiro, and Y. Yang (2007). Processing seismic ambient noise data to obtain reliable broad-band surface wave dispersion measurements. *Geophysical Journal International*, 169(3):1239–1260. doi:10.1111/j.1365-246x.2007.03374.x. Cited on page 36.

Berger, J. (1975). A note on thermoelastic strains and tilts. *Journal of Geophysical Research*, 80(2):274–277. doi:10.1029/jb080i002p00274. Cited on pages 58, 60, 61, 62, and 137.

Beyreuther, M., R. Barsch, L. Krischer, T. Megies, Y. Behr, and J. Wassermann (2010). ObsPy: A Python Toolbox for Seismology. *Seismological Research Letters*, 81(3):530–533. doi:10.1785/gssrl.81.3.530. Cited on pages 15 and 78.

Birch, F. (1961). The velocity of compressional waves in rocks to 10 kilobars: 2. *Journal of Geophysical Research*, 66(7):2199–2224. doi:10.1029/jz066i007p02199. Cited on page 65.

Boué, P., P. Poli, M. Campillo, H. Pedersen, X. Briand, and P. Roux (2013). Teleseismic correlations of ambient seismic noise for deep global imaging of the Earth. *Geophysical Journal International*. doi:10.1093/gji/ggt160. Cited on page 73.

Brenguier, F., M. Campillo, C. Hadziioannou, N. M. Shapiro, R. M. Nadeau, and E. Larose (2008). Postseismic Relaxation Along the San Andreas Fault at Parkfield from Continuous Seismological Observations. *Science*, 321(5895):1478–1481. doi:10.1126/science.1160943. Cited on page 43.

Budiansky, B. and R. J. O'Connell (1976). Elastic moduli of a cracked solid. *International Journal of Solids and Structures*, 12(2):81–97. doi:10.1016/0020-7683(76)90044-5. Cited on page 64.

Campillo, M. and A. Paul (2003). Long-Range Correlations in the Diffuse Seismic Coda. *Science*, 299(5606):547–549. doi:10.1126/science.1078551. Cited on page 31.

Chen, J. H., B. Froment, Q. Y. Liu, and M. Campillo (2010). Distribution of seismic wave speed changes associated with the 12 May 2008 Mw 7.9 Wenchuan earthquake. *Geophysical Research Letters*, 37(18):L18302+. doi:10.1029/2010gl044582. Cited on page 3.

Chlieh, M., J. B. De Chabalier, J. C. Ruegg, R. Armijo, R. Dmowska, J. Campos, and K. L. Feigl (2004). Crustal deformation and fault slip during the seismic cycle in the North Chile subduction zone, from GPS and InSAR observations. *Geophysical Journal International*, 158(2):695–711. doi:10.1111/j.1365-246x.2004.02326.x. Cited on page 9.

Comte, D. and M. Pardo (1991). Reappraisal of great historical earthquakes in the northern Chile and southern Peru seismic gaps. *Natural Hazards*, 4(1):23–44. doi:10.1007/bf00126557. Cited on page 7.

Delouis, B., M. Pardo, D. Legrand, and T. Monfret (2009). The Mw 7.7 Tocopilla Earthquake of 14 November 2007 at the Southern Edge of the Northern Chile Seismic Gap: Rupture in the Deep Part of the Coupled Plate Interface. *Bulletin of the Seismological Society of America*, 99(1):87–94. doi:10.1785/0120080192. Cited on page 7.

Duputel, Z., V. Ferrazzini, F. Brenguier, N. Shapiro, M. Campillo, and A. Nercessian (2009). Real time monitoring of relative velocity changes using ambient seismic noise at the Piton de la Fournaise volcano (La Réunion) from January 2006 to June 2007. *Journal of Volcanology and Geothermal Research*, 184(1-2):164–173. doi:10.1016/j.jvolgeores.2008.11.024. Cited on page 35.

Engdahl, E. R., R. van der Hilst, and R. Buland (1998). Global teleseismic earthquake relocation with improved travel times and procedures for depth determination. *Bulletin of the Seismological Society of America*, 88(3):722–743. Cited on pages 5 and 6.

Engdahl, E. R., R. D. van der Hilst, and J. Berrocal (1995). Imaging of subducted lithosphere beneath South America. *Geophysical Research Letters*, 22(16):2317–2320. doi:10.1029/95gl02013. Cited on pages 5 and 6.

Froment, B., M. Campillo, J. H. Chen, and Q. Y. Liu (2013). Deformation at depth associated with the 12 May 2008 MW 7.9 Wenchuan earthquake from seismic ambient noise monitoring. *Geophysical Research Letters*, 40(1):78–82. doi:10.1029/2012gl053995. Cited on page 3.

Gutscher, M.-A. (2002). Andean subduction styles and their effect on thermal structure and interplate coupling. *Journal of South American Earth Sciences*, 15(1):3–10. doi:10.1016/s0895-9811(02)00002-0. Cited on page 6.

Hobiger, M., U. Wegler, K. Shiomi, and H. Nakahara (2012). Coseismic and postseismic elastic wave velocity variations caused by the 2008 Iwate-Miyagi Nairiku earthquake, Japan. *J. Geophys. Res.*, 117(B9):B09313+. doi:10.1029/2012jb009402. Cited on pages 2, 3, 43, and 52.

Hughes, D. S. and J. L. Kelly (1953). Second-Order Elastic Deformation of Solids. *Physical Review Online Archive (Prola)*, 92:1145–1149. doi:10.1103/physrev.92.1145. Cited on page 64.

Ikuta, R., K. Yamaoka, K. Miyakawa, T. Kunitomo, and M. Kumazawa (2002). Continuous monitoring of propagation velocity of seismic wave using ACROSS. *Geophysical Research Letters*, 29(13):5–5–5. doi:10.1029/2001gl013974. Cited on page 1.

Isacks, B. L. (1988). Uplift of the Central Andean Plateau and Bending of the Bolivian Orocline. *Journal of Geophysical Research*, 93(B4):3211–3231. doi:10.1029/jb093ib04p03211. Cited on page 7.

Jones, E., T. Oliphant, P. Peterson, and others (2001–). SciPy: Open source scientific tools for Python. URL `http://scipy.org/`. Cited on page 51.

Kelleher, J. A. (1972). Rupture Zones of Large South American Earthquakes and Some Predictions. *Journal of Geophysical Research*, 77(11):2087–2103. doi:10.1029/jb077i011p02087. Cited on page 7.

Kennett, B. L. N. and E. R. Engdahl (1991). Traveltimes for global earthquake location and phase identification. *Geophysical Journal International*, 105(2):429–465. doi:10.1111/j.1365-246x.1991.tb06724.x. Cited on pages 17 and 21.

Khaksar, Griffiths, and McCann (1999). Compressional- and shear-wave velocities as a function of confining stress in dry sandstones. *Geophysical Prospecting*, 47(4):487–508. doi:10.1046/j.1365-2478.1999.00146.x. Cited on page 64.

Kumar, P., R. Kind, and X. Yuan (2010). Receiver function summation without deconvolution. *Geophysical Journal International*, 180(3):1223–1230. doi:10.1111/j.1365-246x.2009.04469.x. Cited on page 18.

Li, Y.-G., P. Chen, E. S. Cochran, J. E. Vidale, and T. Burdette (2006). Seismic Evidence for Rock Damage and Healing on the San Andreas Fault Associated with the 2004 M 6.0 Parkfield Earthquake. *Bulletin of the Seismological Society of America*, 96(4B):S349–S363. doi:10.1785/0120050803. Cited on page 1.

Li, Y.-G., J. E. Vidale, K. Aki, F. Xu, and T. Burdette (1998). Evidence of Shallow Fault Zone Strengthening After the 1992 M7.5 Landers, California, Earthquake. *Science*, 279(5348):217–219. doi:10.1126/science.279.5348.217. Cited on page 1.

Li, Y.-G., J. E. Vidale, S. M. Day, D. D. Oglesby, and E. Cochran (2003). Postseismic Fault Healing on the Rupture Zone of the 1999 M 7.1 Hector Mine, California, Earthquake. *Bulletin of the Seismological Society of America*, 93(2):854–869. doi:10.1785/0120020131. Cited on page 1.

Ligorría, J. P. and C. J. Ammon (1999). Iterative deconvolution and receiver-function estimation. *Bulletin of the Seismological Society of America*, 89(5):1395–1400. Cited on page 18.

Lin, F.-C. and V. C. Tsai (2013). Seismic interferometry with antipodal station pairs. *Geophysical Research Letters*, 40(17):4609–4613. doi:10.1002/grl.50907. Cited on page 73.

Lobkis, O. I. and R. L. Weaver (2001). On the emergence of the Green's function in the correlations of a diffuse field. *The Journal of the Acoustical Society of America*, 110(6):3011–3017. doi:10.1121/1.1417528. Cited on page 2.

Lyakhovsky, V., Z. Reches, R. Weinberger, and T. E. Scott (1997). Non-linear elastic behaviour of damaged rocks. *Geophysical Journal International*, 130(1):157–166. doi:10.1111/j.1365-246x.1997.tb00995.x. Cited on page 64.

Maeda, T., K. Obara, and Y. Yukutake (2010). Seismic velocity decrease and recovery related to earthquake swarms in a geothermal area. *Earth, Planets, and Space*, 62:685–691. doi:10.5047/eps.2010.08.006. Cited on page 3.

Malgrange, M. and R. Madariaga (1983). Complex distribution of large thrust and normal fault earthquakes in the Chilean subduction zone. *Geophysical Journal of the Royal Astronomical Society*, 73(2):489–505. doi:10.1111/j.1365-246x.1983.tb03326.x. Cited on page 9.

McEvilly, T. V. and L. R. Johnson (1974). Stability of P an S velocities from Central California quarry blasts. *Bulletin of the Seismological Society of America*, 64(2):343–353. Cited on page 1.

McNamara, D. E. and R. P. Buland (2004). Ambient Noise Levels in the Continental United States. *Bulletin of the Seismological Society of America*, 94(4):1517–1527. doi:10.1785/012003001. Cited on pages 14, 31, 32, and 78.

Meier, U., N. M. Shapiro, and F. Brenguier (2010). Detecting seasonal variations in seismic velocities within Los Angeles basin from correlations of ambient seismic noise. *Geophysical Journal International*, 181(2):985–996. doi:10.1111/j.1365-246x.2010.04550.x. Cited on pages 2 and 61.

Muñoz, N. and R. Charrier (1996). Uplift of the western border of the Altiplano on a west-vergent thrust system, Northern Chile. *Journal of South American Earth Sciences*, 9(3-4):171–181. doi:10.1016/0895-9811(96)00004-1. Cited on page 6.

Nelder, J. A. and R. Mead (1965). A Simplex Method for Function Minimization. *The Computer Journal*, 7(4):308–313. doi:10.1093/comjnl/7.4.308. Cited on page 51.

Nippress, S. E. J. and A. Rietbrock (2007). Seismogenic zone high permeability in the Central Andes inferred from relocations of micro-earthquakes. *Earth and Planetary Science Letters*, 263(3-4):235–245. doi:10.1016/j.epsl.2007.08.032. Cited on page 9.

Nishimura, T., N. Uchida, H. Sato, M. Ohtake, S. Tanaka, and H. Hamaguchi (2000). Temporal changes of the crustal structure associated with the M6.1 earthquake on

September 3, 1998, and the volcanic activity of Mount Iwate, Japan. *Geophysical Research Letters*, 27(2):269–272. doi:10.1029/1999gl005439. Cited on page 1.

Niu, F., P. G. Silver, T. M. Daley, X. Cheng, and E. L. Majer (2008). Preseismic velocity changes observed from active source monitoring at the Parkfield SAFOD drill site. *Nature*, 454(7201):204–208. doi:10.1038/nature07111. Cited on page 1.

Norabuena, E., L. Leffler-Griffin, A. Mao, T. Dixon, S. Stein, I. S. Sacks, L. Ocola, and M. Ellis (1998). Space Geodetic Observations of Nazca-South America Convergence Across the Central Andes. *Science*, 279(5349):358–362. doi:10.1126/science.279.5349.358. Cited on pages 5 and 6.

Obermann, A., T. Planès, E. Larose, C. Sens-Schönfelder, and M. Campillo (2013). Depth sensitivity of seismic coda waves to velocity perturbations in an elastic heterogeneous medium. *Geophysical Journal International*. doi:10.1093/gji/ggt043. Cited on pages 66 and 72.

Paasschens, J. C. J. (1997). Solution of the time-dependent Boltzmann equation. *Physical Review E*, 56:1135–1141. doi:10.1103/physreve.56.1135. Cited on page 66.

Pacheco, C. and R. Snieder (2005). Time-lapse travel time change of multiply scattered acoustic waves. *The Journal of the Acoustical Society of America*, 118(3):1300–1310. doi:10.1121/1.2000827. Cited on page 67.

Pankhurst, R. J. and F. Hervé (2007). Introduction and overview. In *The Geology of Chile* (edited by T. Moreno and W. Gibbons), chapter 1, pages 1–4. The Geological Society, London. Cited on page 5.

Peng, Z. and Y. Ben-Zion (2006). Temporal Changes of Shallow Seismic Velocity Around the Karadere-Düzce Branch of the North Anatolian Fault and Strong Ground Motion. *Pure and Applied Geophysics*, 163(2-3):567–600. doi:10.1007/s00024-005-0034-6. Cited on page 1.

Peterson, J. (1993). Observations and modeling of seismic background noise. Technical Report 93-322, U.S. Geological Survey. Cited on pages 32 and 78.

Peyrat, S., R. Madariaga, E. Buforn, J. Campos, G. Asch, and J. P. Vilotte (2010). Kinematic rupture process of the 2007 Tocopilla earthquake and its main aftershocks from teleseismic and strong-motion data. *Geophysical Journal International*, 182(3):1411–1430. doi:10.1111/j.1365-246x.2010.04685.x. Cited on page 7.

Planès, T., E. Larose, L. Margerin, V. Rossetto, and C. Sens-Schönfelder (2013). Decorrelation and phase-shift of coda waves induced by local changes: multiple scattering approach and numerical validation. Manuscript submitted to Waves in Random and Complex Media. Cited on page 67.

Poupinet, G., W. L. Ellsworth, and J. Frechet (1984). Monitoring velocity variations in the crust using earthquake doublets: An application to the Calaveras Fault, California. *Journal of Geophysical Research*, 89(B7):5719–5731. doi:10.1029/jb089ib07p05719. Cited on page 1.

Pritchard, M. E., C. Ji, and M. Simons (2006). Distribution of slip from 11 Mw $>$ 6 earthquakes in the northern Chile subduction zone. *Journal of Geophysical Research*, 111(B10):B10302+. doi:10.1029/2005jb004013. Cited on page 9.

Ramos, V. A. and A. Alemán (2000). Tectonic evolution of the Andes. In *Tectonic evolution of South America* (edited by U. G. Cordani, E. J. Milani, A. Thomaz Filho, and D. A. Campos), pages 635–685. International Geological Congress, Río de Janeiro. Cited on page 6.

Ratdomopurbo, A. and G. Poupinet (1995). Monitoring a temporal change of seismic velocity in a volcano: Application to the 1992 eruption of Mt. Merapi (Indonesia). *Geophysical Research Letters*, 22(7):775–778. doi:10.1029/95gl00302. Cited on page 1.

Reasenberg, P. and K. Aki (1974). A precise, continuous measurement of seismic velocity for monitoring in situ stress. *Journal of Geophysical Research*, 79(2):399–406. doi:10.1029/jb079i002p00399. Cited on pages 1 and 2.

Reijs, J. and K. McClay (1998). Salar Grande pull-apart basin, Atacama Fault System, northern Chile. *Geological Society, London, Special Publications*, 135(1):127–141. doi:10.1144/gsl.sp.1998.135.01.09. Cited on page 59.

Rivet, D., M. Campillo, N. M. Shapiro, V. Cruz-Atienza, M. Radiguet, N. Cotte, and V. Kostoglodov (2011). Seismic evidence of nonlinear crustal deformation during a large slow slip event in Mexico. *Geophysical Research Letters*, 38(8):L08308+. doi:10.1029/2011gl047151. Cited on page 3.

Roeder, D. and R. L. Chamberlain (1995). Structural Geology of Sub-Andean Fold and Thrust Belt in Northwestern Bolivia. In *Petroleum basins of South America* (edited by A. J. Tankard, R. S. Soruco, and H. J. Welsink), volume 62, pages 459–479. American Association of Petroleum Geologists. Cited on page 7.

Roux, P., K. G. Sabra, P. Gerstoft, W. A. Kuperman, and M. C. Fehler (2005). P-waves from cross-correlation of seismic noise. *Geophysical Research Letters*, 32(19):L19303+. doi:10.1029/2005gl023803. Cited on page 33.

Rubinstein, J. L. and G. C. Beroza (2004). Evidence for Widespread Nonlinear Strong Ground Motion in the MW 6.9 Loma Prieta Earthquake. *Bulletin of the Seismological Society of America*, 94(5):1595–1608. doi:10.1785/012004009. Cited on page 3.

Sawazaki, K. and R. Snieder (2013). Time-lapse changes of P- and S-wave velocities and shear wave splitting in the first year after the 2011 Tohoku earthquake, Japan: shallow subsurface. *Geophysical Journal International*, 193(1):238–251. doi:10.1093/gji/ggs080. Cited on pages 3, 52, and 74.

Scheuber, E., T. Bogdanic, A. Jensen, and K. J. Reutter (1994). Tectonic development of the North Chilean Andes in relation to plate convergence and magmatism since the Jurassic. In *Tectonics of the southern central Andes* (edited by J. Reutter K, E. Scheuber, and P. J. Wigger), pages 121–139. Springer, Berlin. doi:10.1007/978-3-642-77353-2_9. Cited on page 7.

Schurr, B., A. Asch, F. Sodoudi, A. Manzanares, O. Ritter, J. Klotz, G. Chong-Diaz, S. Barrientos, J. P. Villotte, and O. Oncken (2009). The International Plate Boundary Observatory Chile (IPOC) in the northern Chile seismic gap. In *EGU General Assembly* (edited by D. N. Arabelos and C. C. Tscherning), volume 11. Cited on page 11.

Schurr, B., G. Asch, M. Rosenau, R. Wang, O. Oncken, S. Barrientos, P. Salazar, and J. P. Vilotte (2012). The 2007 M7.7 Tocopilla northern Chile earthquake sequence: Implications for along-strike and downdip rupture segmentation and megathrust frictional behavior. *Journal of Geophysical Research*, 117(B5):B05305+. doi:10.1029/2011jb009030. Cited on pages 7, 8, 9, 12, 48, and 49.

Sens-Schönfelder, C. (2008). Synchronizing seismic networks with ambient noise. *Geophysical Journal International*, 174(3):966–970. doi:10.1111/j.1365-246x.2008.03842.x. Cited on page 35.

Sens-Schönfelder, C. and E. Larose (2008). Temporal changes in the lunar soil from correlation of diffuse vibrations. *Physical Review E*, 78:045601+. doi:10.1103/physreve.78.045601. Cited on page 35.

Sens-Schönfelder, C. and U. Wegler (2006). Passive image interferometry and seasonal variations of seismic velocities at Merapi Volcano, Indonesia. *Geophysical Research Letters*, 33(21):L21302+. doi:10.1029/2006gl027797. Cited on pages 2 and 35.

Sens-Schönfelder, C. and U. Wegler (2011). Passive image interferometry for monitoring crustal changes with ambient seismic noise. *Comptes Rendus Geoscience*, 343(8-9):639–651. doi:10.1016/j.crte.2011.02.005. Cited on page 3.

Shapiro, N. M. and M. Campillo (2004). Emergence of broadband Rayleigh waves from correlations of the ambient seismic noise. *Geophysical Research Letters*, 31(7):L07614+. doi:10.1029/2004gl019491. Cited on pages 2 and 31.

Shapiro, N. M., M. Campillo, L. Stehly, and M. H. Ritzwoller (2005). High-Resolution Surface-Wave Tomography from Ambient Seismic Noise. *Science*, 307(5715):1615–1618. doi:10.1126/science.1108339. Cited on pages 2 and 33.

Shapiro, S. (2003). Elastic piezosensitivity of porous and fractured rocks. *Geophysics*, 68(2):482–486. doi:10.1190/1.1567215. Cited on pages 64 and 75.

Shapiro, S. and A. Kaselow (2005). Porosity and elastic anisotropy of rocks under tectonic stress and pore-pressure changes. *Geophysics*, 70(5):N27–N38. doi:10.1190/1.2073884. Cited on pages 64 and 75.

Sheffels, B. M. (1990). Lower bound on the amount of crustal shortening, in the central Bolivian Andes. *Geology*, 18(9):812–815. doi:10.1130/0091-7613(1990)018%3C0812:lbotao%3E2.3.co;2. Cited on page 7.

Skinner, B. J. (1966). Thermal Expansion. In *Handbook of Physical Constants* (edited by S. P. Clark), volume 97 of *Geological Society of America Memoirs*, pages 75–96. Cited on page 66.

Snieder, R. (2004). Extracting the Green's function from the correlation of coda waves: A derivation based on stationary phase. *Physical Review E*, 69(4):046610+. doi:10.1103/physreve.69.046610. Cited on page 31.

Snieder, R. (2006). The Theory of Coda Wave Interferometry. *Pure and Applied Geophysics*, 163(2):455–473. doi:10.1007/s00024-005-0026-6. Cited on pages 1 and 35.

Snieder, R., A. Grêt, H. Douma, and J. Scales (2002). Coda Wave Interferometry for Estimating Nonlinear Behavior in Seismic Velocity. *Science*, 295(5563):2253–2255. doi:10.1126/science.1070015. Cited on pages 1 and 35.

Sodoudi, F., X. Yuan, G. Asch, and R. Kind (2011). High-resolution image of the geometry and thickness of the subducting Nazca lithosphere beneath northern Chile. *Journal of Geophysical Research*, 116(B4):B04302. doi:10.1029/2010jb007829. Cited on pages 23 and 24.

Stern, C. R. (2004). Active Andean volcanism: its geologic and tectonic setting. *Revista geológica de Chile*, 31(2):161–206. doi:10.4067/s0716-02082004000200001. Cited on pages 5 and 6.

Takagi, R. and T. Okada (2012). Temporal change in shear velocity and polarization anisotropy related to the 2011 M9.0 Tohoku-Oki earthquake examined using KiK-net vertical array data. *Geophysical Research Letters*, 39(9):L09310+. doi:10.1029/2012gl051342. Cited on pages 3 and 52.

Thurston, R. N. and K. Brugger (1964). Third-Order Elastic Constants and the Velocity of Small Amplitude Elastic Waves in Homogeneously Stressed Media. *Physical Review Online Archive (Prola)*, 133:A1604–A1610. doi:10.1103/physrev.133.a1604. Cited on page 65.

Toupin, R. A. and B. Bernstein (1961). Sound Waves in Deformed Perfectly Elastic Materials. Acoustoelastic Effect. *Journal of the Acoustical Society of America*, 33(2):216–225. doi:10.1121/1.1908623. Cited on pages 58 and 64.

Tsai, V. C. (2011). A model for seasonal changes in GPS positions and seismic wave speeds due to thermoelastic and hydrologic variations. *J. Geophys. Res.*, 116(B4):B04404+. doi:10.1029/2010jb008156. Cited on page 61.

Wapenaar, K., D. Draganov, R. Snieder, X. Campman, and A. Verdel (2010). Tutorial on seismic interferometry: Part 1 — Basic principles and applications. *Geophysics*, 75(5):75A195–75A209. doi:10.1190/1.3457445. Cited on pages 33 and 34.

Weaver, R. and O. Lobkis (2001). Ultrasonics without a Source: Thermal Fluctuation Correlations at MHz Frequencies. *Physical Review Letters*, 87(13):134301+. doi:10.1103/physrevlett.87.134301. Cited on page 2.

Weaver, R. and O. Lobkis (2002). On the emergence of the Green's function in the correlations of a diffuse field: pulse-echo using thermal phonons. *Ultrasonics*, 40(1-8):435–439. doi:10.1016/s0041-624x(02)00156-7. Cited on page 2.

Wegler, U. and B.-G. Lühr (2001). Scattering behaviour at Merapi volcano (Java) revealed from an active seismic experiment. *Geophysical Journal International*, 145(3):579–592. doi:10.1046/j.1365-246x.2001.01390.x. Cited on page 70.

Wegler, U., B. G. Lühr, R. Snieder, and A. Ratdomopurbo (2006). Increase of shear wave velocity before the 1998 eruption of Merapi volcano (Indonesia). *Geophysical Research Letters*, 33(9):L09303+. doi:10.1029/2006gl025928. Cited on page 1.

Wegler, U., H. Nakahara, C. Sens-Schönfelder, M. Korn, and K. Shiomi (2009). Sudden drop of seismic velocity after the 2004 Mw 6.6 mid-Niigata earthquake, Japan, observed with Passive Image Interferometry. *Journal of Geophysical Research*, 114(B6):B06305+. doi:10.1029/2008jb005869. Cited on pages 3 and 74.

Wegler, U. and C. Sens-Schönfelder (2007). Fault zone monitoring with passive image interferometry. *Geophysical Journal International*, 168(3):1029–1033. doi:10.1111/j.1365-246x.2006.03284.x. Cited on pages 3 and 35.

Winkler, K. W. and X. Liu (1996). Measurements of third-order elastic constants in rocks. *The Journal of the Acoustical Society of America*, 100(3):1392–1398. doi:10.1121/1.415986. Cited on pages 65 and 66.

Winkler, K. W. and L. McGowan (2004). Nonlinear acoustoelastic constants of dry and saturated rocks. *Journal of Geophysical Research*, 109(B10):B10204+. doi:10.1029/2004jb003262. Cited on pages 65 and 66.

Wright, M. H. (1996). Direct search methods: Once scorned, now respectable. In *Numerical Analysis 1995: Proceedings of the 1995 Dundee Biennial Conference in Numerical Analysis* (edited by D. F. Griffiths and G. A. Watson), pages 191–208. Addison Wesley Longman, Harlow, UK. Cited on page 51.

Yamamoto, M. and H. Sato (2010). Multiple scattering and mode conversion revealed by an active seismic experiment at Asama volcano, Japan. *Journal of Geophysical Research*, 115(B7):B07304+. doi:10.1029/2009jb007109. Cited on page 70.

Yuan, X., S. V. Sobolev, R. Kind, O. Oncken, G. Bock, G. Asch, B. Schurr, F. Graeber, A. Rudloff, W. Hanka, K. Wylegalla, R. Tibi, C. Haberland, A. Rietbrock, P. Giese, P. Wigger, P. Rower, G. Zandt, S. Beck, T. Wallace, M. Pardo, and D. Comte (2000). Subduction and collision processes in the Central Andes constrained by converted seismic phases. *Nature*, 408(6815):958–961. doi:10.1038/35050073. Cited on page 7.

Yukutake, H., T. Nakajima, and K. Doi (1988). In situ measurements of elastic wave velocity in a mine, and the effects of water and stress on their variation. *Tectonophysics*, 149(1-2):165–175. doi:10.1016/0040-1951(88)90124-2. Cited on pages 1 and 2.

Zimmerman, R. W., W. H. Somerton, and M. S. King (1986). Compressibility of porous rocks. *Journal of Geophysical Research*, 91(B12):12765–12777. doi:10.1029/jb091ib12p12765. Cited on page 64.

Danksagung

Als erstes möchte ich Rainer Kind dafür danken, dass er mir ermöglichte mich mit einem sehr interessanten Thema zu beschäftigen. Weiterhin danke ich ihm für die exzellente Betreuung und den gewährten Freiraum bei meiner Promotion. Ich möchte auch Christoph Sens-Schönfelder danken, der mich im späteren Abschnitt meiner Promotionszeit, als ich mich mit der Ausnutzung des seismischen Rauschens beschäftigte, durch zahlreiche Anregungen und Diskussionen unterstützte. Außerdem möchte ich mich bei ihm für die gute Zusammenarbeit, insbesondere bei der Erstellung der Veröffentlichung für das Journal of Geophysical Research, bedanken. Ich möchte Christoph Sens-Schönfelder, Rainer Kind und Frederik Tilmann für das Korrekturlesen dieses und des beim JGR eingereichten Manuskripts und die daraus resultierenden Verbesserungsvorschläge danken. Danken möchte ich meinem Kollegen und Leidensgenossen Felix Schneider für zahlreiche, interessante Diskussionen, gemeinsamem Aha-Momente und allgemein eine schöne Zeit im Büro und darüber hinaus. Ich danke auch allen anderen Mitarbeitern in der Arbeitsgruppe Seismologie des Geoforschungszentrums in Potsdam für die angenehme und offene Arbeitsatmosphäre. Ich danke insbesondere den anderen Doktoranden Amerika, Felix, Martina, Mohammed, Muzli, Peter und Shantanu, die beim gemeinsamen Plauschen der Motivation zum Steigen verhalfen.

Ich danke den Menschen, die es mir ermöglichten bei mehreren Feldeinsätzen dabei zu sein. Felix Schneider, Ben Heit, Xiaohui Yuan, Shantanu Pandey und Forough Sodoudi danke ich für die schöne Zeit in Spanien beim Aufbau von seismischen Stationen sowie Günter Asch für die gemeinsame Zeit in der Atacama-Wüste und die lecker gegrillten Hähnchen.

Ich möchte mich bei Christoph Sens-Schönfelder, Michael Korn und Klaus Dieter Bataille bedanken, die mir ermöglicht haben, einen Monat an der Universidad de Concepción zu arbeiten. Marisol und Klaus Bataille danke ich für die tolle Gastfreundschaft in Concepción.

Ich möchte mich bei Günter Asch, Bernd Schurr, den französischen Kollegen und allen anderen involvierten Menschen für den Aufbau und die Instandhaltung der seismischen Stationen des IPOC-Netzwerks in Nordchile sowie für die Veröffentlichung der Daten bedanken. Pia Victor danke ich für die Bereitstellung der Temperatur-Daten der Creepmeter-Station nahe des Salar Grande. Großer Dank gilt den Entwicklern von ObsPy. Ich finde, dass sie mit der integrativen Veröffentlichung dieser Software als Open

Source hervorragende Arbeit und einen großen Dienst für die Seismologie-Community leisten. Außerdem möchte ich mich auch bei den Entwicklern der MIIC-Software, Eraldo Pomponi und Christoph-Sens-Schönfelder, bedanken.

Letztendlich danke ich meiner Familie, meinen Freunden und meiner Freundin Sophie für die Unterstützung während, vor und nach meiner Promotion!

Erklärung

Hiermit versichere ich, dass ich die vorliegende Arbeit selbständig verfasst, keine anderen als die angegebenen Quellen und Hilfsmittel benutzt sowie Leistungen anderer nicht als meine eigenen ausgegeben habe.

Tom Richter
Potsdam, Januar 2014